technische universität
dortmund

FAKULTÄT PHYSIK - EXPERIMENTELLE PHYSIK EVB

Study of Extragalactic Very High Energy Gamma Ray Sources:

Monitoring and Discoveries of Blazars with the MAGIC Telescopes

DISSERTATION

ZUR ERLANGUNG DES AKADEMISCHEN GRADES EINES
DOKTORS DER NATURWISSENSCHAFTEN
(DR. RER. NAT.)

VORGELEGT VON

DIPL.-PHYS. MALWINA UELLENBECK

Dortmund, Juli 2013

Prüfer der Dissertation:
Prof. Dr. Dr. Wolfgang Rhode
Prof. Dr. Carsten Westphal

ABSTRACT

This thesis is dedicated to the young field of extragalactic **V**ery **H**igh **E**nergy (VHE) γ-ray astrophysics. In particular, to extragalactic sources like the **A**ctive **G**alactic **N**ucleus (AGN), one of the most powerful sources of energy known so far in the Universe, which are studied in detail in the energy range from 70 GeV to 10 TeV with the **M**ajor **A**tmospheric **G**amma **I**maging **C**herenkov (MAGIC) telescopes. This type of extragalactic sources contain a **S**uper **M**assive **B**lack **H**ole (SMBH) inside of the mass of $(10^6 - 10^{10})M_\odot$. It is believed that a SMBH converts the potential energy of matter in an accretion process to radiation and collimated jets with an particle outflow. As of now, there exist various subclasses of AGNs. The most numerous detected subclass, where the objects present one jet oriented at small angles with respect to the line of sight of an observer, is known as a blazar. Until today, most of the blazars in the VHE regime have been discovered within the last ten years of ground based telescopes using the **I**maging **A**ir **C**herenkov **T**echnique (IACT). The three major IACT experiments are MAGIC, **H**igh **E**nergy **S**tereoscopic **S**ystem (H.E.S.S.) and **V**ery **E**nergetic **R**adiation **I**maging **T**elescope **A**rray **S**ystem (VERITAS). The numerous discoveries of AGNs among others have been possible thanks to permanent improvements in sensitivity and the extension of the energy range of these instruments.

This thesis is focused on a study of blazars and their redshift dependent properties, starting from the very first discovery of these sources in the TeV range. In particular, the research study presented in this work can be divided into an experimental/analytical and a phenomenological part, the former conducted as a member of the MAGIC Collaboration. The first part of this work is dedicated to a long-term study of the blazar 1ES 1959+650 during a seven year survey of the MAGIC observation. Furthermore, new blazar discoveries and detections of 1ES 0033+595, B3 0133+388 and PKS 1717+177 in the VHE γ-ray range are presented. In the second part of the thesis the results of the phenomenological work are reported, where a population study for all (since today) known blazars (with well known spectral parameters) is performed with a special focus on the evolution of the Universe.

1ES 1959+650 one of the closest ($z = 0.48$) known VHE γ-ray emitting blazars was observed regularly with the MAGIC telescopes from 2005 to 2012. In this

long-term study, the data collected from 2009 to 2012 is combined with previous observations (from 2005 to 2008). This very extended survey makes 1ES 1959+650 one of the longest and unique studied blazar at energies above 300 GeV. A conclusion of this long-term study is that the overall flux above 300 GeV from 2005 to 2012 shows only a modest variability on yearly timescale within a factor 3 corresponding to a variation between 4% to 12% of the Crab Nebula flux. Only one distinct "flare" (strong flux enhancement) on May 30th 2009 has been detected during the long-term study. The integral flux of this flare corresponds to ~70% of the Crab Nebula flux. Interestingly evidence for a correlation with a delay of 1-2 days (where γ-radiation appear to lead radio) between the flux levels in simultaneously taken radio and VHE γ-ray data during the flare has been found. This result strongly indicates that the nearly coincident flux enhancement in both wavelengths have a common emission region which is undoubtedly produced in the jet region and not in the **B**road **L**ine **R**egion (BLR).

In the case of the uncertain distance (HBL) object 1ES 0033+595 the discovery at VHE γ-ray (E>100 GeV) is reported. 1ES 0033+595 was detected at clear significance level of 5.5 σ. The temporal study yields a low flux level of (2.2±0.4)% of the Crab Nebula flux above 150 GeV with no significant variability. Since the redshift of this source is uncertain, a new value of $z = 0.34 \pm 0.5$ has been derived using an empirical approach based on comparing the spectral slopes in the **H**igh **E**nergy (HE) and VHE γ ranges.

Within the framework of this thesis, the discovery of a second blazar known as B3 0133+388 (RGB 0136+3905) with an unknown redshift is reported. This blazar is currently still not fully classified as a **H**igh frequency peaked **BL** Lac (HBL) class object. Different authors argue that this source should be classified as a **I**ntermediate frequency peaked **BL** Lac (IBL) object due to it's synchrotron peak at $\nu_{\mathrm{peak}} = 10^{16.59}$ Hz. As a result of the data analysis in this work B3 0133+388 has been detected at significance level of 5.6 σ. However, no significant variability could be detected and the temporal study yields a flux level of (3.6±0.9)% of the Crab Nebula flux above 150 GeV. Similar to 1ES 0033+595 a new redshift estimation was performed on the HE and VHE γ-ray spectra. The new redshift was calculated to be $z = 0.46 \pm 0.05$.

The final experimental and analytical part of this thesis deals with the **L**ow frequency peaked **BL** Lac (LBL) object PKS 1717+177. This source was detected at a significance level of 6 σ in the observation period between April to August 2009 in stand-alone mode with M I. It is one of only four LBL objects currently seen in the VHE γ-ray range. A preliminary temporal study indicates a flux

level of ~4% of the Crab Nebula flux above 200 GeV.

The phenomenological part of this thesis consist of a population study off all currently known LBL, IBL and HBL objects in low state with a well measured VHE γ-ray spectra. The spectral properties of the observed sources are compared and correlated with each other. The main results are:

1. A strong correlation of the spectral softening and the source distance has been found. Reasonable explanations could be on the one hand the evidence of VHE γ-ray absorption on the **E**xtragalactic **B**ackground **L**ight (EBL) and on the other an artifact due to TeV blazar selection bias.

2. The obtained γ-**R**ay **h**orizon (GRH) shows that in most cases the IACT observations are indeed detecting a decreasing flux with larger redshifts given by the GRH feature. The estimations from different EBL models show that the Universe is more transparent to VHE γ-rays than previously thought and that further investigation of the EBL in order to understand the opacity of VHE γ-ray photons when traveling throughout the Universe evolution are needed.

The improved sensitivity due to the stereoscopic upgrade of the MAGIC telescopes was crucial in order to discover new blazars in the low energy range (70 – 250 GeV) of the VHE γ-ray regime and thus in obtaining a unique population study during this work. Future observations with sensitivity improved IACT instruments like the **C**herenkov **T**elescope **A**rray (CTA) have the potential to probe the here arose questions in a more quantitative manner.

KURZFASSUNG

Diese Arbeit widmet sich dem jungen Feld der extragalaktischen sehr hochenergetischen γ-Astroteilchenphysik. Insbesondere behandelt die Arbeit Aktive Galaktische Kerne (AGN), die derzeit zu den stärksten Energiequellen im Universum gehören und die mit den MAGIC Teleskopen auf der Kanarischen Insel La Palma im sehr hochenergetischen (VHE) γ-Strahlungsbereich von 70 GeV bis 10 TeV beobachtet werden. Diese Art von Galaxien bestehen in der Kernregion aus einem supermassereichen Schwarzen Loch mit einer Masse zwischen $(10^6 - 10^{10})M_\odot$, um das sich eine Akkretionsscheibe bildet. Heutzutage wird angenommen, dass die potentielle Energie der Materie die durch das supermassereiche Schwarzen Loch angezogen wird zur Bildung von Strahlung und gebündelten Jets (relativistische Ausströmungen von Plasma die Längen bis zu Megaparsec erreichen können) führt. Diese bilden sich senkrecht zur Ebene der Akkretionsscheibe. Gegenwärtig werden AGNs vorrangig nach dem Winkel zwischen dem Beobachter und der Achse des Jets klassifiziert. Die derzeit am häufigste detektiere Unterklasse von AGN sind die Blazare, bei denen wir als Beobachter direkt oder mit wenigen Grad Abweichung in den Jet hineinschauen. In dem VHE γ-Strahlungsbereich wurden die meisten Blazare in den letzten zehn Jahren mit Hilfe der abbildenden Luft-Cherenkov-Teleskope entdeckt, zu denen auch die MAGIC Teleskope gehören. Dank der permanenten Verbesserungen solcher Experimente in Hinblick auf die Detektorempfindlichkeit sowie die Erweiterung der Energiebereiche konnten somit zahlreiche neue Objekte im Bereich der VHE γ-Strahlung entdeckt werden.
Der besondere Fokus dieser Arbeit liegt auf der Untersuchung von Blazaren und ihren rotverschiebungsabhängigen Eigenschaften, beginnend mit der ersten Entdeckung dieser Quellen im VHE γ-Bereich. Insbesondere gliedert sich diese Arbeit in einen experimentellen/analytischen und einen phänomenologisch Teil. In dem ersten experimentellen Teil wird eine Langzeitstudie des Blazaren 1ES 1959+650 während einer siebenjährigen Beobachtung mit MAGIC vorgestellt. Darüber hinaus werden in diesem Kontext die Neuentdeckungen und Detektionen der Blazaren 1ES 0033+595, B3 0133+388 sowie PKS 1717+177 in VHE γ-Strahlung-Bereich präsentiert. Im zweiten Teil der Arbeit werden die Ergebnisse der phänomenologische Studie dargelegt. Dort wird eine Populationsstudie aufgezeigt, in der die bis heute bekannten VHE γ-Strahlungsblazare (mit bekannten Spektralparametern) mit besonderem Fokus auf die Entwicklung des Universums untersucht werden.

Der Blazar 1ES 1959+650 gehört zu den nähsten ($z = 0,48$) bekannten VHE γ-Strahlungsquellen, die regelmäßig mit den MAGIC Teleskopen zwischen 2005 und 2012 beobachtet wurden. In dieser Arbeit werden insbesondere die Daten aus den Beobachtungsjahren zwischen 2009 und 2012 präsentiert, die anschließen mit früheren Beobachtungen (zwischen 2005 und 2008) verglichen werden. Die hier präsentierte Studie von 1ES 1959+650 gehört derzeit zu den wenigen, die je über einen so langen Zeitraum für einen Blazaren oberhalb von 300 GeV durchgeführt wurde. Aus der Langzeitstudie konnte ermittelt werden, dass der Fluss der VHE γ-Strahlung oberhalb von 300 GeV in dem Zeitraum zwischen 2005 und 2012 nur eine geringe Variabilität (Faktor~3) aufweist. Diese entspricht zum Vergleich einem Fluss von (4 – 12)% des Krebsnebelflusses. Des Weiteren konnte auschließlich am 30. Mai 2009 ein γ-Strahlungsausbruch ein sogenannter "Flare" beobachtet werden. Die mittlere Flussstärke dieses Flares betrug ~70% des Krebsnebelflusses. Im Flare Kontext konnte eine Korrelationsstudie mit anderen Multiwellenlängenbeobachtungen durchgeführt werden. Bei der Untersuchung zwischen dem Radiobereich bei 15 GHz und dem VHE γ-Bereich konnte ein fast gleichzeitiger Flussanstieg (Verzögerung von 1 – 2 Tagen) in beiden Wellenlängenbereichen gefunden werden. Dieses Ergebnis ist ein sehr starkes Indiz dafür, dass die in beiden Fällen gemessene starke Flusszunahme einen gemeinsamen Ursprungsort haben muss, die zweifellos in der Jet-Region und nicht in der BLR vorzufinden ist.

Erstmalig wurde im Zuge dieser Arbeit am 27. Oktober 2011 in dem VHE γ-Bereich der Blazar 1ES 0033+595 mit den beiden MAGIC Teleskopen entdeckt. Dieser konnte mit einer Signalstärke von 5,5 σ nachgewiesen werden. Die gefundene Lichtkurve für den VHE γ-Bereich zeigt einen mittleren Fluss von (2,2±0,4)% des Krebsnebelflusses oberhalb von 150 GeV in der keine signifikanten Variabilitäten festgestellt werden konnten. Da die Rotverschiebung dieser Quelle unsicher ist, wurde ein neuer Wert von $z = 0,34 \pm 0,5$ mit dem empirischen Ansatz, basierend auf dem Vergleich der Spektralindizes in den HE und VHE γ-Berichen, bestimmt.

Im Rahmen dieser Arbeit ist auch eine zweite Entdeckung eines Blazars mit der Bezeichnung B3 0133+388 (RGB 0136+3905), der ebenfalls eine unbekannte Rotverschiebung besitzt, gelungen. Die Analyse der Beobachtungsdaten resultierte in der Detektion dieses Objektes bei einer Signalstärke von 5,6 σ. Des Weiteren konnte aus diesen Daten keine erhöhte Variabilität in der Lichtkurve, in der ein mittlerer Fluss von (3,6±0,9)% des Krebsnebelflusses oberhalb von 150 GeV gemessen wurde, festgestellt werden. Da die Rotverschiebungen auch für diese Quelle unbekannt ist, erfolgte ähnlich zur vorherigen

Quelle 1ES 0033+595 eine neue Rotverschiebungsbestimmung. Die daraus resultierende Rotverschiebung wurde zu $z = 0,46 \pm 0,05$ berechnet.

Der letzte experimentelle und analytische Teil dieser Arbeit befasst sich mit der Analyse des Blazars PKS 1717+177, der eine Rotverschiebung bei $z = 0,137$ besitzt. Dieser Blazar wurde bei einem Signifikanzniveau von $6\,\sigma$ nachgewiesen. Dieses Objekt ist derzeit das vierte, das im VHE γ-Bereich detektiert wurde, welches die Synchrotron-Energieverteilung im optischen/ultravioletten Bereich des Spektrums ihr Maximum hat. Die vorläufige Lichtkurve zeigt einen mittleren Fluss von ~4% des Krebsnebelflusseses oberhalb von 200 GeV.

Der phänomenologische Teil dieser Arbeit bestehen aus einer Populationsstudie in der alle derzeit bekannten Blazare, die im Ruhezustand ein gut vermessenes VHE γ-Spektrum aufweisen, untersucht werden. Die Eigenschaften der Spektralparameter dieser Objekte werden untereinander verglichen und korreliert. Die wichtigsten Ergebnise dieser Studie sind:

1. Es konnte eine starke Korrelation zwischen den Spektralindizes und der Rotverschiebung gefunden wurden. Eine mögliche Erklärungen für diesen Zusammenhang könnte auf die extragalaktische Hintergrundstrahlung (EBL) hindeuten, die einen "Abdruck" aufgrund der VHE γ-Strahlungs-Absorption in den VHE γ-Spektrum hinterlässt. Auf der anderen Seite könnte es sich hierbei aber auch um einen Artefakt, einen Selektions-Bias der Quellen, handeln, der in diesem Fall die starke Korrelation verursacht.

2. Der aus den Ergebnissen dieser Arbeit gewonnene γ-Strahlen Horizont (GRH) zeigt, dass in den meisten Fällen die IACT Beobachtungen in der Tat einen abnehmenden Fluss mit größerer Rotverschiebungen, die durch die GRH Funktion gegeben ist, detektieren. Es zeigt sich aber auch, dass das Universum transparenter für die VHE γ-Strahlung ist, als man bisher angenommen hatte.

Die Erweiterung des MAGIC Teleskops zu einem Stereo-System war entscheiden bei der Entdeckung von neuen Blazaren im VHE γ-Bereich mit großer Rotverschiebung sowie auch bei der Erstellung der einzigartigen Populationsstudie in dieser Arbeit. Zukünftige Beobachtungen im VHE γ-Bereich mit einer weiteren Empfindlichkeitssteigerung der IACT Instrumente, wie Beispielsweise das geplante CTA Projekt, werden das Potenzial haben die hier während der Arbeit entstandenen Fragen präzise beantworten zu können.

CONTENTS

List of Acronyms and Abbreviations

2MASS	**2** **M**icron **A**ll **S**ky **S**urvey
ADC	**A**nalog **D**igital **C**onverter
AGILE	**A**strorivelatore **G**amma a **I**mmagini **Le**ggero
AGN	**A**ctive **G**alactic **N**ucleus
ADC	**A**nalog **D**igital **C**onverter
AMC	**A**ctive **M**irror **C**ontrol
BLR	**B**road **L**ine **R**egion
BAT	**B**urst **A**lert **T**elescope
CATS	**A**strophysical **C**atalogues **S**upport **S**ystem
CANGAROO	**C**ollaboration of **A**ustralia and **N**ippon (Japan) for a **GA**mma **R**ay **O**bservatory in the **O**utback
CBL	**C**osmic **B**ackground **L**ight
CoG	**C**enter **o**f **G**ravity
CMB	**C**osmic **M**icrowave **B**ackground
CRB	**C**osmic **R**adio **B**ackground
CIB	**C**osmic **I**nfrared **B**ackground
CUVOB	**C**osmic **U**ltra-**V**iolet **O**ptical **B**ackground
CXB	**C**osmic **X**-ray **B**ackground
CGB	**C**osmic γ-ray **B**ackground
CCD	**C**harge **C**oupled **D**evice
CCF	**C**ross **C**orrelation **F**unction

CORSIKA	**CO**smic **R**ay **SI**mulations for **KA**scade
CR	**C**osmic **R**ays
CTA	**C**herenkov **T**elescope **A**rray
DAQ	**D**ata **A**c**Q**uisition
DRS2	**D**omino **R**ing **S**ampler 2
DT	**D**iscriminator **T**hreshold
EBL	**E**xtragalactic **B**ackground **L**ight
EC	**E**xternal **C**ompton
EGRET	**E**nergetic **G**amma **R**ay **E**xperiment **T**elescope
FACT	**F**irst G-**A**PD **C**herenkov **T**elescope
FADC	**F**lash **A**nalog **D**igital **C**onverter
FoV	**F**ield **o**f **V**iew
FSRQ	**F**lat **S**pectrum **R**adio **Q**uasar
FWHM	**F**ull **W**ith **H**alf **M**aximum
GRB	**G**amma-**R**ay-**B**urst
GRH	γ-**R**ay **h**orizon
HBL	**H**igh frequency peaked **BL** Lac
HE	**H**igh **E**nergy
HEGRA	**H**igh **E**nergy **G**amma **R**ay **A**stronomy
H.E.S.S.	**H**igh **E**nergy **S**tereoscopic **S**ystem
IACT	**I**maging **A**ir **C**herenkov **T**echnique
IAC	**I**maging **A**ir **C**herenkov
IBL	**I**ntermediate frequency peaked **BL** Lac
IC	**I**nverse **C**ompton
ICRC 2011	**I**nternational **C**osmic **R**ay **C**onference 2011

IGMF	**I**nter **G**alactic **M**agnetic **F**ield
INTEGRAL	**Inte**rnational **G**amma-**R**ay **A**strophysics **L**aboratory
IR	**I**nfra**R**ed
IRAS	**I**nfra**R**ed **A**stronomical **S**atellite
IRAM	**I**nstitut de **R**adio**A**stronomie **M**illimétrique
LBL	**L**ow frequency peaked **BL** Lac
LED	**L**ight **E**mitting **D**iodes
LUT	**L**ook **U**p **T**ables
MAGIC	**M**ajor **A**tmospheric **G**amma **I**maging **C**herenkov
MARS	**M**AGIC **A**nalysis and **R**econstruction **S**oftware
MHD	**M**agneto **H**ydro **D**ynamic
MC	**M**onte **C**arlo
MRF	**M**etagalactic **R**adiation **F**ield
MOJAVE	**M**onitoring **O**f **J**ets in **A**ctive galactic nuclei with **V**LBA **E**xperiments
NOT	**N**ordic **O**ptical **T**elescope
NRAO	**N**ational **R**adio **A**stronomy **O**bservatory
NSB	**N**ight **S**ky **B**ackground
OVRO	**O**wens **V**alley **R**adio **O**bservatory
phe	photoelectrons
PMT	**P**hoto **M**ultiplier **T**ube
PSF	**P**oint **S**pread **F**unktion
PWN	**P**ulsar **W**ind **N**ebula
RATAN	RATAN rus.: Academy of Science Radio Telescope
RF	**R**andom **F**orest

RMS	**R**oot **M**ean **S**quare
ROSAT	**RO**entgen **SAT**elit
RXT	**R**ossi **X**-ray **T**elescope
RXTE	**R**ossi **X**-ray **T**iming **E**xplorer
SED	**S**pectral **E**nergy **D**istribution
SMBH	**S**uper **M**assive **B**lack **H**ole
SNR	**S**uper **N**ova **R**emnant
SSC	**S**ynchrotron **S**elf **C**ompton
ToO	**T**arget **o**f **O**pportunity
TRUEE	**T**ime-dependent **R**egularized **U**nfolding for **E**conomics and **E**ngineering problems
UV	**U**ltra**V**iolet
UVOT	**U**ltra**V**iolet/**O**ptical **T**elescope
USTA	**U**tah **S**even **T**elescope **A**rray
VERITAS	**V**ery **E**nergetic **R**adiation **I**maging **T**elescope **A**rray **S**ystem
VLA	**V**ery **L**arge **A**rray
VLBA	**V**ery **L**ong **B**aseline **A**rray
VLBI	**V**ery **L**ong **B**aseline **I**nterferometry
VHE	**V**ery **H**igh **E**nergy
XRT	**X**-**R**ay **T**elescope

PREFACE

The discovery of infrared radiation in sunlight by Friedrich Wilhelm Herschel in 1800 was one of the most important milestones giving a hint that there must be an invisible form of light beyond the visible spectrum. Fascinating, new discoveries are being made with the technological progress revealing further wavelengths in the range from low frequencies, used for modern radio communication, to γ-radiation with their high frequencies, which are today valuable for studying high-energy objects or regions in the Universe. The discovery of the first VHE γ-ray signal on a 9-standard deviation level by the Whipple collaboration of the Crab Nebula dates back to 1989. Since then, 1989 is assumed as the birth year of ground based γ-ray astrophysics. In the last twenty-five years, a large effort has been done to explore the γ-ray Universe: new experimental techniques have been developed as well as new detectors (both ground based and space borne) have been constructed. Arising from these improved techniques, a very successful field studying VHE γ-ray sources in the energy range from 50 GeV to some tens TeV, from Earth, could be developed. These new techniques were brought and implemented into the third generation of imagining atmospheric Cherenkov telescopes. Today, the three most known imagining atmospheric Cherenkov telescopes are MAGIC, **H**igh **E**nergy **S**tereoscopic **S**ystem (H.E.S.S.) and **V**ery **E**nergetic **R**adiation **I**maging **T**elescope **A**rray **S**ystem (VERITAS).

This thesis presents results achieved with MAGIC, a system of two telescopes located in the Canary island on La Palma, in the field of extragalactic VHE γ-ray astrophysics. In the first place, a detail study of VHE γ-ray emission from the blazar 1ES 1959+650 observed with MAGIC in stand-alone mode and also by the stereoscopic system will be discussed. Moreover, the discoveries of the blazars with the name 1ES 0033+595, B3 0133+388 in the VHE γ-ray range will be presented as well as PKS 1717+177 which was also detected for the first time during this work. Due to different distances and also spectral properties of all four objects a population study including further known VHE γ blazars was also obtained and illustrated in this work. This study based mostly on the interaction of VHE γ-ray photons with the diffuse light distribution in the ultraviolet to hard-infrared wavelengths. It is believed, that this background light (the so-called EBL) contains important evolution informations about the first born stars and prototype galaxies in the early Universe throughout the redshift space. For this reason, the VHE γ-ray astrophysics is a very promising

field that can shed some light in the cosmic evolution.

The thesis work can be thematically divided into three parts:

Part I: The physics behind the VHE γ-ray observations

In Chapter 1 a brief introduction to VHE γ-ray astrophysics and the sources emitting such radiation is given. In particular, the physical mechanisms which are responsible for the emission of VHE γ-ray photons are discussed. Furthermore, the absorption of VHE γ-ray photons by the EBL, which substantially attenuates the measured VHE γ-ray spectra of distant extragalactic sources, as well as its importance for the Universe evolution, is described. At the end, the AGNs the class of objects, this thesis is dedicated to, are introduced.
Chapter 2 is devoted to the unique detection technique so-called IACT of VHE γ-rays by ground based telescopes. A particular importance will be given to the explanation of the development of extended air showers in the atmosphere, which is used as calorimeter in this detection technique, and the subsequent emission of Cherenkov light in the extended air shower itself.
In Chapter 3 the main hardware components and the significant hardware changes of both MAGIC telescopes are described. Emphasis is put on the elements that lead to a significant performance improvement, e.g. the camera and the readout system.
Chapter 4 gives a brief overview of the MAGIC data analysis chain which was used in particular in this thesis. A special focus is also put on the differences between the analysis of a stand-alone and stereoscopic observation and their analysis framework.

Part II: VHE γ-ray extragalactic results

In the second part of the thesis the main emphasis is given to the obtained results from extragalactic VHE γ-ray sources.

The Crab Nebula plays a very important role in the calibration of the VHE γ-ray analysis. This galactic source has a constant high-level flux of γ-rays and thus it is known as the "standard candle" of VHE γ-ray astrophysics. In Chapter 5 the properties of this source as well as one example of a referenced analysis within the MARS framework is presented.
Chapter 6 is dedicated to the seven years of observations of the bright HBL object 1ES 1959+650 observed with the MAGIC telescopes from 2005 to 2012. A special focus lies on the last three years of MAGIC observations where an usual flux enhancement so-called "flare" was detected and on the compar-

ison with previous data. Out of this findings additionally a long term study of the properties of the emitted radiation is performed. In this context especially the energy spectra and light curves are investigated in detail. Furthermore, correlation studies with other wavelengths are finally performed as well es the spectral energy distribution (SED) for this source and the corresponding modeling attempts.
In Chapter 7 the first discovery of the HBL 1ES 0033+595 in the VHE γ-ray range is presented. This is one of the very first sources observed with the stereoscopic system during the commissioning phase in August 2009. For this reason, a special emphasis on the telescopes performance improvement is given. Since optical observations of this source could not resolve the host galaxy for a photometric redshift determination so far a new redshift determination was derived from the HE and VHE γ-ray results. Moreover, the very first results from the temporal and spectral findings and the first SED modeling is finally presented.
In similar way as Chapter 7, Chapter 8 is devoted to another discovery of a blazar with the name B3 0133+388. This source was for the first time observed with MAGIC in November 2009 during stereoscopic observations. Since this source has also an uncertain redshift a new estimation was also performed for this source. Finally, the temporal and spectra analysis results as well as the modeling of the SED for B3 0133+388 will be given.
The last analysis chapter (Chapter 9) deals with a preliminary detection of the low-frequency BL Lac (LBL) object PKS 1717+177. This object was observed from April to August 2009 mostly in the stand-alone mode with M I. The very first temporal and spectral results are discussed in this chapter.

Part III: Phenomenological study

The final part of this thesis is a phenomenological work regarding the blazars and their hidden information about the Universe evolution which can be derived from a population study.

Chapter 10 is devoted to a comparison of the characteristic properties of the sources discussed in this thesis and other well known blazars with known spectral properties. In particular, different correlation studies of characteristics of the observed VHE γ-ray emission are presented. Finally, the GRH will be explained and illustrated for the most known blazars detected so far, giving an outlook towards the opacity of the Universe for VHE γ-ray radiation.

The final and concluding remarks in Chapter 11 summarize the most relevant findings of this thesis and give an outlook towards new source detection

perspectives with the upcoming **C**herenkov **T**elescope **A**rray (CTA).

CHAPTER 1

BRIEF INTRODUCTION TO ASTROPARTICLE PHYSICS

Astroparticle Physics is a new filed of research emerging at the intersection of astronomy, astrophysics, particle physics, detector physics and cosmology. In this Chapter, a brief overview of the history and the current status of astroparticle physics is given. A special focus is addressed to recent developments and still open questions in the cosmic ray field. In addition, it will be explained why photons are the ideal particles to carry fascinating information about the development of the Universe. The point of origin of VHE γ-ray photons like their emitting sources and the physical mechanisms involved will also be discussed in this Chapter.

1.1 Cosmic rays

The early stage of the research filed of astroparticle physics dates back to the beginning of the twenty century. In 1912, Victor Hess, an Austrian physicist, discovered energetic particles coming form the Universe which were today known as **C**osmic **R**ays (CR). In his balloon experiments Victor Hess systematically measured the radiation at altitudes up to 5.3 km during 1911-1912. He found out that the observed ionizing radiation permanently impinging on the Earth's atmosphere and the level of radiation increased considerably with higher altitude. Today, more than 100 year ago, cosmic ray are the elementary particle the astroparticle physics deals with. They consist mainly of charged particles like protons (79%), alpha particles and also heavier nuclei (15%), as well as photons and (to a small fraction) electrons. It is believed, that the energy which can be measured by different experiment is one information cosmic rays can provide, but the most important one (beside also the particle

type) that remains is the location of the astrophysical object and thus their origin. Figure 1.1 illustrates the cosmic ray spectrum measured by different experiments of all particles building the cosmic rays. The spectrum extends over energies from a few hundred MeV to 300 EeV ($=3\times10^{20}$ eV) and show a characteristic spectral signature. It can be described by a segmented power law of the form:

$$\frac{dN}{dE} \propto E^{-\alpha} \tag{1.1}$$

with the spectral index changing from:

$$\alpha = 2.7 \text{ for } 10^{10} < E < 10^{16}\,\text{eV} \tag{1.2}$$

$$\alpha = 3.0 \text{ for } 10^{16} < E < 10^{18}\,\text{eV} \tag{1.3}$$

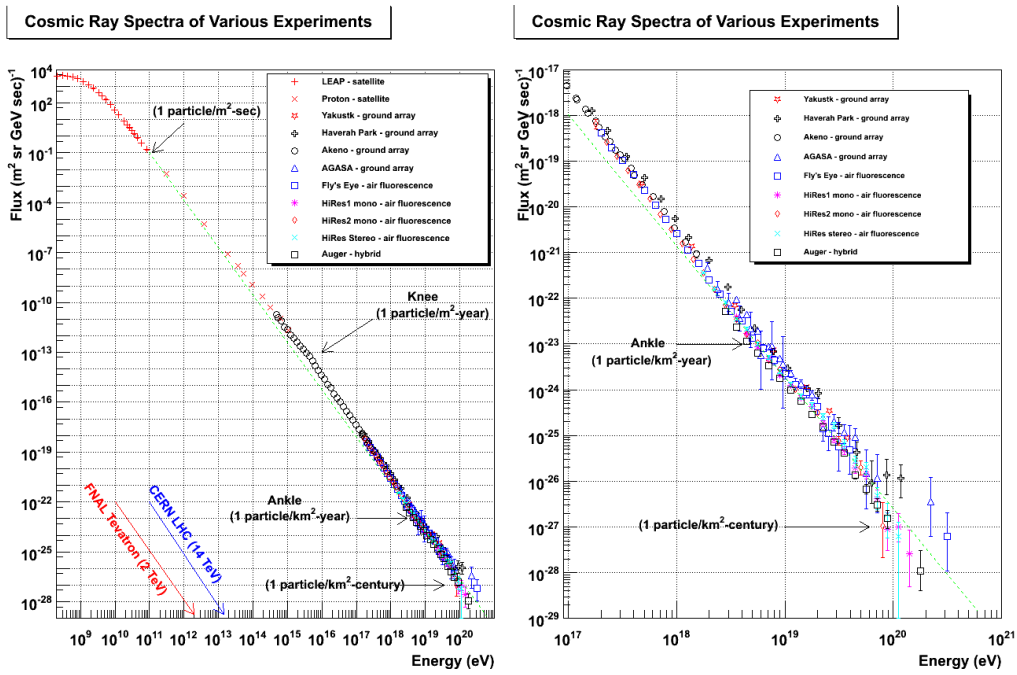

Figure 1.1: The differential cosmic ray energy spectrum measured by different experiments. The left spectrum shows the full energy range, while the right spectrum illustrates the very-high-energy and ultra-high-energy end of the spectrum. The figure is taken from [Han13].

In the cosmic ray spectrum there is a small spectral break near 5×10^{15} eV, commonly refereed to as the *knee*, where the spectrum turns down. In addition to that a second spectral break occurs at 3×10^{18} eV, and is usually called

the *ankle*. In this part the spectrum turns up again. The interpretation of the sources that are responsible for the characteristic shape of the cosmic ray spectrum engage the scientist since more than 50 years. Up to the ankle the cosmic rays are usually interpreted as originating from supernova explosions, i.e. those cosmic ray particles are thought to be galactic in origin; however, since today the details of particle accelaration in this objects are not clear yet. What is also not clear is the point that we still don't know exactly what the origin of the *knee* is, and more interesting what physical processes can give such a rise to particle energies in the energy range from the *knee* to the *ankle*.
Moreover, recent results show that the particle beyond the ankle have to be from the extragalactic origin, because the Lamor radii in the galactic magnetic filed are too large. Another possibility is that this argument could be overcome if those particle were very heavy nuclei as Fe. In addition due to interaction with the **C**osmic **M**icrowave **B**ackground (CMB) there is a strong cut-off expected. Above a threshold energy of 50 EeV ($=5\times10^{19}$ eV) the cosmic ray spectrum is attenuated by photo-hadronic interactions with the CMB photon field, producing unstable delta-resonances and therefore, converting high energetic protons to lower energetic ones, as shown in equation 1.4

$$p+\gamma_{\mathrm{CMB}} \rightarrow \Delta^{+} \rightarrow p+\pi^{0} \text{ or } p+\gamma_{\mathrm{CMB}} \rightarrow \Delta^{+} \rightarrow n+\pi^{+} \tag{1.4}$$

The expected cut-off is called the GZK cut-off after its discoverers Greisen, Zatsepin and Kuzmin. Nowadays, the most challenging interpretation lies in the existence of the high energy cosmic rays beyond the GZK cut-off which is still not understood fully. However, looking at the composition of the particles that represent the cosmic rays it becomes clear that nearly all cosmic rays are charged and therefore suffer deflections from their original locations by the weak magnetic fields ($\ll 1$ Gauss) in the Milky Way and, if the origin location was in the extragalactic space, also by very week extragalactic magnetic fields. Unfortunately, since now, the direction and size of such magnetic fields remains still unknown. Moreover, cosmic rays up to about few times 10^{19} eV are in most cases randomized in their direction and therefore they cannot be associated with any astrophysical objects in this energy range. The only particles that could serve as messengers are the neutral one. There are two types of such particles that fall into this category these are on the one hand the photons and on the other hand the neutrinos. All other, up to now, known neutral particles are too short-lived to survive over large cosmic distances. For example the neutron has a lifetime below 15 minutes in its rest frame and can therefore be ruled out being a promising neutral particle candidate. Comparing Neutrinos and looking at their characteristic it is known that they are weakly interaction particles. In addition, they are also very difficult to detect

and huge volumes of dense material are essential to observe their sparse interactions. Currently, there is only one particle, the VHE γ-ray, that can be used very effective for messengers of their origin locations in the Universe. In the VHE γ-ray Universe the most challenging aspect remains in the interpretation of their two fundamentally different production processes or a combination of these. These are the leptonic and hadronic processes which will be described in details in the following section.

1.2 Gamma-rays and Their Production Processes

As mentioned above, γ-rays, the main object of study of this work, are the only particles that can be used very effective as messengers of their origin in the Universe. Usually they are produced in interactions of charged, high-energy cosmic rays (e^+ or e^- or protons) with different matter of galactic or extragalactic fields. Usually the nomination of γ-ray radiation is used when photons carry an energy higher than some MeV. Today, the range from 10^6 to 10^{20} is assumed as the research band of γ-ray astronomy. This huge energy band is subdivided into 6 areas as listed in Table 1.1. For this work the most relevant area of the energy range in γ-ray astronomy are the HE and VHE γ-ray ranges. The particle interactions that are responsible for such HE and VHE γ-ray emission will be briefly summarized in the following paragraphs, more extended treatments can be found in, e.g. [Lon11, RL79].

Table 1.1: **Definition of the γ-ray band** which is divided into 6 areas of low (LE), high (HE), very high (VHE), ultra high (UHE) and extremely high (EHE) energy particles.

Description	Abbrev.	Energy range
X-rays		$E_\gamma \leq 1$ MeV
γ-rays		$E_\gamma > 1$ MeV
low γ-rays	LE	1 MeV $< E_\gamma <$ 30 MeV
high γ-rays	HE	30 MeV $< E_\gamma <$ 30 GeV
very high γ-rays	VHE	30 GeV $< E_\gamma <$ 100 TeV
ultra high γ-rays	UHE	100 TeV $< E_\gamma <$ 100 PeV
low γ-rays	EHE	100 PeV $< E_\gamma <$ 100 EeV

Up to date it is known that thermal radiation emitted by stars is characterized by black body spectra. This radiation can be explained by photons in the range of visible to **U**ltra**V**iolet (UV) light and in some few cases (AGN accretion disk emission) also up to X-rays in the keV energy range. In order to

reach higher energy ranges, i.e. the HE and VHE γ-ray bands, non-thermal processes are necessary. In AGN, the main topic of this work, one observe a large variety of non-thermal processes that are highlighted below.

Hadronic production: Decay of neutral pions

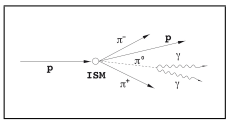

[Ton06]

The decay of neutral pions π^0 take place in hadronic interactions. Whenever accelerated protons or heavier nucleons interact with other protons, photons or nucleons in stellar environments or cosmic gas clouds then dominantly charged and neutral pions are produced. Normally, charged pions decay in two-step process into e^+ or e^- and two neutrinos while neutral pions decay with 99% probability into two γ quanta. The decay processes are the following one:

$$p + X \longrightarrow p^{'} + X^{'} + \pi^+ + \pi^- + \pi^0 \tag{1.5}$$

$$\pi^+ \longrightarrow \mu^+ \nu_\mu \longrightarrow e^+ + \nu_e + \bar{\nu}_\mu + \nu_\mu \tag{1.6}$$

$$\pi^- \longrightarrow \mu^- \bar{\nu}_\mu \longrightarrow e^- + \bar{\nu}_e + \nu_\mu + \bar{\nu}_\mu \tag{1.7}$$

$$\pi^0 \longrightarrow \gamma + \gamma \tag{1.8}$$

Electromagnetic production: The synchrotron radiation

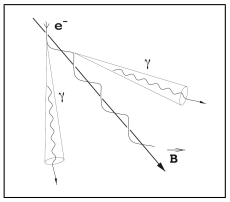

[Ton06]

The synchrotron radiation plays an important role in astroparticle environments with strong magnetic fields that exist in jets of AGN, as described in detail in Subsection 1.5.2. Whenever electrons move near the speed of light they can radiate photons by the synchrotron process as they spiral around a magnetic field as illustrates by the figure in the left top corner. The characteristic peak emission is defined by:

$$E_{\text{peak}} = 5 \cdot 10^{-9} B_\perp \gamma_e^2 \tag{1.9}$$

with the transverse component of the magnetic field $B_\perp$ given in units of Gauss and the electron Lorentz factor γ_e^2. The radiated photons, typically measured in the keV energy range, serve also usually as seed photons for inverse Compton upscatter, as described below.

Electromagnetic production: The inverse Compton scattering

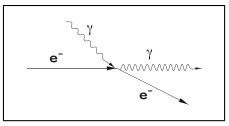

[Ton06]

As mentioned above, in this process electrons e^- upscatter low energy photons ($\gamma_{\text{low energy}}$) over a broad energy range above the initial one and create the VHE gamma (γ_{VHE}) photons.

$$e^- \gamma_{\text{low energy}} \longrightarrow e^-_{\text{low energy}} + \gamma_{\text{VHE}} \tag{1.10}$$

For the case when:

$$E_e E_\gamma \ll m_e^2 c^4 \tag{1.11}$$

the cross-section for this process is known as the Thomson cross-section of the from: $\sigma_T \frac{8}{3} \pi r_e^2$.
In addition, for:

$$E_e E_\gamma \approx\ll m_e^2 c^4 \tag{1.12}$$

the Klein-Nishina formula has to be used followed by the cross-section formula for ultrarelativistic electrons with:

$$\sigma_{KN} = \pi r_e^2 \frac{1}{\epsilon} \left(\ln 2\epsilon + \frac{1}{2} \right) \text{ with } \epsilon = \frac{E_\gamma}{m_e c^2} \tag{1.13}$$

During this interaction the electrons suffer large energy looses and the maximum energy can be reached by:

$$E_{max} \approx\ll 4\gamma^2 E_\gamma \tag{1.14}$$

When photons of energy around few keV are existing and high Lorentz factors of $\gamma 100$ – 1000 are also present then the seed photons are upscattered into the GeV – TeV regime. Such production mechanism take place in one zone **S**ynchrotron **S**elf **C**ompton (SSC) models that will be described in detail in Section 6.10.

Electromagnetic production: The Bremsstrahlung

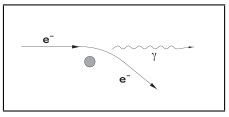

[Ton06]

Bremsstrahlung occurs whenever charged particles are deflected during acceleration in electric fields. This could be the case when an electron approaches a nucleus and its Coulomb field. The interesting aspect is that the bremsstrahlung spectrum follows a power law with the same spectral parameters (photon index) as the one of the particles that are accelerated, in this case electrons.

In contrast to the emission processes of VHE γ-ray photons there are also absorption processes that play a key role in the understanding of the development of the Universe. The most relevant aspects are discussed in the following section.

1.3 The Cosmic Background Light

Creatures on earth are illuminate by the sun (or, indoors, by artificial illumination). Looking from a viewpoint of a single planet the Universe seems to be an empty space, with some clumps of dark matter harboring galaxy clusters and galaxies. Most of the light in the Universe (like the **C**osmic **B**ackground **L**ight (CBL)) is not emitted from stars or other astronomical objects at all but from the **C**osmic **M**icrowave **B**ackground (CMB). The CMB is the light from the early Universe, generated before there were any distinct objects at all, visible today as a so-called black body temperature of T=2.725 K. From Figure 1.2 it becomes visible that there is roughly the same amount of energy in the **C**osmic **I**nfrared **B**ackground (CIB) as in the optical. In consequence, the Universe compromise diffuse electromagnetic radiation, with an energy spanning the entire electromagnetic spectrum. Commonly the different backgrounds are conventionally subdivided into following categories; from low to high energies:

Cosmic Radio Background (CRB)

This part of the cosmic background consist of the diffuse extragalactic light at wavelengths above 1 m. In comparison with the **C**osmic **U**ltra-**V**iolet **O**ptical **B**ackground (CUVOB), which will be described below, it is significantly weaker giving a sign into non thermal processes in the Universe.

Cosmic Microwave Background (CMB)

Up to now, the best-studied background component is that in the microwave range, as depicted in Figure 1.3, which includes the most of the electromagnetic energy of the Universe and fill it almost uniformly. Its origin is from the time when the Universe became transparent therefore the CMB with its temperature of T=3000 K reveals the Universe some 350 000 years after the Big Bang [BS12].
This time corresponds to a redshift of z $\simeq$ 1100 and the peak emission $\nu_{\max}(z = 1100) \simeq 3.1 \times 10^{12}$ Hz is redshift down to $\nu_{\max}(z = 0) = 2.8 \times 10^{11}$ Hz, which can be transfered to the known black body temperature of T=2.725 K. Apart from

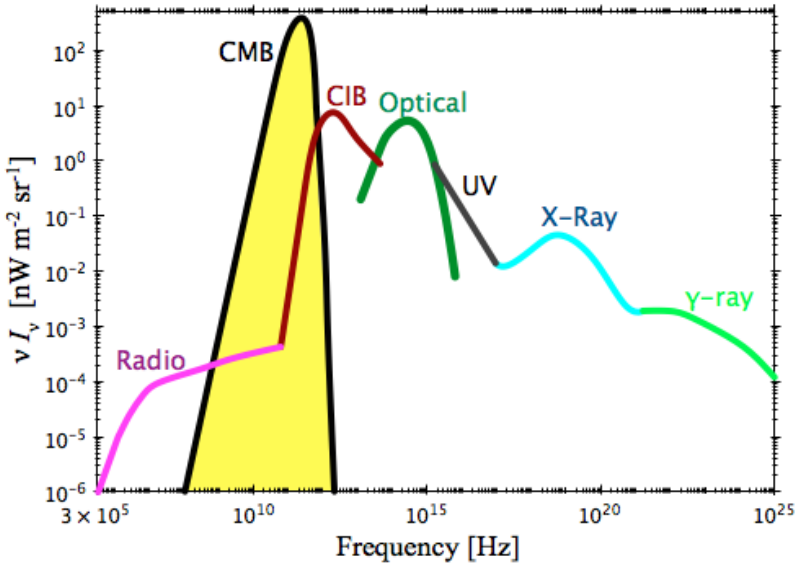

Figure 1.2: The spectrum of the background light filling our Universe. Shown is the intensity of the "background light" integrated over all sources in the Universe. The horizontal axis gives the frequency of electromagnetic radiation — from the radio at the far left, to the CMB, the CIB, optical light in the middle, and on to UV, X-ray and γ-ray light at far right. The height of each curve is proportional to the intensity of the background, the amount of energy falling on a square meter of area per second coming from a particular direction on the sky from [Dol13].

the dominant CMB the other background radiation for instance the γ-ray radiation has its origin after the Universe became transparent, known as the recombination epoch [BS12].

Cosmic Infrared Background (CIB)

As the optical cosmic background contribution the infrared component is also very week. This component has its seeds from stellar light re-emitted by dust which heats up and in turn glows in the infrared. Additionally it is also a accumulated emission from early galaxy populations on large scales. Furthermore, like the CUVOB it contains also a zodiac light contribution plus galactic components (e.g. thermal emission of asteroids) thus it builds all in all a summary of the collective star forming events, star-burst activity and other emitting light cosmic events over the elapsing time.

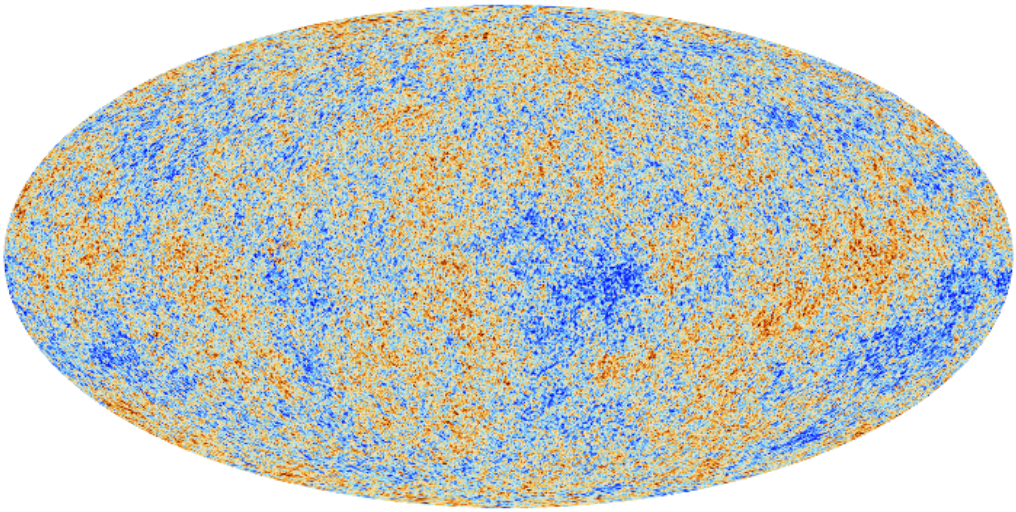

Figure 1.3: Cosmic microwave background seen by Planck observatory. The image was taken from [Pla13].

Cosmic Ultra-Violet Optical Background (CUVOB)

This cosmic background fraction is formed dominantly by photons which are emitted by the stellar light and redshifted by the expansion of the Universe. In particular the observations of an UV extragalactic background is difficult as the Universe begins to be opaque at short range of redshifts resulted from cosmologically distributed Lyman-limit absorbers [BS12]. Moreover, the zodiac light, emitted within our Solar System, plays also an important role in the formation of this background light.

Cosmic X-ray Background (CXB)

Like the **C**osmic γ-ray **B**ackground (CGB), the CXB is composed by a galactic and an extragalactic fraction. For the galactic fraction it is believed that this part has its origin in nearby hot gases heated by falling into clusters of galaxies on large scales. In contrast the extragalactic contribution is thought to be a combination of many unresolved and resolved sources. It is believed that the X-rays are produces by very energetic collisions between particles that happen in the environments around black holes as matter falls in. In this context the X-ray luminosity functions of AGNs are important to test whether the emission from this sources at hard X-rays can explain the CXB. There are already high-quality measurements of the CXB performed by *BeppoSAX*, *Swift* and INTEGRAL. As presented in [MBH$^+$80] the **S**pectral **E**nergy **D**istribution

(SED) peaks around 30 keV with a total intensity of 10% of the CMB. This makes the CXB to the background which contribute most of the electromagnetic output in the Universe (apart from the CMB, which does not originate from individual sources). Therefore it is still vital to understand which sources are in particular responsible for the CXB emission. Recent results show that galaxy cluster with temperature of few keV cannot be the main contributors at the peak around 30 keV, nor can starburst galaxies make a huge fraction of the CXB [BS12], this dominant fraction, as proved by the deep surveys with Chandra, is coming from different AGNs sources.

Cosmic γ-ray Background (CGB)

This part of the CBL contain emission from the Milky Way (our Galaxy) as well as the extragalactic γ-background light. It is believed that the former contribution includes photons emitted during the interaction with the cosmic rays (see Section 1.1) with the interstellar medium of our Galaxy. In contrast the second contribution is today still unknown. However, [VP12] proposed that the intrinsic emission of unresolved, extragalactic point sources, e.g. γ-ray–emitting radio galaxies could be a sizable contribution to the extragalactic γ-background light. Another important issue is the point that many of these extragalactic point sources are in particular sources of HE and VHE γ-rays, which interact with the emitted photons from the CUVOB / CIB and which is today known as the EBL that will be described in detail in Section 1.4.

As depicted in Figure 1.2 the most dominant component of the CBL is indeed coming from the CMB, followed by the CUVOB and CIB components. The latter components (CUVOB and CIB) merging both together forms the EBL which plays an important role in the VHE γ-ray spectra reproduction. This light may interact by pair production with VHE photons

$$\gamma_{\mathrm{VHE}} + \gamma_{\mathrm{EBL}} \rightarrow \mathrm{e}^{+} + \mathrm{e}^{-}$$

from extragalactic objects, e.g. blazars, causing a deformation of the intrinsic spectrum. A short overview about further EBL interactions is given in the following section.

1.4 Absorption of VHE γ-rays: The Extragalactic Background Light

As introduced above the EBL is formed by diffuse light distribution in the UV to hard-**I**nfra**R**ed (IR) wavelengths. This background light contains important informations about the first born stars and prototype galaxies in the early Universe plus a fraction from galaxies throughout the redshift space [BS12]. Today, the spectrum and the strength of the EBL is still not well known. The resulting SED (see Figure 1.4) compromises two distinct peaks: the first peak appears in the near infrared, λ =1 – 2 μm which is thought to be produced by starlight, while the second becomes evident in the range around $\lambda \approx$100 – 200 μm, which has in addition roughly equal brightness and originates from light absorbed and re-emitted by dust. Moreover, the long wavelength end

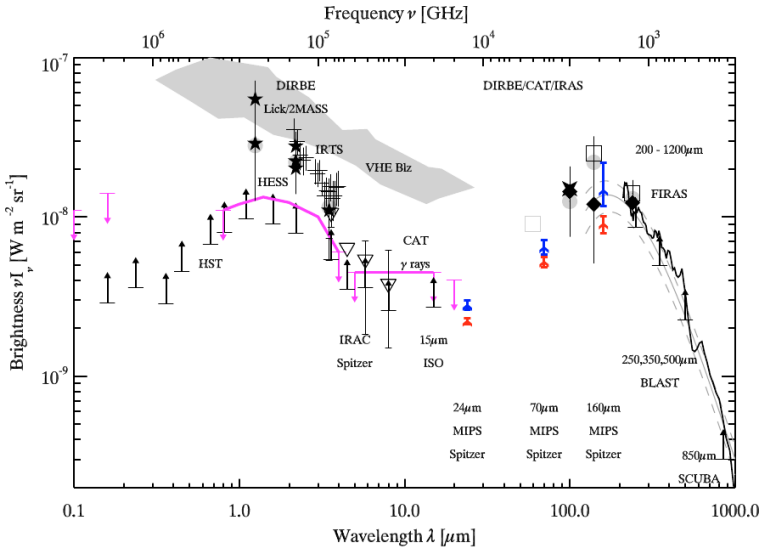

Figure 1.4: EBL measured with direct and indirect techniques in the optical to infrared range. The H.E.S.S. γ-ray data of blazars put strong constrains on the EBL in the range λ=0.8 – 4 μm. The figure is taken from [BDB$^+$10].

($\lambda >$ 300 μm) of the SED is superseded by the 2.725 K CMB radiation [Wag08]. In this context it is important to stress that like any background radiation, except the CMB, the present EBL consist of the integrated electromagnetic radiation which undergoes an evolution process. Thus, the evolution of optical to UV fraction provides valuable informations on the phase of early galaxy formation. Nowadays, there are many direct and indirect measurements from various experiments that contribute to the understanding of the EBL forma-

tion. In case of direct EBL measurements, this contribution suffer from large uncertainties, as they are dominated by large foregrounds of galactic and zodiac light. In contrast, the indirect methods like the source number counts or opacity of TeV photon studies (see Subsection 10.3.4) can provide plenty of upper and lower limits determinations which become more and more stringent (see Figure 1.4). In this context of upper limits determinations, a strong contribution in the range of λ=0.8 – 4 μm is given by the H.E.S.S. experiment using blazar spectra measurements in the TeV range.

Limits from TeV photon study

As mentioned before, TeV photons emitted by extragalactic sources like blazars interact with EBL photons by pair production (see Section 1.3 for formula). The outcome of this interaction imprints in the distant VHE blazar spectra showing an observable deformation. In particular, upper limits on EBL and its energy density can be determinate by assuming basic properties in the original spectrum of extragalactic TeV emitters. The general requirement for such study is a most accurate assumption on the intrinsic shape of this particular sources. One of the key results presented from the H.E.S.S. collaboration is that upper limits obtained with this indirect method are quite close to the lower limits obtained with the other experiments and techniques (see the H.E.S.S. data points in Figure 1.5). Furthermore, as EBL cannot be measured

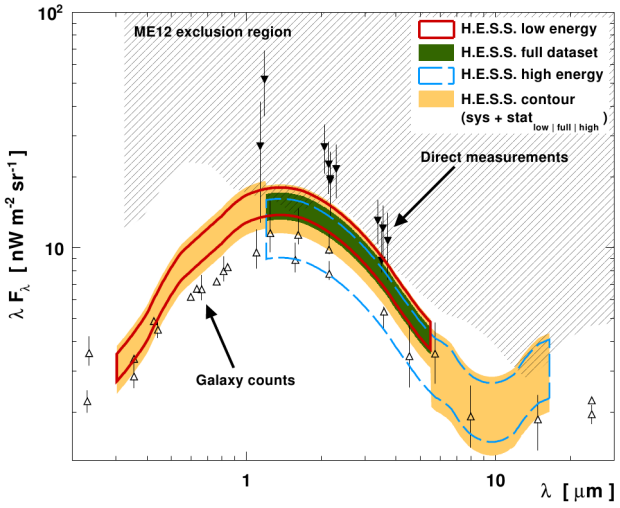

Figure 1.5: EBL measured indirect by H.E.S.S. Lower limits based on galaxy counts and direct measurements are respectively shown with empty upward and filled downward pointing triangles. The figure is taken from [HAA+13b].

directly, empirical or theoretical models have to be employed. Up to date, a couple of models have been developed in the last decade in order to constrain the EBL evolution. One of the most well-known models based on stellar light production and reprocessed in evolving galaxies development was developed by [KD10] and [DPR$^+$10]. More details about this approach will be discussed in Chapter 10.
In this Section the importance of the absorption of VHE γ-ray photons by low energy photons (γ_{EBL}) was pointed out giving an outlook to objects that emit γ-rays. The following section gives an overview about such objects with a focus on extragalactic sources, known as blazars.

1.5 Astrophysical Emitters of γ-rays

As anticipated above, there are various sources in the Universe that are believed to be responsible for the VHE γ-ray emission. Today, these source are subdivided into two groups. The first group consists of galactic sources where **S**uper **N**ova **R**emnant (SNR), **P**ulsar **W**ind **N**ebula (PWN) or binary systems, also known as microquasars, are the original sources of VHE γ-rays. The second group is formed by the extragalactic sources, which are represented by Starburst Galaxies (young galaxies with high star formation rate), **G**amma-**R**ay-**B**urst (GRB)s and AGN, the most powerful sources of energy in the Universe. The latter is also the main topic of this work and thus it is explained in a dedicated Subsection 1.5.1. In case of GRBs, these are flashes of γ-rays which are today associated with extremely energetic explosions. The short duration of GRBs (milliseconds to a few hundred seconds) give a hint of very compact sources that interact with each other. Currently, the origin of such energetic events is still not well understood, but it is assumed that a collision of two neutron stars or even two black holes is the most favored scenario of such energetic emissions. Typically, luminosities of $(10^{51} - 10^{54})\,\mathrm{erg\,s^{-1}}$ are released in this very short phenomena [Wag08].

1.5.1 Active Galactic Nuclei

AGN are today the most known fascinating energetic objects in the Universe. They have been a rich field of research since their discovery in the 1940s by Carly Seyfert [BS12]. Today, there are several number of characteristic of AGN that could be derived from various observations over the years. The central engine is believed to contain a super massive black hole of the mass between $(10^4 - 10^{10})\mathrm{M}_\odot$. Black holes convert the potential energy of matter in an accretion process to radiation and particle outflow.

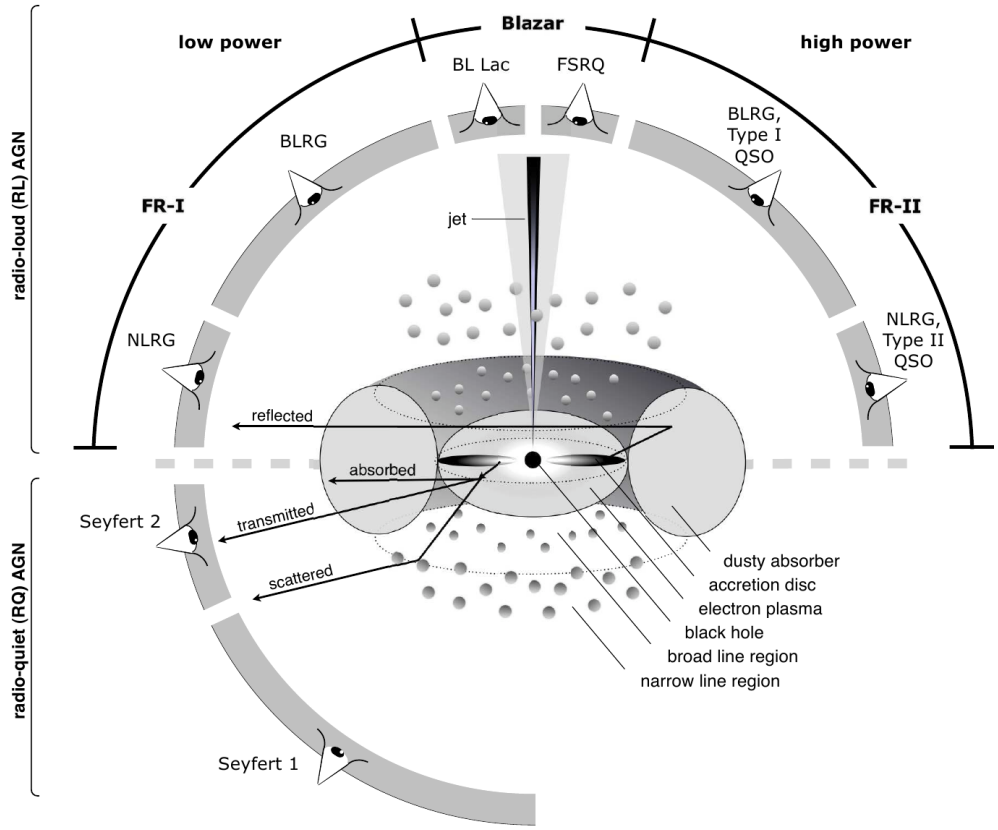

Figure 1.6: The AGN overview. The type of AGN subclasses we see depends on the viewing angle, whether or not the AGN produces a significant jet emission. The figure is taken from [BS12].

Figure 1.6 presents the unified scheme of AGNs which are comprised of a super massive black hole, an accretion disk surrounding the black hole, a large dust torus in the same plane as the accretion disk, randomly distributed molecular clouds and one or two jets perpendicular to the accretion disk. AGNs are in general classified by the variety of observational features as a function of the viewing angle [UP95]. In this classification there are two types of AGNs: on the one hand the radio-loud AGN s which are assumed to display a jet (upper half of Figure 1.6) and on the other hand the radio-quite objects (e.g. Seyfert 1-2) (lower part of Figure 1.6). This classification was obtained due to the reason that radio emission is a signature of relativistic outflow in form of a jet, as it produces at the same time synchrotron radiation [BS12]. In the case when a galaxy is viewed edge-on, i.e. the jets and the line of sight

form an angle of 90°, the thick dust torus is considered to hide the emission from the core. In this particular situation the radio emission from the jets is clearly dominating and the AGN is seen as radio galaxy or as radio-loud AGN [Ste12], [UP95]. When the source is observed under small viewing angle conditions, the synchrotron emission becomes here the dominant radiate from the jet. For a viewing angle of 0°, the observer is directly looking down the jet and the sources that are observed under such particular conditions are named Blazars which will be described in detail below. Further informations about AGNs, their observations, features and classifications can be found in [BS12], [BHH12] and [UP95].

1.5.2 Blazars

The main study of this work is focused on a particular interesting subclass of AGN known as blazars ("blazing quasars"). Up to date, blazars are the most commonly detected extragalactic VHE γ-ray sources with steadily increasing numbers in the very high energy regime (VHE, E> 100 GeV) in the past 15 years of ground-based γ-ray astronomy. They are thought to be AGNs in which a relativistic jet is pointing at the observer, or very close to the observer's line of sight. One of the most known defining features of blazars is the absence of strong, broad emission lines in their optical spectra. In this case, the object is classified as BL Lacertae (BL Lac), named after the prototype source with these properties [UP95]. In contrast, if the emission lines are apparent, the blazar is called **F**lat **S**pectrum **R**adio **Q**uasar (FSRQ). Blazars characteristic properties are strong continuum emission extending from the radio all the way to the γ-ray regime, high polarization (at both optical and radio frequencies) and rapid variability (at all frequencies and on all time scales probed so far). From this type of AGN subclass at least two broad emission components (also known as "camel's back") is detectable, with the bumps being synchrotron and inverse Compton spectra, respectively (see Figure 1.7). The first bump has its maximum in the optical to X-ray band and the second bump is located in the γ-ray bands. Furthermore, depending on the location of the first bump (synchrotron peak) BL Lacs are additionally subdivided into **L**ow frequency peaked **BL** Lac (LBL), **L**ow frequency peaked **BL** Lac (LBL) and **H**igh frequency peaked **BL** Lac (HBL):

LBL This subclass of BL Lacs has its synchrotron peak at low energies (i.e., in the far-IR or IR band or $\nu_{\text{peak}} \leq 10^{14}$ Hz). In addition, their X-ray emission is flat ($\alpha_x \approx 0.4 - 0.7$) due to the rising part of the inverse Compton component [AAA+10c]. Furthermore, LBL blazars generally show higher bolometric luminosities than HBL blazars and in general there is

a trend observed that the higher the peak frequency of the first bump in the SED the lower the overall luminosity, with
$\nu_{\rm peak}^{\rm FSRQs} \leq \nu_{\rm peak}^{\rm LBLs} \leq \nu_{\rm peak}^{\rm IBLs} \leq \nu_{\rm peak}^{\rm HBLs}$.
This relation is commonly called the *blazar sequence* [FMC+98]. A LBL object was also analyzed during this work and the corresponding analysis can be found in Chapter 9.

IBL For this objects the synchrotron emission peaks at intermediate energies (10^{14} Hz $< \nu_{\rm peak} < 10^{15}$ Hz). In this case, the X-ray band includes both the tail of the synchrotron emission and the rise of the inverse Compton component as shown in Figure 1.7. In this thesis also an IBL candidate with the name B3 0133+388 was analyzed and the results are presented in Chapter 8.

HBL The last and most detected subclass are the HBLs. Their emission peaks at UV or even higher energies ($\nu_{\rm peak} > 10^{15}$). Finally, also in this work two HBLs namely 1ES 1959+650 and 1ES 0033+595 are analyzed and discussed in detail in Chapter 6 and Chapter 7.

As briefly described above, the rapid variability, high bolometric luminosities and apparent superluminal motions have motivated the concept of relativistic beamed emission. There the non-thermal continuum emission of blazars is produced in $\lesssim 1$ light day sized emission regions, propagating with relativistic speed $\beta = v/c$ along the jet [Boe10]. In general, the resulting Doppler boosting is determined by the beaming factor δ. Here the Doppler factor δ is defined as:

$$\delta = \frac{1}{\gamma(1-\beta cos\theta)} \tag{1.15}$$

with θ the (small) angle between the line of sight and the direction of the relativistic jet (plasma moving) and γ the bulk Lorentz factor of the emission region. Furthermore, the ratio between the synchrotron and inverse Compton luminosity is given by

$$\frac{L_{IC}}{L_{\rm sync}} \simeq \frac{U_{\rm rad}}{U_B} = \frac{L_{\rm sync}}{4\pi R^2 c U_B \delta^4} \tag{1.16}$$

with U_B the magnetic filed density and $U_{\rm rad}$ the radiation density and the spherical source with the Radius R. The δ^4 dependency occurs from the Doppler boosting, mainly from the difference in speed between the observer's frame and that of the relativistic medium. In addition, because the ratio of flux and the observed frequency ν^3 is Lorentz invariant, it can be written

$$\frac{f_\nu}{\nu^3} = \frac{f_\nu^{'}}{\nu'^3} \tag{1.17}$$

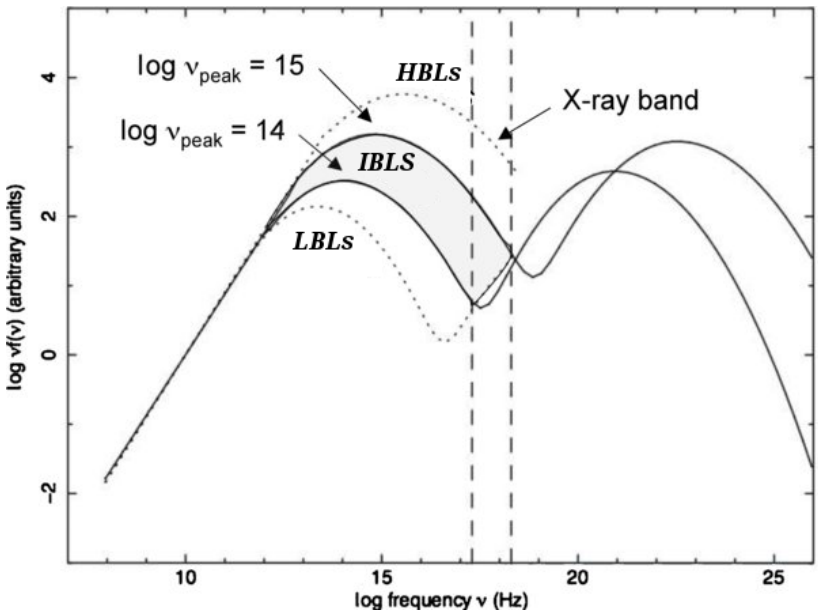

Figure 1.7: Schematic view of different blazar types based on the peak of the synchrotron component ($\nu_{\rm peak}$) in their SED. Low synchrotron peaked blazars, or LBLs, are located at frequencies lower then 10^{14} Hz (e.g., lower dotted line). For intermediate synchrotron peaked sources, or IBLs, 10^{14} Hz < $\nu_{\rm peak}$ < 10^{15} Hz, (illustrates by the SED with peak within the gray area) while for high synchrotron peaked blazars, or HBL, $\nu_{\rm peak} > 10^{15}$ Hz. Figure adapted from [AAA+10c].

The observed frequency ν is then related to the emitted frequency $\nu^{'}$. In particular, for the observer the frequency is shifted by the Doppler factor $\nu = \delta\nu^{'}$ and in equation 1.17 ν can be substitute with:

$$\frac{f_\nu}{(\delta\nu^{'})^3} = \frac{f_\nu^{'}}{\nu^{'3}} \tag{1.18}$$

and for this reason the energy fluxes are connected through: $f_\nu = \delta^3 f_\nu^{'}$. Finally, when integrating the frequency the δ^4 dependency can be derived:

$$f = \int_\infty^0 f_\nu d\nu = \delta^4 f^{'} \tag{1.19}$$

When assuming a spheric "blob" as emission region [GM96] the radius of this sphere can be determined from the measured variability time scale due to: $R = c\,t_{\rm var}$. Furthermore, because the emitting region is also Doppler boosted

toward the observer the equation for the Radius has to be modify to

$$R = c\, t_{\mathrm{var}} \frac{\delta}{1+z} \tag{1.20}$$

In consequence, the intrinsic variability on a timescale t_{var} will be observed on a timescale $t_{\mathrm{var}} = t^{'}_{\mathrm{var}}(1+z)/\delta$ [Boe10]. It has to be stressed in this context that the simple relations only apply if one homogeneous spherical plasma is considered to be the source of the synchrotron and inverse Compton emission. This issue is also referred to the one-zone model which will be described in detail in Chapter 6, Section 6.10. In the next chapter an overview about the most successful detection method of VHE γ-ray photons emitted from different galactic and extragalactic sources is given.

CHAPTER 2

DETECTION METHODS OF IMAGING ATMOSPHERIC CHERENKOV TELESCOPES

Today, The Imaging Atmospheric Cherenkov Technique is the most successful detection method to observe γ-rays of energy above 50 GeV from the Earth. Since our atmosphere is opaque to a fraction of electromagnetic waves, the main messengers from the Universe, only measurements above the atmosphere or indirect methods are possible. In order to detect γ-ray photons in the range from 50 GeV to 50 TeV on Earth, indirect detection methods are necessary. In this case the Earth's atmosphere is used as a calorimeter and the Cherenkov light emitted by the charged particle is measured by the camera of an imaging telescope. In this chapter the dependencies between the air shower development and the Cherenkov light transmission throughout the atmosphere and its detection on the surface of the Earth is explained.

2.1 Extensive Air Showers

Our Universe emits electromagnetic waves over the entire electromagnetic range (10^{-15} – 10^{18})eV. Only a small fraction of the energy band, namely in the optical and radio range, can be directly measured from the Earth (see Figure 2.1). Observations in nearly all other wavelengths need detectors that are located outside the Earth's atmosphere. In case of γ-rays they can be detect in two ways. The first method based on direct detection can be obtained via satellite-born experiments. This direct method allow to detect γ-rays mostly in the HE γ-ray range. One of the main disadvantages of this detection technique are the very restricted possible payload and the detection area size.

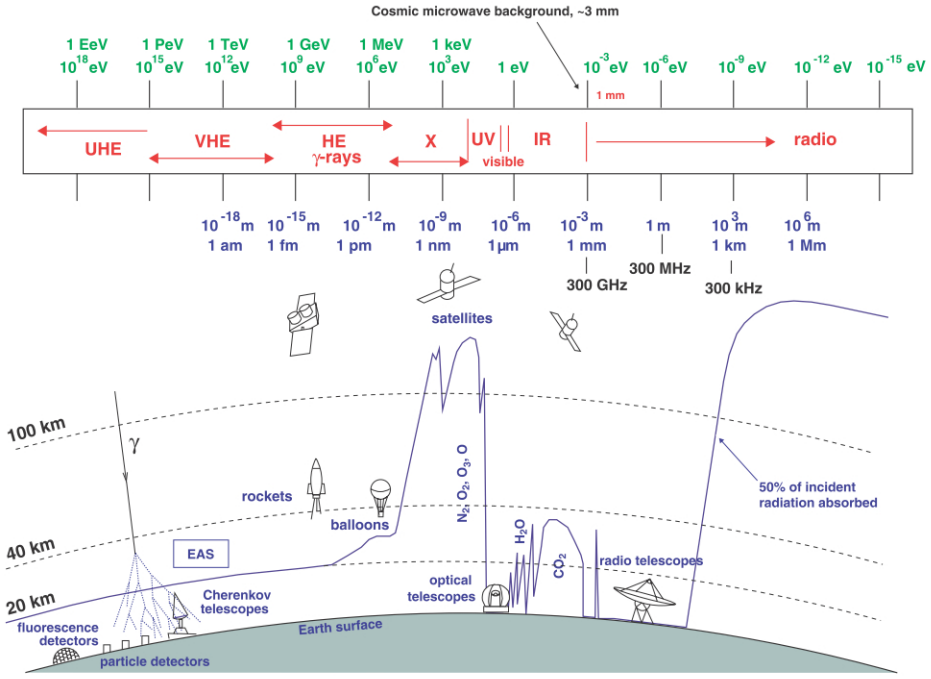

Figure 2.1: The electromagnetic range and its atmospheric window for the direct observation of the Universe. It can be seen that due to atmospheric absorptions the γ-rays among other energetic wavelengths cannot be detected directly by ground based instruments. The figure is taken from [Wag08, Lon92].

In consequence, these limitations affect their effective area and thus their sensitivity and source detection possibility at energies exceeding the HE γ-ray and reaching the VHE γ-ray range, since the photon flux is rapidly decreasing in this energy regime. To overcome this issue, an indirect detection method was developed using **I**maging **A**ir **C**herenkov **T**echnique (IACT), as described in detail in Subsection 2.2.2, which are equipped with huge detector volumes and very good sensitivity. These telescopes make use of the atmosphere as part of the detector. Whenever, a high energy particle ($E \geq 5\,\mathrm{GeV}$) hits the Earth's atmosphere, an extended air shower is initiated. The high energy particle interacts with a nucleus in the upper layers of the atmosphere and produces secondary particles, mostly electrons and positrons, which interact again with the air nucleus and consequently more and more secondary particles are generated. The iteratively produced particles carry less energy than their initiated particle. After the shower reached the point where the individual particle does not carry enough energy to split up further particles and

when further ionizations and absorption processes in the atmosphere dominate, the cascade disappears. There are in general two types of extended airs showers with characteristic shape of their cascade giving informations about the primary particle that initiated the air shower. While charged leptonic particles can interact electromagnetically, the heavier hadronic particles interact dominantly hadronically due to the hadronic cross-section which is much larger than the electromagnetic one. This finding plays a key role in the IACT since only γ-rays are of most interest whereas most particles hitting the atmosphere are of hadronic origin and are treated as background that has to be rejected. In the following subsections an overview about the difference in the air shower between the induced-primary particles (see Figure 2.2 for electromagnetic: γ and hadronic: proton shower shape) as well as the connection with the Cherenkov light development is given.

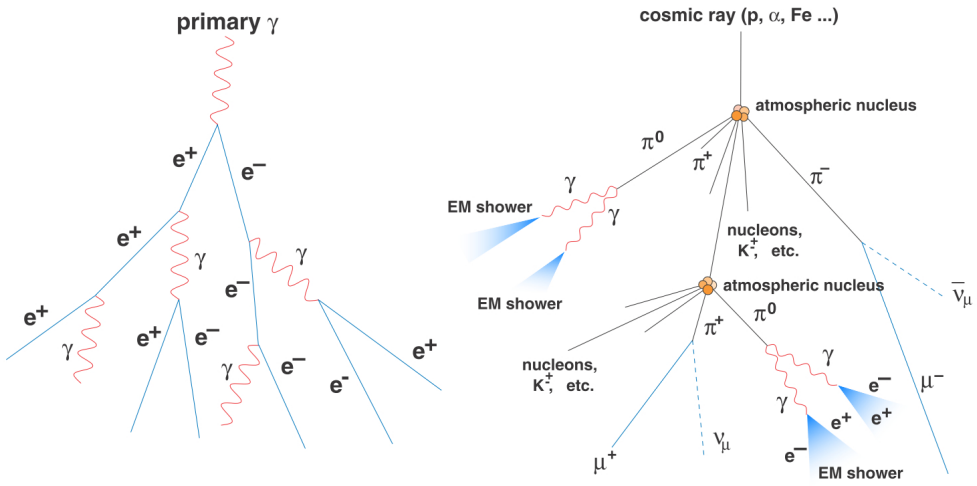

Figure 2.2: Illustration of two different types of extended air showers: electromagnetic shower (left) and hadronic shower (right). The figure is taken from [Sid08].

2.1.1 The Electromagnetic Showers

The electromagnetic showers are mainly affected by two interaction processes. On the one hand there is a pair production process (e^- e^+) in the presence of an air nucleus when a γ-ray reached the atmosphere above a critical energy of 20 MeV. On the other hand the emerged electrons and positrons in turn produce high energy photons via bremsstrahlung (see below). Due to this interactions a particle cascade is formed with an increasing number of secondary

particles. Notably, the electromagnetic shower maximum is reached when the average energy of the cascade particles is decreased toward the critical energy [Wag08], which is introduced and explained in detail below.

Bremsstrahlung

As already mentioned in Section 1.2, whenever a charged particle is deflected in the electric filed (Columb field) of a nucleus, it emits electromagnetic radiation. This process can be described by the following equation:

$$e + X \rightarrow e + \gamma + X \tag{2.1}$$

The strength of the emitted bremsstrahlung depends on the distance to the nucleus, as well as the strength of the Columb field. The energy loss of electrons crossing of matter and producing bremsstrahlung is proportional to its energy. For particle energies above a critical value $E_{\text{crit.}}$ this process dominate over the emission compared to the energy loss by ionization and excitation of air molecules. The critical energy is defined in this context as :

$$-\frac{dE}{dx}|_{\text{E}_{\text{crit. brems.}}} = -\frac{dE}{dx}|_{E_{\text{crit. ionis.}}} \tag{2.2}$$

In this particular case (see equation 2.2) the energy loss of a charged particle throughout bremsstrahlung and ionization along the way in the atmosphere, with the distance x, are in balance. In the air the critical energy is $E_{\text{crit.}}$=83 MeV, [Per91]. When the electron energies fall below this value in air they will rather dissipate their energy by ionization and excitation. In the case of high-energy particles in the TeV range this finding builds the basic requirement for the formation of electromagnetic cascades. In addition, in case of relativistic bremsstrahlung, the energy losses are of exponential form and thus it is possible to define the radiation length X_0 as the mean path. Over this path the charged particles loses a fraction (1-1/e) of its energy as follows [Ste12]:

$$-\frac{dE}{dx} = -\frac{E}{X_{0_{\text{air}}}} \text{ with } X_{0_{\text{air}}} = 37.1\text{g/cm}^2 \text{ in air} \tag{2.3}$$

Pair Production

Primary photons or those that were created during the bremsstrahlung process can convert themselves in the presence of an air nucleus and its electric field or a single electron into a e^+ e^- pair. In this process the presence of an interaction partner is necessary in order to ensure the energy and momentum conservation. Furthermore, a pair production process can be induced when

the energy of the photon E_γ is at least twice as large as the rest energy of an electron:

$$E_\gamma \geq 2 \cdot 0.511\,\text{MeV}. \tag{2.4}$$

The mean distance that a γ-ray travels before it interact with an air nucleus and undergoes a pair production is given by

$$\lambda_{\text{pp}} = \frac{9}{7} X_0 \tag{2.5}$$

with X_0 the radiation length (it is the characteristic distance in the traversed matter).

2.1.2 The Hadronic Showers

Like photons also hadronic particles, which are many orders of magnitude more numerous than a γ-induced shower, can initiate a high energetic air shower. These particles are charged cosmic ray particles dominantly represented by protons. The critical length for hadrons is the hadronic absorption length, where elastic scattering does not produce secondaries and does not reduce energy [Wag08]. In this process mainly pions (90%), kaons (10%) as well as light baryons are generated. Hadrons in general are able to transfer significant transverse momenta to their decay products which is indicated in the wider lateral spread in hadronic-induced air shower shapes. Furthermore, the interaction length of hadrons is much larger compared to the electromagnetic length of γ-rays and electron and positrons, leading to a deeper penetration into the atmosphere. For this reason, the large hadronic interaction way length leads to a higher fraction of fluctuations that is no longer describable by a simplified model.
The most important secondary particles, which play a role in the further development of the Hadronic shower, are π-mesons. Especially the neutral pions almost instantaneously decay ($\tau = 8.4 \cdot 10^{-17}$ s) in two photons and can thus trigger a further electromagnetic shower, that was already described above. These new electromagnetic showers carry roughly one third of the energy of the primary particle and can be compared to a γ-induced air shower cascade with only one third of the energy of the hadron. In addition, not only neutral mesons (π^0) are generated during a hadronic interaction in an air shower but also charged mesons ($\pi^\pm$). In contrast to their neutral siblings, the charged pions live long enough ($\tau = 2.6 \cdot 10^{-8}$ s), depending on the primary particle energy, either to trigger more interaction or to decay in further particles like muons and neutrinos. Especially muons, which decay also into electrons and neutrinos ($\tau = 2.2 \cdot 10^{-6}$ s) have due to the relativistic time dilation sufficient

lifetime to reach the ground. These particles can also be detected in general with appropriate detectors. In the next subsection the most important findings, discussed so far, between the hadronic and γ-ray-initiated shower are summarized.

2.1.3 Differences between both Air Showers

The distinction between the two types of shower is crucial in the IACT since the background crated by hadronic cosmic rays is usually many orders of magnitude more numerous. The methods that can distinguish between the background and signal induce-shower are based on differences between the two shower types as described above. Following characteristics properties are summarized in following list:

- Hadronic showers are more extended and develop their shower maxima deeper in the atmosphere as in comparison to the electromagnetic showers of the same energy.
- The multiplicity in hadronic air showers is much higher in comparison to the electromagnetic one.
- Hadronic showers are in general broader and more irregular than electromagnetic showers. This is the result of the mean transverse momentum transfer in hadronic interactions that is larger than that of electromagnetic interactions and also a larger fluctuations in the shower development.
- Secondary showers initiated by π^0 decay are responsible for the less compact structure of hadronic showers.
- In general, hadron-induced showers produce less Cherenkov light than γ-induced showers.
- Finally, the most relevant aspect for the background suppression is the fact that γ-ray showers point back to their origin of their primary γ-rays, while the arrival direction of cosmic-ray initiated air shower, due to the presence of galactic and extragalactic field, is isotropized.

As already anticipated above, air showers contain a large fraction of relativistic charged particles that travel the atmosphere with a speed close to the speed of light in vacuum. At the same time these particles exceed the local speed of light of traversed medium producing the characteristic Cherenkov light in the atmosphere. This effect is subject of the next section.

2.2 Cherenkov Light Production

Cherenkov light is produced whenever charged particles travels through a dielectric medium at a speed which is greater than the speed of light in the medium itself. The charged particle interacts electrically with the molecules in the dielectric medium and disturbs their neutrality. The result of this interaction is an asymmetrical polarization of this medium along the particle trajectory while a dipole filed arises temporarily which leads to an electromagnetic radiation. Along the way throughout the dielectric medium, each dipole is swinging with the same phase parallel to the trajectory and in consequence radiating short electromagnetic pulses. The short electromagnetic pulses overlap according to the Huygens' Principle to a wavefront from spherical waves that are depicted in Figure 2.3.

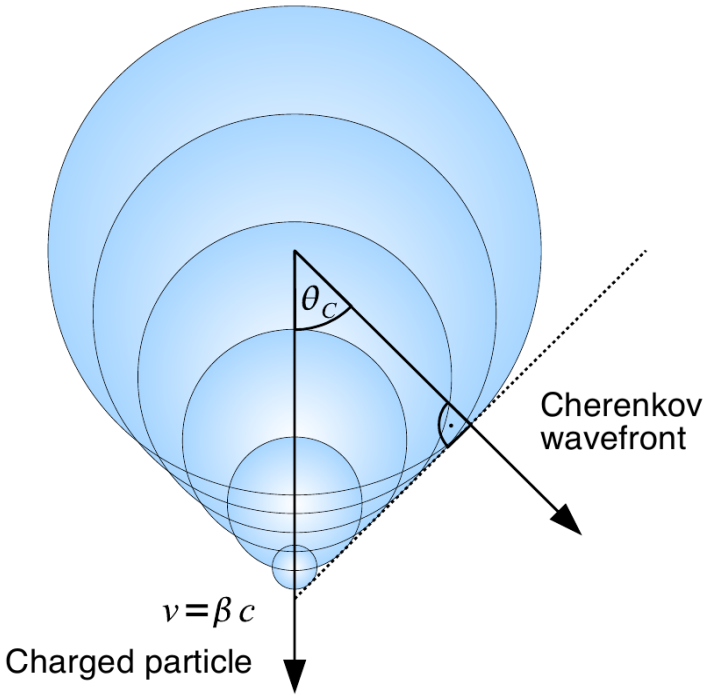

Figure 2.3: Propagation of the Cherenkov light radiation. The spherical waves are caused by the electric field (dipole) of a charged particle moving throughout a dielectric medium with a velocity exceeding the speed of light in the medium. The spherical waves overlap according to the Huygens' Principle. For a threshold velocity β_{th} a wavefront occurs, that is developing according to the direction of the Cherenkov angle θ_C. The figure is taken from [Ste12].

In this context the angle θ_C of the resulting Cherenkov radiation relative to the charged particle trajectory is therefore:

$$cos\,\theta_C = \frac{1}{\beta \cdot n} \text{ with } \beta = \frac{v}{c}\,. \tag{2.6}$$

Where n represents the refractive index of the medium and $\beta = v/c$ the particle velocity over the vacuum seed of light. For a certain medium, this equation is connected with a threshold velocity β_{th} for Cherenkov radiation that is given by

$$\beta_{\text{th}} = \frac{1}{n} \tag{2.7}$$

In this case, this minimum charged particle velocity is needed in order to produce Cherenkov light. At the same time, the maximum Cherenkov angle θ_{Cmax} is assumed for β=1.

2.2.1 Cherenkov Light Production in the Atmosphere

The Cherenkov light, as indicated in the previous sections, plays an important role in the indirect detection of VHE γ-rays. The amount of emitted light by an air shower is in first order proportional to the energy of the air shower and is therefore proportional to the induced primary particle energy. The threshold energy for Cherenkov radiation depends on the mass, since the speed of any particle is determined by its mass and its momentum. For this reason, the condition for Cherenkov light emission can be translated as follows:

$$E_{\text{min}} = \frac{m_0 \cdot c_0}{\sqrt{1 - \frac{1}{n^2}}}\,. \tag{2.8}$$

Here m_0 represents the rest frame mass of the charged particle and n is the refraction index of the dielectric medium. In the atmosphere a γ-ray induced air shower starts its first interaction at altitudes between 20 – 25 km and extends down to several km. The shower maximum occurs at 10 km altitudes where the common characteristic Cherenkov angle is close to 1° and the Cherenkov radiation is only visible in forward direction. In case of $e^{\pm}$ induced air shower particles the Cherenkov emission angle at 2200 m a.s.l. is θ_C [Wag08]. A typical altitude of IAC telescopes is found to be $\approx$ 2 km due to the connection and proximity to the shower maximum.
In the Earth's atmosphere the speed of light is not constant at all altitudes but changes by the density of the atmosphere. The refraction index as a function of altitude in the atmosphere gives the threshold or minimum energy needed to emit Cherenkov light. The minimum energy for different particles on their

way throughout the atmosphere emitting Cherenkov light has an exponential behavior. Particularly, the threshold energy of the electrons and positrons is at the lowest level which in consequence emit the most fraction of Cherenkov light. In contrast, the other particles must have considerably higher energies in order to emit Cherenkov light. Furthermore, because the secondary particles have different inclination angle to the trajectory of the induced primary particle, the emitted Cherenkov light of the air shower has not always a shape of a circle on the ground but a superposition of many circles and ellipses for a given particle above the energy threshold. The cumulative Cherenkov light of all extended air shower is known as the Cherenkov light pool. In this pool the total photon density is proportional to the energy of the air shower induced primary particle, since nearly a constant fraction of the primary energy is converted into the emitted Cherenkov photons. Figure 2.4 illustrates the differential photon density $dN/d\lambda$ in the environment of a Cherenkov light pool for different altitudes, resulting from γ-induced showers with different energies.

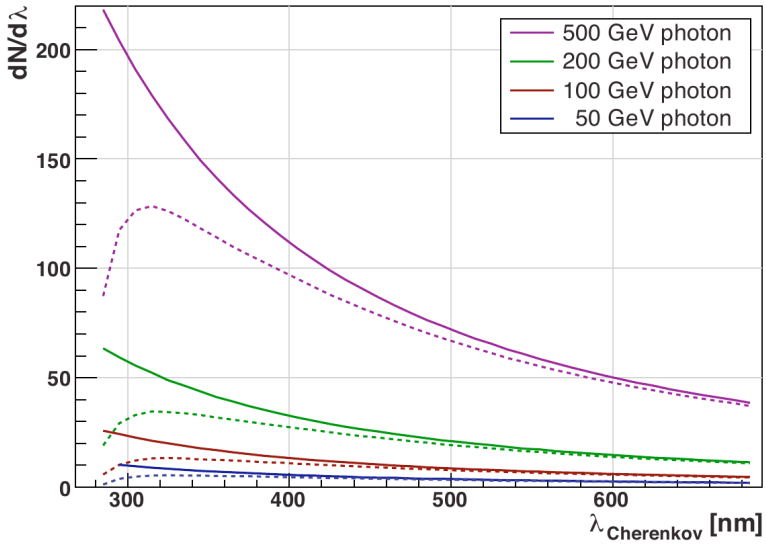

Figure 2.4: The characteristic spectra of Cherenkov light induced by γ-ray showers of different energy. The solid line shows the spectra at $\approx$ 10 km altitude, the dashed lines represent the corresponding spectra at $\approx$ 2 km a.s.l. These spectra are affected by different absorption processes as discussed in the text. The figure is taken from [Wag08].

From this Figure it becomes visible that the differential density is increasing with smaller wavelengths of Cherenkov light [Ste12]. Additionally, up to distances of $\approx$120 m from the shower axis, a flat distribution occurs in which the

Cherenkov photon density is proportional to the energy of the air shower induced primary particle [Wag08]. Another important aspect concerning the Cherenkov light and its development are several attenuation processes while traveling throughout atmosphere. Especially the Cherenkov light spectrum is very important in order to optimize the response of the **P**hoto **M**ultiplier **T**ube (PMT)s and to understand the attenuation processes, in particular the refraction and absorption effects, in the atmosphere. The Cherenkov light is composed of photons in the UV to IR range. The highest emission is found towards smaller wavelengths. More precisely the highest emission occurs at UV and blue optical wavelengths when assuming that the refraction index is constant with wavelength (λ). In this case the basic intensity can be described as follows:

$$I(\lambda) =\propto \lambda^{-2} \tag{2.9}$$

In addition, as already mentioned above, the Cherenkov light suffer from attenuation processes, which are in general wavelength dependent. Unfortunately, the highest intensity fraction of Cherenkov light is almost totally absorbed. In this context it has to be stressed that Cherenkov photons with λ < 280 nm do not reach the detection level due to the intense absorption of ozone and oxygen molecules in the atmosphere. Moreover, further dominant attenuation processes are caused by the Rayleigh and Mie scattering. In the Rayleigh-scattering the Cherenkov photons scatter off air molecules (d<λ). In this process mainly the higher energy part (UV/blue) of the spectrum is strongly attenuated due to the proportionality of λ^{-4}. The Mie scattering is mainly caused by particles (aerosols and dust) in the air which are of the same order or even larger compared to the wavelength of the Cherenkov light (d≈λ). This scattering has an effect for the whole Cherenkov photon spectrum. Additionally, light with $\lambda > 800$ nm (IR) is affected by absorption by water (H_2O) and carbon dioxide (CO_2) [Wag08]. All the here anticipated effects lead to a attenuation of the Cherenkov light at ground level (2200 m), as depicted in Figure 2.5.

Last final aspect that should be also mentioned is the faint and very short spread in the arrival times of Cherenkov light. The Cherenkov light has a density from 100 to several 100 photons/m^2 for a primary γ-ray photon with an energy of 1 TeV depending on the altitude [Ste12]. Furthermore, the time span in which the whole emitted Cherenkov light reaches the PMTs of the camera system is only a few nanoseconds long. For this reason, all up to day developed Cherenkov telescopes must have large optical reflector (glass or aluminum mirrors), cameras with PMTs that are sensitive to the corresponding Cherenkov light wavelength and a very fast response and a short integration time of the readout system. If these aspects would not be taken into ac-

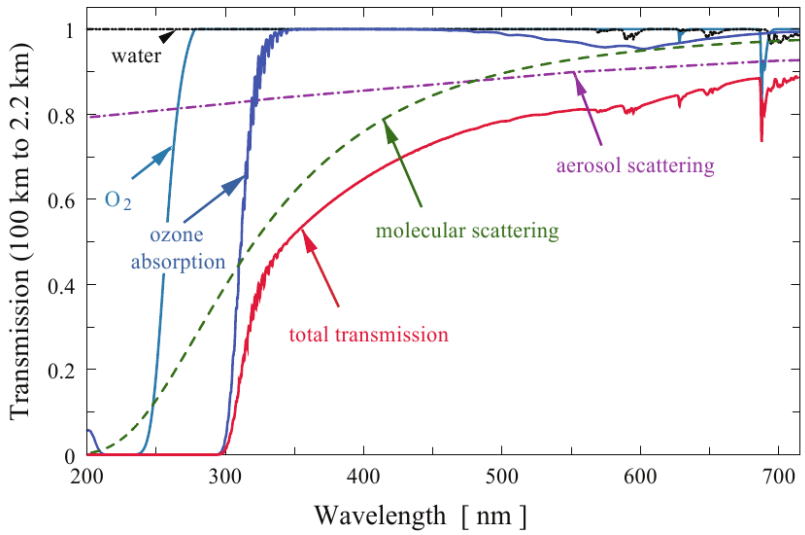

Figure 2.5: Attenuation effects of the Cherenkov light and their wavelength dependence. The figure is taken from [Ber00].

count the night sky background would be much more dominating and the Cherenkov light would not be detectable. Today, the IACT is the most leading indirect detection method of γ-ray induced showers taking all difficulties regarding the properties of the air showers, as discussed above into account. This important technique and its setup will be described briefly in the following subsection.

2.2.2 The Imaging Atmospheric Cherenkov Technique

The **I**maging **A**ir **C**herenkov **T**echnique (IACT) uses Cherenkov photons for the determination of primary particles, their energy and direction when interacting with the atmosphere. In Figure 2.6 the basic setup for MAGIC stereoscopic IACT observations is illustrated. An extended air shower develops speed close to the speed of light and, as described already above, produces a short pulse of Cherenkov light (3 ns for γ-induced and 10 ns for hadronic-induced-showers, respectively). In order to obtain the Cherenkov light image, the telescopes must be located inside the Cherenkov light pool where it is projected onto a pixelized (imaging) camera that consist of very sensitive PMTs. Due to a limited camera size, the shower image in the camera can be truncated if a particular shower has a high energy and large impact parameter. These truncated air showers suffer from worse energy and direction reconstruction if one compares these showers with fully contained images. In case of MAGIC where the

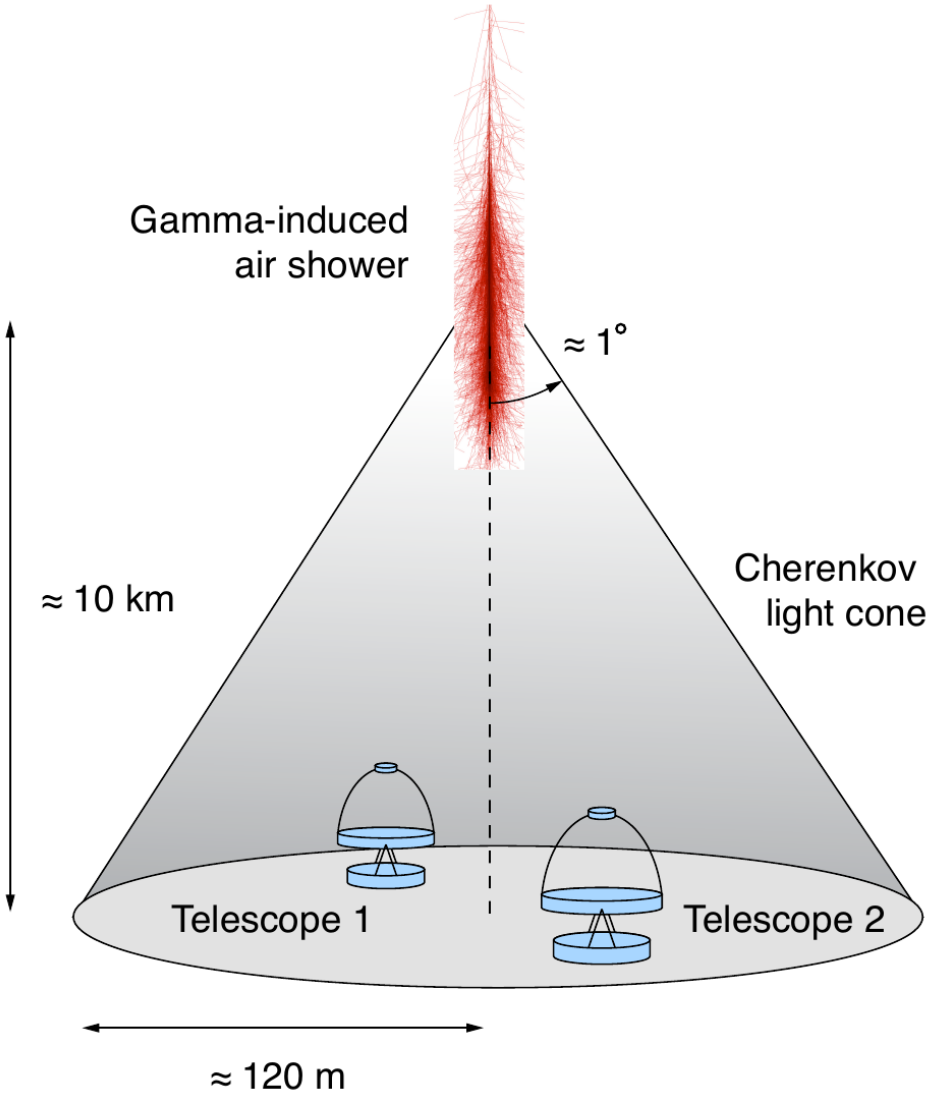

Figure 2.6: Illustration of IACT for MAGIC stereoscopic observations. The air shower is induced by a γ-photon and starts its first interactions in altitudes between 20 – 25 km where it extends down to several km. The shower maximum occurs at ≈10 km developing the characteristic Cherenkov angle close to 1°. At typical altitude of IAC telescopes of ≈ 2 km the Cherenkov light pool has a diameter of 240 m. The figure is taken from [Ste12].

camera has a diameter of one telescope of 3.5 degree the camera is able to image air showers completely only in a defined range of energies and impact parameters. At the same time, the limited size of any IACT camera limits the effective collection area where detected air showers can be used for analysis. Nonetheless, since the collection area of MAGIC is in the order of 10^4 m^2 is allow this telescope system to detect even the very faint fluxes of very distant galaxies as it will be shown in Chapter 7 and Chapter 8. Finally, the advantage of detecting air shower images via the Cherenkov light in a much larger area compared to the size of the telescopes itself and the large detectable energy interval from 50 TeV up to 50 TeV makes the IACT still an excellent method in the field of VHE γ-ray astrophysics. In the following chapter the most important components of the IAC telescopes MAGIC will be described in detail.

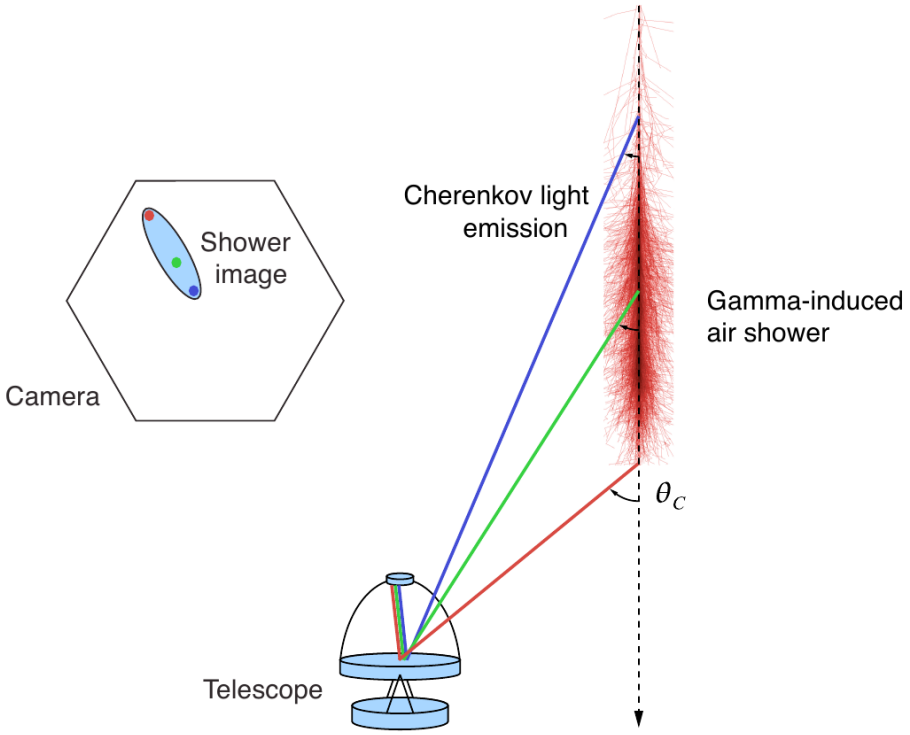

Figure 2.7: Schematic view of the projection of a γ- induced air shower in the imaging plane of one MAGIC telescope. The Cherenkov light image in the camera is of elliptical shape. The asymmetric deformation is indicated by the air shower due to the non linear mapping function where the image is slightly deformed and light from the shower middle in not centered but shifted to the head of the shower image. The figure is taken from [Ste12].

CHAPTER 3

THE MAGIC TELESCOPES

The Major Atmospheric Gamma-ray Imaging Cherenkov (MAGIC) telescopes is the most sensitive observatory of VHE γ-rays on the Earth's surface in the range from (50-300) GeV. In this chapter an overview about the main components of the two telescopes is introduced. The main focus is laid on the changes between the MAGIC I and MAGIC II camera and the improved performance due to the stereoscopic system that played a relevant part in the discovery of new sources.

3.1 Introduction

IACT, as described in detail in previous chapter, is currently the most efficient way to detect VHE γ-ray sources and the MAGIC telescope system, that consist of two telescopes, is one of the three most known observatories on Earth that make use of this technique. The MAGIC telescopes (see Figure 3.1) are two 17 m dish telescopes located at the Roque de los Muchachos observatory (28.8°N, 17.8°W, 2200 m a.s.l.), on the Canary Island of La Palma. The telescopes are build 85 m away of each other. The first MAGIC telescope (M I) started its operation already at the beginning of 2004 and was commissioned until 2005. One year later, after the commissioning phase where M I provided very promising results, it was decided to construct a second telescope to enable stereoscopic observations and thus to improve the detection performance. The commissioning phase of the second MAGIC telescope M II began in December 2008 and ended in Autumn 2009. Since then both telescopes operated in the so-called full stereoscopic mode. In addition, since M II was constructed in order to contain many design improvement of M I it is often called an improved clone. In the following sections the main technical components of M I as well as the improved elements of M II e.g. camera or the readout system will be explained.

Figure 3.1: Photograph of the MAGIC telescopes on the Roque de los Muchachos on the Canary Island of La Palma. The photograph is taken from [Wag09].

3.2 The Telescopes Structures

The two MAGIC telescopes have a light weight structure of the reflector (stiff carbon fiber-epoxy structure) and the light weight camera in common. These components allow to reduce the moment of inertia of both telescopes and resulting in fast reposition movement in order to detect short transient phenomena like GRB's, as anticipated in Section 1.5. Each telescope has a total weight of 60 tons and a maximum position time of 100 s to point to any position in the sky. Today these telescopes are, with an average position time of 40 s, the fastest moving Cherenkov telescopes in the world.

3.3 The Reflectors

The reflector of the MAGIC telescopes consists of a 17 m diameter parabolic dish, which focuses the faint Cherenkov light (see Subsection 2.2.1) from ex-

tensive air showers (see Section 2.1) on the pixelized camera, that will be described later on. The large mirror surface of 236 m^2 (M I) and 247 m^2 (M II), is the main feature that results in a low energy threshold of 50 GeV and makes this telescope system the most sensitivity observatory of VHE γ-rays on the Earth's surface in the range from (50-300) GeV. In addition, the parabolic shape of the reflector ensures the preservation the temporal structure of the Cherenkov light events on the focal plane [DBB+08]. This structure permits to extract timing information from the recorded images [AAA+09c]. For M I, 964 single mirrors consisting of a diamond-milled aluminium surface with a dimensions of 49.5 m × 49.5 m build its reflector. In case of M I the **P**oint **S**pread **F**unktion (PSF)[1] of the adjusted M I reflector is of ≈10 mm diameter in the focal plane. In comparison, the reflector of M II consist out of 247 1 m^2 quadratic mirrors. For the mirrors two different materials are used: the central 143 mirrors consist of diamond-ground aluminium mirrors that are stabilized by an aluminium honeycomb support structure (like M I). The outer 104 mirrors are made of glass plates (2 mm). The optical performance of this mirrors compositions give a slightly improved PSF of 9 mm. The reflectivity performance of these two different mirror types is ≈80% for all-aluminium and ≈85% for the glass-aluminium mirrors, respectively. Furthermore, the focusing of the mirrors is performed for each pointing direction and corrects the bending of the carbon fiber-epoxy frame. This **A**ctive **M**irror **C**ontrol (AMC) adjusts the mirror position independently of their materials. While the aluminium mirrors have a hole drilled in the middle to support the AMC laser needed to track the panel position, the glass mirrors have mounted the lasers at the corner of each mirror. For more information about the AMC see [BGA+08]. In addition, another component that is needed due to the slight bending of the frames is a system that checks the pointing accuracy. This is done by the star guider system which consist of a **C**harge **C**oupled **D**evice (CCD) camera in the center of the reflector. The star guider CCD camera observes simultaneously the night sky, along with the MAGIC photo multiplier cameras (PMT) that are described below.

3.4 The Cameras

As already mentioned in the introduction section the two MAGIC telescopes have been reconstructed 5 years apart (2004 (M I) and 2009 (M II), respectively), which, due to technological development and progress along the time, led to

[1] A point-like γ-ray source yields a sky distribution well fitted by a 2-dimensional Gaussian, whose standard deviation defines the instrument angular resolution and is known as γ-ray PSF.

significant differences in the two telescopes. The main difference is found in the camera components. Both cameras are located in the focal plane of each telescope, sustained by a tubular mast and several stabilizing steel cables anchored to the structure. The pixels consist of PMTs of high quantum efficiency, and are protected behind a plexiglass window as depicted in Figure 3.2 and Figure 3.3.

Figure 3.2: MAGIC I camera.

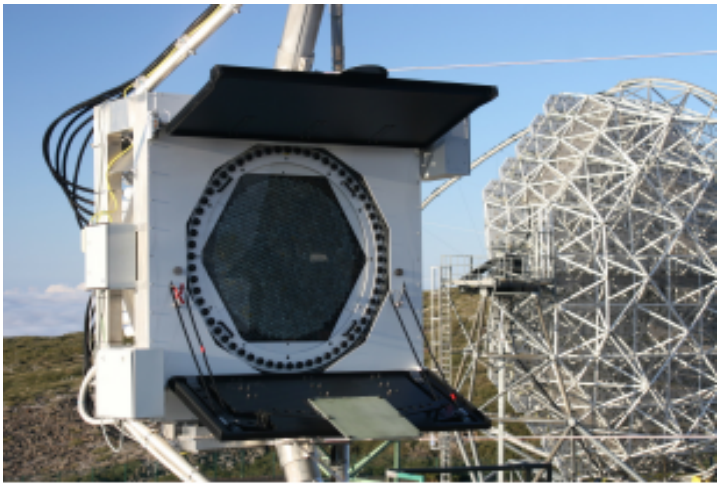

Figure 3.3: MAGIC II camera.

The camera of M I is equipped with 577 hexagonal shaped PMTs with an an-

gular size of 0.1° in the inner part of the camera and 0.2° in the outer part. In contrast, the M II camera is very different from the one in M I as shown in Figure 3.4. The only similar parameter is the **F**ield **o**f **V**iew (FoV) of 3.5°. The M II camera has a round shape and is equipped with 1039 PMT pixels (the same as the small pixels in M I). Besides, another difference is given in the PMTs itself. The PMTs of the M I camera consist with a wavelength shifter in order to increase the sensitivity where the Cherenkov light is mainly emitted (UV waveband) and to enhance the quantum efficiency (≈30% at wavelength of 350 nm, where the Cherenkov light of extensive air showers has its highest intensity). In case of the M II camera, the PMTs (Hamamatsu R1408) are operating without coating and have a quantum efficiency of ≈32%. These PMTs lead to an enhancement of the sensitivity over the M I camera and also to a huge part of the whole telescopes performance.

3.5 The Trigger System

MAGICs trigger system can distinguish between a Cherenkov shower event and a **N**ight **S**ky **B**ackground (NSB) light. The main idea lies in the selection criterion of fast pulses (<5 ns) which are detected simultaneously in a dens region of the camera. The basic difference between both possibilities is the intensity of the light collected by the camera. The light from an extensive atmospheric air shower is more intense than the NSB one and at the same time it involves several neighbor pixel. The trigger system itself consists of three different levels. However, currently only the first two are in use, namely: Level-0 and Level-1, which will be explained later on. As discussed in the camera section the trigger system is also affected by technical differences that are caused due to technological progress. The trigger area of M I covers only an inner camera section of radius of 0.95°, whereas for M II the complete camera with its 1039 pixel of a radius of 1.25° is used. Both trigger areas, as shown in Figure 3.4 consist of a logical combination of 19 overlapping macrocells. Furthermore, the different distribution of the macrocells in the MI II camera leads to a increasing trigger area size (factor 1.7) and also in this case to an improved sensitivity. In order to generate a trigger a number of n next neighbor (NN) pixels must be fired in coincidence in any macrocells. The different trigger conditions es are shown on the example of the M I trigger area below.

The Level-0 trigger

The first trigger, Level-0, is a individual pixel trigger. In this case only the inner 325 pixels of the M I camera contribute to the trigger area. This area is about

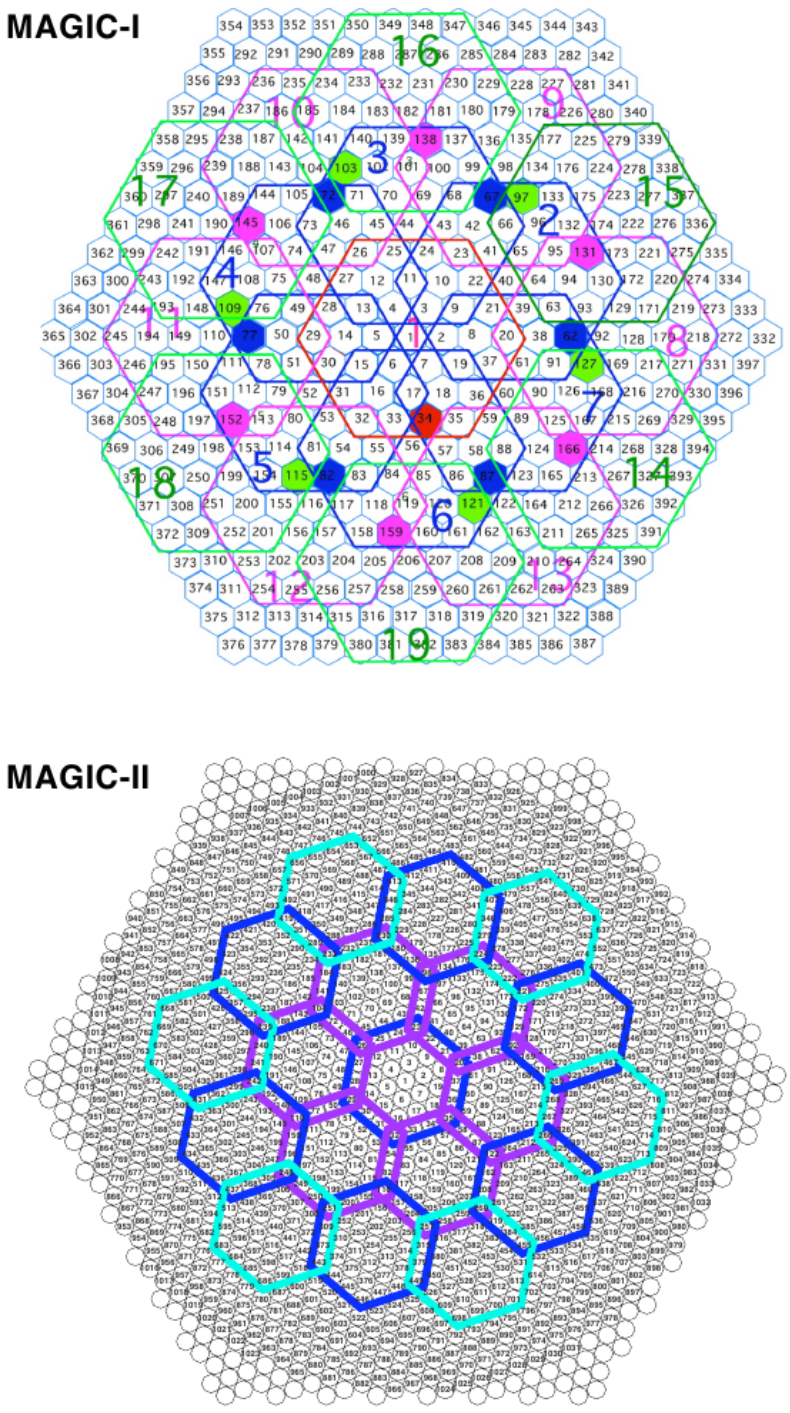

Figure 3.4: Camera layouts with 19 macrocells defining the trigger areas. On top: M I, On bottom: M II. The figure is taken from [Ste12].

one degree from the camera center. The level-0 trigger itself is hosted in the receiver boards: they generate digital signals for those channels with an input signal above certain **D**iscriminator **T**hreshold (DT). These the DT values are programmable for individual settings. The most common application of the DT is to keep a stable rate even under variable light conditions. Moreover, the threshold level is adjustable by a PC and is usually set such that the individual pixel rate is around 100 kHz. The conditions that could change the usual rate are for example, the star field inside the FoV or very bright moon conditions. Passing the Level-0 trigger, the digital signals are then sent to the level-1 trigger, which will be described in the following section.

The Level-1 trigger

In a different way as the Level-0 trigger, the Level-1 trigger is a topological trigger. It is active in 19 overlapping hexagonal macrocells, each consisting of 37 pixels that are overlapping one another. Fore example when a 4NN pixel aligned in a compact region fulfill the Level-0 trigger within 6 ns, then Level-1 trigger is issued. However, due to a huge number of possibilities, it is technically very difficult to accept all possible 4NN conditions. It should be also mentioned that although 4NN is the standard for stand-alone observations, the multiplicity of the next neighbor can be adjusted for other observations, e.g. stereo observation using a 3NN condition. In particular, in case of stereo observations only events that triggered both telescopes are recorded. In this trigger condition each telescope must have 3 pixels above a certain threshold (Level-0 trigger) in a compact NN topology in order to fulfill the Level-1 trigger. The 3NN trigger makes a time coincidence between both telescopes and considers also the delay due to the relative position (85 m away) of the telescopes and their pointing direction. In this stereoscopic mode the individual trigger rates are of the order of several kHz [Ste12], whereas the stereo trigger rates (L3 rates) are in the range of 150-200 Hz [CSC+11].

3.6 The Data Acquisition System - The Readout System

The **D**ata **Ac****Q**uisition (DAQ) system for M I consist of a readout based on optical multiplier and a **F**lash **A**nalog **D**igital **C**onverter (FADC), which is robust and has a very good performance but is also expensive and bulky. One FADC digitalized 16 readout channels in succession, for each of them the signals are delayed corresponding to their readout order [Ste12]. For M II the readout was based on the **D**omino **R**ing **S**ampler 2 (DRS2) chip that are used to store the

analogue signal before digitalization. In this case all signals are sampled at the ultra-fast speed of 2 GSample/s, which allows a very precise measurement of the signal arrival times in all pixels. When a positive trigger feedback is given the multi-capacitor buffer is read out and the signal are digitalized by a 12 bit **A**nalog **D**igital **C**onverter (ADC). This alternative readout is inexpensive and compact but performing worse in terms of intrinsic noise, in particular when comparing dead time and linearity. More information about the readout of MAGIC can be found in [TAB+09].

3.7 The Calibration System

In the last step before the digitalized signal can be analyzed a calibration system is needed. For M I there exist three distinct methods to calibrate the measured ADC counts to photons. These methods make use of three different colour **L**ight **E**mitting **D**iodes (LED) that emit light at three different wavelengths (370 nm, 460 nm and 520 nm). This LED configuration enables to check a wavelength dependent calibration of each individual PMT when the camera is uniformly illuminated with ultra fast pulses (3-4 ns **F**ull **W**ith **H**alf **M**aximum (FWHM)). In comparison for the M II calibration the F-factor method is used. In this case the calibration light is emitted by a phase locked Nd-YAG laser which is operating at the third harmonic (λ = 355 ns) and producing pulses of 700 ps FWHM duration. The laser intensity can be adapted by two consecutively mounted filter wheels which have four identical filters each. With 16 combination of the filters a wide range of intensities from 1-1000 photoelectrons (phe) in each camera pixel can be covered. Such method enables precise monitoring of linearity of the complete signal chain. In order to guarantee a homogeneous illumination of the camera pixels, an integrating sphere (known as Ulbricht sphere) is used to diffuse the laser light before reaching the camera of the telescope [Jog09]. More details on the calibration can be found in [BGF+09].

3.8 The Observation Mode

Since 2008 the MAGIC observations are performed mostly in the so called false source tracking or wobble mode. This observation method allows the simultaneous recording of ON and OFF data at different places in the camera. In order to avoid systematic effects due to sensitivity differences in the camera, the pointing direction alternates every 20 min between two positions, offset by $\pm 0.4^\circ$ in RA from the source [FSLo94]. These two positions are called wob-

ble 1 (W1) and wobble 2 (W2) as illustrated in Figure 3.5. In this context it should be noted, that not similar starfields are presented in the camera for W1 and W2 and, thus the trigger efficiency may not be the same for both wobble positions. The corresponding data for background is estimated by calculating

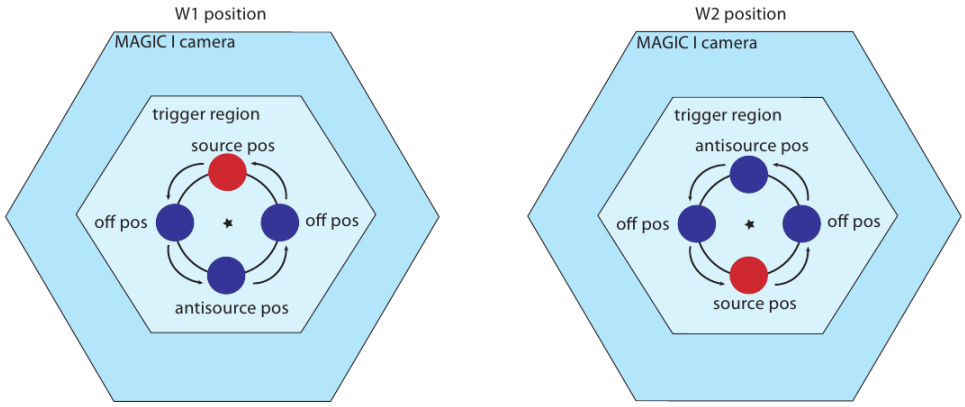

Figure 3.5: Schematic view of the two wobble positions. The source is at the center of the red circle whereas the blue circles represent the regions of the background. The star in the middle indicates the center of the camera which is tracked alternately for 20 min. When the wobble position is changed, the source and antisource position swap their places. Taken illustration is taken from [Jog09].

the shower image parameters with respect to an OFF-source position. These different positions lie on a ring with a radius r=0.4° around the camera center. In addition, they are rotated by 90°, 180° and 270° with respect to the source position [Jog09].
As shown in all subsections above, due to the technological progress along the time the systems of both telescopes changed significantly. For this reason, in the years from 2011 to 2012 MAGIC underwent a major upgrade program to improve and to unify the stereoscopic system of the two telescopes. The new improved components mostly based on the old replaced M I camera is shown in the upcoming MAGIC collaboration documentations in 2013.

In the next chapter the MAGIC standard analysis chain is introduced with a special focus on the different analysis modes between the stand-alone and stereo observations.

CHAPTER 4

THE MAGIC DATA ANALYSIS CHAIN

The MAGIC data analysis chain is divided into several steps. Each analysis step, from signal reconstruction, calibration to identification, spectral and temporal characterization of γ-ray emitting sources is performed by an independent program forming the standard analysis chain. This chapter describes the standard analysis chain, called MARS, that is programmed in the ROOT environment, for the analysis of both mono and stereo data with a special focus on their differences.

4.1 MAGIC Analysis standard chain - MARS

At the beginning of each analysis process in the IACT-astronomy one has to manage huge amount of raw data files which are stored usually in various data center. For this reason the main task of each analyzer lies in the data selection and the data processing in order to obtain physical information. To do so and to figure out all crucial information from the data a data analysis software is needed. In case of MAGIC a specific ROOT[1]-based analysis package for the analysis of the MAGIC data has been developed [MGC+09], [Lom11]. The software is named MARS, an acronym for **M**AGIC **A**nalysis and **R**econstruction **S**oftware (MARS). MARS is written in C++ programming language and it includes predominately different mathematic classes that relies on the ROOT software framework developed at CERN. Furthermore, this analysis software was constantly developed during different MAGIC hardware upgrade processes and the MARS version which has been used during this work was MARS 2.8.4. The main idea behind MARS itself is to create a software analysis chain, where each program is responsible for a dedicated analysis

[1]ROOT was originally designed for particle physics analysis. It is available at http://root.cern.ch

task. At the same time each program produces the input for the subsequent one. Another important aspect is the **M**onte **C**arlo (MC) simulation which is crucial for the background rejection, determination of the effective area and the induced primary particle energy to enumerate only few. Thus, after describing the raw data analysis chain the MAGIC MC simulations chain will be also considered in the following chapter.

4.1.1 The raw data - `Merpp`

The first step in the MAGIC standard analysis chain reduces the raw data files into ROOT files that have a binary format and are compatible with the MARS software. Furthermore, the data must also include all relevant information about the telescopes subsystems i.e drive system, camera control, pyrometer etc.) before it can be calibrated. The merging process with the event image data and the subsystems information is executed by the program called `Merpp`. From now on all essential information for the data analysis can be easily recovered in the .root data files.

4.1.2 Calibration - `Callisto`

Whenever the DAQ system records raw data and the data already includes all subsystems information obtained by the executable `Merpp`, the data has to be calibrated. In order to extract the signal pulses from the recorded time slots, several extraction methods can be used: namely the spline method, the digital filter method and the sliding window method. These methods differ slightly in their performances depending on the data and the requirements in connection with the speed and precision of timing information of the analysis [Jog09]. When one of the extraction method is applied to the data, information about the signal arrival time, its amplitude and intensity in FADC counts are extracted. More information about the different extraction methods can be found in [A$^+$08]. After the signal extraction, the F-factor method is applied [MLP$^+$97]. This method uses calibration events to estimate the proportional relation between phe which are proportional to the number of Cherenkov photons and FADC counts. In order to obtain such proportional relation for each individual pixel calibration constants are needed. These constants are obtained during special data runs of pedestal and calibration events that are taken during source observations. In case of pedestal events they are obtained randomly triggering the telescope, so that no shower signal is recorded in the pixels. These data can be used later on to determine the baseline of the signals and its fluctuations. On the contrary, the calibration data events are generated by short (2 ns) light pulses of intensity comparable to the real Cherenkov sig-

nals. Furthermore, interleave calibration event are taken with a rate of 25 Hz to monitor any changes during data taking [Jog09]. Both described processes (signal extraction and calibration of the signal intensity) are performed by the `Callisto` program of the MARS analysis software.

4.1.3 Image Cleaning - `Star`

When the program `Callisto` has processed the data, the calibrated data still consist of the full information (all pixels) which is present in the telescopes camera. Furthermore, it is known that many of the camera pixels contain images that are caused by the night sky background fluctuations. Therefore an algorithm is needed that rejects these fluctuations. This process is called the image cleaning and the name can be taken literally because pixels which do not belong to the showe images i.e. night sky background fluctuations are set to zero [Jog09]. The image cleaning has two stages in order to identify pixels belonging to a shower. In the first stage, pixels whose number of phe larger than a threshold value are selected. These pixels are named as core pixels. During the second stage, another threshold value is applied for the pixels which are the neighboring pixels of the core pixels. These pixels are called boundary pixels. The first and second threshold values can be 10 phe and 5 phe, or 7 phe and 5 phe for core and boundary pixels respectively. A recent advancement on image cleaning is the inclusion of arrival time of each photons. The method is based on the logic that Cherenkov photons from a γ-ray event should be spread in a few seconds whereas NSB arrive the camera pixels randomly. This method gives an additional requirement to select core and boundary pixels, which results in reducing the threshold of number phe in core and boundary pixels. Lowering the phe threshold will increase the probability of keeping the low energy γ induced images. In this method, the time difference between the arrival time of core pixels should be in 4.5 ns whereas that for core and boundary pixels should be in 1.5 ns. The cleaning parameters that are used for the analysis in stand alone-mode are 6 phe and 3 phe, for core pixels and boundary pixels respectively and for the stereo analysis 6 phe and 3 phe (M I) and 9 phe and 4.5 phe (M II) respectively. In addition, these pixels should have at least one next-neighboring pixel above the same threshold in a time coincidence of 1.5 ns for core pixels and 4.5 ns for boundary pixels [Ste12, Lom11].
After the image cleaning, the shower parameters introduced by [Hil85] and also known as Hillas parameters are calculated. The Hillas parameters, calculated as image moments up to the second order, are strongly related to physical interactions of an extensive air shower. Figure 4.1 illustrates the main idea of some Hillas parameters that will be described below.

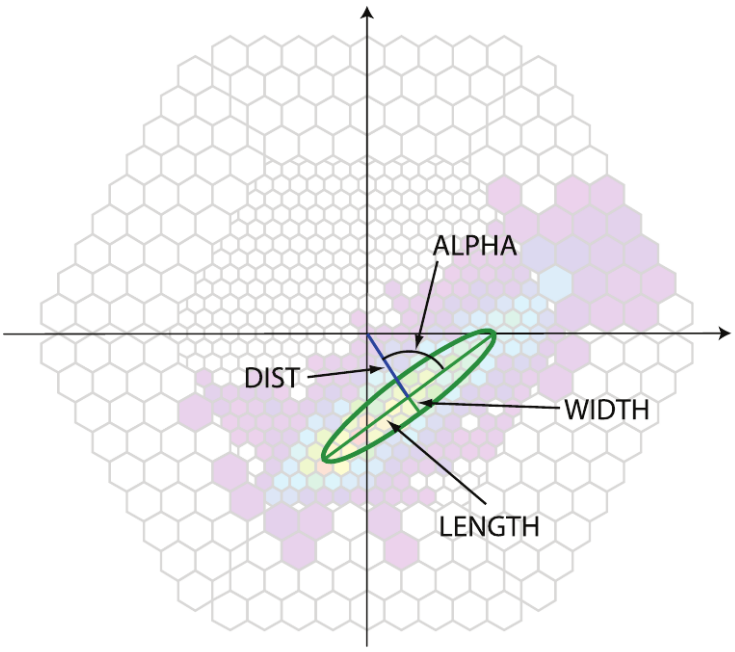

Figure 4.1: Illustration of a parametrization of a shower image with different Hillas parameters. The illustration is taken from [AAA+08b].

`Size:` describes the total charge in phe that is contained in the image. It is related to the energy of the primary particle initiated the extensive air shower.

`Width:` represents the **R**oot **M**ean **S**quare (RMS) spread of the Cherenkov light along the minor axis of the ellipse when fitting the image. Additionally, for a given `Size`, the `Width` is smaller for γ-ray images than for particles of hadronic origin and therefore provides strong discrimination power in the background rejection.

`Length:` this parameters describes the same properties as the `Width` but this time for the major axis of the ellipse. It is connected to the projection of the shower longitudinal development. Moreover, like the `Width` the `Length` is also smaller for a given γ-ray images than for hadronic particle (for a given `Size`). This is cause by the smaller average transverse momentum in electromagnetic shower initiated by γ-ray photons. For this reason, this parameter plays also an important role in the background rejection.

`Dist:` allows to estimate the shower impact parameter and to improve the energy estimation of the primary particle. It is the angular distance between

the **C**enter **o**f **G**ravity (CoG) of the shower image and the expected source position in the camera plane.

`Alpha`: represents the absolute value of the angle between the major axis of the shower image and the line connecting the CoG image and the camera center. γ-induced showers are in average characterized by small values of `Alpha`. In contrast, hadronic showers being isotropic distributed on the camera plane, have a flat `Alpha` distribution.

The image cleaning part as well as the parametrization is done by a MARS program called `Star`.

Up to this point the parametrization of the individual telescope images was processed independently. For a stereo analysis there also exist a program, known as `Superstar`, that merge the two separate telescope data streams into one single data file. The resulting file contains the stereo events with the information of the two telescopes. Moreover, for the stereo event reconstruction different stereo parameters were assigned in order to improve the telescopes performance. The new stereo parameters use the main axis and centroid position of both telescope images, as shown in Figure 4.2. The most important stereo parameter that improve the analysis performance are listed below:

`Impact`: describes the perpendicular distance between the shower axis and the telescope pointing axis.

`MaxHeight`: represents the reconstructed height of the shower maximum above the telescopes.

In particular, the `Impact` parameter significantly improves the energy reconstruction whereas the `MaxHeight` parameter increases the background rejection. This parameter plays a key role in the rejection of muon induced showers at low distances above the telescopes at height < 4 km, which have a nearly identical image distribution as low γ-ray events. In consequence, this parameter increases the sensitivity of the stereoscopic system at low energies.

As already discussed above some image parameters are strongly correlated with the characteristic behavior of a primary particle having an induced air shower. Such correlations are very crucial since they play a major role during a γ/hadron separation and energy estimation which will be described in the next subsections.

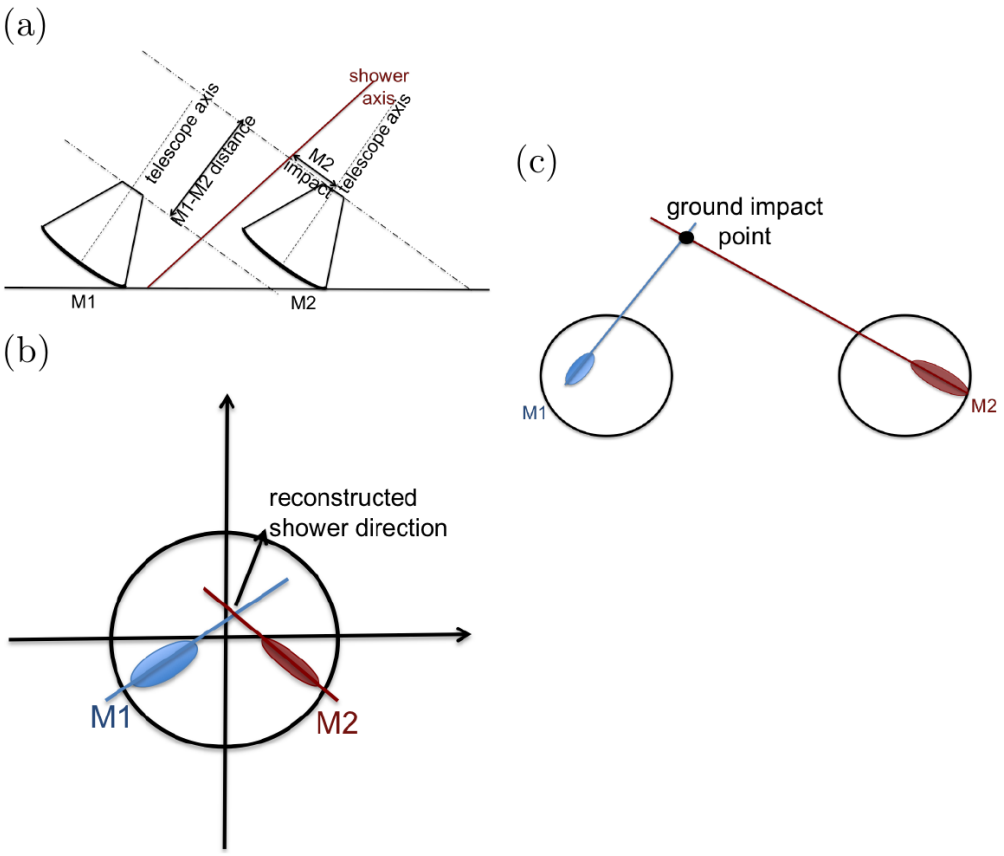

Figure 4.2: Illustration of shower axis reconstruction in a stereoscopic observation. a) Geometry definition. b) Reconstruction of the shower direction. The intersection of the air shower major axes , once superimposed the two images is taken into account. c) The reconstruction of the shower impact point on the ground is obtained, when taking the intersection of image major axes starting from the telescopes position. The figure is adapted from [Zan11b].

4.1.4 Gamma/Hadron Separation - Osteria / Coach

γ/hadron separation plays one of the most important roles in an IACT-analysis. This process is very important since the rate of cosmic rays is much higher in the VHE γ-ray range than of the strongest γ-ray emitting sources. The MAGIC telescopes trigger three different kind of events these are:

`Cosmic-ray events:` Cherenkov light from extensive air showers induced by hadrons and γ-rays.

`Myon events:` Cherenkov light from myons. These particles travel with ultra-relativistic velocities throughout the atmosphere, generating rings or section of rings on the camera.

`Randomize events:` consist of mainly fluctuations of the signal due to background light e.g. strong moon light, NSB or a car which is driving near the telescopes and produces a light flash.

Figure 4.3 shows few examples of different shower images formed on the M II camera.

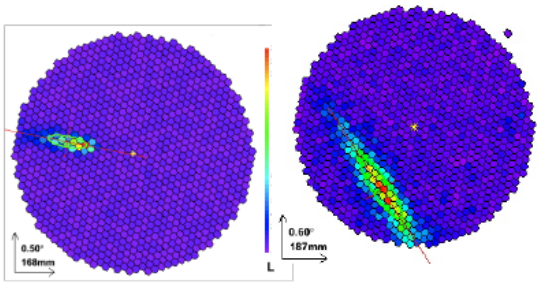

a) γ-ray candidate b) hadron candidate

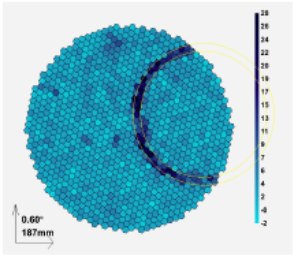

c) muon event

Figure 4.3: Cherenkov particle images formed on M II camera. a) γ-ray candidate. b) hadron candidate c) myon candidate. Taken from [Zan11b].

In order to discriminate between these three events the first discrimination is performed already at the hardware level where the trigger system is optimized for accepting γ-induced events. In case of stand-alone (one telescope) observations the myon trigger rate is five times smaller than the hadron rate, and the randomize rate is lower than 1 Hz [Zan11b]. In comparison, in stereoscopic observations the rate is at level of few Hz. However also the coincidence trigger (L3 trigger), which exclude most of these events and which make the trigger threshold of the two telescopes much lower than in stand-alone mode, cannot suppress all the background events significantly. In addition, the average rate after image cleaning for low zenith observations in stand-alone mode is around 100 Hz, while the average γ-ray rate of the Crab Nebula (see Chapter 5) is about 0.1 Hz [Jog09]. In consequence, this example shows very well that a further suppression of hadron induced events by a factor of 1000 is needed in order to make significant detections in an IACT-analysis. The MAGIC analysis chain make use, in order to suppress the background significantly, of multidimensional classification system based on the construction of decisional trees. Especially in the MARS software, where the image parameters and time parameters of the shower images are exploit, such method known as the **R**andom **F**orest (RF) method is used [AAA+08a]. This method uses the image parameters from stand-alone observation or stereoscopic observations (`Size, Length, Width, Impact, MaxHeight`) as well as timing informations to create one single parameter called `Hadronness`. `Hadronness` build an interval from 0 to 1. Images produced by hadrons have a `Hadronness` spread in the whole range from 0 to 1 whereas γ-rays tend to produce `Hadronness` close to zero. This special parameter is used to separate γ(0)- from hadron-like(1) events by a dedicated `Hadronness`-cut. In MARS the RF classification is trained with a dedicated program called `Osteria` (mono analysis) or `Coach` in case of stereo analysis. These programs use for the RF training need two samples of data. On the one hand a MC simulation sample of simulated γ-ray events, that will be describe later on. On the other hand a real observation sample taken mostly from deep observations without any known γ-rays sources (Off sample) and therefore ideal used as background events.
One of several applications of the RF is found in the reconstruction of the direction of a primary particle. Here the crossing point of the main axes of the shower images is adopted to the `DISP` method, where the arrival direction is determined [LBC+01]. The `DISP` parameter, which is the distance from the shower image center to the estimated source position, is obtained from the RF. Like in the previous cases, the `DISP-RF` is trained on MC γ-events and delivers one individual estimation of the `DISP` parameter for each telescope. When combining the `DISP` parameter with the geometrical information from

the axes crossing point a unique source position is determined. In case of a position disagreement the events are rejected, which is another method for an additional background rejection.
More details about the RF and its usage in the MAGIC analysis can be found in [AAA+08a], [Jog09] and [Zan11b].

4.1.5 Energy reconstruction and energy resolution - Melibea

In the next analysis step different reconstructions of the shower direction and its energy are carried out. Also for this task a dedicated program with the name Melibea was developed. The main task of the Melibea program is to apply the RF algorithm determined by Osteria (stand-alone analysis) or Coach (stereo analysis) to the events of the analyzed data sample. In this process the information about Hadronness of the event, its reconstructed energy, and the reconstructed shower direction on the camera can be obtained. In IACTanalysis the energy reconstruction is based on the direct proportionality of the event energy and the number of produced secondary particles at the maximum of the corresponding air shower. Usually there are two ways in order to estimate the energy in the MAGIC analysis chain. For the mono analysis it is done by means of a RF (more precisely by a regression method of the RF [AAA+08a]) in case of stereo observations it is performed by using **L**ook **U**p **T**ables (LUT)s.

For the mono analysis the RF is trained over a test sample of MC γ-rays events whose energy is known (E_{true}). The used parameters are mainly Size and zenith angle, since Size is proportional to the energy of the primary induced-air shower particle, as described above. The decision threes of the RF are built in such a way where an optimal cut in each three nodes is chosen. In general, it is the cut which minimize the variance of the known E_{true} of the events [Zan11b].

In case of stereo analysis LUTs based on a single model describing the total distribution of Cherenkov photons on the ground is used, where the Cherenkov radius as well as the Cherenkov density is taken into account. The LUTs are build for each telescope independently by dividing a test sample of MC γ-ray events, with known E_{true}, in bins of Size, Impact and MaxHeight. The final energy estimation, E_{est} is the weighted average value for both telescopes. Here the weighted average is estimated by the uncertainty associated to the corresponding bin.

The energy resolution is defined as the standard deviation σ of a Gaussian fit to the peak of (E_{est}-E_{true}/E_{true}) distribution of MC γ-ray events. The differ-

ence from zero of this distribution gives the mean energy bias and the energy reconstruction is as good as it is close to the zero value. In the medium energy range (from 300 GeV to 1 TeV) for a mono analysis, the energy resolution is as good as ≈25% in comparison to the stereoscopic system the energy resolution could be improved in the same energy range to ≈16%. For higher energies >1 TeV the energy resolution slightly worsens mostly due to the large fraction of truncated images and worser statistics in the training sample [Ste12]. In case of lower energies $E < 300$ GeV the energy resolution also slightly worsens in this range. The main problem is the relative high noise and the lower photon numbers which lead to a worse estimation of the arrival direction and which consequently spoils the precision of the `Impact` parameter reconstruction as described in details in [AAA+12d].

Out of E_{true} there is also a possibility to estimate the analysis threshold. This is done usually by the estimation of the energy threshold when fitting the peak of the E_{true} distribution either before or after the applying the gamma selection cuts. A detail example of an energy threshold estimation is shown in Subsection 5.3.2.

4.1.6 Signal search - `Odie`

The detection of a signal from a dedicated source plays an important role for the further procedure of an analysis. In MARS there are two possibilities to derive a distribution of a signal for a given source which are known as *Alpha*- and θ^2-plot and are shown in Figure 4.4. These distributions peak at small values for γ-ray events and flatten up in contrast for hadron events. Both distributions define in consequence the so-called signal regions. As anticipated above, in MARS both distributions can be chosen. The selection criteria depends on the kind of analysis one wants to perform. For a source-independent analysis the θ^2 distribution is chosen. This distribution make use of image parameters whose definition does not depend on an known source position. In addition, the θ^2 distribution is reconstructed through the `DISP` method, as described in Subsection 4.1.4 and the RF for the γ-hadron separation is trained only with source-independent parameters. For a source-dependent analysis, which is known as *Alpha*-analysis, the assumption are based on the source position on the camera plane. From this assumption new source-dependent parameters can be derived, mainly `DIST` as additional discrimination parameter that also is used in the RF γ/hadron separation. Furthermore, including time parameters like the time gradient, which are also strongly correlated with the `DIST` parameter, results in significant improvement of the *Alpha*-analysis performance. For this reason, the *Alpha*-analysis is mostly performed in case of a

point-like source with known position in the stand-alone observation mode. In case of stereoscopic observations the θ^2-analysis has a better signal determination performance, which takes advantage from the DISP method and from other discriminating source-independent stereoscopic parameters i.e. MaxHeight. In MARS the program that is responsible for the θ^2 distribution is called Odie.

In order to claim a discovery of a new VHE γ-ray emitting source, an excess with a significance of at least $5\,\sigma$ is required as it will be shown in Chapter 7, Chapter 8 and Chapter 9. The calculation of the significance from a γ-ray signal results from the equation derived by Li and Ma [LM83] (equation 17).

$$S = \sqrt{2}\left(N_{\text{on}} \ln\left[\frac{1+\alpha}{\alpha}\left(\frac{N_{\text{On}}}{N_{\text{on}}+N_{\text{off}}}\right)\right] + N_{\text{off}} \ln\left[1+\alpha\left(\frac{N_{\text{off}}}{N_{\text{on}}+N_{\text{off}}}\right)\right]\right)^{1/2} \tag{4.1}$$

where N_{On} and N_{Off} are number of events in the signal and background region of the source, respectively. The parameter α is defined as the fraction of:

$$\alpha = \frac{t_{\text{On}}}{t_{\text{Off}}} \tag{4.2}$$

and is the ratio between the effective observation time of the source region compared to the background region. This relation implies that $N_{\text{background}} = \alpha \cdot N_{\text{Off}}$, thus the number of γ-ray like events from the source becomes:

$$N_{\text{ex}} = N_{\text{On}} - \alpha \cdot N_{\text{Off}} \tag{4.3}$$

In this equation the meaning of α is a normalization factor of the background events to apply the correct background estimation for the observation time. For the signal distributions calculated for different sources in this thesis, α is defined as the fraction of On events over Off events in a region far away from the signal region and the distribution tails[2]. An example of such normalization region is depicted in Figure 4.4 where a strong signal of the Crab Nebula is shown using the *Alpha* and θ^2 distribution.

4.1.7 Sky maps - Caspar

In MARS the executable called Casperproduce histograms containing the arrival directions of all γ-ray-like events after the subtraction of expected background. The histograms are presented in sky coordinates (RA. DEC.). Casper produces sky maps using the source-independent parameter DISP and the

[2]The normalization region in the θ^2 plot has a range from 0.1°-0.3°, whereas in the *Alpha*-plot it spans from 20°-80°.

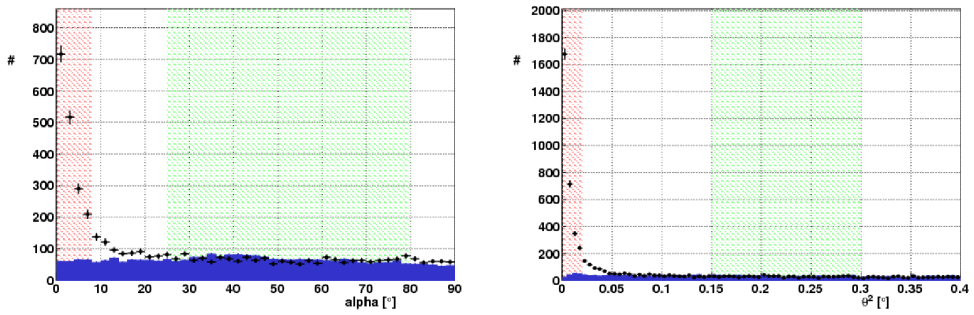

Figure 4.4: *Alpha* (*left*) and θ^2-plot (*right*) from the Crab Nebula. The red shadow region represents the signal region whereas, the green shadow areas identify the normalization regions. The figure is taken from [Zan11b].

corresponding method which reconstructs the shower arrival direction in an unbiased way [Zan11b]. Moreover, the obtained sky map excess, as shown in Figure 5.6, is smoothed using a Gaussian function with σ equal to the angular resolution of the corresponding observation mode (stand-alone or stereo). Finally, sky maps are often obtained of well known point like sources e.g. AGNs in order to check the telescopes pointing accurateness.

4.1.8 Flux and Light curve determination - `Fluxlc` / `Flute`

To obtain most interesting results of a VHE γ-ray emitting source, high level VHE γ-ray analysis results are needed. These results, which are in particular a differential energy spectrum and a temporal resolved integral flux (denoted light curve) provide direct information about the possible acceleration mechanism in the source itself. In MARS there are two different programs known as `Fluxlc` (for mono analysis results) and `Flute` (for stereo analysis results) that can be used to obtain such high level results. The differential γ-ray energy spectrum is defined as:

$$\phi(E) = \frac{dF}{dE}(E) = \frac{dN_\gamma}{dE \cdot dA_{\text{eff}} \cdot dt_{\text{eff}}} \; [\text{photons TeV}^{-1}\text{cm}^{-2}\text{s}^{-1}] \tag{4.4}$$

where N_γ is the number of detected γ-rays, t_{eff} is the effective observation time and A_{eff} is the effective observation area. For the spectrum all quantities are calculated in small energy bins (average binning is 28 (`Fluxlc`) or 30 (`Flute`). The parameter A_{eff} represents the effective area. It characterizes the detection efficiency for γ-ray induced showers and is calculated from an MC γ-event test sample. This MC sample is independent from the sample used for the RF training. There are different factors that can affect the effective area

i.e. the trigger efficiency, the reflectivity of the mirrors, the FoV of the trigger and the camera, the zenith angle observations as well as the cuts applied on the analysis chain to name only a few. In Figure 4.5 a typical effective area is shown. For low energies A_{eff} has a steep rise due to the trigger probability of the γ-ray induced showers which is rapidly increasing in this energy range. It is known that, whenever the energy of the primary particle is low, the less Cherenkov light is emitted by the extensive air shower and thus the lower the trigger probability. When the shower fluctuations became small in comparison to the total amount of light, the trigger probability becomes more stable and the effective area remains almost constant. Further important parameter

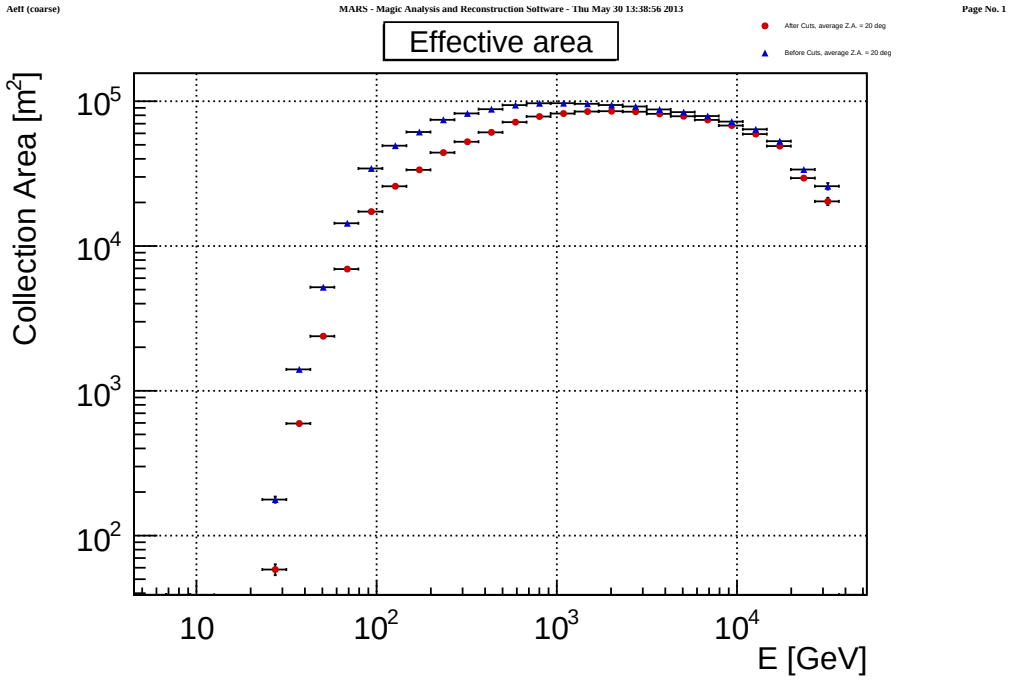

Figure 4.5: A typical shape of the effective Area A_{eff} as a function of estimated energy. A_{eff} is shown before (blue triangle) and after (red dots) the applied cuts.

in the equation of the differential spectrum is the effective observation time t_{eff}. It is the time in which the telescope was effectively recording events. The dead time of the detector system is mainly the reason why the effective observation time does not coincide with the real observation time. The distribution of cosmic events in time follows a Poissonian distribution and thus the distribution of time differences between successive events follows an exponential

decrease of the form:

$$\frac{dN}{d(t)} = ce^{-rt} \tag{4.5}$$

with N the number of events and c as a constant. The fit parameter r is the ideal average event rate (no dead time). The effective observation time is then derived from the exponential fit parameter c:

$$t_{\text{eff}} = \frac{N_{\text{total}}}{c} \tag{4.6}$$

where N_{total} is the total number of events.
As anticipated in this subsection above, another important high level analysis results is the temporal resolved integral flux over a specific energy range versus time. The integral flux is defined as:

$$F(E > E_0) = \int_{E_0}^{\infty} \frac{dN_\gamma}{dE \cdot dA_{\text{eff}} \cdot dt_{\text{eff}}} dE \text{ [photons cm}^{-2}\text{s}^{-1}\text{]} \tag{4.7}$$

with E_0 the specific energy above which the integral flux is calculated. The integral flux is determined for bins in time, where t_{eff} is the bin width and A_{eff} is derived for the zenith angle distribution of the analyzed data in each bin. In case of the integral flux the most important quantity to be chosen is the lower (specific) energy. The systematic uncertainty of an integral flux is in the low energy ranges mostly dominated by the uncertainty of the events and A_{eff} as already mentioned above. In order to avoid huge errors, E_0 can not be set arbitrary low. For this reason in general significant integral fluxes (light curves) are determined above energies of (100 – 200) GeV for a zenith angle distribution between 5° – 35°.

4.1.9 Spectral Unfolding - `Unfolding`

With the last final analysis step, known as the unfolding procedure, the estimation of a real/true observable by correcting the measured observable from its natural distortions due to finite resolution of the detector is obtained. In the particular case of IACT-analysis only few parameters can be measured or derived i.e. parameter `Size`, estimated energy (E_{est}) (can be computed by means of statistical algorithms) in the analysis itself, but there are also parameters like the true energy (E_{true}) which remains undetermined. However, the detector itself, mostly its response, can be described by a function M(x,y) and the measured distribution g(y) can be expressed in terms of the true distribution f(x) as:

$$g(y) = \int M(x,y) f(x) dx + b(y) \tag{4.8}$$

here x is the true energy and y indicates the estimated energy. For this reason, the main aim of the unfolding procedure is to determine f given M and g. In Matrix notation the unfolding is commonly written as:

$$Y = M \cdot S \tag{4.9}$$

where Y represents the measured distribution and S the real one. The aim of the unfolding method in matrix notation is now to obtain S by inverting equation 4.9. The migration Matrix M is usually not of type $n\,x\,n$ and in consequence the solution of S can be found by minimizing the least square expression

$$\chi^2 = (Y - M \cdot S)^{\mathrm{T}} \cdot K^{-1} \cdot (Y - M \cdot S) \tag{4.10}$$

In general, although technically correct, the solution to equation 4.10 can be affect with large errors (large fluctuations) to overcome this problem usually an unfolding with regularization of the form:

$$\chi^2 = \frac{\omega}{2} \cdot \chi_0^2 + Reg(S) \tag{4.11}$$

is used. With ω the regularization parameter, which is steering the strength of the regularization and *Reg(S)* is the regularization term, which describes the smoothness of S. In the MARS environment different unfolding methods, using different *Reg(S)* terms, were implemented.
These method are denoted as *Bertero* [Ber89], *Schmelling* [Sch94], and *Tikhonov* [TA77]. In addition, there are also further unfolding methods and programs that were developed recently. One of the most known and already adapted programs in the MARS environment is the unfolding program **T**ime-dependent **R**egularized **U**nfolding for **E**conomics and **E**ngineering problems (TRUEE) developed by [MDK+13]. More information about the details of the program TRUEE and its implementation in MARS can be found in [Dor13].

4.2 MAGIC Monte Carlo Simulations

As already mentioned in the previous sections, **M**onte **C**arlo (MC) simulations are essential in the high energy physics. All detectors in this research field need to be calibrated. In case of accelerator experiments the common procedure is a calibration in a test beam where the most important parameters e.g. energy, particle type, direction and also timing are known. Comparing accelerator experiments with cosmic ray physics it becomes visible that in the latter adequate test beam environments are not possible. To overcome this problem, nowadays, simulations are used for the calibration of individual

detectors. These simulations (simulation algorithms) include mostly physics laws in the environment of a dedicated detector. In particular these are: interactions between accelerated particles, Earth's magnetic field, atmospheric parameters from meteorology as well as all possible detector components and their extrapolations and assumptions. In case of MAGIC MC simulations a huge amount of computing power is needed. The air shower simulation are the most time consuming simulation part in the whole MAGIC MC simulation chain. In the first simulation part simplifications have to be used because until now it is not possible to trace all the low energy particles in the shower itself. In addition, also to trace all Cherenkov photons is still impossible nowadays. Another important aspect is also the simulations of the hadronic air shower component. For example the number of muons in hadronic air showers is still not proven to be the corrected predicted one. The problem lies still in the multi-TeV/PeV energy range which are up to now unfortunately not precisely known. Since the computing power steady increases nearly annually in the last decade, in about next 10 – 20 years this computing power development will allow us to simulate also the missing number of events and to trace nearly all Cherenkov photons in a VHE shower.
The MAGIC collaboration uses for their MC simulations a chain which includes three main programs called, CORSIKA, Reflector and Camera. During the simulation process the air shower events, which can be detected with MAGIC, are simulated from the point when the primary particles e.g. a γ quanta or a proton enters the atmosphere as well as the response of the reflector and camera electronic. In the following subsections, a brief overview about the three MAGIC MC simulation programs is given.

4.2.1 CORSIKA

COsmic **R**ay **SI**mulations for **KA**scade (CORSIKA) is an extended air shower simulation program. It simulates the interaction of primary particles with the atmosphere's molecules and the resulting extensive air shower propagation. More precisely, particles which are created from former interactions are tracked on their way through the atmosphere down to a chosen observation level by the user. In case of IACT observations, the most important Cherenkov photons, as described in Section 2.2, are simulated and the important information are stored. For the MAGIC MC simulation chain an adapted version of CORSIKA has been developed. There new parameters as well as changes in the code of the 'standard' version were implemented.

In particular following adaptations have been done for the MAGIC CORSIKA version itself.

1. particle type
2. energy range
3. range of incident angles
4. special Cherenkov wavelength band
5. observation level: 2200 m
6. magnetic field on the Canary Island of La Palma
7. atmospheric conditions

4.2.2 *Reflector*

The first part of the detector's simulations is done by a program called *Reflector*. In this part the *Reflector* program simulates the atmosphere's absorption of the Cherenkov photons on their way to the telescopes reflectors (mirror dish) as well as the reflection of the photons from the mirrors of each telescope itself. In case of the MAGIC telescopes following steps are simulated by the *Reflector* program.

1. The Cherenkov photons can interact during their way through the atmosphere in two ways. On the one hand there is the Rayleigh-scattering from the air's molecules and on the other the Mie-scattering from aerosols. During the simulation process the absorption caused both of these effects for the Cherenkov photons is taken into account.
2. In the next step the algorithm of the *Reflector* program checks if the incoming photons hit the mirror dish. In the situation that some photons do not reach the mirror dish they are neglected further on.
3. In the third step, the absorption of the mirrors that are covered with aluminum for M I and glass-aluminium for M II for the photons that hit the mirror dishes are simulated.
4. In addition, also the reflectivity itself is taken into account.
5. In the final steps, the algorithm checks which reflected photons reach the camera and calculate at the same time the arrival time for the incoming photons.

The output of the *Reflector* simulation program is a binary file which contains all informations about the Cherenkov photons, as already shown in the enumeration above, and which can be now processed by the last MAGIC detector simulation program called *Camera*.

4.2.3 *Camera*

The *Camera* program is responsible for the simulation of the PMT behavior, the trigger system, the read-out of the electronics - in particular the FADC. Moreover, *Camera* takes also into account the NSB which plays an important role during the observation of γ-ray sources. In particular following steps are in this program of importance:

1. In the first step of *Camera* the individual pixels are filled with the light conditions contributions (NSB).

2. Tn the second step *Camera* starts to read all photons from the shower in particular three steps are taking into account: pixelization, phe production, channel response.

3. At the final step the trigger is simulated. In the beginning it has to be checked whether generated analog signal exceeds a particular discriminator threshold or not. At the same time a digital output signal of a given length for those pixels is generated. Once this process is done the first level trigger, by checking the next neighbor conditions (NN) at a given time, as already described in Section 3.5, is simulated. Following trigger conditions are considered in the simulation process:

   a) Multiplicity: Gives the minimum number of pixels that are required to fulfill the trigger condition.

   b) Topology: Gives the distribution of the pixels in the camera.

4. In case the trigger condition is fulfilled then a first level trigger signal is generated as well as the process of the digitalization (FADC) is written.

When all showers are processed and the geometric properties of the mirrors and their reflectivity are read then all informations are stored in two output files. The first one is a text file and it contains all information about the trigger statistics whereas the second files is a root file. The latter has a structure that is very similar to a real data file. This file can be processed further on with the standard MAGIC analysis software MARS, just like the data files. Furthermore, the *Camera* program has also the option to create the pedestal and the calibration files. During an observation night, those pedestal and calibration

runs are taken additionally to the data runs, as describe in Section 3.7. In a simulation this process is also taken into account. The created pedestal and calibration files have to be given together with the simulated data runs to the first analysis step (`Callisto` see Subsection 4.1.2) in the MARS analysis chain.

4.3 Systematic Uncertainties

Since the Earth's atmosphere is used in IACT as calorimeter it cannot be guarantied that each observation night is taken under the same observation condition. There are small deviations of the density profile from the one assumed in MC simulations as well as the still not perfectly well known atmospheric conditions and transmissions. This factor is one of the most known where systematic uncertainties are introduced into the analysis chain. In this particular case, this affects the absolute energy scale, with an uncertainty of ≥10% [AAA+12d].
Another uncertainty factor is the amount of light focused by the mirrors. These effect produces a systematic error on the energy scale of ≈8%. In addition, further systematic errors of 6-8% on energy range are found by the flatfielding procedure, which is performed to homogenize the camera response as well as to equalize the product of the quantum efficiency of the PMT. In this context uncertainties in the conversion coefficient of photons detected by the PMTs to detectable phe are thought to introduce additional systematic errors. In particular these are uncertainties in the light collection of the Winston cone (≈4%), in the electron collection efficiency of the first PMT dynode (≈5%), in the quantum efficiency (≈4%) and also in the F-factor value of the PMT calibration (see Subsection 4.1.2) (≈10%) [AAA+12d]
Whenever an observation is performed also a mispointing can be introduced. Usually the mispointing is not larger than ≤ 0.02° [BDW+09].
As already mentioned above, MC simulations cannot fully describe the processes that happened in the atmosphere. Furthermore, discrepancies between data and MC introduce further dependence and in consequence further systematic errors of the reconstructed spectra on the applied signal cuts. In the low energy regime ($E \leq 250$ GeV) the systematic uncertainties are around 15% whereas in the medium range (> 250 GeV – 3 TeV) they decrease to 10%.
There are also uncertainties introduced during the unfolding procedures (see Subsection 4.1.9). These uncertainties affect mostly the indices of the spectra in the order of 0.1 [AAA+07d].
All in all, taking all these factors into account when observing with an stereoscopic system, the total systematic uncertainty for the indices of a spectrum is estimated to be 0.15. In the low energy range, the total error on the flux

normalization is estimated to be ≈19% and for the medium energy ranges it is determined to be ≈11%. Moreover, the total systematic uncertainty in the absolute energy scale is established to be ≈17% at low energies and ≈15% for medium energies [AAA+12d].
The following chapter deals with the most well studied VHE γ-ray source, the Crab Nebula, that is used for the calibration of an IACT-analysis.

CHAPTER 5

MAGIC ANALYSIS OF THE CRAB NEBULA

The Crab Nebula is a supernova remnant in the constellation Taurus. The corresponding explosions was observed in 1054 AD. Today this object is one of the best studied galactic sources throughout the entire electromagnetic spectrum. In case of the IACT this source plays an important role for the calibration of a VHE γ-ray analysis since it is always detectable with a steady and strong emission flux in a certain energy range. In this chapter, one example about a referenced Crab Nebula analysis that corresponds to a blazar analysis obtained during this work, is given.

5.1 The Crab Nebula

The Crab Nebula is one of the most observed remnants of supernova explosions and **P**ulsar **W**ind **N**ebula (PWN) throughout the entire electromagnetic spectrum. Its complex structure is displayed in Figure 5.1. This galactic object consist of a neutron star, also known as PSR B0531+21, inside the Nebula with a rotation period of 33 ms and a spin-down luminosity of 5×10^{38} erg s^{-1}, [MBFH05]. The first pulsed emission of the Crab pulsar has been observed in the radio band at the Arecibo Observatory in Puerto Rico in 1968 [SR68]. Since then pulsed emission from the Crab pulsar has been detected at all accessible energies up to γ-rays. In the γ-regime the **E**nergetic **G**amma **R**ay **E**xperiment **T**elescope (EGRET) detector was the first experiment which detected a pulsed γ-ray emission up to 5 GeV from this object in 1993 [NAB$^+$93]. Later the new generation satellites like **A**strorivelatore **G**amma a **I**mmagini **Le**ggero (AGILE) or the *Fermi* LAT satellite also confirmed this discovery in the

Figure 5.1: The complex structure of the Crab Nebula detected in different wavelengths. The optical bands (purple and red colors) and the X-ray band (blue and white colors) are shown. The white dot near the center is the pulsar, PSR B0531+21. The inner X-ray ring is thought to be a shock wave that marks the boundary between the surrounding nebula and the flow of matter from the pulsar. Energetic particles move outward to brighten the outer ring and produce an extended X-ray glow. The figure ist taken from [Cha09].

HE γ-ray range [AAA$^+$10a]. In addition, the Fermi collaboration performed a spectral analysis for this source fitting a power law to the spectrum and claiming an exponential cut-off at $E_c = (5.8 \pm 0.5_{\text{sys}} \pm 1.2_{\text{stat}})$ GeV, [AAA$^+$10e]. Surprisingly, the ground-based IAC telescopes, like MAGIC and VERITAS could detect pulsed emission from the Crab Nebula at even higher γ-ray energies as shown in Figure 5.2: 25 GeV by MAGIC [AAA$^+$08c]; 100 GeV by VERITAS [VAA$^+$11] and 400 GeV by MAGIC [KGL$^+$12] and ruling out the cut-off hypothesis.
Since the detection of pulsed emission succeeds up to the VHE γ-ray range, it is believed that strong particles shock accelerations are ongoing in this object. In particular, nowadays the assumption is established that the rotational energy of the pulsar is mostly carried away by a relativistic wind of electrons and positrons. At the same time the interaction of this wind with the surrounding medium develops a relativistic shock wave and consequently accelerated the leptons to higher energies [AGK$^+$01]. An alternative assumption for the

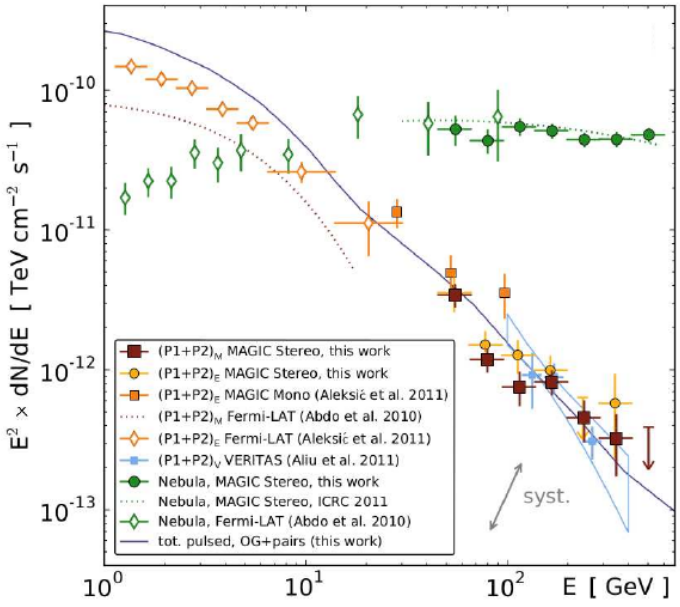

Figure 5.2: Spectral measurements of the Crab pulsar by various experiments. Together with *Fermi* LAT data the power law extend from 5 GeV to 400 GeV, connects well with the results from VERITAS and MAGIC and consequently excluding the cut-off hypothesis. The figure is taken from [Gia13].

acceleration scenario could be the reconnection of the alternating magnetic filed at the pulsar wind termination shock [Lyu03]. At this point, the wind ram pressure balances the total pressure of the nebula. Furthermore the leptons are accelerated in the shock and subsequently loose their energy by synchrotron emission processes [AAA$^+$08b]. This synchrotron radiation can be measured as the most dominant radiation part of the Crab Nebula from the radio to X-ray regime. In addition, it is believed that the same population of accelerated leptons is responsible for the HE and VHE γ-ray emission by **I**nverse **C**ompton (IC) scattering of low energy photons. Another photon field component such as the CMB or local IR photons can also be responsible for HE and VHE γ-ray via the IC process. In this context is should be noted that it is also believed that a hadronic component of the wind contributes to the VHE γ-rays emission and beyond due to decaying neutral pions π^0 [BB03].
The considered synchrotron and IC emission makes the Crab Nebula detectable at all wavelengths. Its size decreases with increasing the frequency as shown in Figure 5.3. This remarkable PWN was the first object to be well-established as a γ-ray source in the VHE range. In 1989, the Whipple telescope detected for the first time a clear signal (at 9σ confidence level) above

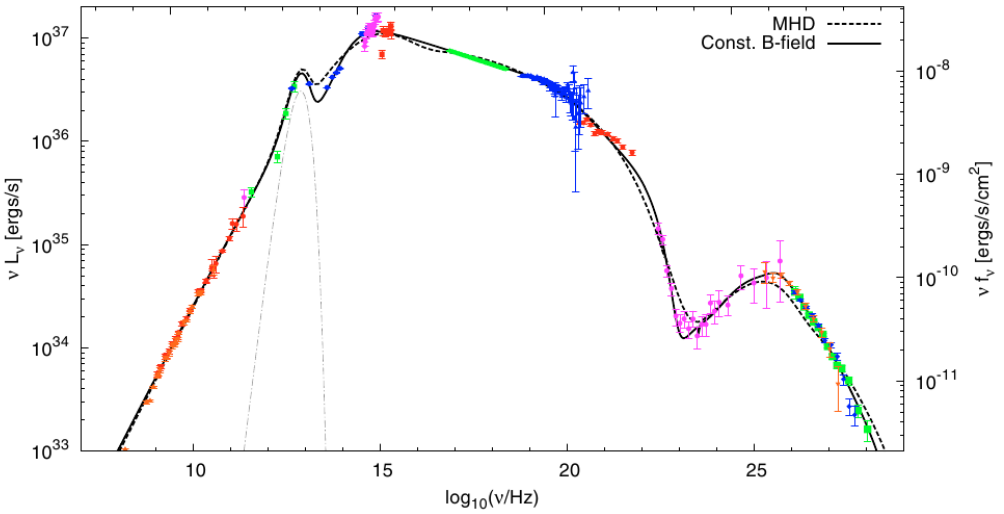

Figure 5.3: The SED of the Crab Nebula from submillimeter range to VHE γ-ray band. Including the best fits with a constant B-Filed model and the **M**agneto **H**ydro **D**ynamic (MHD) model. The figure is taken from [MHZ10].

an energy of 700 GeV coming from the nominal position of the Crab Nebula [WCF+89]. In the following 20 years, the IACT was successfully used for further observations of the Crab Nebula in the range from 60 GeV to 100 TeV by experiments like MAGIC, H.E.S.S., VERITAS, Whipple, **H**igh **E**nergy **G**amma **R**ay **A**stronomy (HEGRA), **C**ollaboration of **A**ustralia and **N**ippon (Japan) for a **GA**mma **R**ay **O**bservatory in the **O**utback (CANGAROO) and Milagro showing a steady and strong emission flux of VHE γ-ray photons. Due to its steady behaviour it has become the reference source for all ground based IAC telescopes. The improved sensitivity of the *Fermi* LAT and the MAGIC stereoscopic system, in 2011 at the **I**nternational **C**osmic **R**ay **C**onference 2011 (ICRC 2011) the first complete curvature of the IC peak from the Crab Nebula was presented, as illustrated in Figure 5.4. This result emphasized very well that the Crab Nebula is still one of the most exceptional galactic sources regarding the exploration of astroparticle physics.

5.2 The Crab Nebula data samples

As already mentioned above, the Crab Nebula plays an important role for the calibration of VHE γ-ray analysis. For each presented blazar analysis in the following Chapter 6, Chapter 7, Chapter 8 and Chapter 9 a corresponding Crab Nebula reference analysis was performed.

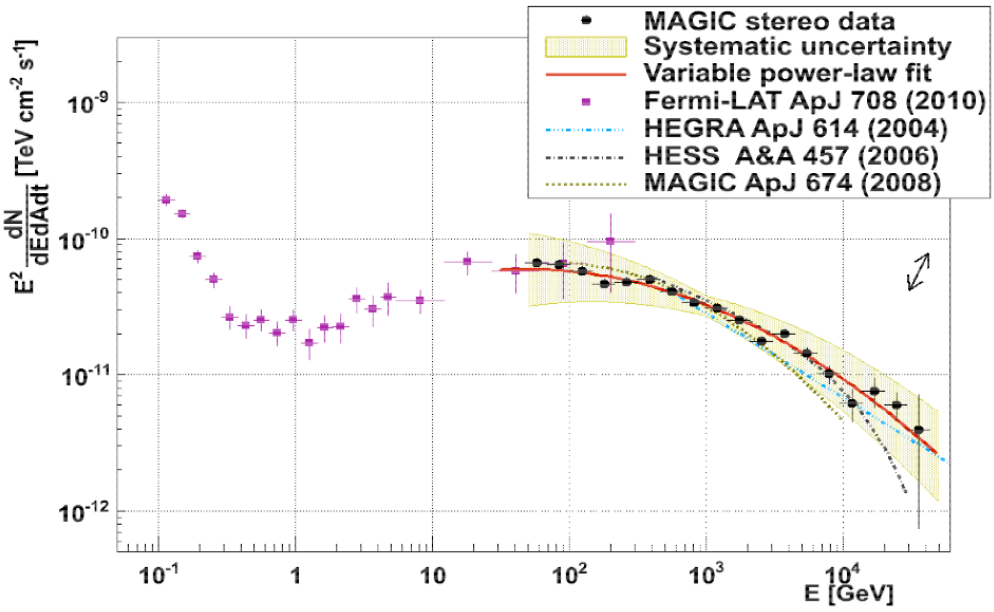

Figure 5.4: The Spectral energy distribution of the Crab Nebula from LE to VHE γ-ray range. For the first time a complete curvature of the inverse Compton peak from the Crab Nebula has been presented at the ICRC 2011.The figure is taken from [Zan11a].

The Crab Nebula data samples were selected in such way that the observation conditions were as similar as possible to the analyzed blazar source, that is with the same zenith angle distribution and period of observation (detector conditions). In order to find the cuts which would give the best significance and sensitivity, after applying the RF matrices to the Crab Nebula data by the analysis tool `Melibea` (see Subsection 4.1.5), all combinations of `Hadronness`, `Size` and α values in given ranges were tested:

- α: 6°-10° in steps of 2°
- `Size`: 100-400 phe in steps of 50
- `Hadronness`: 0.04-0.16 in steps of 0.02

The other parameters like i.e. `Leakage` or `Number of Islands` were set to default values. The first referenced analysis for the blazar 1ES 1959+650, as described in Section 6.3, is presented in the following subsection. This analysis serves as an example procedure of each corresponding Crab Nebula analysis for every blazar analyzed in the framework of this work. The results of the other Crab Nebula analysis are reported in the Appendix A.

5.3 Data sample for stand-alone MI analysis in 2009

As already mentioned, this Chapter gives an overview about how a Crab Nebula analysis can be used as a reference testing the analysis chain and verifying the applied signal/background separation cuts. The data for the first reference analysis was taken in January and March 2009. The main difficulty in order to perform a reference Crab Nebula analysis lies mostly in the selection of a best matching data set to the one of the analyzed source. In this case only few observation nights, that matched the high zenith observation conditions of 1ES 1959+650, were recorded from the Crab Nebula at the beginning of 2009. After applying quality selections, mainly based on rate stability and weather conditions the data from 3 nights with an effective observation time of only 1.8 hours, as listed in Table 5.1, was used.

Table 5.1: Crab Nebula reference sample - for 1ES 1959+650 in the first observation period in 2009.

Date	$T_{\text{eff}}[h]$	Zenith[°]	Mean Rate[Hz]
21 / 01 / 2009	0.38	35-45	180
25 / 01 / 2009	0.66	32-43	183
21 / 03 / 2009	0.75	27-46	155

5.3.1 The Crab Nebula signal

In order to find cuts which result in the best significance and sensitivity combination the following values were obtained for the Crab Nebula data sample: `Hadronness`= 0.07, `Size`= 300, and $\alpha = 6$ resulted in 22.97 σ and a sensitivity of 2.06%. Figure 5.5 shows the corresponding *Alpha*-plot with the achieved cuts. A second *Alpha*-plot (see Figure A.7) was also computed for a `Size` cut larger than 150 phe resulting in a sensitivity of 2.83% and a significance of 19.99 σ. This value is the minimum `Size` cut for the calculation of the light curve and energy spectra of the analyzed blazar 1ES 1959+650 defined also by the effective energy threshold, as described below. For completeness also a significance skymap of the Crab Nebula sample was computed, as displayed in Figure 5.6. One can see a clear excess of 30 σ which is in addition consistent to the Crab Nebula sky position (empty cross).

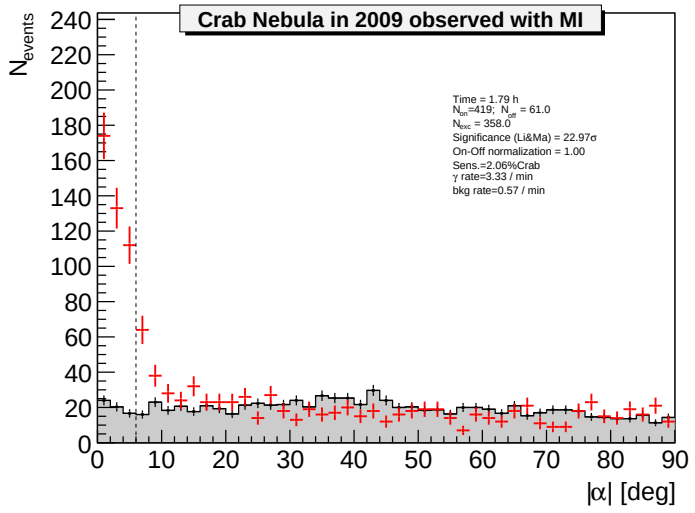

Figure 5.5: *Alpha* distribution of the Crab Nebula signal and background estimation from 1.79 hr of M I taken between January 21st and March 21st 2009. The data, taken under high zenith conditions (35°-46°) shows a strong signal with a significance close to 23 standard deviations and serves to verify the calibration and the performance of the stand-alone M I telescope in this period.

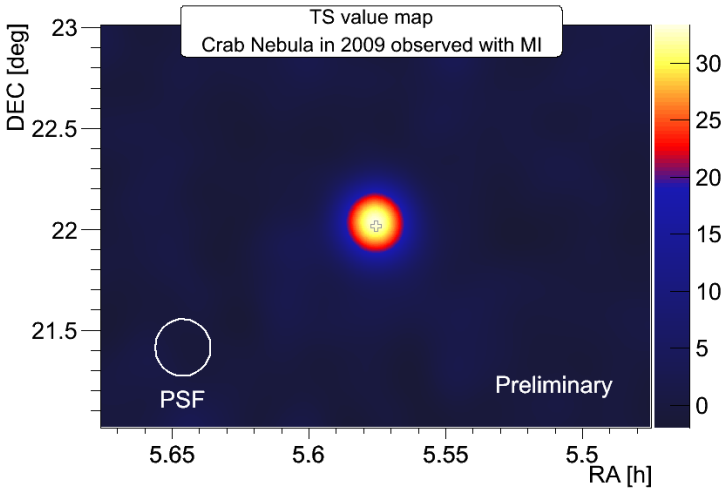

Figure 5.6: Significance skymap of the sky region around the Crab Nebula from 1.79 hr of MAGIC observations taken between January 21st and March 21st 2009 under high zenith conditions. The Crab Nebula position is marked with an empty cross. The **P**oint **S**pread **F**unktion (PSF) of about 0.10 degree is also displayed.

5.3.2 Analysis Threshold

Since the standard trigger threshold of MAGIC is about 70 GeV, one has to keep in mind that the impossibility to efficiently discriminate the background events below a certain Size of the images increases the effective energy threshold to higher values as presented here. The effective energy threshold of an analysis is estimated using a MC test sample (see Section 4.2), that is statistically independent from the sample used for the RF (see Subsection 4.1.4) training. The background separation procedures obtained in the same way as well as the energy estimation are applied to the Crab Nebula data and to the MC sample. Such a comparison of both samples allows to estimate the energy threshold after the analysis cuts (but also to estimate the efficiency of all the possible cuts). The effective energy threshold is defined as the peak of the reconstructed energy distribution, as shown in Figure 5.7, for a given size cut. For the MC high zenith sample used here a `Size` cut of 150 phe and `Hadronness` of 0.07 resulted in 285 GeV.

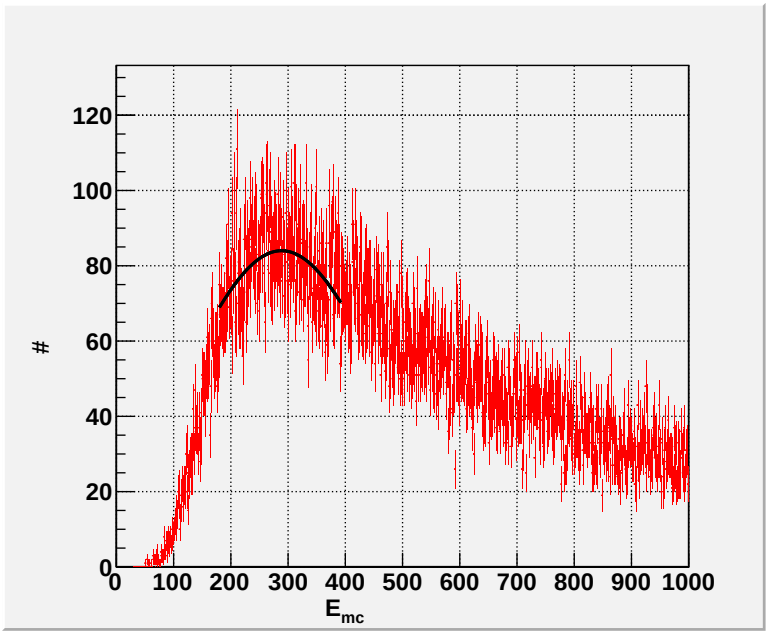

Figure 5.7: Crab Nebula analysis energy threshold for `Size` cut of 150 phe. The energy threshold is determined by the position of the peak in the distribution of the reconstructed energy in the MC (black curvature).

5.3.3 Flux stability of the Crab Nebula

In order to check further analysis quality criteria of the analysis chain of the Crab Nebula, a light curve and spectrum have been computed and will be presented in the following subsections. The light curve of the Crab Nebula has been computed for energies above 300 GeV, as illustrated in Figure 5.8, which is in agreement with the energy threshold of 285 GeV. The daily measurements of the Crab Nebula flux (blue points) indicate a constant flux of $F(>300\,\mathrm{GeV}) = (1.17\pm0.09)\times10^{-10}\,\mathrm{cm}^{-2}\,\mathrm{s}^{-1}$. This value is in good agreement with the reference value (red dashed line) of the Crab Nebula flux from M I reported in [AAA+08b].

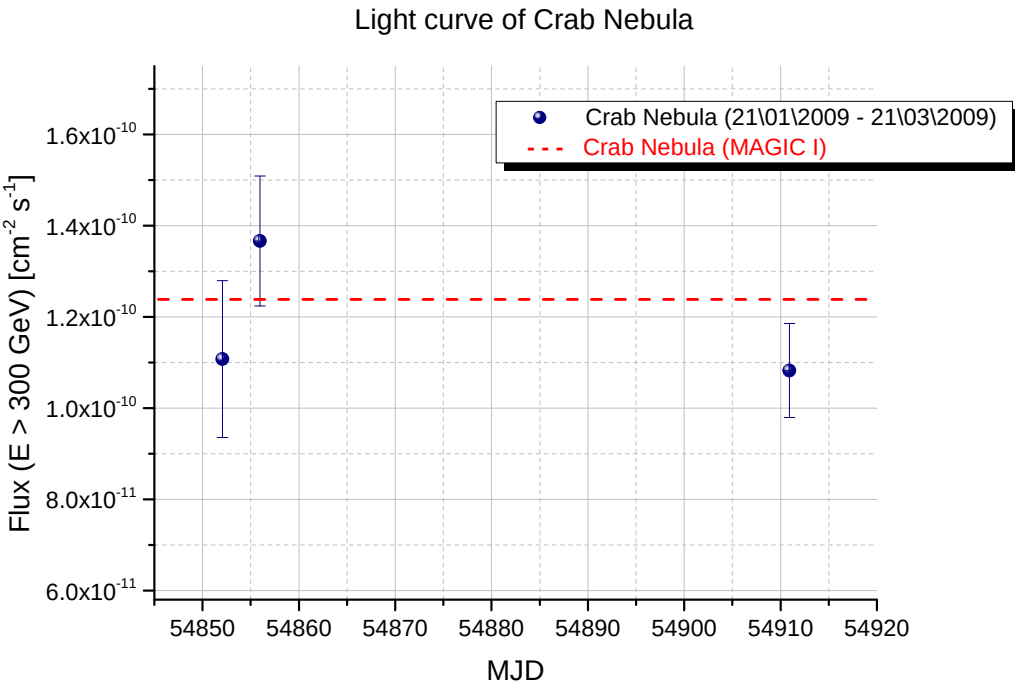

Figure 5.8: Light curve of the Crab Nebula between January and March in 2009. A constant flux of $F(>300\,\mathrm{GeV}) = (1.17\pm0.09)\times10^{-10}\,\mathrm{cm}^{-2}\,\mathrm{s}^{-1}$ has been measured that is in good agreement with the referenced value (red dashed line).

5.3.4 Spectrum of the Crab Nebula

Figure 5.9 shows the results of the differential flux analysis of the Crab Nebula sample in the energy range from 200 GeV to 4 TeV for three different unfolding methods, as described in detail in Subsection 4.1.9. The unfolded spectrum can be fitted with a simple power law of the form

$$\frac{\mathrm{d}N}{\mathrm{d}E} = N_0 \left(\frac{E}{1\ \mathrm{TeV}} \right)^{\Gamma}, \tag{5.1}$$

with a photon index Γ, a normalization constant at 1 TeV and flux N_0. The results of the fits are given in Table 5.2. It can be seen, that all three unfolding methods agree within their error ranges and thus confirm again the stability and consistency of the Crab Nebula analysis chain.

Table 5.2: Crab Nebula spectra unfolding results - for three different unfolding methods (*Bertero, Schmelling* and *Tikhonov*).

Unfolding method Name	Photon index Γ	Flux N_0 $[\times 10^{-11}\mathrm{cm}^{-2}\mathrm{s}^{-1}\mathrm{TeV}^{-1}]$	Fit goodness $[\chi^2/\mathrm{NDF}]$
Bertero	-2.51±0.08	(2.54±0.16)	3.32/4
Schmelling	-2.76±0.09	(2.53±0.19)	10.17/4
Tihkonov	-2.55±0.09	(2.56±0.22)	1.00/4

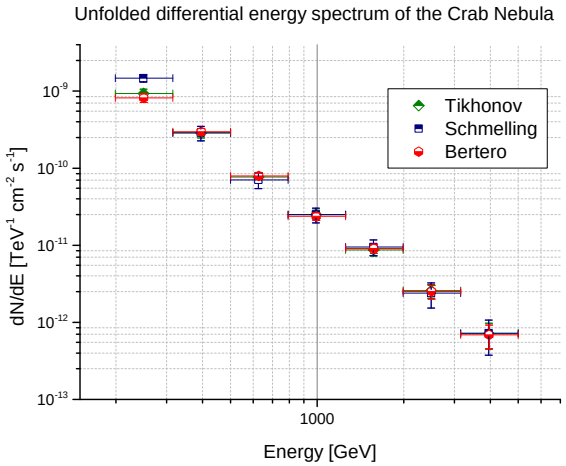

Figure 5.9: Comparison of the three different unfolding methods of the Crab Nebula spectrum. All methods agree within their error ranges, thus confirming the stability of the Crab Nebula analysis chain.

5.4 Summary and Conclusions

In this chapter the properties of the Crab Nebula and its interest for the VHE γ-ray analysis were discussed. It has been the reference source and standard candle for the VHE γ-ray analysis calibration. The Crab Nebula analysis shown here, which is an example for all other analysis of the Crab Nebula obtained separately for each blazar analyzed in this work, delivers results compatible with the reference values of previous measurements with M I. For this reason the light curve and the spectrum can be regarded as confirmed in this case and consequently the used set of cuts can be applied to the analysis of 1ES 1959+650 as it will be described in the next Chapter 6. Furthermore, the three unfolding methods (*Bertero, Schmelling and Tikhonov*) showed nearly similar results confirming the stability of the analysis chain.

CHAPTER 6

MONITORING OF 1ES 1959+650 WITH MAGIC

The BL Lac object 1ES 1959+650 was discovered as VHE γ-ray emitter in 1997 by the Utah Seven Telescope Array. After the discovery, since 2004 MAGIC started to observe this source regularly in order to monitor its activity. In this chapter the analysis of the data taken from 2009 to 2012 is presented and the corresponding results combined and compared with previous findings. In particular, the signal search as well as the main physical results related to the differential spectrum and integral flux analysis are described. The results from a power law fit of the differential energy spectrum of the here analyzed years are compatible with a steady mean photon index of $\Gamma = -2.57 \pm 0.06$. During the last three years of observations this blazar shows only marginal variability, in the range from 5% to 12% of the Crab Nebula flux above 300 GeV. Besides, the spectral changes of one distinct flare in May 30$^{\text{th}}$ 2009 are discussed in detail in this chapter. From simultaneous radio observations during this flare a strong correlation between both wavelengths is found, supporting the assumption of γ-ray flaring emission in the parsec-scale jet of this blazar. In contrast, simultaneous optical observation did not reveal any connection between both wavelengths and thus confirming previous results that in this blazar also different structure of the emitting plasma and thus synchrotron radiation are at work. Finally, a combination of the mean spectrum measured at VHE γ-range with archival data available for other wavelengths is presented in a SED. This particular distribution can be modeled with a two zone SSC model which is quite unusual for a BL Lac object and confirming again its different VHE γ-ray emission mechanism and locations.

6.1 The Blazar 1ES1959+650 and its properties

The blazar 1ES 1959+650 is an elliptical galaxy, located between the constellation of Draco and Cepheus at RA: 19 h 59 m 59.8 s, DEC.: +65 d 08 m 55 s, in EquJ2000.0 coordinates. From the historical point of view 1ES 1959+650 was first observed in the radio band as a part of 4.85 GHz survey performed with the 91 m **N**ational **R**adio **A**stronomy **O**bservatory (NRAO) Green Bank telescope [GC91],[BWE91]. One year later in 1992 it was observed in the X-ray band by the Einstein Observatory and consequently listed for the first time in the first catalog of the Einstein Slew Survey as 1ES 1959+650 [EPS+92].

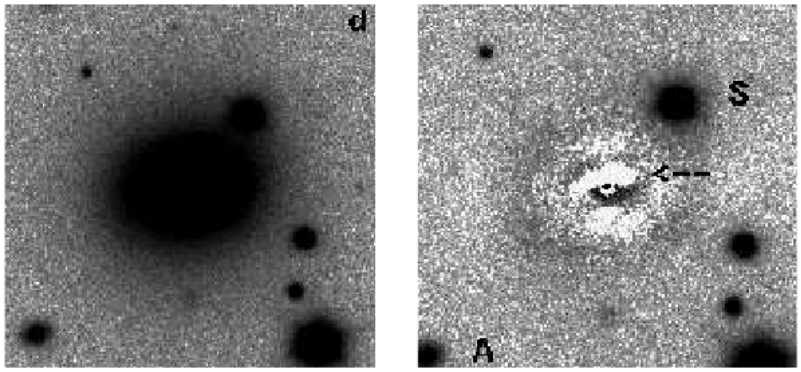

Figure 6.1: Optical view of 1ES 1959+650 before (left) and after the galaxy subtraction (right) taken with the NOT on La Palma. The arrow in the right image indicates an absorption feature of about 1“ to the north of the center [HNS+99].

The morphologically discovery of this source dates back to 1993, when radio, optical, and X-ray observations reveal its identification as BL Lac type object [SSP+93]. Especially in the optical high-resolution observations with the **N**ordic **O**ptical **T**elescope (NOT) its profile shows an unusual brightness in a complex structure composed by an elliptical galaxy plus a disc and an absorption dust lane as shown in Figure 6.1. In addition, in the optical R-band this source shows, comparing the flux with the other here presented blazars like 1ES 0033+595 (Chapter 7), B3 0133+388 (Chapter 8) or PKS 1717+177 (Chapter 9), very high variability (see Figure 6.2).
In order to classify 1ES 1959+650 to one of currently three known possible subclasses of BL Lac objects (HBL, IBL, and LBL respectively), as explained in detail in Subsection 1.5.2, the resolution of the peak position of the synchrotron component in the SED is necessary to know. Previous observations performed by Metsähovi in the radio band, the **I**nfra**R**ed **A**stronomical **S**atellite (IRAS)-

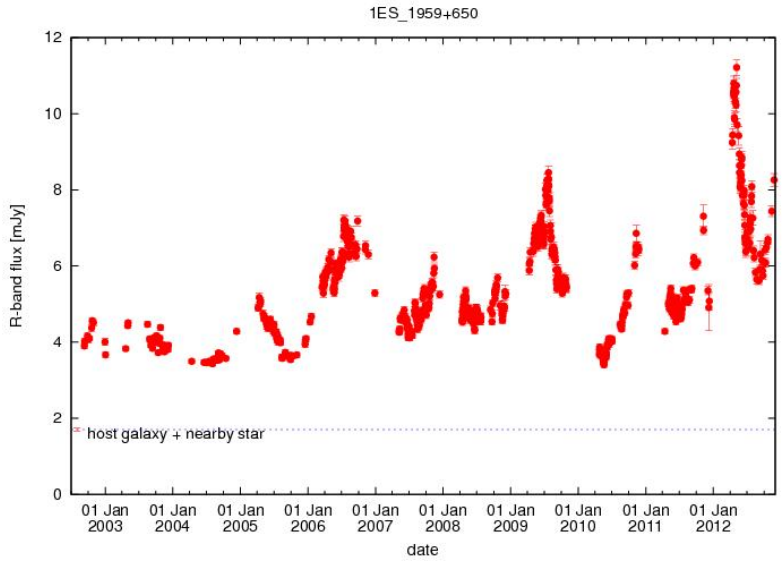

Figure 6.2: 1ES 1959+650 optical light curve between 2003 and 2012, from Tuorla/KVA telescopes. The figure is taken from [Nil13].

and **2** **M**icron **A**ll **S**ky **S**urvey (2MASS) observations in the IR band as well as optical data provided by **A**strophysical **C**atalogues **S**upport **S**ystem (CATS) and X-ray data from Einstein- and **RO**entgen **SAT**elit (ROSAT)-catalogues resolved together for the first time, as presented in [NTV06], the synchrotron component of the 1ES 1959+650 blazar (see Figure 6.3). Furthermore, recent studies by [Bac11] could fully resolve the synchrotron peak of 1ES 1959+650, claiming a synchrotron peak value of $\nu^{\mathrm{syn}}_{\mathrm{peak}} = 1.71 \times 10^{17} \pm 1.34 \times 10^{15}$ Hz. Consequently, both results confirm very well the position of the synchrotron peak to be located well above 10^{16} Hz and thus classified 1ES 1959+650 to be a HBL object.

As many other BL Lac objects this galaxy hosts also a **S**uper **M**assive **B**lack **H**ole (SMBH) inside. Comparing all three most known methods that are used to derive the mass $M_{\odot}$ of a central black hole, on the one hand by study the variability time scale and on the other hand the velocity dispersion of the central area around the black hole as well as the host luminosity, then a mean value of about $10^{8.3} M_{\odot}$ can be determined [Bac11]. In case of 1ES 1959+650 the SMBH is also considered to be the main engine for the observed VHE γ-ray emission. Such emission is beamed usually along one major jet toward the earth that allow us to observe the VHE photons boosted in the jet itself.

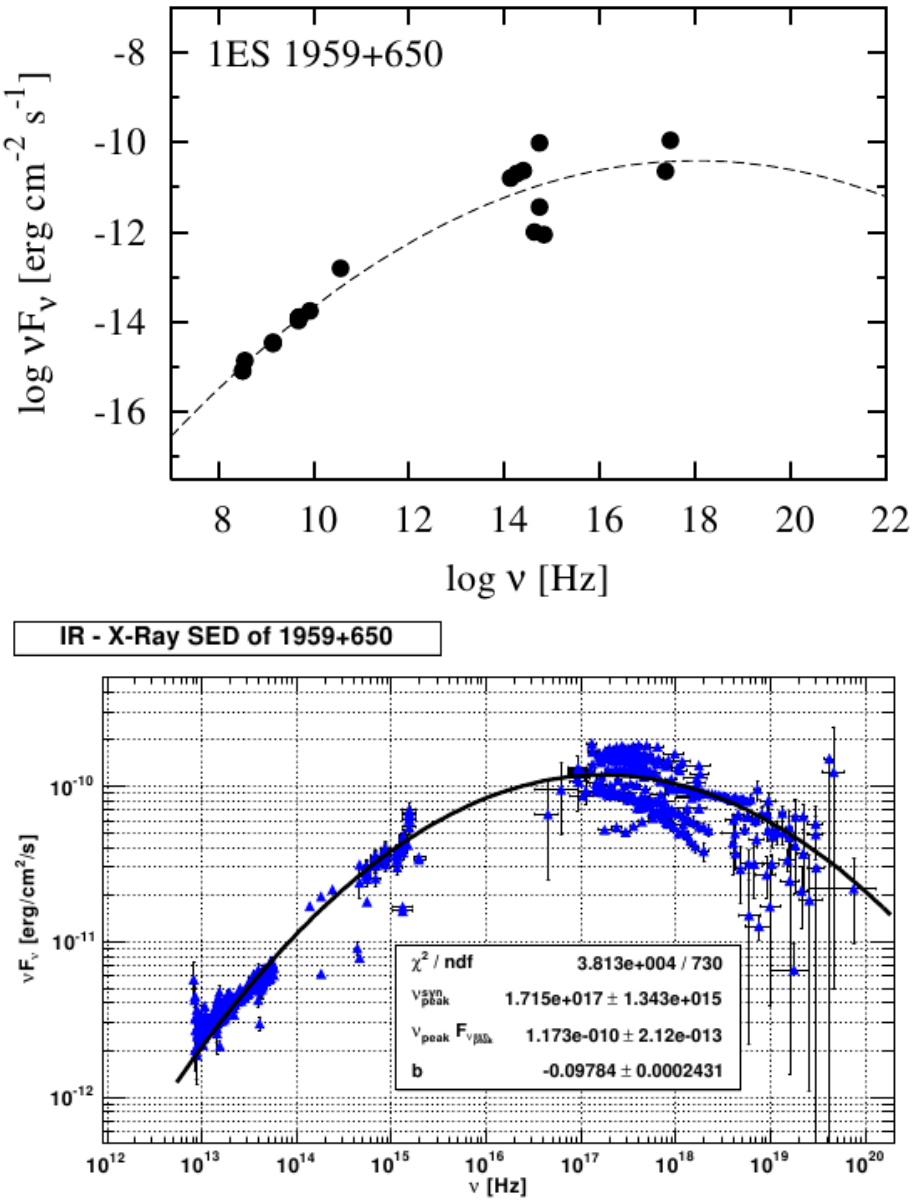

Figure 6.3: The synchrotron peak of 1ES 1959+650 taken from [NTV06] (top) and the recent synchrotron peak estimation by [Bac11] (bottom).

6.2 Observations of 1ES 1959+650 in the VHE γ-ray band

As anticipated above and predicted by many different authors already fifty years ago before the first detection of VHE γ-ray emission could be indeed measured in one of the nearest ($z = 0.031$) and brightest blazars, Markarian 421 (Mrk 421) in 1992. The Whipple collaboration performed the first experiment, with its 10 m telescope that made the first discovery of such blazar possible [PAC+92]. Since then, various blazars have been discovered, among others 1ES 1959+650 in 1997. The Whipple collaboration observed this source in 1996 also after the discovery of Mrk 421, but unfortunately due to the source low state they could report only flux upper limits for this object [CBB+97]. In the following year, in 1997, the **U**tah **S**even **T**elescope **A**rray (USTA) observed 1ES 1959+650 too, this time claiming for the first time a tentative discovery of 1ES 1959+650 with $3.9\,\sigma$ and subsequently, after including addition data, passing the commonly applied $5\,\sigma$ limit for source discoveries [Nis99]. Five years later in 2002, the Whipple collaboration could confirm the discovery, when the source underwent a strong activity in the VHE γ-ray range [HBB+03]. In parallel, also the HEGRA system of Cherenkov telescopes measured this strong VHE γ-ray activity from May until June in 2002 [Hor03], [AAB+03]. Subsequently, the strong VHE γ-ray activity from 1ES 1959+650 in 2002 triggered a multi-wavelength campaign, with simultaneous radio, optical, X-ray, and γ-ray observations, during which the first *orphan flare* was observed [KHH+04]. *Orphan flares* are γ-ray flares without any contemporaneous X-ray flaring activity. Such unusual events are not expected from simple **S**ynchrotron **S**elf **C**ompton (SSC) models and thus not describable in these models. In order to explain the *orphan flare* of 1ES 1959+650 observed in 2002, different hadronic synchrotron models have been developed (i.e. [RBP05]), making this source one of the most promising blazar in which hadronical interactions are responsible for the VHE γ-ray emission. Since then the interest to observe this source in the whole electromagnetic spectrum grew and the first detection with the MAGIC telescope occurred in 2004, followed by annual observations until 2010, as outlined below in detail in Subsection 6.2.2.

6.2.1 The redshift of 1ES 1959+650

From the optical observations, more precisely from the optical spectroscopy measurements, one is usually able to estimate the redshift of different galactic and extragalactic objects. Unfortunately, in case of blazars more than a half of the AGNs classified as BL Lac objects have unknown or uncertain redshifts.

The main reason for this condition lies in their dominant jet emission of these objects that hides any feature of the system. During the past twenty years the situation improved a bit due to new improved instruments and spectrometric and photometric techniques. In case of 1ES 1959+650 the latest published optical spectroscopy performed with the optical data from the 2.1 m telescope and the Goldcam spectrograph at Kitt Peak National Observatory shows a featureless spectrum with no emission lines and only few absorption lines, as shown in Figure 6.4. Therefore, a redshift of $z = 0.048$ could be estimated for this blazar. Moreover, during these optical observations the polarization and the polarization angle have been observed and determined in [PSS+96] supporting also in this case the BL Lac classification of 1ES 1959+650.

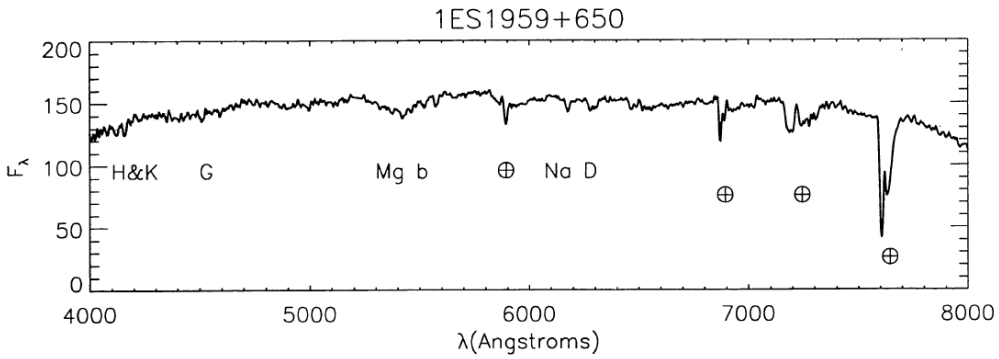

Figure 6.4: Spectroscopy measurements of 1ES 1959+650 showing a featureless spectrum with no emission lines [PSS+96].

6.2.2 MAGIC monitoring program

The long-term monitoring with new generation of IAC telescopes, like MAGIC, can give valuable inputs and consequently improve our knowledge on blazar physics, not only by participation in multiwavelength observations, but also by performing an emission state independent observations of peculiar bright blazars. The advantages of such long-term observations are on the one hand the possibility to obtain an unbiased distribution of flux state and on the other hand the possibility to collect data of low flux states which are still sparse. Nowadays, any statistical study which requires high statistics on various flux levels, in order to claim an extraordinary behavior, is still difficult. An alternative interesting aspect to favor monitoring observations is the investigation of spectral changes during time periods of different flux states, which can be used for further study toward acceleration and emission regions in

the jets of blazars. Another application of such survey is the trigger function for other observatories and experiments. The **T**arget **o**f **O**pportunity (ToO) observations can be performed by the IAC telescopes issuing the ToO and consequently allowing to increase the time coverage of observatories or experiments in other energy/wavelength regions. The low duty cycle of $\sim$ 10% leads to a very precious observation time of IAC telescopes and sparse observation time has to be scheduled very carefully in order to achieve the right balance between the AGN monitoring program and other (e.g. galactic) observations. In case of such long-term monitoring programs, in particular IAC telescopes like the Whipple telescope, which was leading an AGN monitoring program since the beginning of 2005 ([Pf09]), and the new developed **F**irst G-**A**PD **C**herenkov **T**elescope (FACT) ([ABB$^+$13]), one of the former HEGRA telescopes are used for this purpose. The MAGIC collaboration started its first monitoring program like the Whipple telescope in 2005. The target sources were the three nearest and brightest blazars (Mrk421: $z = 0.031$, Mrk 501: $z = 0.034$ and 1ES 1959+650: $z = 0.048$). A large part of the MAGICs monitoring observations ($\sim$ 60%) has been performed under moderate moonlight or twilight conditions, keeping the impact on the overall observation schedule low and improving the available duty cycle up to 12%. In order to achieve a dense sampling, up to 40 short observations per source are scheduled, evenly distributed over the observable time [HST$^+$09]. Such short flux measurements should be enough to detect a given source minimum flux level taking into account the sensitivity of the telescope system (for more details about the MAGIC performance see [CGS$^+$09] and [AAA$^+$12d]). In case of Mrk 421 and Mrk 501 which are one of the most brightest TeV blazars, usually 15 – 30 min observation time are scheduled for them. For 1ES 1959+650, being fainter, an observation time of at least 30 minutes per single exposure should be assigned.

6.2.3 MAGIC observations of 1ES 1959+650

Short after its commissioning phase in 2004 MAGIC observed with the standalone telescope MAGIC I, here after M I, 1ES 1959+650 where a clear signal of 8 σ was detected [AAA$^+$06b, Ton06]. One year later, in 2005, a regular monitoring program of the three brightest and closest blazars was started (for detail description of the monitoring program see the previous Subsection 6.2.2). The most important results of the MAGIC monitoring program have been already published in [GBB$^+$08, HST$^+$09, SHB$^+$09] and [Wag11]. The corresponding MAGIC analysis of each observation year can be found for 2005 and 2006 in [Zan06, Hay08], respectively as well as for the years 2007 and 2008 in [Sat10] and [UM09]. The whole overview about the six year MAGIC monitoring observations and the corresponding detections for each monitoring year can be

found summarized in Table 6.7. In the following Sections (Section 6.3 - Section 6.5), the monitoring results of 1ES 1959+650 of the MAGIC observation years 2009, 2010 as well as the 2012 observations during a ToO project (Section 6.6) will be presented and discussed.

6.3 Observations with MAGIC I in 2009

In 2009, the observations of 1ES 1959+650 with MAGIC were carried out in two different observation conditions. The first observation period of this source started from May 20th until July 29th and was performed with the stand-alone M I telescope whereas in the second period (since fall 2009) MAGIC was operated as a system of two telescopes in stereo mode [CGS$^+$09]. The corresponding analysis for the second observation period will be described in detail in Section 6.4. In this section the analysis procedure and results from the first observation period in 2009 are discussed.
Like in previous monitoring observation years, 1ES 1959+650 is unfortunately only observable from La Palma under relatively high ($36° - 48°$) zenith angle conditions. Furthermore, when not in a high state like in 2002 when the flux was 2-3 factor higher than the one of the Crab Nebula (for more details see also Section 6.2), the source is rather faint showing a flux of 8-10% of that Crab Nebula flux above 300 GeV during the monitoring observations from 2005 until 2008. All the data analyzed here are taken in wobble mode, as already explained in Section 3.8. The overall summary of the observations performed in this period is presented in Tables B.1 and B.2 in Appendix B.

6.3.1 Data quality selection

Usually the data quality selection in the standard MAGIC analysis is done after the image cleaning (after the program `Star` as described in Subsection 4.1.3) by each analyzer independently. Bad quality data is commonly rejected and therefore not used anymore in further analysis steps. These selections are essential for a correct data reduction and later for a good signal to noise ratio. The selection criteria in the MAGIC analysis are base on bad weather conditions and / or hardware problems or changes. In case of bad weather conditions for example when thick clouds passing by the field of view of the telescopes or when the dust from the sahara desert, called calima, occurred then the sky transparency decreases and the opacity increased. Consequently, the event rate during such observations conditions decreases or is very unstable and the threshold of the analysis increases, since low energy events are strongly reduced. Other important aspects, as already mentioned shortly

Table 6.1: 1ES 1ES 1959+650 2009 M I data set used in this study after data quality selection. From left to right: dates in dd / mm / yy, effective time of observation in hours, zenith angle distribution, rate of the event after the image cleaning in Hz and the significance of each observation night.

Date	Eff. time [h]	Zenith [°]	Mean Rate [Hz]	Significance [σ]
20 / 05 / 2009	0.71	42-47	100	3.40
21 / 05 / 2009	1.16	42-47	101	4.79
25 / 05 / 2009	0.25	36-38	203	1.33
30 / 05 / 2009	0.18	42-49	110	4.76
19 / 06 / 2009	1.98	35-42	147	3.75
20 / 06 / 2009	1.31	40-46	148	3.58
22 / 06 / 2009	0.39	41-46	214	1.35
24 / 06 / 2009	0.27	41-46	135	0.42
25 / 06 / 2009	0.33	41-46	119	1.68
26 / 06 / 2009	0.32	41-46	130	0.91
27 / 06 / 2009	0.32	41-46	185	0.47
28 / 06 / 2009	0.32	41-46	170	1.93
30 / 06 / 2009	0.33	41-46	141	0.84
01 / 07 / 2009	0.46	41-46	124	2.30
02 / 07 / 2009	0.33	41-46	132	4.10
03 / 07 / 2009	0.59	41-46	107	3.74
05 / 07 / 2009	0.51	41-46	120	4.36
29 / 07 / 2009	1.75	41-46	212	2.71
30 / 07 / 2009	1.23	41-46	100	3.58
31 / 07 / 2009	0.28	41-46	148	1.69

above, are hardware problems or changes in the telescopes subsystems affecting the data quality strongly. In particular, the most relevant telescopes hardware component responsible for the quality of the date are: mirror reflectivity, pointing accuracy, and camera response. Due to a huge number of bad pixels in the camera for example as side effect a camera inhomogeneity (especially in the stand alone analysis) may occur. Unfortunately, part of the here analyzed data were taken under such circumstances leading to a fully or partly rejection of such data. The other important parameters which are used as selection criteria for the data are: stable rates > 100 Hz, # corr. stars > 15, cloudiness < 40%.

6.3.2 Signal search during the first observation period in 2009

As mentioned in Subsection 4.1.6, the detection of a signal from a dedicated source plays an important role for the further procedure of an analysis. In case of the data set from the M I telescope the distribution of the parameter `alpha` is applied. As in detail described in Subsection 4.1.6, the distribution of the parameter `alpha` stands in connection to the incoming direction of the primary particle that induced an atmospheric air shower. Figuratively, images originated from a VHE primary γ-ray photon have this parameter close to zero because of their observed direction, while images caused due to hadron particles have a uniform distribution of `alpha` in consequence of its nearly isotropic arrival direction. In Figure 6.5 the *Alpha*-plot of the events obtained from M I observations of 1ES 1959+650 in 2009, after applying a `Size` cut of 300 phe and a `Hadronness` cut of 0.07 is shown. These cut are tested on a corresponding Crab Nebula sample, as described in detail in Chapter 5.

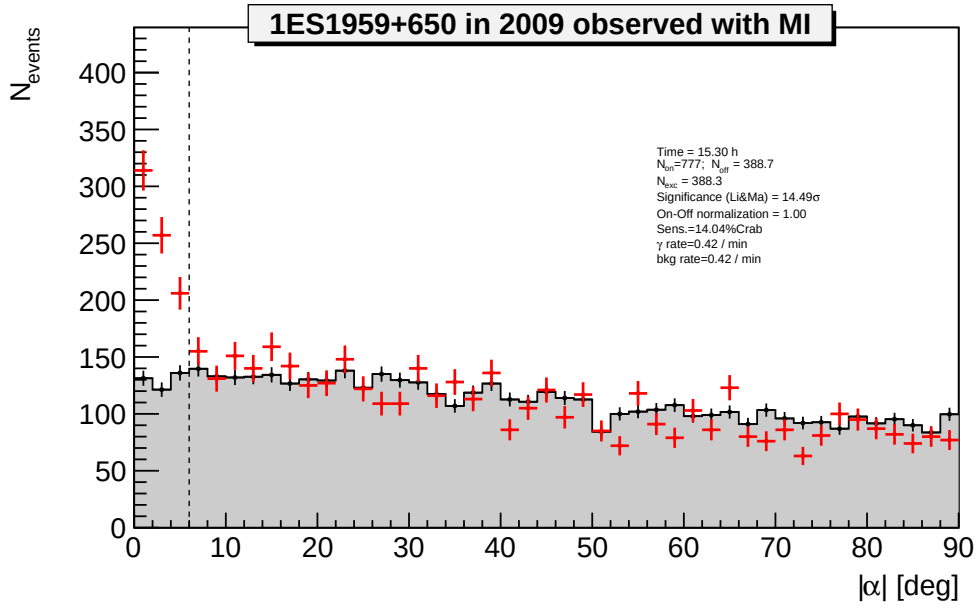

Figure 6.5: The *Alpha* distribution of the 1ES 1959+650 signal and background estimation from 15.30 hr of M I observations taken between May 20th and July 29th in 2009. The distribution of the obtained signal events is shown as red crosses in the plot while the background data is shown as the gray region. An excess of 388.3 events was observed with a corresponding strong detection of 14.5 σ.

During this observation period an excess of 388.3 events was observed above a background of 388.7 events for $\alpha < 8°$. The described *Alpha*-plot shows a strong detection of 1ES 1959+650 in the first period of 2009 with a significance of 14.5 σ during an effective observation time of 15.30 hours.
Looking at the corresponding VHE γ-ray skymap the excess agrees excellent with the nominal position of 1ES 1959+650 as shown in Figure 6.6. The emission is point-like for the angular resolution of M I.

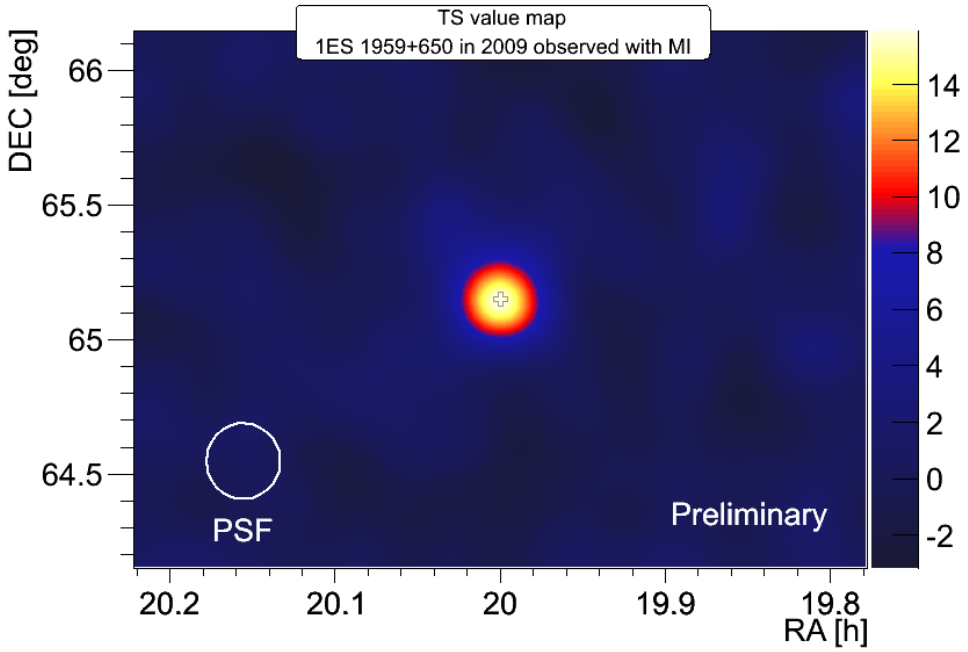

Figure 6.6: The corresponding significance of the 1ES 1959+650 with M I in 2009 obtained from each sky position. The source position is shown by the cross in the center of the skymap and agrees excellent with excess events coming from the same position. Furthermore, the emission is point-like for the angular resolution of M I and the PSF of 0.1 degrees is shown in the bottom left corner.

6.3.3 Temporal behavior of 1ES 1959+650 in the first observation period in 2009

In order to investigate and to compare the temporal evolution of 1ES 1959+650 emission with previous MAGIC monitoring years, the integral flux emission above 300 GeV has to be estimated. The temporal bins are selected according to each observation night (night-by-night binning).

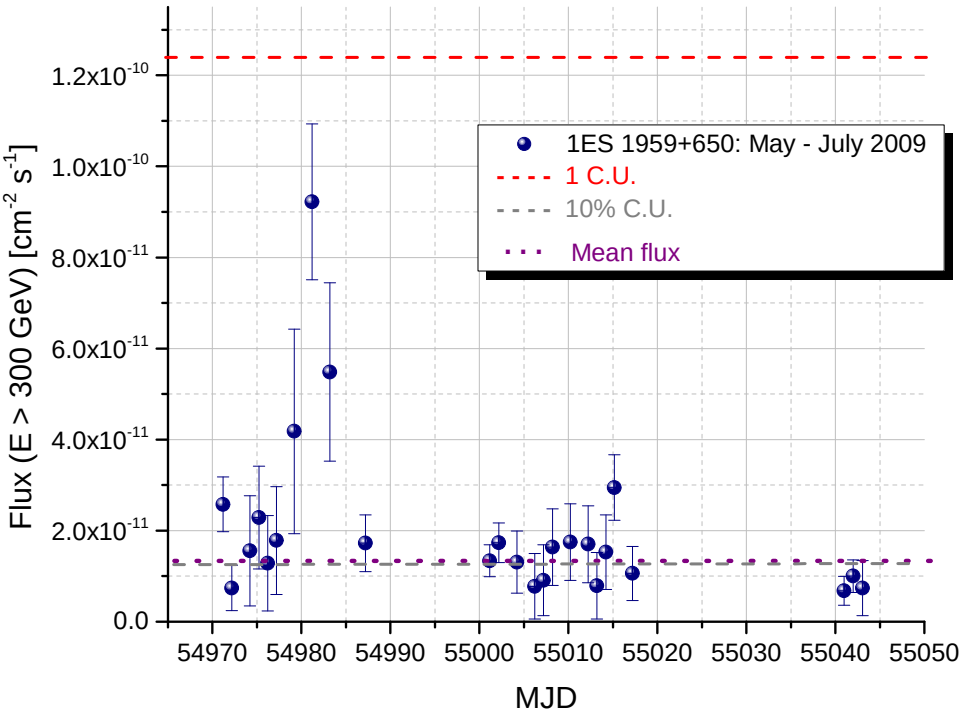

Figure 6.7: 1ES 1959+650, light curve between May and July 2009 above an energy threshold of 300 GeV, and with a daily time-scale binning. This time strong variability is seen in the data. The purple dashed horizontal line represents the mean flux and constant function from the fit to the data.

As it can be seen in Figure 6.7, only one distinct flare is observed on 30th May, reaching a flux level of ~0.70% C.U. [1] above 300 GeV. The periods immediately before and after the flare show comparatively low flux levels (≈9% C.U.), which make the flare outstanding and well suited for further flare mechanism study. When fitting the light curve by a constant fit a clear variability is found from this observation period yielding $F(>300\,\mathrm{GeV})=(1.22\pm0.12)\times10^{-11}$ cm^{-2} s^{-1} with χ^2/NDF=41.97/18 (probability of a constant flux ~ 0.11%). This is the first time that 1ES 1959+650 shows a clear variability since the very fist observation and the highest state in 2002 reported by Whipple and HEGRA experiments. The unique observation night on May 30$^{\mathrm{th}}$ is subjected to a closer inspection, as it shows a unusual variability pattern for this source and will be described in detail in Subsection 6.3.5.

[1] A Crab Unit (C.U.) is marking the flux state of the Crab Nebula above 300 GeV (2.24×10^{-10} cm^{-2} s^{-1}).

6.3.4 Spectral properties of 1ES 1959+650 in the first observation period in 2009

The differential energy spectrum observed with M I of 1ES 1959+650 in the first observation period of 2009 is studied in detail in this subsection. For the spectrum reconstruction the emission in intervals of reconstructed energy (or true energy in the case of unfolded spectrum) is investigated. In case of the first 2009 sample, where a clear significance of 14.49 σ (see Figure 6.5) has been detected, 28 bins in logarithmic scale between 5 GeV to 50 TeV were set using a size cut of 150 phe. The cuts in `Hadronness` and α are dynamical i.e. their definition is based on their cut efficiency as estimated from γ–like MC simulation events leading to energy dependent cuts. The cuts are chosen in such way that 90% and 70% of the simulated γ–like events survive the cuts respectively. Looking further on the unfolded spectrum which is characterized by the same bins scaled by a factor 1.4, it allows to perform the true energy reconstruction procedure. Figure 6.8 shows the differential energy spectrum of 1ES 1959+650 after this correction procedure, performed with different unfolding algorithms (*Forward, Bertero, Schmelling and Tikhonov*), as described in detail in Subsection 4.1.9.

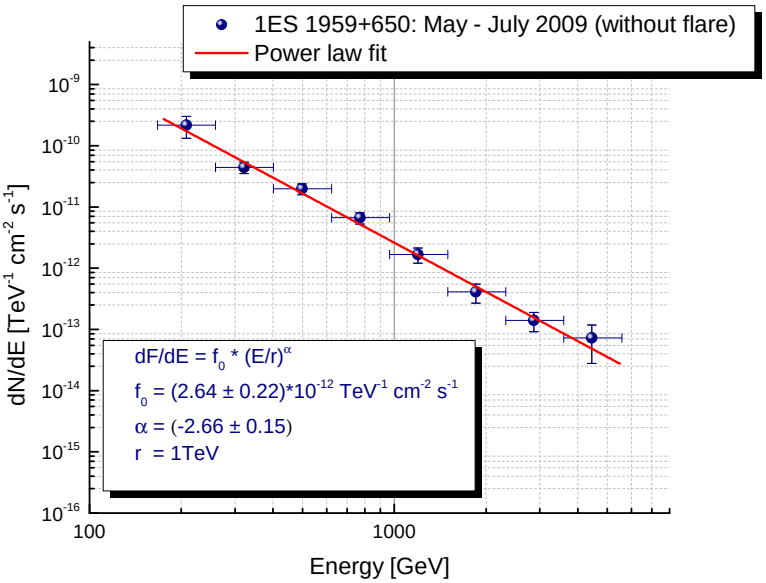

Figure 6.8: 1ES 1959+650 differential energy spectrum measured by MAGIC between 150 GeV and 5.5 TeV in the first observation period in 2009. The power law fit to the data is also shown (red line).

All unfolding algorithms are in very good agreement among each other. For further analysis steps and comparison process the *Bertero* unfolding algorithm has been selected giving the best probability of the fit. The spectrum in the energy range 150 GeV to 5.5 TeV can be well fitted by a power law of the form:

$$\frac{\mathrm{d}N}{\mathrm{d}E} = N_0 \left(\frac{E}{1\ \mathrm{TeV}} \right)^{-\Gamma} \tag{6.1}$$

with photon index $\Gamma = 2.66 \pm 0.15$, and a normalization constant at 1 TeV of $N_0 = (2.64 \pm 0.22) \times 10^{-12} \mathrm{cm}^{-2} \mathrm{s}^{-1} \mathrm{TeV}^{-1}$, with a fit goodness of χ^2/NDF=2.58/4 and a corresponding probability of 63%. These results are in agreement with previous determinations of the source spectrum as shown in Section 6.7. In addition, it should be noted that this presented spectrum was calculated without the particular flare day, on May 30$^{\mathrm{th}}$, in order to perform a low state spectrum parameter determination. Finally, due to not sufficient exposure time in order to reach a spectrum range of >10 TeV, where interactions between the VHE γ-rays and the EBL via pair production at distances of $z = 0.048$ could become evident, no further EBL studies can be derived. For a detail description about the EBL see Section 1.3 and Subsection 10.3.4. Nevertheless, the here achieved results will be used for further spectra comparison study as described in Section 6.7. The particular flare day analysis and results are discussed in the following Section 6.3.5.

6.3.5 Results of the flare analysis on May 30$^{\mathrm{th}}$

As already pointed out in Subsection 1.5.2 and Subsection 6.3.3 the emission level of blazars is strongly variable on all timescales accompanied by frequent changes of the emission level of the electromagnetic radiation often by more than one order of magnitude. One example is the recently observed very strong flare in the blazar Mrk 421 in 2013 where its emission level was 11 times higher than the Crab Nebula flux above 300 GeV. In contrast, in the previous years its baseline emission level was found to be only few percent of the Crab Nebula flux [Cor13]. The detected different flaring states of blazars in the VHE γ-ray regime are usually correlated with a flux increase in the X-ray band and sometimes also in the optical and radio energy band. In addition, during such flaring states also changes of the spectral shape with the enhanced flux level have been measured. In order to investigate the exceptional flare on May 30$^{\mathrm{th}}$ (MJD 54982) of 1ES 1959+650 regarding such changes a correlation study and spectral shape comparison is conducted.

Observation condition

During the monitoring program (as described in detail in Subsection 6.2.2) in 2009 the observation time was usually scheduled for 10 – 20 min per night. In case of the observation on May 30$^{\text{th}}$ the hole exposure took only 18 minutes, starting at at 04:46 UT and ending at 05:04 UT. This observation was performed under moderate moonlight conditions and the data was taken at zenith angles between 36° and 37° in wobble mode. Unfortunately, during this observation night the online analysis was not working properly, thus the operators did not know that 1ES 1959+650 was flaring at that time. Consequently, extended observation time was not assigned on that particular night.

Signal distribution

In order to check how strong the flare on May 30$^{\text{th}}$ in 2009 was, a dedicated *Alpha*-analysis has also been performed separately for this particular day. From the *Alpha*-plot using common detection cuts with `Size` of 300 phe and a relaxed `Hadronness` cut of 0.1 (due to the short exposure), a strong signal of 5.4 σ has been measured. Figure 6.9 shows the *Alpha*-plot with only 1 off region (top) (as the data was unfortunately recorded) and with 3 off region (bottom) only for comparison reason. Interestingly and confirming the flare appearance is the high γ-rate of ~ 4/min. In comparison the usual 1ES 1959+650 γ-rate in quiescent state is ~ 1/min.

Flare spectral distribution

To investigate the spectral changes during the flare of 1ES 1959+650 a spectrum was calculated for this particular day. Figure 6.10 shows the result of the differential energy spectrum analysis of this particular flare. Due to the short exposure time of only 18 minutes the range of this spectrum is rather short and covers only the interval from 150 GeV to 550 GeV. The power law fit of the form

$$\frac{\mathrm{d}N}{\mathrm{d}E} = N_0 \left(\frac{E}{250\,\mathrm{GeV}} \right)^{-\Gamma} \tag{6.2}$$

gives a photon index of $\Gamma = -2.29 \pm 0.29$, a normalization constant at 250 GeV and a corresponding flux value of $N_0 = (1.82 \pm 0.25) \times 10^{-9} \mathrm{cm}^{-2}\mathrm{s}^{-1}\mathrm{TeV}^{-1}$ with a fit goodness of χ^2/DNF=3.09/4 and P(χ^2)=0.43.
Comparing the fit results of the differential flux analysis of the SED of the form:

$$E^2 \frac{\mathrm{d}F}{\mathrm{d}E} = E^2 N_0 \left(\frac{E}{250\,\mathrm{GeV}} \right)^{-\Gamma} \tag{6.3}$$

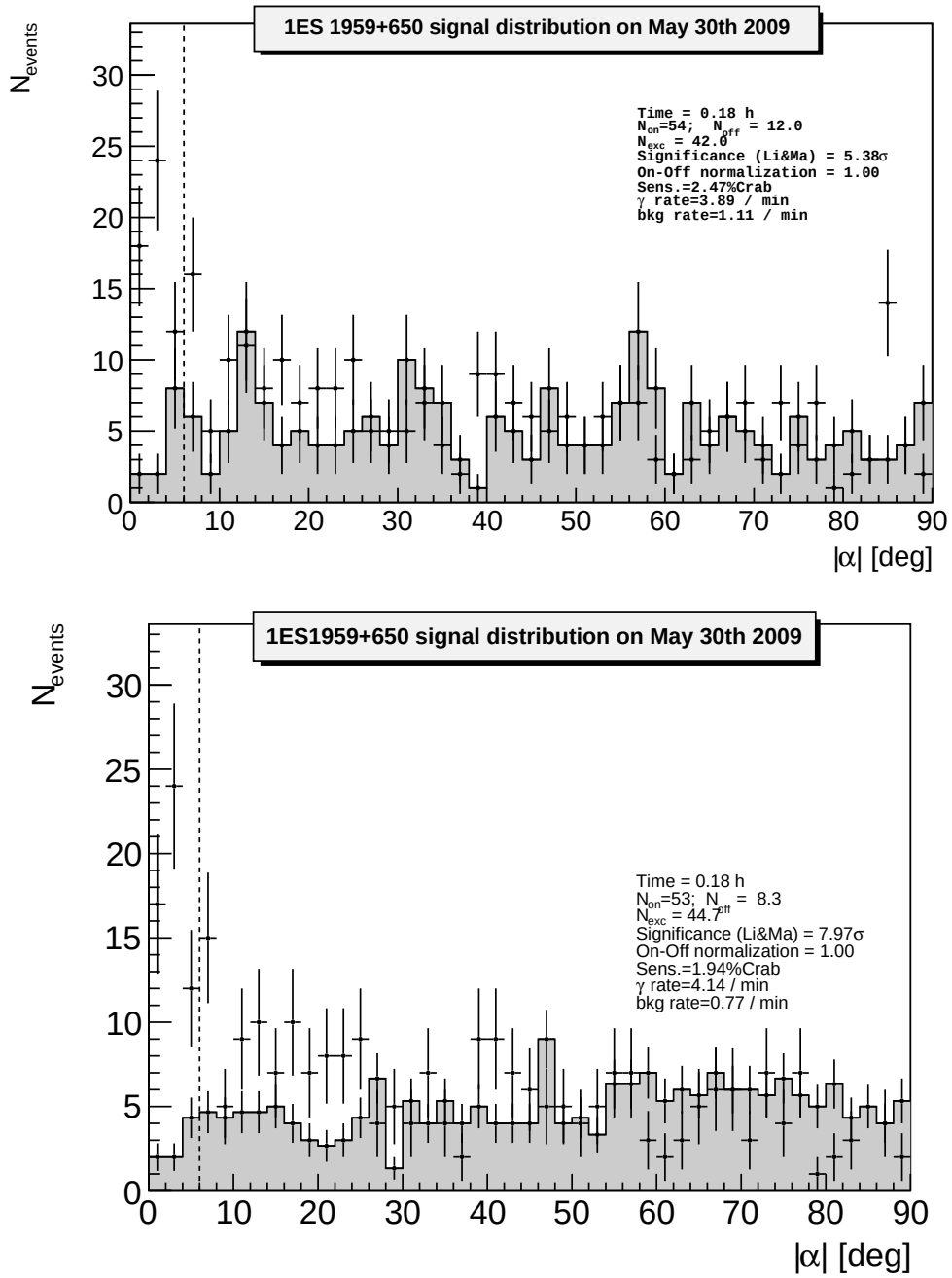

Figure 6.9: *Alpha*-plot from May 30th in 2009 with 1 and 3 off regions for comparison.

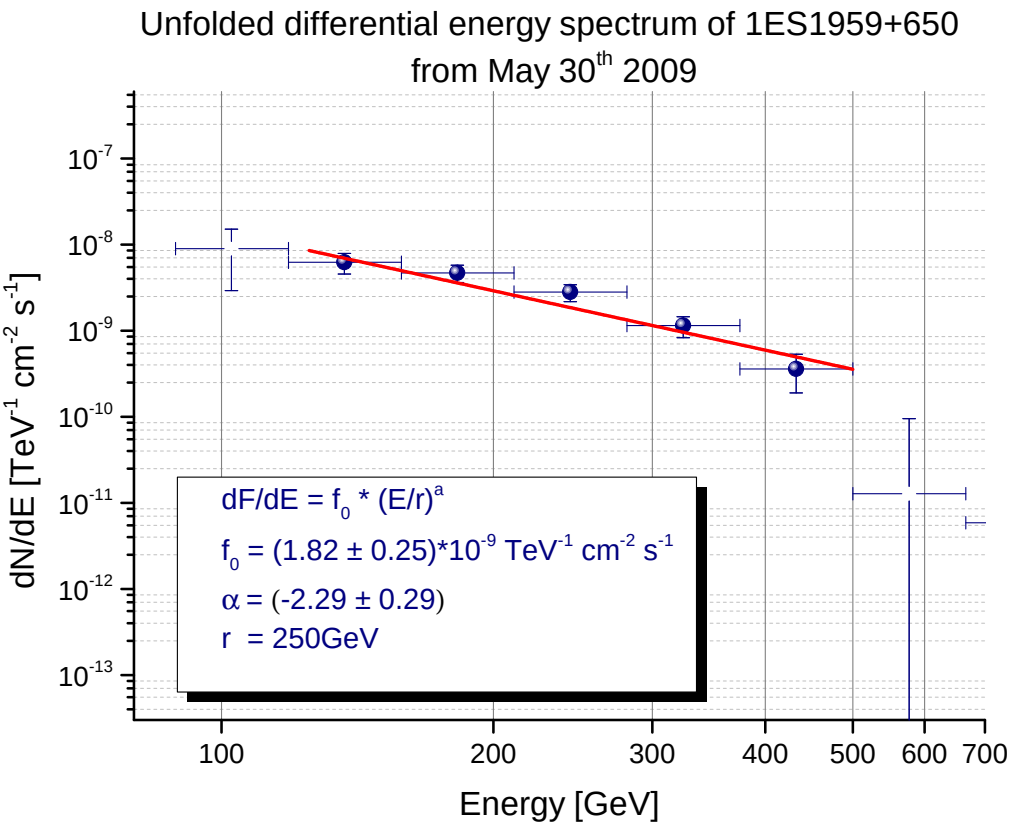

Figure 6.10: Differential energy spectrum of May 30th in 2009.

as shown in Figure B.1 and Figure B.2 then a simple power law fit in this case is no longer a adequate fit function. Another fit approach is usually found in a curved power law fit followed by the equation:

$$\frac{\mathrm{d}N}{\mathrm{d}E} = N_0 \left(\frac{E}{\mathrm{r}}\right)^{\mathrm{a}+\mathrm{b}\log_{10}(\mathrm{E/r})} \tag{6.4}$$

The corresponding values for this fit are: $a = -2.34 \pm 0.34$, $b = -2.00 \pm 0.02$ and a normalization constant at 250 GeV of $N_0 = (2.18 \pm 0.30) \times 10^{-9} \mathrm{cm}^{-2}\mathrm{s}^{-1}\mathrm{TeV}^{-1}$. Applying this fit on the SED the goodness of the curved power law fit is estimated to be χ^2/DNF=0.32/3 with the probability of 95% which is much better than the goodness of the pure power law fit (see above). This finding demonstrates very well, as already observed for Mrk 421 in 2010 and reported in [Ste12] that the VHE γ-ray spectra of different HBL flares show a much obvious curvature shape. Another aspect is, if one compares the average spectrum with the one containing the flare, as depicted in Figure 6.11, then a significant higher flux, as expected, is also evident. In addition, the spectrum show

a hardening with increasing flux level, ranging from a mean low state spectrum described by a photon index of $\Gamma = -2.66 \pm 0.15$ to flare spectral index of $\Gamma = -2.29 \pm 0.29$. Such behavior was already observed in different blazars as reported in [Wag08] or [Ste12].

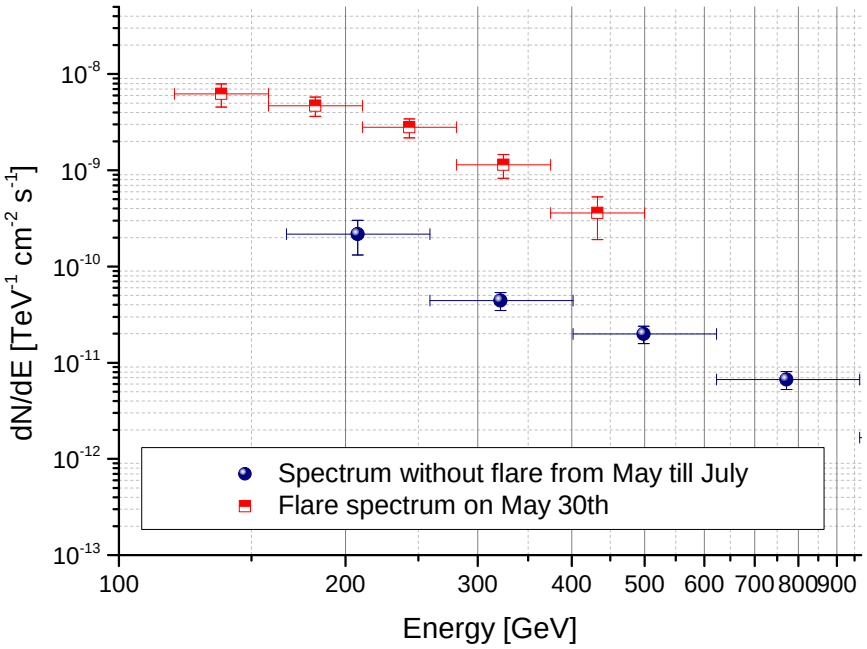

Figure 6.11: Comparison of the differential energy spectrum of 1ES 1959+650 in a low average sate with that on the flare day on May 30th in 2009. The blue points represent the average 2009 spectrum whereas the red points show the flare day.

Flare multiwavelength correlations

To prove possible correlations in different wavelengths, light curves with a dense sampling are necessary. Unfortunately, as depicted in Figure 6.12, for this interesting period, the X-ray (*Swift*, **R**ossi **X**-ray **T**iming **E**xplorer (RXTE)) and HE γ-ray (*Fermi* LAT) observations were not frequent enough to claim or disprove a possible multiwavelength correlation. Even if the evolution of the X-ray light curve gives again a hint of an *orphan flare* (for a detail explanation of an *orphan flare* see Section 6.2 or [KHH$^+$04]), if one compares Figure 6.12 (top and bottom panel) and Figure 6.13 with each other, no precise conclusions at the current stage can be made.

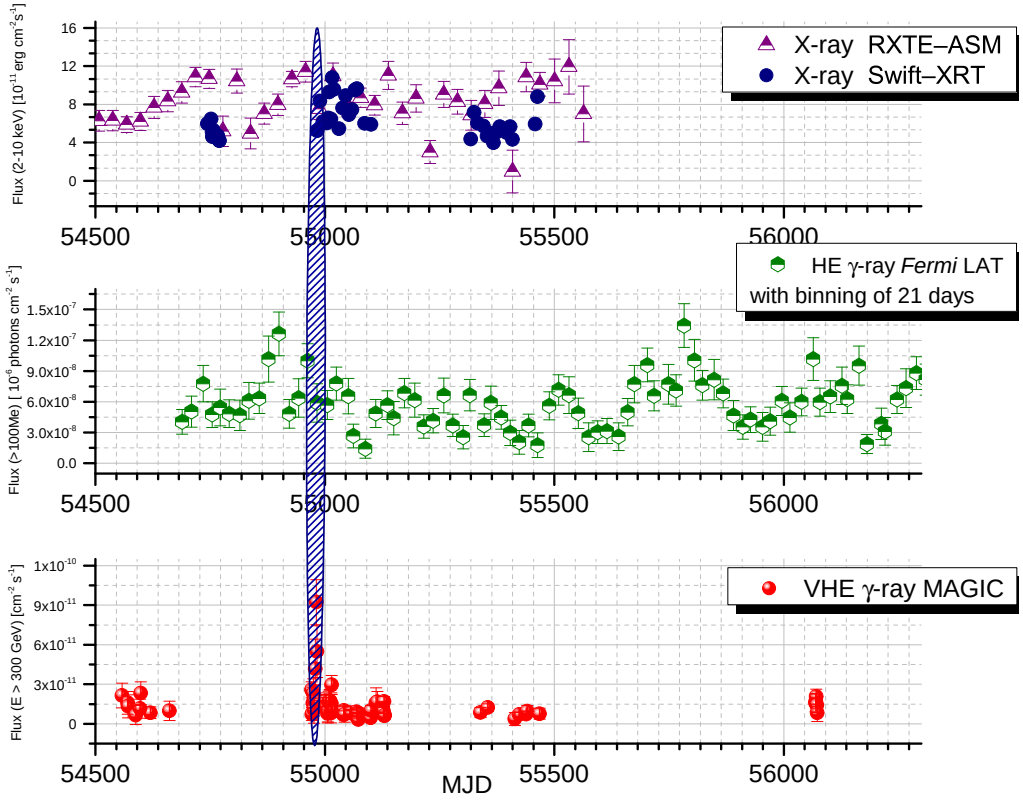

Figure 6.12: Multiwavelength light curve from the X-ray, HE and VHE γ-ray range from 2008 to 2012. Again an *orphan flare* seems to occur when comparing the X-ray and the VHE γ-ray light curve.

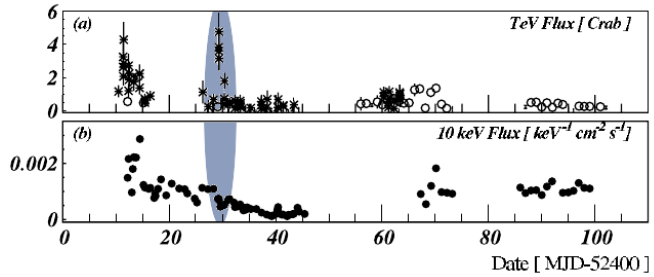

Figure 6.13: The prominent *orphan flare* observed in 2002 form 1ES 1959+650 by Whipple, HEGRA above 600 GeV and 2 TeV, respectively as well as the RXTE (X-ray at 10 keV) measurements (bottom panel). Adapted from [KHH+04].

The only experiments that could provide a dense sampling of that particular period are the optical observation from the Tuorla/KVA observatory and the radio observations performed by the **V**ery **L**ong **B**aseline **A**rray (VLBA) [Moj13] and **O**wens **V**alley **R**adio **O**bservatory (OVRO) at 15 GHz [OVR13], respectively. Figure 6.14 shows in the bottom panel the optical light curve in the R-band, where a strong variability of this sources is visible. In the middle panel the light curve of the present MAGIC results above 300 GeV is presented.

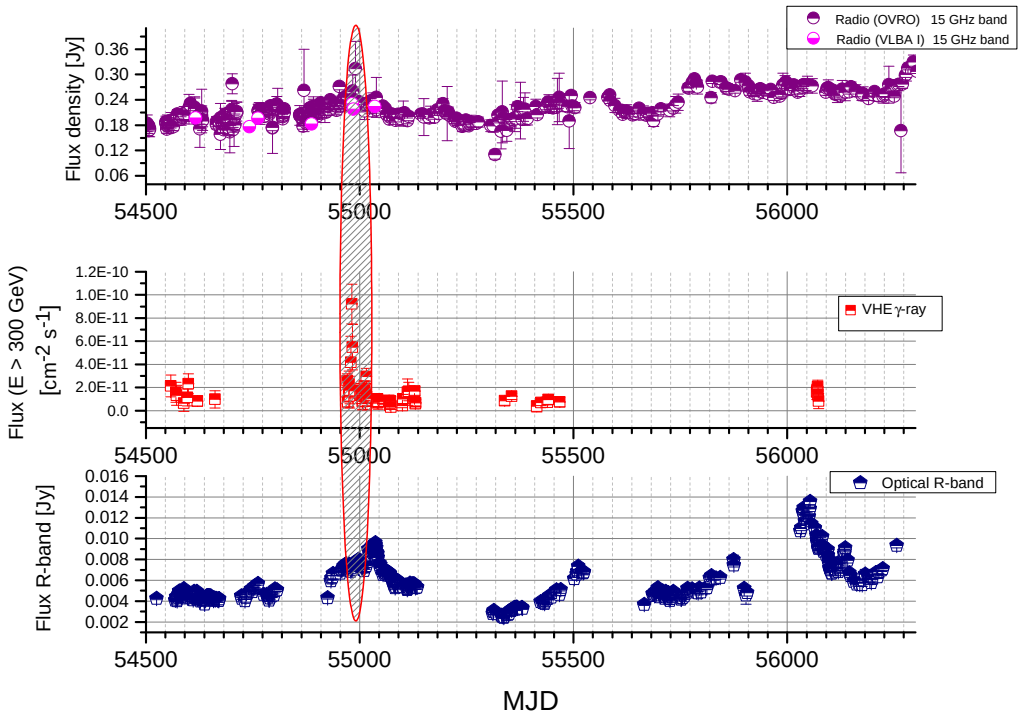

Figure 6.14: Multiwavelength light curve from the radio, optical and VHE γ-ray range from 2008 to 2012. In this light curves a correlation between the radio and the VHE γ-ray range becomes evident.

In addition, in the top panel, the radio data taken at 15 GHz from the observatories described above with the corresponding observation periods are shown. At first glance, comparing the radio measurements from the OVRO with the VHE γ-ray one, a correlation between both wavelengths becomes evident. This flux enhancement is also confirmed by the core flux measurements of the VLBA I observatory where a local maximum is found on June 1st, as listed in Table 6.2. Besides, also new radio components as reported by the **M**onitoring **O**f **J**ets in **A**ctive galactic nuclei with **V**LBA **E**xperiments (MOJAVE)

program and as illustrated in Figure 6.15, occurred during the same observation period.

Table 6.2: 1ES 1959+650 VLBA core flux measurements showing a maximum state (F=231 mJy) on June 1st in 2009.

Date	Flux [mJy]
23 / 07 / 2009	224
03 / 06 / 2009	218
01 / 06 / 2009	**231**
25 / 02 / 2009	181
23 / 10 / 2008	196
03 / 10 / 2008	176
30 / 05 / 2008	197
08 / 02 / 2008	89
31 / 10 / 2003	151
09 / 06 / 2003	160
09 / 06 / 2000	147
06 / 03 / 2000	129

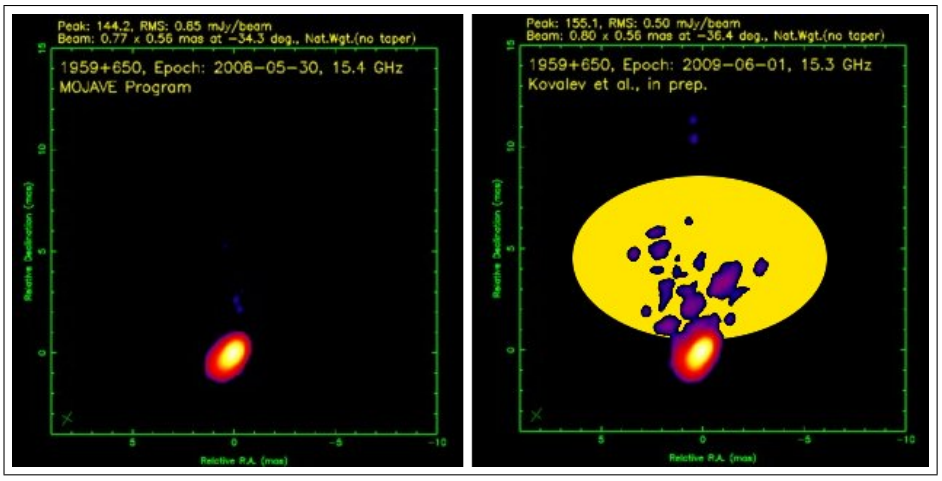

Figure 6.15: MOJAVE skymap showing new radio components on June 1st in 2009 (right side) in comparison with previous observations (left side) performed one year earlier where no new radio components are visible. Adapted from [Moj13].

In order to confirm this correlation appearance in the multiwavelength light curves a **C**ross **C**orrelation **F**unction (CCF) was applied. This mathematic function of two time series, in this case for the VHE γ-ray, radio and optical light curve, reveals the magnitude and significance of characteristic lag times between the two series.The length of a possible delay, τ, is related to the light travel time between the γ-ray source and the reprocessing region [BS12]. In case of the radio and the VHE γ-ray light curves, the observations were sampled at intervals of 2 days over that time span. The in this analysis considered lags on time scales of 0-120 days. A peak in the CCF, as shown in Appendix B, Figure B.3, indicates that the radio emission is delayed relative to the γ-rays by about 1-2 days with a correlation coefficient of $c_{\text{coeff}} = 0.75$ (γ-ray leads radio). Shifting the radio light curve of 1-2 days towards the flare in the γ-ray flare, as depicted in Figure 6.16, then a nice matching of both light curves occurs. This finding give the first strong indication that the emission of both wavelengths have a common radiation region. In the second case, a comparison of the

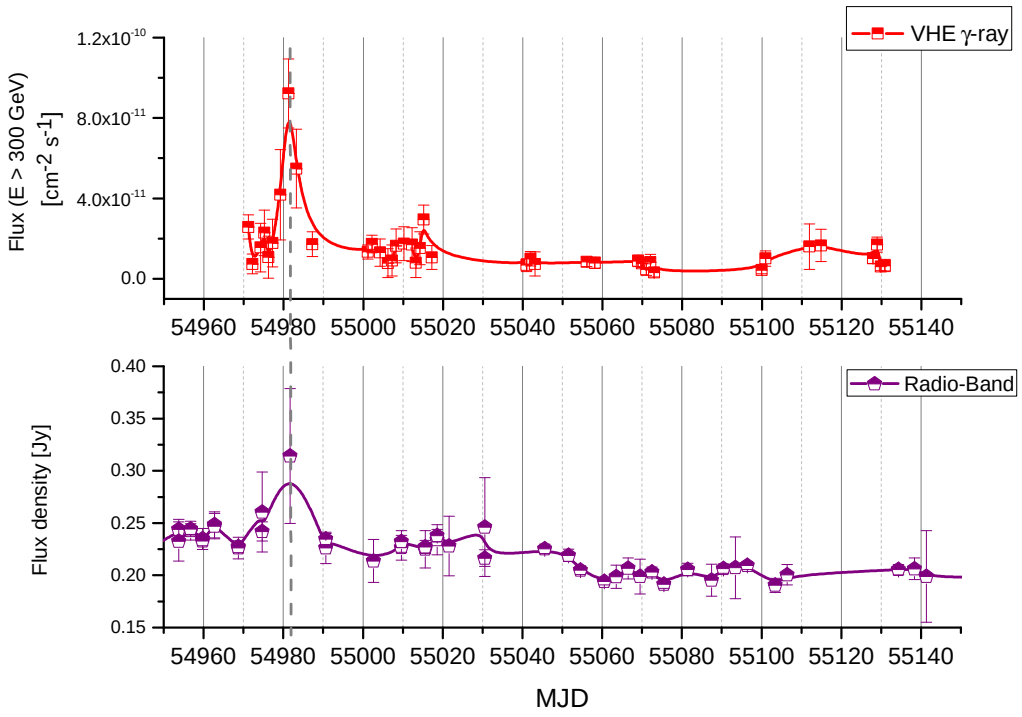

Figure 6.16: Multiwavelength light curve from the radio, optical and VHE γ-ray range from May 20$^{\text{th}}$ to July 31$^{\text{st}}$.

optical and VHE γ-ray light curves is performed, applying the same CCF settings as in the previous case but considering a slightly higher time scale lags of

0-200 days. The CCF result is showing the highest peak (see Appendix B Figure B.4) at a position of 55 indicating that the optical emission is delayed relative to the γ-rays by about 55 days (γ-ray leads optical). Figure 6.17 shows the shifted optical light curve by 55 days towards the γ-ray flare. In this case the matching of both light curves is not clearly evident, comparing especially the measurements of MJD < 54980 where a dense sampling of VHE data is missing. Moreover, it should be noted, that the correlation coefficient of $c_{\text{coeff}} = 0.5$ does not reveal a clear correlation confirmation between both wavelengths. Thus, any strong conclusion about a possible accompaniment of both wavelengths, even if such time delays were already reported by [JSN+12], are not possible in this study.

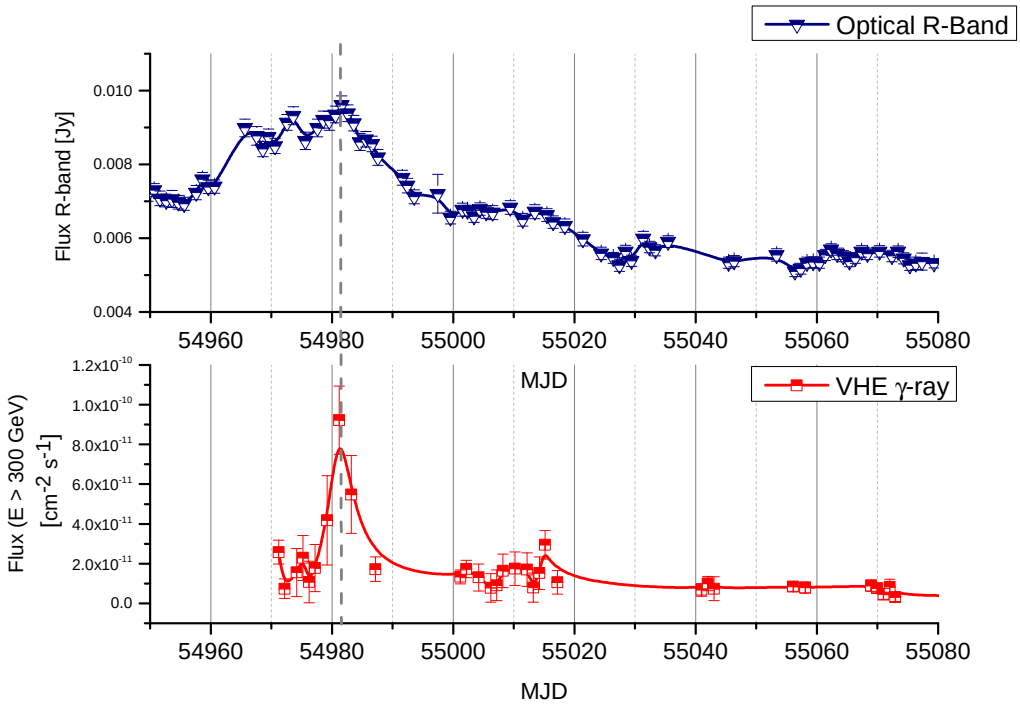

Figure 6.17: Multiwavelength light curve from the radio, optical, and VHE γ-ray range from May 20$^{\text{th}}$ to July 31$^{\text{st}}$.

Flare discussion

Today, it is very well known that blazars are strongly variable sources that occasionally show extraordinary flares visible in various energy bands. These flares are often, but not always accompanied by a counterpart in different wavelengths. In this section such interesting flare correlation behavior in the particular blazar 1ES 1959+650 was discussed. The obvious correlation between the VHE γ-ray results and the 15 GHz radio band gives a strong indication of the common region radiation in this blazar. This finding was already found by different authors i.e. [NTV+11] who additionally found out that the flux correlation is actually real and not an effect of instrumental flux limits. Besides, [KAA+09] and [TVT+94] have already pointed out that blazars detected by *Fermi* LAT are often flaring in radio or are at least in active state and that the radio emission is undoubtedly produced in the jet region and not in the BLR. Consequently, the here presented findings support very well the assumption that both wavelengths have a co-spacial origin and that the γ-rays are produced most likely in a blob region downstream in the jet as supported by the new radio components (blobs) found in the MOJAVE skymaps. Another interesting aspect recently reported by [JSN+12] is the result that in a number of cases the peak of optical flares are found to be delayed with respect to the γ-ray peaks which would again confirm the here presented findings, although the correlation coefficient of $c_{\text{coeff}} = 0.5$ does not fully confirm or discard this assumption. Such delays are expected in case of a moving shock and different opacities of the medium or also as an effect of reprocessing as already reported by various authors (e.g. [ESR12]). Furthermore, the timescales of variability in flux distribution and spectral changes during flares can be interpreted in terms of electron cooling time, the light propagation time and the electron acceleration time to resolve and to understand the structure of relativistic jet and their environments. All in all, such correlation studies are still essential in order to shed light in the fascinating acceleration processes in blazars. In the next section the results of the second MAGIC monitoring period in 2009 are presented and discussed.

6.4 Observations of 1ES 1959+650 in stereo mode in 2009

The monitoring observations continued shortly after the final installation of the second MAGIC telescope, here after M II. The results presented were carried out from the commissioning phase of the first stereo observations in the so called "soft stereo trigger mode". These commissioning observations of 1ES 1959+650 lasted from August 13th until October 27th in 2009. Compared to the standard trigger mode adopted for regular stereo observations (the so-called "full stereo trigger mode", where the Cherenkov events are triggered simultaneously by both telescopes), the "soft stereo trigger mode" has slightly less sensitivity at the energies below ~150 GeV, because both telescopes were triggered independently. In order to take the non-standard trigger condition during the analysis into account, a dedicated MC γ-ray simulation sample has been generated at the high-performance computing cluster in Dortmund and adapted accordingly to in the analysis chain.
Finally, the whole analysis procedure was validated step by step on compatible datasets from observations of the Crab Nebula, as described in detail in Chapter 5. In case of quality cuts for the data selection in the commissioning phase looser cuts for the L3 rate after cleaning of >25 Hz were chosen. The other quality cuts i.e regarding the weather conditions (see Subsection 6.3.1) were applied at the same way as for the first observation period for the stand-alone telescope, MI. After the described selection criteria were applied to the whole observation sample of 12.80 h a subsample of 10.35 of good quality data, as shown in Table 6.3 was used to derive further analysis results. The data analysis for the soft stereo data is performed with the standard MAGIC analysis and reconstruction software MARS, developed for the analysis of stereo data, as described in Chapter 4. In this analysis of the first stereo observations of 1ES 1959+650 the advantage of a new direction reconstruction method is used. After the calibration [A$^+$08] and the image cleaning of the events recorded by each telescope, the information coming from the individual telescopes are combined and the calculation of basic stereo image parameters is performed. For a detail description of the complete MAGIC stereo analysis chain described above see Chapter 4 or [AAA$^+$12d].

Table 6.3: 1ES 1959+650 2009 stereo data set used in this study after data quality selection. From left to right: dates in dd / mm / yy, effective time of observation in hours, zenith angle distribution, rate of the event after the image cleaning in Hz and the significance of each observation night.

Date	Eff. time [h]	Zenith [°]	Mean Rate [Hz]	Significance [σ]
13 / 08 / 2009	0.67	42-47	30	4.70
15 / 08 / 2009	0.73	42-47	30	4.17
26 / 08 / 2009	0.50	36-38	30	4.22
27 / 08 / 2009	1.21	36-38	35	5.97
28 / 08 / 2009	0.38	36-38	30	2.58
29 / 08 / 2009	0.58	36-38	35	2.90
30 / 08 / 2009	0.82	42-49	50	2.58
26 / 09 / 2009	1.22	40-48	53	3.90
27 / 09 / 2009	0.32	35-42	52	3.63
08 / 10 / 2009	0.08	41-46	40	2.58
11 / 10 / 2009	0.13	41-46	60	3.94
24 / 10 / 2009	1.59	41-46	40	4.69
25 / 10 / 2009	0.60	41-46	75	3.61
26 / 10 / 2009	1.89	41-46	68	4.44
27 / 10 / 2009	0.64	41-46	45	3.17

6.4.1 Signal search from first stereo observations in 2009

For the first detection out of the soft stereo data, a signal search using the θ^2 distribution was applied. As anticipated in Chapter 4 the θ^2 distribution is a squared angular distance between the estimated and the true source position (camera center in case of the wobble center). In this case, especially the angular distance between the center of gravity of the image and the shower direction, the so–called `DISP` is reconstructed (for more information see Subsection 4.1.4). Figure 6.18 indicates an excess of 185.6 γ-events on the 14.3 σ level during the second monitoring observation period of 1ES 1959+650 in 2009. The cuts which were here applied are the standard full range cuts with following settings applied in the program `"Odie"`:

```
Odie.cuts: MHadronness.fHadronness < 0.16
           && MHillas_1.fSize > 125
           && MHillas_2.fSize > 125
           && MStereoParDisp.fEnergy >250
Odie.signalCut: 0.01
Odie.psf40: 0.063
```

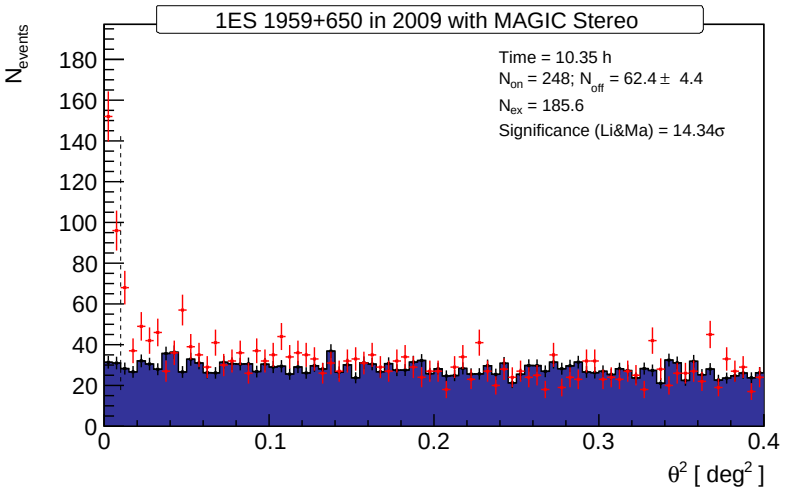

Figure 6.18: θ^2-plot of the 1ES 1959+650 signal and background estimation from 10.35 hours of the first MAGIC stereo observations taken between August 13th and October 27th 2009, above an energy threshold of 250 GeV. A clear signal of 14.3 σ can be measured also in the second period of the monitoring observations of 1ES 1959+650.

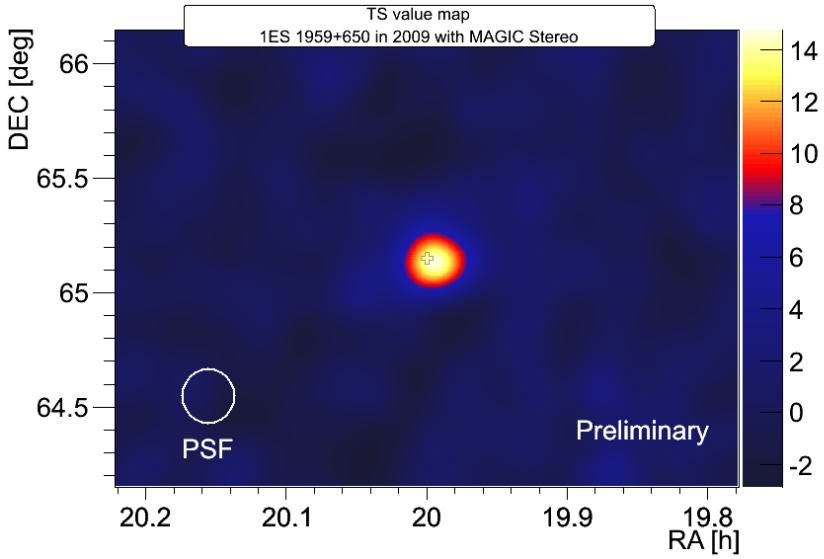

Figure 6.19: The skymap obtained with the same cuts as for the θ^2 distribution. Again a clear signal at 14 σ significance level is visible. This result also confirms the excess from the nominal position of 1ES 1959+650 . The PSF of 0.063 degrees is also displayed in the bottom left corner.

These cuts were optimized by means of contemporaneous Crab Nebula data and MC simulations in previous analysis test validated by various MAGIC analyzers. Moreover, the skymap result (see Figure 6.19), applying the same cuts as for the θ^2 distribution, confirms very well the excess events coming from the nominal position of 1ES 1959+650 with a hot spot at 14 σ significance level.

6.4.2 Temporal behavior of 1ES 1959+650 in the second observation period in 2009

The overall light curve for the second observation period in 2009 is shown in Figure 6.20. The integral flux for γ-rays is found to be $F(300 > \text{GeV}) = (5.86 \pm 0.61) \times 10^{-12} \text{cm}^{-2}\text{s}^{-1}$ corresponding to the level of about (4.73±0.49)% of the Crab Nebula flux above 300 GeV. In addition, the light curve indicates moderate changes of the flux level with $\chi^2/\text{NDF} = 34.32/15$ and a corresponding probability of 0.31% which is not compatible with a steady flux, although no major flares could be detected during this observation period. As a conclusion, the here presented light curve suggests, in contrast to the first observation period in 2009, a quiescent state of 1ES 1959+650. Such low state behavior was mostly observed from this object during the long-term monitoring observations with MAGIC since 2005 to 2008 yielding a flux level not higher than 12% of the Crab Nebula flux, as already reported in [HST+09].

6.4.3 The VHE γ-ray spectrum of 1ES 1959+650 in the second observation period in 2009

As discussed above, 1ES 1959+650 has also been observed in the second period of 2009 during the commissioning phase of M II. Since no major changes in the flux level of 1ES 1959+650 were observed during this period, thus only one mean differential energy spectrum was calculated. The stereo analysis cuts are adapted in similar way as for the stand-alone analysis to the efficiency on MC simulation data. For the θ^2 cut and for the `Hadronness` cut values of 90% are set, respectively. These very loose cuts (efficiency 90%) were applied in order to avoid some systematics related to hardware inefficiencies of the new M II camera at the begin of the first stereo observations. The corresponding differential energy spectrum is outlined in Figure 6.21.
Furthermore, the spectrum can be again well fitted by a pure power law between 200 GeV and 5 TeV yielding following parameters

$$\frac{\mathrm{d}N}{\mathrm{d}E} = (2.07 \pm 0.25) \times 10^{12} \left(\frac{E}{1\ \text{TeV}}\right)^{-2.48\pm011} \text{TeV}^{-1}\text{cm}^{-2}\text{s}^{-1} \qquad (6.5)$$

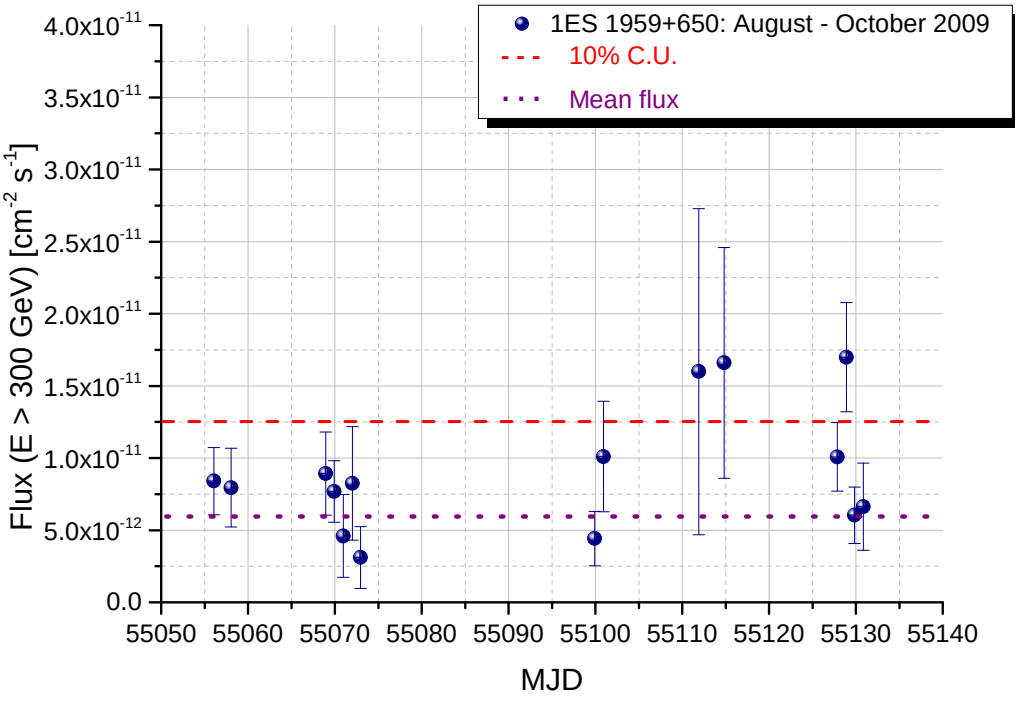

Figure 6.20: 1ES 1959+650, light curve between August and October 2009 above an energy threshold of 300 GeV, and with a daily time-scale binning. No strong variability is seen in the data. The dashed purple horizontal line represents the constant function resulting from the fit to the data.

and skipping the first point at 150 GeV which lies far below the estimated energy threshold, as described in Chapter 5. The power law fit describes the data acceptably well with χ^2/NDF = 1.20/4 as a probability of 88%. Since also this spectrum does not extend up to energies of more than > 10 TeV, an energy domain at which non-negligible absorption of the EBL is expected, no further studies in this respect could be performed. To sum up, 1ES 1959+650 shows during the second observation period in 2009 no significant flare activity and it seems that the source has returned to its usual quiescent state.

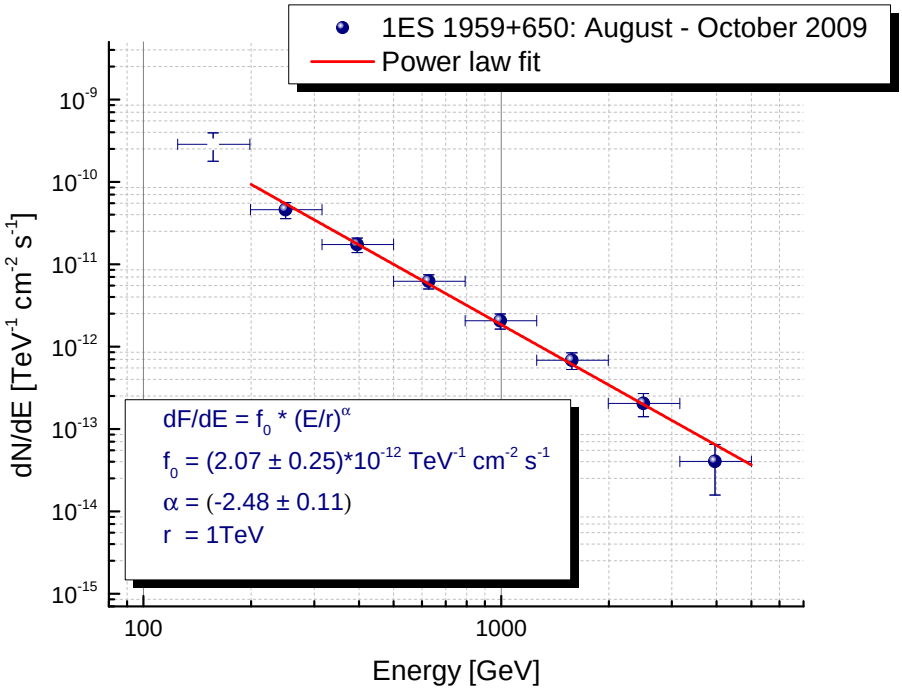

Figure 6.21: 1ES 1959+650 differential energy spectrum measured by MAGIC between 200 GeV and 5 TeV in the second observation period in 2009. The power law fit to the data is also shown (red line).

6.5 1ES 1959+650 observations with MAGIC in 2010

As pointed out at the beginning of Section 6.4 the commissioning phase of the second MAGIC telescope finished at the end of October 2009. Since then both telescopes worked in the full stereo mode with improved angular and energy resolution as well as improved integral sensitivity of 0.8% of the Crab Nebula flux above 300 GeV in 50 h of observations [AAA+12d]. Above a few hundred GeV the MAGIC stereo system sensitivity is a factor of two better than of only one telescope. In addition, the improvement is even larger by a factor of about 3 in the energy range between (50-200) GeV. These improvements are results of an efficient usage of the stereo parameters in the analysis chain and the intrinsic reduction of the muon background in the stereo system (for a detailed description of the MAGIC stereo system see Chapter 4 and [AAA+12d]). Such observations of 1ES 1959+650 were also performed during the last MAGIC monitoring observations in 2010. The findings of the observa-

tions in 2010 are presented and discussed in the following section.
During the last year of MAGIC monitoring observations in 2010, 1ES 1959+650 was observed in total for only 5.55 hours in this period, covering the same zenith angle range as in the previous years between 36 to 48 deg. Like in the past monitoring years the whole data sample was taken in the false-source tracking (wobble) mode, in the period starting from May 23th until September 29th. After quality selection, as mentioned in previous sections (i.e. see Subsection 6.3.1) and applying a mean L3 rate cut of >50 Hz, in total only 5.5 hours of good quality data has been analyzed. Moreover, the selected good quality data sample was analyzed with the standard MARS analysis framework for stereo observations as described in the previous section. The whole selected sample along with the daily observation time, the mean rate after cleaning, the zenith angle distribution, and the significance for each observation day is listed in Table 6.4.

Table 6.4: 1ES 1959+650 2010 data set used in this study after data quality selection. From left to right: dates in dd / mm / yy, effective time of observation in hours, zenith angle distribution, rate of the event after the image cleaning in Hz and the significance of each observation night.

Date	Eff. time [h]	Zenith [°]	Mean Rate [Hz]	Significance [σ]
23 / 05 / 2010	0.46	42-47	82	4.17
08 / 06 / 2010	1.30	36-38	108	7.53
06 / 08 / 2010	0.34	42-49	50	2.05
16 / 08 / 2010	0.83	36-39	85	1.93
20 / 08 / 2010	1.13	40-48	53	1.56
31 / 08 / 2010	1.33	35-42	52	3.66
02 / 09 / 2010	0.78	40-46	104	3.94
29 / 09 / 2010	0.49	41-46	68	2.68

6.5.1 Signal search from stereo observations in 2010

Due to improved sensitivity of the MAGIC stereo system, 1ES 1959+650 has been detected again even in this short observation period of 5.55 hours clearly. The strength of the signal has been calculated using standard cuts as already described in Subsection 6.4.1. In the same way, as for the soft stereo 2009 observations, the signal search was performed using the θ^2 distribution. The corresponding θ^2-plot is depicted in Figure 6.22. It indicates an excess of 103.0 γ-events on the 10.30 σ level. In addition, the skymap in Figure 6.23 shows the position of the computed excess events which is well matched within the nominal position of this source (empty cross).

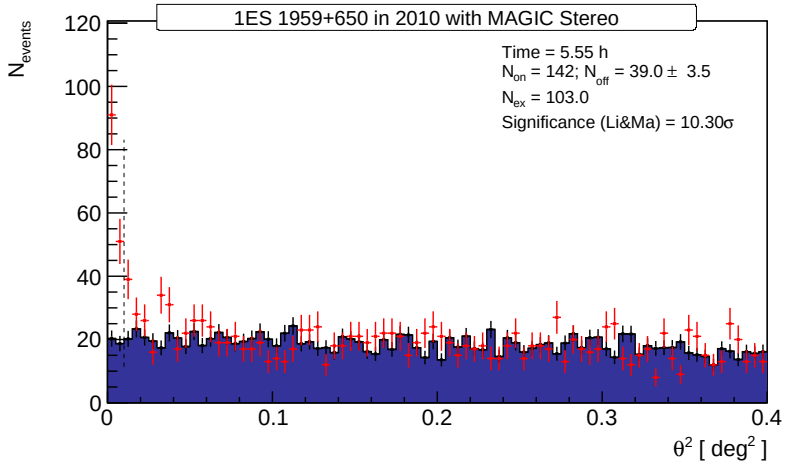

Figure 6.22: θ^2 distribution of the 1ES 1959+650 signal and background estimation from 5.55 h of MAGIC stereo observations taken between May 23th and September 29th 2010. The region between zero and the vertical dashed line (at 0.016 degrees) represents the signal region.

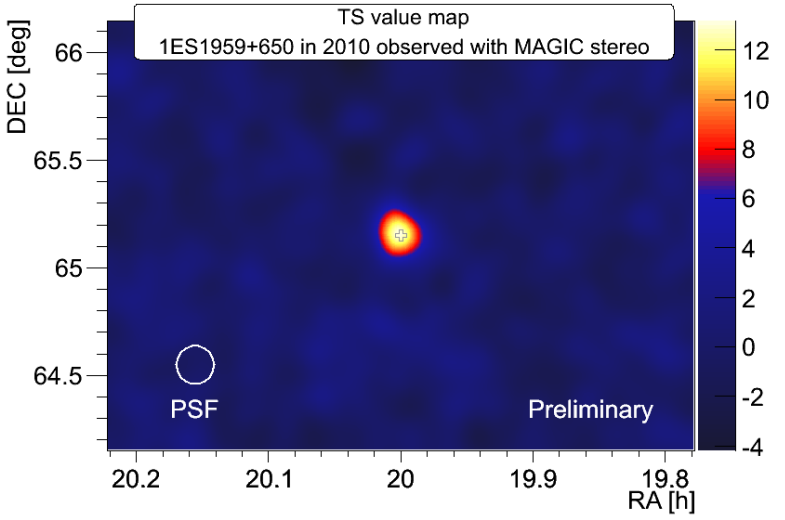

Figure 6.23: Significance skymap of the sky region around 1ES 1959+650 from 5.55 h of MAGIC stereo observations taken in 2010. The 1ES 1959+650 position is marked with an empty cross. The PSF of about 0.07 degrees is also displayed.

6.5.2 The temporal behavior of 1ES 1959+650 in 2010

Looking back to previous temporal analysis results of 1ES 1959+650 the source was usually found in its quiescent state during the last five years of MAGIC monitoring observations. In order to check the time evolution also in the last monitoring year, again the integral flux as a function of time (MJD) has been studied. As shown in Figure 6.24 the mean integral flux above 300 GeV is $F(>300\,\mathrm{GeV}) = (7.25 \pm 0.14) \times 10^{-12}\ \mathrm{cm}^{-2}\ \mathrm{s}^{-1}$, corresponding to $(5.85 \pm 1.16)\%$ of the Crab Nebula flux. In comparison to previous observations also in this case, no variability hints could be detected. In fact, fitting the light curve (see Figure 6.24) with a constant flux hypothesis yields a $\chi^2/NDF = 4.1/6$, corresponding to a probability of $P(\chi^2) = 0.67$.

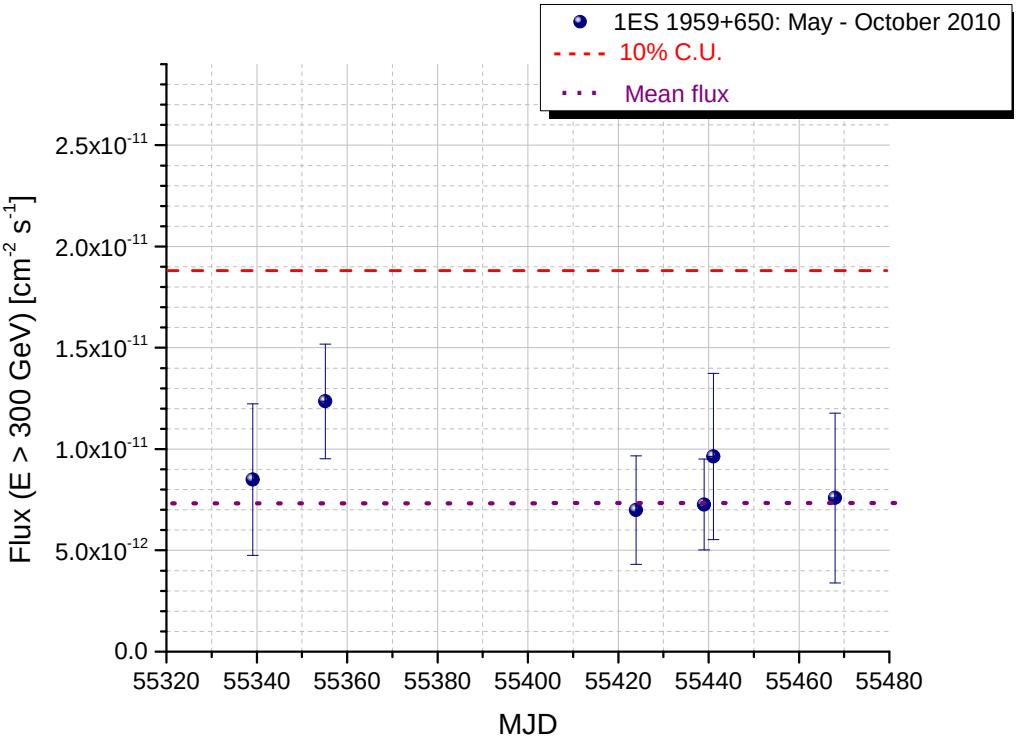

Figure 6.24: VHE γ-ray light curve of 1ES 1959+650 for $E > 300$ GeV measured by the MAGIC stereoscopic system in 2010.

6.5.3 The VHE γ-ray spectrum of 1ES 1959+650 in 2010

As reported above, no variability in the flux of 1ES 1959+650 in 2010 could be found, therefore again only one differential energy spectrum has been derived. For the spectrum all data listed in Table 6.4 was used. Like in the previous analysis the energy spectrum has been reconstructed using different unfolding algorithms to take into account and also to investigate the energy resolution of the full stereo system as well as the biases in the energy reconstruction. The results of the different unfolding methods show a good agreement within the uncertainties. For further analysis steps and comparison process the *Bertero* unfolding algorithm has been selected giving the best probability of the fit also in this case. In comparison to the previous observation years and already presented VHE γ-ray spectra results in this work, the spectrum from 2010 observations can also be well described by a simple power law with following values:

$$\frac{\mathrm{d}N}{\mathrm{d}E} = (2.10 \pm 0.30) \times 10^{-12} \mathrm{cm}^{-2}\mathrm{s}^{-1}\mathrm{TeV}^{-1} \left(\frac{E}{1\ \mathrm{TeV}}\right)^{-2.47\pm0.18} \tag{6.6}$$

between 125 GeV to 6 TeV with χ^2/NDF=3.15/5 and P(χ^2=0.68).
For the first time due to improved sensitivity of the stereo system the spectrum extends down from 125 GeV, as can be seen in Figure 6.25. Also in this case due to short exposure time of only nearly 6 hours the spectrum cannot be used alone for any further EBL studies.
In this section the last 1ES 1959+650 results of the MAGIC monitoring observations in 2010 were presented. The source shows again in this period its usual steady state and the calculated spectral parameters are well matched within uncertainties with previous results. After the monitoring program of 1ES 1959+650 has been finished at the end of 2010 no further regular observations in the following year in 2011 were performed. Nevertheless, in 2012 a maximal historical optical R-band brightness has been recorded by the KVA observatory of 1ES 1959+650 and consequently triggered further MAGIC observations in that year. The analysis results of the 1ES 1959+650 ToO observations in 2012 are the central theme of the next section.

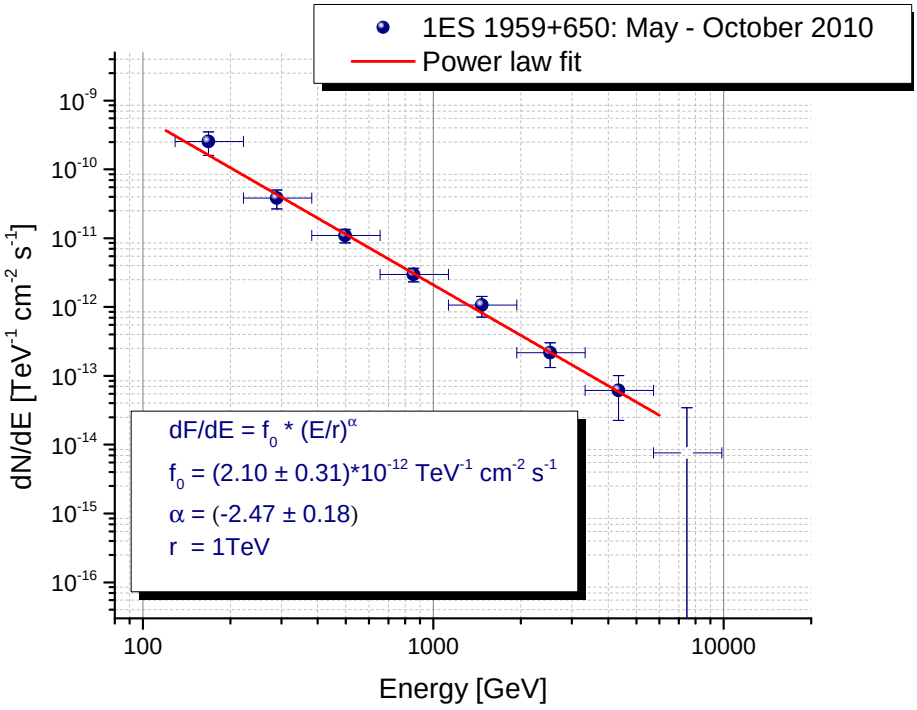

Figure 6.25: Differential energy spectrum of 1ES 1959+650 measured by MAGIC in 2010. The power law fit to the data is also shown by the red line.

6.6 MAGIC observations of 1ES 1959+650 in 2012

As shortly mentioned above, in 2012 further 1ES 1959+650 MAGIC observations were triggered by the strongest optical outburst in the R-band, revealed by the Tuorla/KVA telescopes. Figure 6.26 illustrates the strongest optical outburst and the MAGIC observation window (yellow band and bottom panel). Unfortunately, due to M I camera failure the whole observations were performed in stand-alone mode only with M II. 1ES 1959+650 has been observed with M II from May 22nd until May 26th for more than 1 hour each night. The quality of this sample is surprisingly good, thus all the collected data, as listed in Table 6.5, can be used for the successive steps of the analysis. The following results were evaluated again with the standard MAGIC analysis software MARS but this time in stand-alone mode and with a dedicated sample of MC simulation data for M II. In particular, given that the observations were conducted only with one telescope, the whole analysis is performed with the *Alpha* approach as described in Section 6.3.

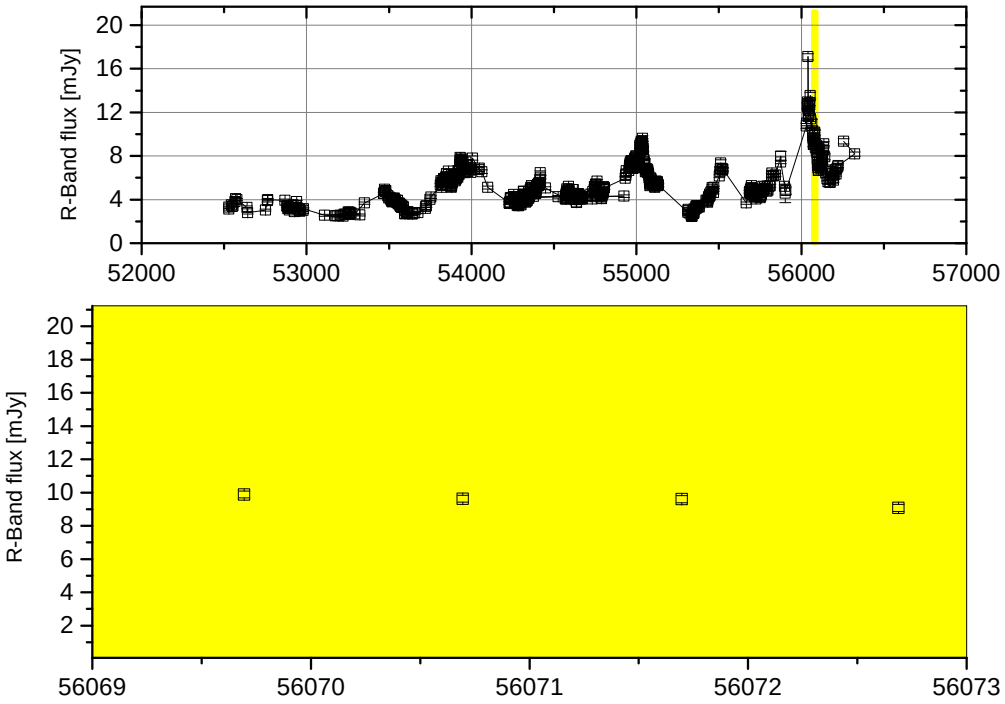

Figure 6.26: Optical light curve from the the Tuorla / KVA telescopes. At the beginning of 2012 the strongest optical outburst in the R band is observed. The MAGIC observation window is highlighted with the yellow band. The data was provided by [Lin12].

Table 6.5: 1ES 1959+650 ToO observations in 2012 From left to right: dates in dd / mm / yy, effective time of observation in hours, zenith angle distribution, rate of the event after the image cleaning in Hz and the significance of each observation night.

Date	Eff. time [h]	Zenith[°]	Mean Rate [Hz]	Significance[σ]
22 / 05 / 2009	1.31	36-39	325	6.51
23 / 05 / 2009	1.39	38-42	300	7.04
24 / 05 / 2009	1.45	39-45	300	5.81
25 / 05 / 2009	1.47	39-45	330	1.98
26 / 05 / 2009	1.26	41-49	290	3.47

6.6.1 Signal search of 1ES 1959+650 in 2012

For the signal search in the 2012 data the same procedure as for the first observation period in 2009 was applied. The only difference in this analysis to the one presented in Section 6.3 is the telescope itself. M II in stand-alone mode is slightly more sensitive than the M I telescope alone. In Figure 6.27 the *Alpha* distribution of the events obtained from the stand-alone M II observations of 1ES 1959+650 in 2012 is shown. During this observations an excess of 355.3 events was observed above a background of 479.7 events for $\alpha < 8°$. The here applied cuts (`Size` = 300 phe and `Hadronness` = 0.07) were similar to that one found for the stand-alone analysis in 2009, since no Crab Nebula data under the same zenith angle conditions were available in 2012. During an effective observation time of only 6.90 hours a strong detection of 12.37 σ from this source has been observed. The corresponding VHE γ-ray skymap, as outlined in Figure 6.28, confirms very well the direction of the detected excess events with the position of 1ES 1959+650. Also in this case the emission is point-like for the angular resolution of M II.

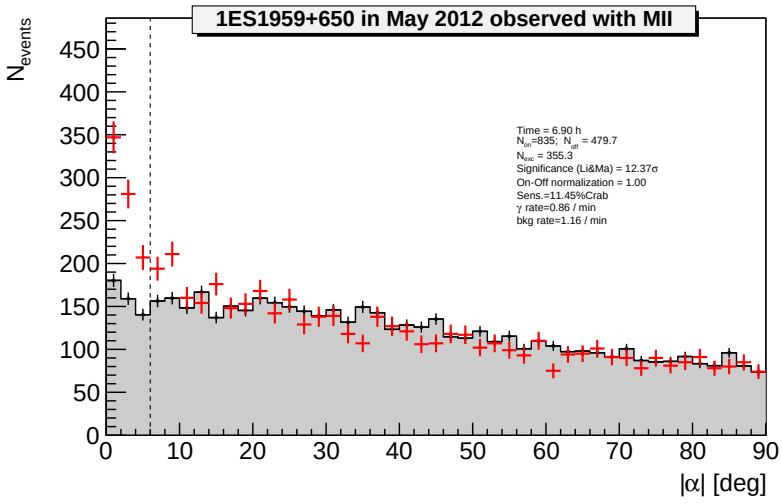

Figure 6.27: *Alpha* distribution of the 1ES 1959+650 signal and background estimation from about 7 hours of M II observations taken in May 2012 during the strongest optical flare in the R-band. As in previous observations 1ES 1959+650 is again detected with a significance of 12.37 σ.

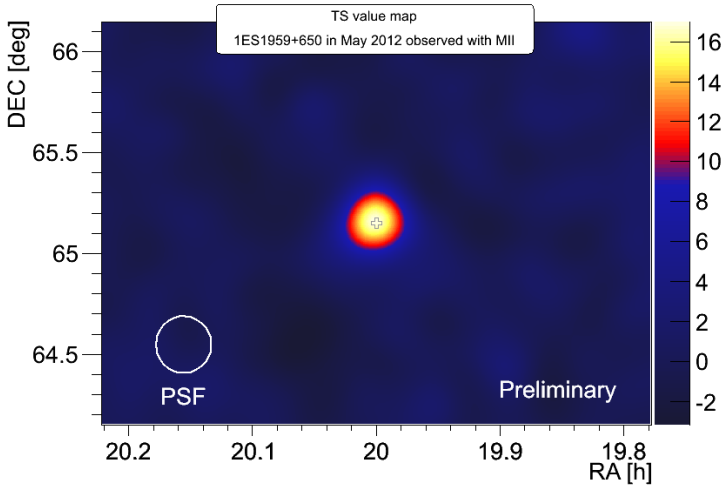

Figure 6.28: Significance skymap of the sky region around 1ES 1959+650 from about 7 hours of M II observations taken in May 2012 during the strongest optical flare in the R-band. The 1ES 1959+650 position is marked with an empty cross. The PSF of about 0.1 degrees for M II is also displayed.

6.6.2 Temporal behavior of 1ES 1959+650 in 2012

In order to drive constraints on models of VHE γ-ray emissions in connection with a possible optical-γ-ray correlations it is important to observe such sources simultaneously. In case of MAGIC, such observations were already successfully performed, where the optical band triggered VHE γ-ray observations of AGN since the start of its operations. The triggers have been provided by the Tuorla blazar monitoring program and the ToO project. Such simultaneous observations in both wavelength regions resulted already in the discoveries of five new VHE γ-ray emitting sources (Mrk 180, [AAA$^+$06a]; 1ES 1011+496, [AAA$^+$07b]; S5 0716+714, [AAA$^+$09d]; B3 2247+381, [AAA$^+$12b]; and 1ES 1215+303 [AAA$^+$12b]). In contrast in many other cases it has not been possible to confirm with high statistical significance if the sources during high optical activity were always in a higher VHE γ-ray state. There are long-term studies for example for Mrk 421 and PG 1553+133 that show controversial results on the correlation between the two energy ranges. Thus, such connection between the optical and VHE γ-ray states remains an interesting field of study. For this reason, the nearly simultaneous 1ES 1959+650 VHE γ-ray light curve with the observed R-band maximum has been computed in order to check if a possible correlation during the strongest optical flare in 2012 is evident.

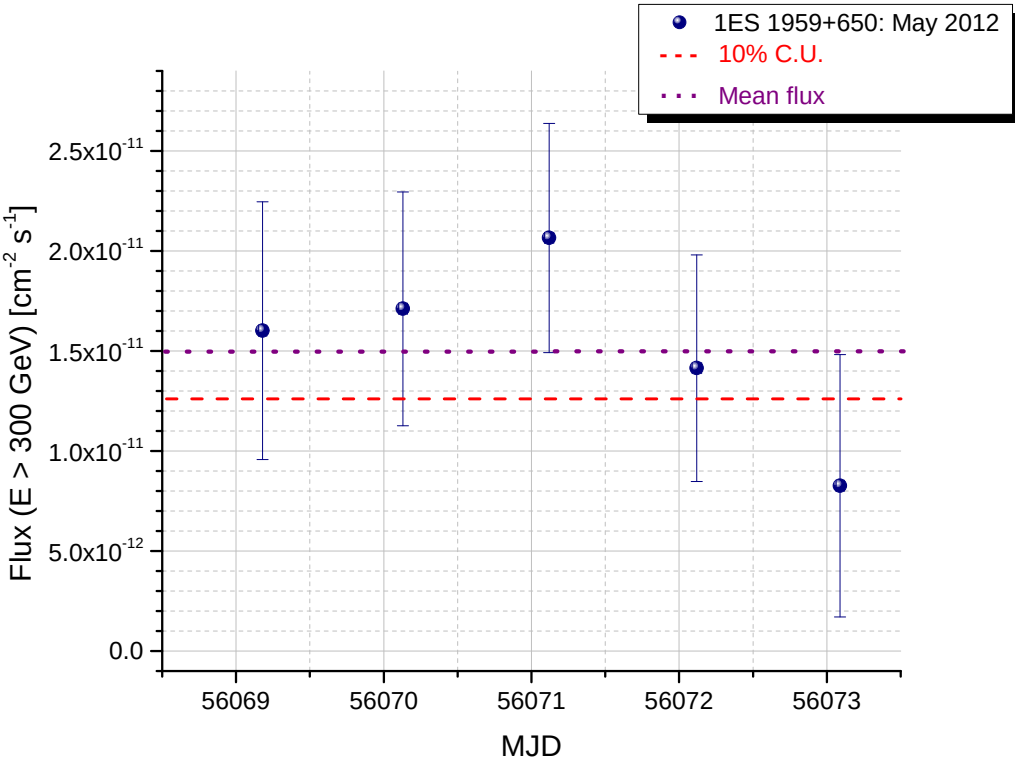

Figure 6.29: VHE γ-ray light curve of 1ES 1959+650 for E > 300 GeV measured by MAGIC in 2012.

In Figure 6.29 the integral flux during five observation nights above 300 GeV is given. The light curve, showing no major flare activity, can be well-fitted by a constant yielding a integral flux of $F(>300\,\mathrm{GeV})=(1.46\pm0.16)\times10^{-12}$ cm^{-2} s^{-1} with χ/NDF=5.2/4 and corresponding probability of 27%. The here reported flux is only about a factor 3 higher (11.81±1.31% C.U.) than in the previous monitoring years in autumn 2009 and 2010 and additionally within the uncertainties reported in 2009. Since there are no strong flux enhancements measured like on May 30$^{\mathrm{th}}$ in 2009 (see Subsection 6.3.5) or even in 2002 [KHH$^+$04] this result gives also a hint that both wavelengths and their emission regions are not directly connected with each other.

Intra-night variability

Since blazar can also show an intra-night variability, as already reported by various authors especially for the most prominent blazars Mrk 421 and Mrk 501 with flux-doubling times down to 2 minutes ([AAA$^+$07c],[AAA$^+$10g]), this sam-

ple of five nights in series with an exposure time of more than 1 hour has also been used for an intra-night variability check. Figure 6.30 shows a intra-night light curve for energies above 300 GeV for the extended observations on May 22nd until May 26th in a 15 min binning. For this particular study a χ^2-Test for each observation night has been performed. The results are listed in Table 6.6.

Table 6.6: 1ES 1959+650 2012 data set and result from the short variability study. From left to right: dates in dd / mm / yy, effective time of observation in minutes, χ^2/NDF results and the probability for the data points to be distributed uniformly around the mean value.

Date	Eff. time [h]	χ^2/NDF]	Probability
22 / 05 / 2012	1.31	3.71/4	0.47
23 / 05 / 2012	1.39	0.76/5	0.98
24 / 05 / 2012	1.45	8.05/5	0.15
25 / 05 / 2012	1.47	8.76/5	0.12
26 / 05 / 2012	1.26	2.01/4	0.73

The probability for the data points to be distributed uniformly around the mean value (about 10% of the Crab Nebula flux) differ significantly. For the May 24th and May 25th (purple points in Figure 6.30) the mean values is 1.5% and 1.2%, respectively whereas for the May 23th and May 26th the mean values are 98% and 73%, respectively. Thus, the constant function cannot be rejected as a fit and an intra-night variability for 1ES 1959+650 cannot be claimed.

6.6.3 Spectral behavior of 1ES 1959+650 in 2012

After the study of the temporal behavior of 1ES 1959+650 in 2012 it is also interesting to check if the spectral properties like the slope (index) changed significantly during the strong optical flare in May 2012. The differential flux and thus the spectrum were calculated using a cut efficiency of 90% for the `Hadronness` and α, respectively and a detection `Size` cut of 300 phe. Figure 6.31 shows a well matched spectrum within uncertainties with the found results of the three previous observation years of 1ES 1959+650. The exact measured values are:

$$\frac{\mathrm{d}N}{\mathrm{d}E} = (2.84 \pm 0.38) \times 10^{-12} \mathrm{cm}^{-2} \mathrm{s}^{-1} \mathrm{TeV}^{-1} \left(\frac{E}{1\ \mathrm{TeV}} \right)^{-2.92 \pm 0.19} \tag{6.7}$$

in the range from 225 GeV to 6 TeV with χ^2/NDF=3.15/5 and P(χ^2=0.68).

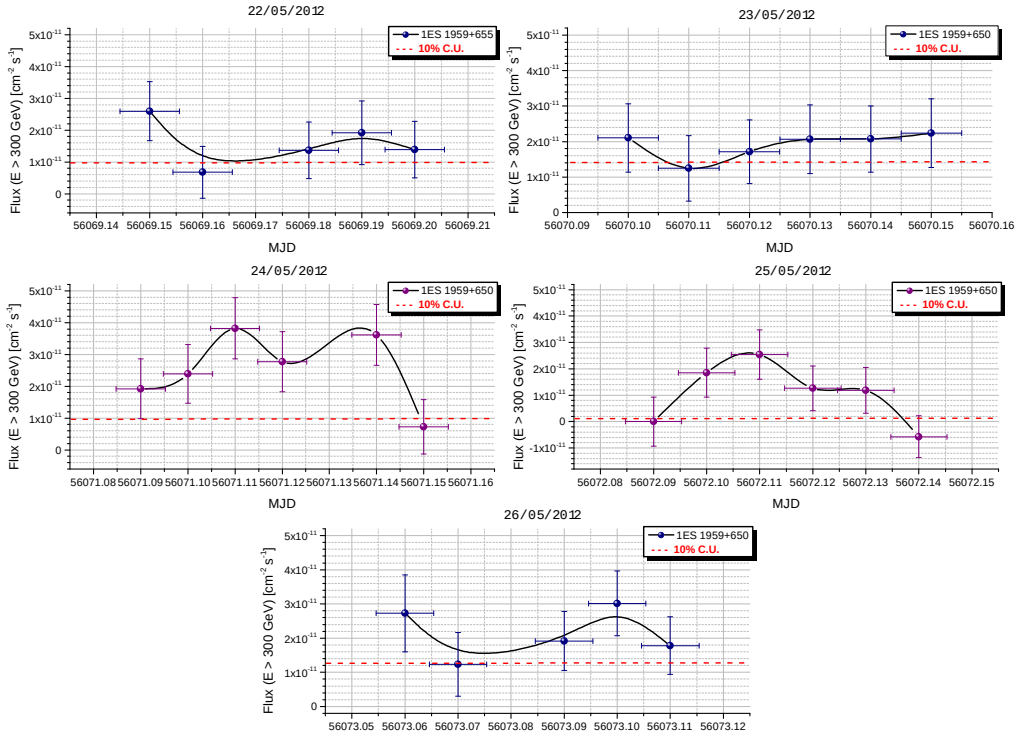

Figure 6.30: Intra-night light curve for each observation night for energies above 300 GeV of 1ES 1959+650 in 2012. Shown is a 15 min binned measurement of the source flux (blue and purple points) and the 10% Crab flux level for orientation. For a better orientation, the measurements are fitted with a B-spline function. An intra-night variability for 1ES 1959+650 cannot be claimed.

Finally, taking all findings of the 2012 analysis together into account and comparing the overall multiwavelength light curve of 1ES 1959+650 as outlined in Figure 6.32, in the optical R-band and the corresponding VHE γ-ray range, no correlation approach of both wavelengths can be claimed. The only common feature at first glance could be the higher integral flux of a factor 3, but since moderate flux enhancement were also found without the presence of strong optical flares in previous observation years, no further correlation conclusions can be made. In addition, comparing the radio band (top panel) with the optical R-band (bottom panel) against each other also in this case no significant correlation is visible. The only obvious relation, as marked with the dashed ellipse in Figure 6.32, is the steady but higher flux density state in the radio band with the one in the VHE γ-ray range. This result would confirm again the previous findings in Subsection 6.3.5 where a strong cor-

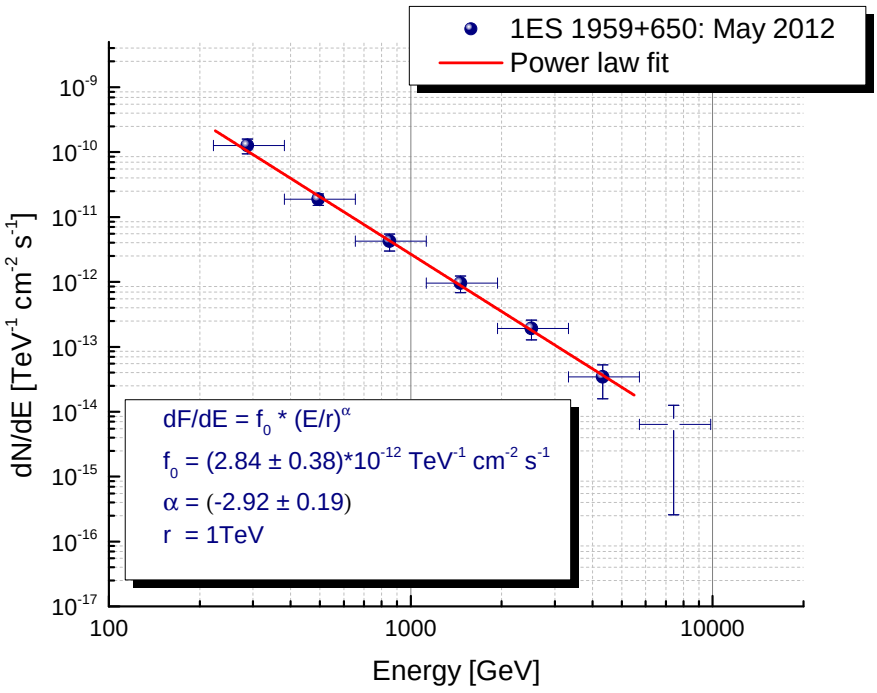

Figure 6.31: Differential energy spectrum of 1ES 1959+650 measured by MAGIC in 2012. The power law fit to the data is also shown by the red line.

relation between both wavelength bands was found. Consequently, the found results over a seven year survey in the optical and VHE-γ-ray band, indicate strongly that no direct connection between both wavelength in this source is given. At the same time, this result is also inconsistent with the SSC model, which predicts a correlation between the synchrotron and the IC emission, related to the same electron population. All in all, this indicates again that in 1ES 1959+650 different emission mechanisms are at work or that the two emissions originate from different regions. In the next section of this chapter an overall comparison of the obtained results during this work with results from previous observations of 1ES 1959+650 with MAGIC is presented.

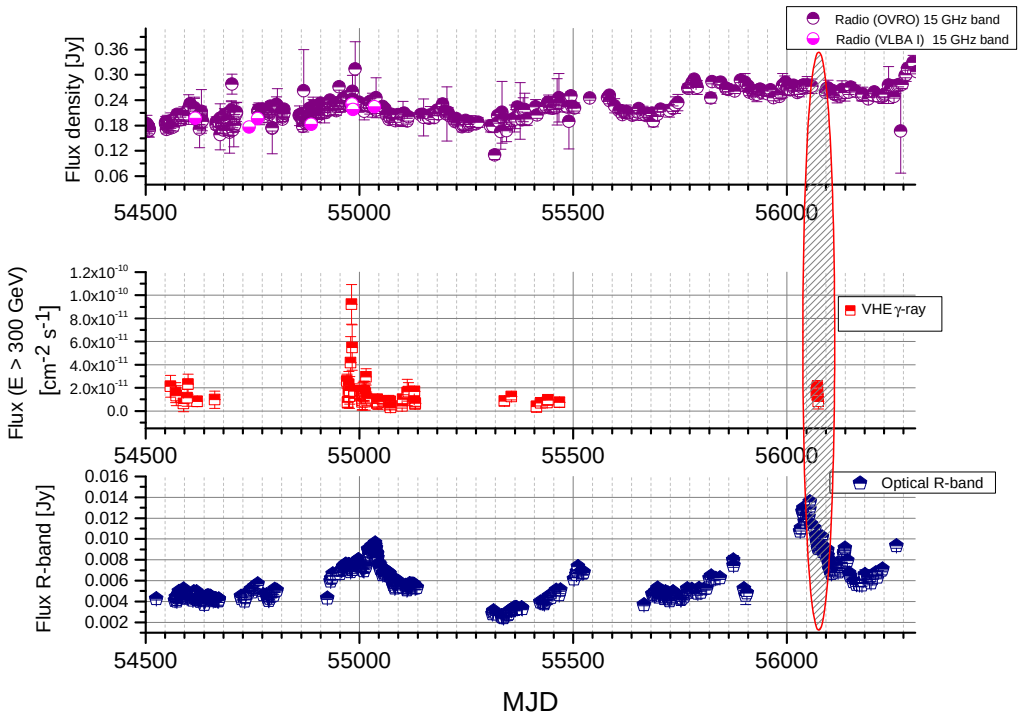

Figure 6.32: 1ES 1959+650 multiwavelength light curve from 2008 to 2012. The dashed ellipse represents the simultaneous observations between the radio, optical and the VHE γ-ray bands in May 2012.

6.7 Comparison of 1ES 1959+650 observations with MAGIC

In order to explore the VHE γ-ray emission of 1ES 1959+650 from each MAGIC observation year a comparison of the results obtained in this work with previous observations related to significance, the integral flux and the spectral values has been compiled. A first overview about the seven years of MAGIC observations with the corresponding observation time and significance is given in Table 6.7. It can be seen that in all observation years this source has been detected with a significance larger than $5\,\sigma$.

Table 6.7: 1ES 1959+650 six years data of MAGIC monitoring observations. From left to right: observation year [m* - MI stand-alone observation] [s* - MAGIC stereo observations], observation time in hours, effective time in hours, significance in each observed year, the square root of the significance and the references for the corresponding analysis results.

Year	Obs. time [h]	Eff. time [h]	σ	$\sigma/\sqrt{h}$	Reference
2005 [*m]	22.3	19.6	6.3	1.4	[Zan06], [Hay08]
2006 [*m]	17.4	14.3	10.4	2.8	[Zan06], [Hay08]
2007 [*m]	18.79	12.77	10.6	3.0	[Sat10], [UM09]
2008 [*m]	13.80	4.91	5.1	2.0	to be published
2009 P1 [*m]	22.30	15.30	14.49	3.7	this work
2009 flare [*m]	0.3	0.3	5.38	9.8	this work
2009 P2 [*s]	12.78	10.35	14.34	4.4	this work
2010 [*s]	6.68	5.55	10.30	4.4	this work
2012 [*m]	6.90	6.90	12.37	4.7	this work

6.7.1 The integral flux of seven year MAGIC observations

In this subsection the integral fluxes above 300 GeV from 2009 to 2012 are compared with previously reported flux states (from 2005 to 2008) of this particular source. Figure 6.33 demonstrates very well, apart from only one flare during a seven years survey, the quiescent state of this blazar. The integral fluxes measured above 300 GeV lie in the range from ~5% to 12% of the Crab Nebula flux measured by MAGIC as listed in Table 6.8: the highest flux level is recorded in 2006 and 2012 (~12% C.U.), and is a factor 2-3 larger than the one measured in the second observation period in 2009 (~5% C.U.) and 2010 (~6% C.U.). Furthermore, the here reported changes in the flux level of 1ES 1959+650 are quite moderate in comparison to other monitored blazes like Mrk 421 or Mrk 501, where the flux variations exceed one order of magnitude [FBB+08]. Nevertheless, such moderate flux changes as observed in 1ES 1959+650 were already found in other blazar e.g. PG 1553+113 ([AAA+12d]) where the flux variability was of the same order as for 1ES 1959+650 over a long term study of five years. In general, the results presented here from the 2009 to 2012 study are consistent with the flux levels reported earlier (from 2005 to 2008). Marginal flux variability (beside one flare in 2009, see Section 6.3.5) have been observed from 1ES 1959+650 during a seven year survey. Consequently, one would assume that also the spectral behavior of the source might not change significantly. This assumption will be investigated in the next subsection below.

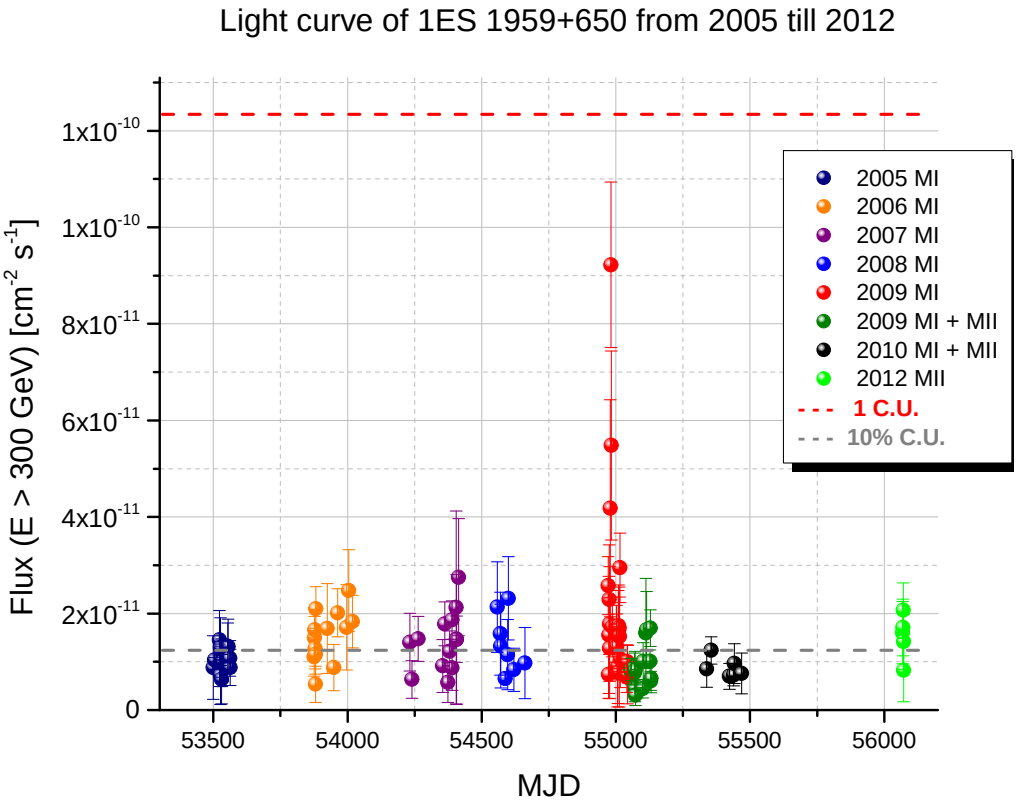

Figure 6.33: Light curve of 1ES 1959+650 from 2005 until 2012 above 300 GeV.

Table 6.8: 1ES 1959+650 flux results during seven year MAGIC observations

Year	Flux>300 GeV	Crab Unit [C.U.]	Reference
2005	$(1.04 \pm 0.24) \times 10^{-11}$	$(8.3 \pm 1.96)\%$	[HBK+08]
2006	$(1.53 \pm 0.53) \times 10^{-11}$	$(12.4 \pm 4.3)\%$	[HBK+08]
2007	$(1.22 \pm 0.12) \times 10^{-11}$	$(9.8 \pm 0.99)\%$	[UM09]
2008	$(0.88 \pm 0.35) \times 10^{-11}$	$(7.1 \pm 0.28)\%$	to be published
2009 P1	$(1.22 \pm 0.12) \times 10^{-11}$	$(9.8 \pm 0.99)\%$	this work
2009 P2	$(5.86 \pm 0.61) \times 10^{-12}$	$(4.73 \pm 0.49)\%$	this work
2010	$(7.25 \pm 1.43) \times 10^{-12}$	$(5.85 \pm 1.16)\%$	this work
2012	$(1.46 \pm 0.16) \times 10^{-11}$	$(11.81 \pm 1.31)\%$	this work

6.7.2 Combined spectra of seven year MAGIC observations

As for the integral flux a comparison between the differential spectra observed from 1ES 1959+650 by MAGIC every year from 2005 to 2012 is obtained. In Figure 6.34 and Figure 6.35 all MAGIC monitoring spectra plus the results from the 2012 ToO observations are shown.

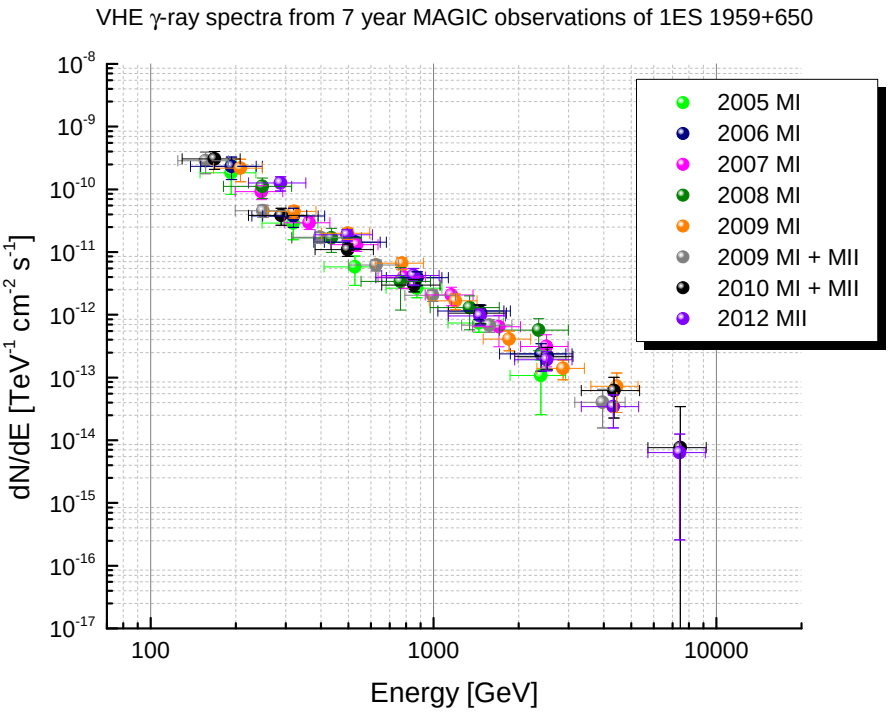

Figure 6.34: Measured spectra of 1ES 1959+650 for individual observation period (from 2005 to 2012).

In summary, as already noted before, each spectrum can be well fitted with a power law function. The resulting flux values are listed in the second column of Table 6.9 and the corresponding indices are listed in the last column of Table 6.9. As previously mentioned in Subsection 6.7.1 no major flux variability has been observed from this particular blazar. Comparing the obtained spectral results from 2009 to 2012 with previous finding by i.e. [HBK+08], [UM09], one can clearly see that all results fit together perfectly well, confirming the steady state of 1ES 1959+650 over a seven year survey. Moreover, since all measured spectra of this sources are derived in the quiescent state and agree perfectly well and in order to strengthen the here presented results, the aver-

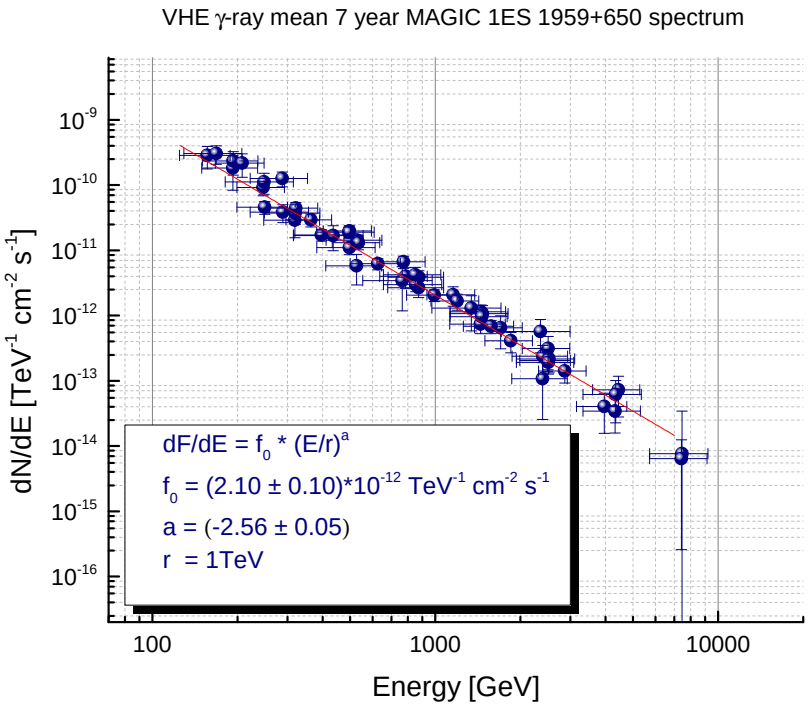

Figure 6.35: Measured spectra of 1ES 1959+650 for individual observation period (from 2005 to 2012) with a mean power law fit.

Table 6.9: 1ES 1959+650 differential power law flux results from seven year MAGIC observations.

Year	$F_{1\,\mathrm{TeV}}[10^{-12}\mathrm{TeV}^{-1}\mathrm{cm}^{-2}\mathrm{s}^{-1}]$	Photon index Γ	Reference
2005	(1.58 ± 0.28)	(-2.62 ± 0.25)	[HBK+08]
2006	(2.67 ± 0.36)	(-2.58 ± 0.18)	[HBK+08]
2007	(2.52 ± 0.42)	(-2.47 ± 0.19)	[UM09]
2008	(2.54 ± 0.80)	(-2.45 ± 0.40)	to be published
2009 P1	(2.64 ± 0.22)	(-2.66 ± 0.15)	this work
2009 P2	(2.07 ± 0.25)	(-2.48 ± 0.11)	this work
2010	(2.10 ± 0.31)	(-2.47 ± 0.18)	this work
2012	(2.84 ± 0.38)	(-2.92 ± 0.19)	this work

age mean flux and spectral index of all MAGIC monitoring observation plus the one from 2012 is calculated, as shown in Figure 6.35.
The average mean spectral values are shown to be:

$$F(E) = (2.10 \pm 0.10) \times 10^{-12} \times \left(\frac{E}{1\,\mathrm{TeV}}\right)^{-2.56\pm0.05} \mathrm{ph\ TeV^{-1} cm^{-2} s^{-1}} \tag{6.8}$$

This result is in perfect agreement with previous results reported by [Bac11]:

$$F(E) = (2.12 \pm 0.08) \times 10^{-12} \times \left(\frac{E}{1\,\mathrm{TeV}}\right)^{-2.57\pm0.06} \mathrm{ph\ TeV^{-1} cm^{-2} s^{-1}} \tag{6.9}$$

Both values are the exactest power law spectra for this source. The latter one corresponds to the period from (from 2005 to 2009), the value obtained during this work to the period from (from 2005 to 2012).

6.8 The Inverse Compton curvature of 1ES 1959+650

Today, the higher energies in X-ray and the γ-ray radiation are believed to be the result of Compton scattering causing in the γ-ray range a prominent second curvature in the SED (see Figure 6.40). The particles responsible for this characteristic shape are comptonized electrons which are formed by the same population as those emitting the synchrotron radiation. Unfortunately up to now, the source of the seed photons is not precisely known. There are already several promising models that could explain such scenario. One well known model suggests that the synchrotron photons generated within the jet scatter on the same electrons and in consequence produced them [BS12]. In that case one would observe a synchrotron SSC emission as described in more detail in Section 6.10. Another alternative approach could be that the seed photons could emanate from outside the jet, for instance from the BLR region or even the disk location, where a rich population of optical-UV photons is given [BS12]. In this particular case an **E**xternal **C**ompton (EC) model would be needed. In general, the best way in order to shed more light on these issues is throughout the compilation and interpretation of simultaneous multiwavelength data. The *Fermi* LAT satellite, which is a pair-conversion γ-ray telescope, launched into a low-Earth orbit on June 11$^{\mathrm{th}}$ in 2008 provides annually detailed studies of time-resolved broad-band γ-ray spectra of different AGNs. In Figure 6.36 four different blazar energy spectra from a *Fermi* LAT analysis are displayed.
The two left sources are the prominent Markarians 421 and 501. Both blazars are the archetype example of extreme HBL objects. Their spectra are hard

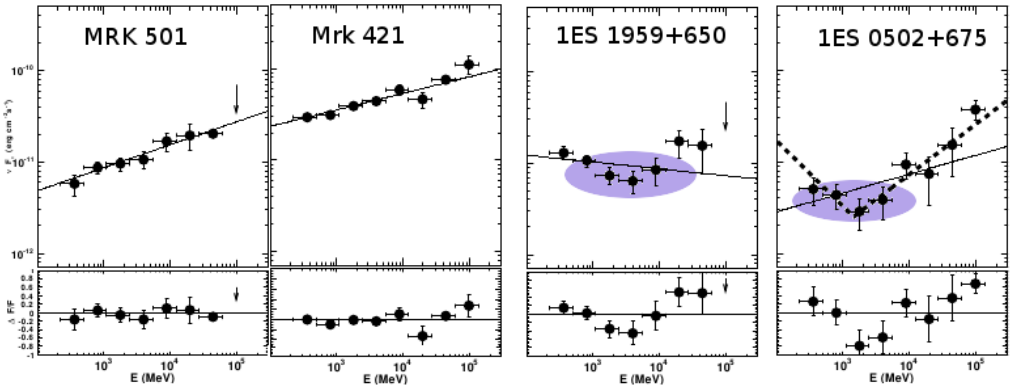

Figure 6.36: *Fermi* LAT spectra from Mrk 421, Mrk 501, 1ES 1959+650, and 1ES 0502+675 from the collected data from August 4th, 2008 until February 1st, 2009. A clear difference in the spectral shape between Mrk 421, Mrk 501 and 1ES 1959+650, 1ES 0502+675, respectively is visible. The figure is adapted from [AAA+10d].

(Mrk 421: $\Gamma = 1.78 \pm 0.02$ [AAA+11a]; Mrk 501: $\Gamma = 1.75 \pm 0.06$ [AAA+10d] and do not exhibit any sign of curvature, which make them ideal candidates for a study with SSC emission model.
In contrast, the two right sources 1ES 0502+675 and the blazar analyzed here 1ES 1959+650, both also classified as HBL objects, show an usual concave energy spectrum and thus open many interesting questions.
As discussed in [AAA+10d] one possible but still extraordinary scenario could be the existence of a second companion. In that case, this shape could be a spurious feature resulting from the spacial confusion of both sources, a hard and a soft one. Unfortunately, neither 1ES 0502+675 nor 1ES 1959+650 show evidence for a second source closed by [AAA+10d]. Another suggestive approach is that these two particular spectral shapes indicate either two emitting components (e.g. SSC and EC), as shortly described above, in the context of leptonic models in the HE γ-ray SED. Furthermore, it could also be a turnover from the synchrotron to the HE γ-ray component. This interpretation remains still unclear due to not simultaneous low frequency and high frequency SED coverage for both sources which are the crucial factor in proving an interpretation.

The 1ES 1959+650 inverse Compton peak

In order to resolve fully and simultaneously the inverse Compton curvature of 1ES 1959+650, data taken from the same observation periods between 2008 and 2010 from the *Fermi* LAT and MAGIC are used for this study. In Figure 6.38 the first simultaneous quiescent state IC curvature of 1ES 1959+650 is presented. Besides, as already presented by [Bac11], it becomes evident that a very good agreement between both experiments (*Fermi* LAT and MAGIC) is given. According to several studies and model predictions, the inverse Compton peak, in the following IC peak, of the SED of 1ES 1959+650 lies close to 100 GeV [TGG+10]. As already indicated in Subsection 6.3.5 the IC peak position should be strongly dependent on the VHE γ-ray flux level in case the peak moves to higher energies with increasing flux level as suggested by [AAA+10h], discussed in [Wag08] and shown in Figure 6.37.

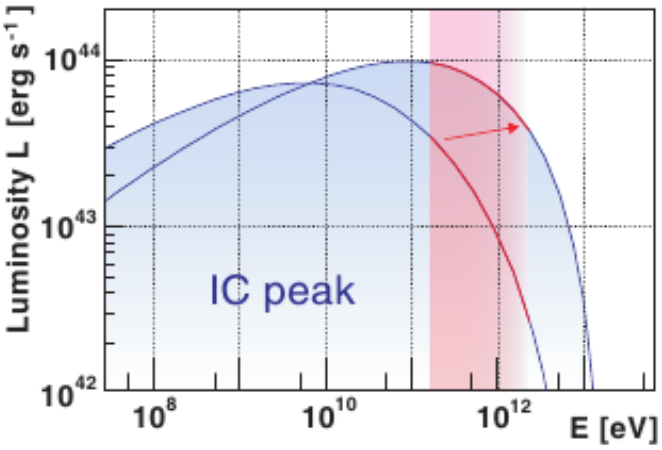

Figure 6.37: Model for the moving IC peak twards higher energies with increasing VHE γ-ray flux. From [Wag08].

In order to test a possible indication of such IC peak moving behavior, the curvature of the quiescent state and the flare day are examined. In the first step the average peak of the quiescent state is determined. For this reason a logarithmic parabola is fitted to the *Fermi* LAT and MAGIC data (see Figure 6.38) in following vertex notation:.

$$\nu F_\nu = \nu^{\mathrm{IC}}_{\mathrm{peak}} F_{\nu^{\mathrm{IC}}_{\mathrm{peak}}} \times 10^{b[\log(\nu/\nu^{\mathrm{IC}}_{\mathrm{peak}})]} \tag{6.10}$$

where $\nu^{\mathrm{IC}}_{\mathrm{peak}} F_{\nu^{\mathrm{IC}}_{\mathrm{peak}}}$ is the peak flux at the peak frequency $\nu^{\mathrm{IC}}_{\mathrm{peak}}$ and b the curvature parameter.

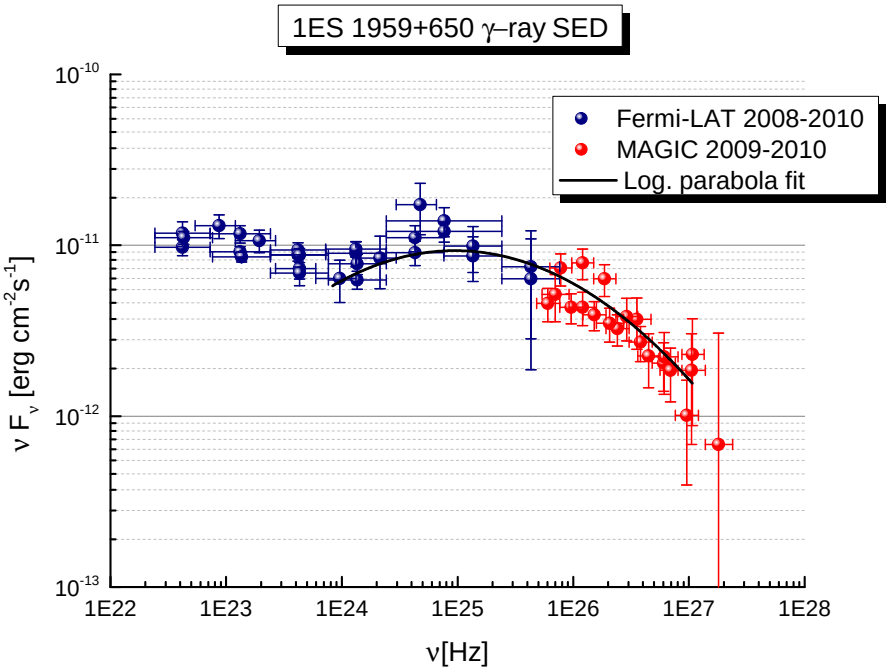

Figure 6.38: First simultaneous quiescent state Inverse Compton curvature of 1ES 1959+650 with an excellent agreement between *Fermi* LAT and MAGIC.

As already predicted by [TGG+10] the values evaluated here of $(8.46 \pm 0.35) \times 10^{24}$- corresponding to (34.98 ± 1.4) GeV confirm the results very well. In addition, comparing the peak position from a quiescent state spectra with a flare one of 1ES 1959+650, as listed in Table 6.10 and shown in Figure 6.39, then a shift to higher energies also seems to occur. Due to missing contemporaneous HE γ-ray data of this particular flare only an interpolation of the HE and VHE γ-ray data can be derived with a resulting peak at $(1.39 \pm 0.15) \times 10^{24}$- corresponding to (54.48 ± 6.20) GeV. Such correlation between flux level and peak position was lately observed during a Mrk 421 survey of MAGIC in 2010 (for more details see [Ste12]).

Table 6.10: IC peak values during different flux states of 1ES 1959+650. A evident shift of the IC peak to higher frequency during the flare is visible.

Status	$\nu^{\mathrm{IC}}_{\mathrm{peak}} F_{\nu^{\mathrm{IC}}_{\mathrm{peak}}}$	$\nu^{\mathrm{IC}}_{\mathrm{peak}}$	b
Quiescent	$(9.30 \pm 0.55) \times 10^{-12}$	$(9.46 \pm 3.85) \times 10^{24}$	-0.08±0.05
Flare	$(7.98 \pm 0.35) \times 10^{-10}$	$(1.39 \pm 0.15) \times 10^{25}$	-0.41±0.02

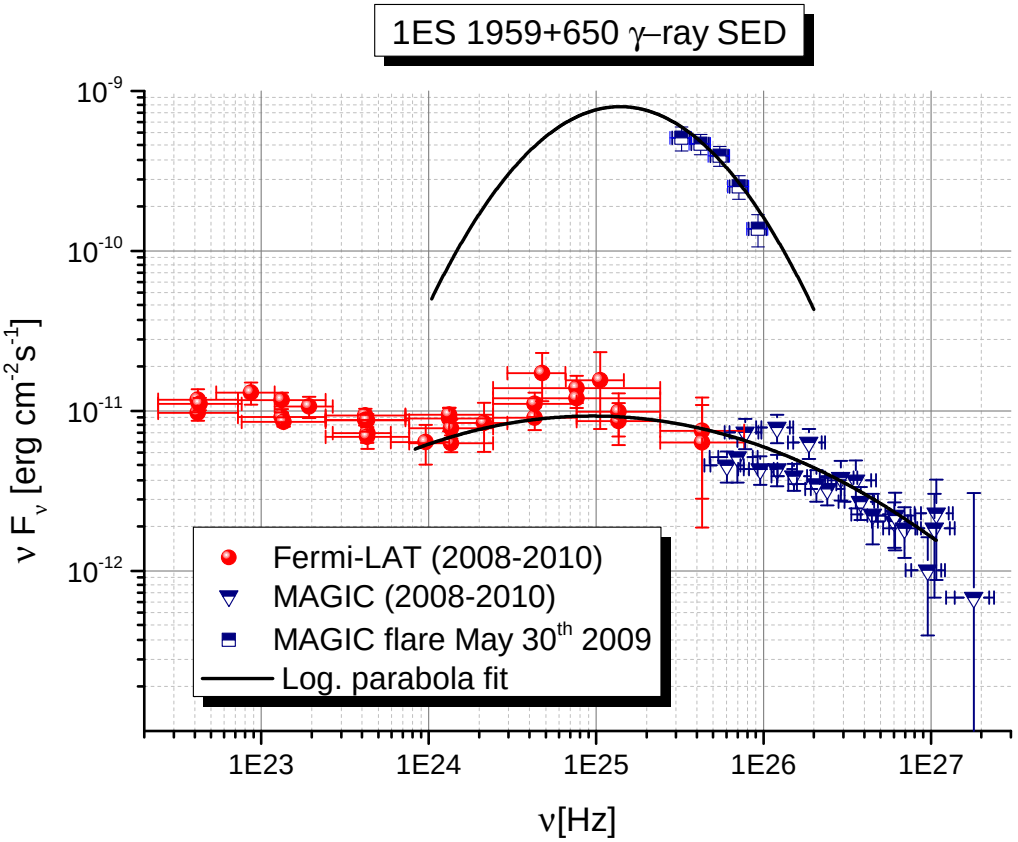

Figure 6.39: The IC peak of 1ES 1959+650 during different flux states.

6.9 Spectral energy distribution of 1ES 1959+650

In order to understand the different non thermal emission processes driving a blazar, one has to observe (in best case) the source throughout the whole electromagnetic range simultaneously and then study each of the different emission region. Such simultaneous observation were already performed but still only for a few blazars (e.g. Mrk 421 see Figure 6.40). By investigating the simultaneously measured different energy ranges one can draw a complete and unambiguous empirical imprint followed in turn by a preexisting theoretical model. One of the common methods of displaying such SED is done, by plotting the number of photons per unit time and unit area versus the frequency, as already shown in Figure 6.40. The data presented in Figure 6.41 for 1ES 1959+650 is not taken simultaneously (apart from the optical, HE and VHE γ-ray observations). Nevertheless, a dense observation, covering all important wavelengths of the SED with several experiments is given, showing at

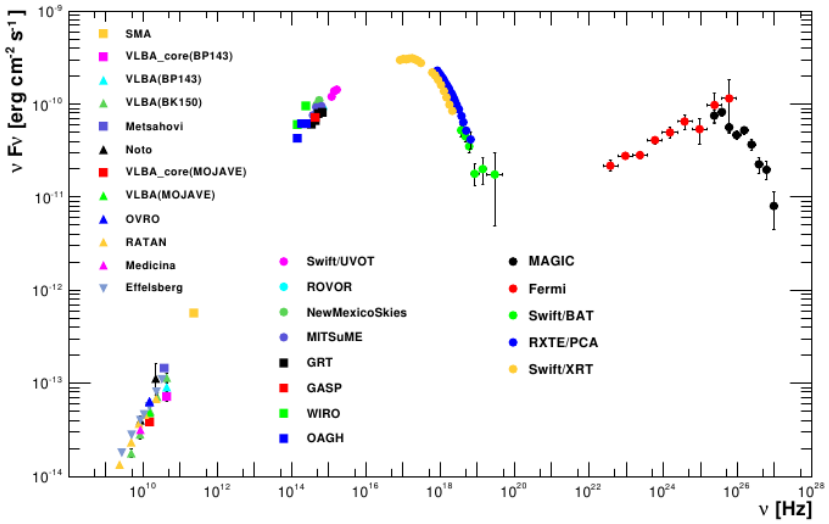

Figure 6.40: SED of Mrk 421 over all the observations taken during the multifrequency campaign from January 19th (MJD 54850) until June 1st (MJD 54983), 2009. The figure is taken from [AAA+11b].

the same time one of the best covered SED of any studied HBL so far. A short description of various observatories which observed 1ES 1959+650 in different observation periods is given below.

6.9.1 Radio observations

In the range between ($10^8 - 10^{12}$ Hz - yellow data points in Figure 6.41) the low frequency part of the SED is measured by observatories like the radio telescope RATAN-600, Effelsberg 100 m, IRAM,VLBI and VLBA with measurements of the core emission region. The first 1ES 1959+650 radio observations were already performed in 1991. A detail measurement listing of the used data can be found in Appendix B and in [Bac11].

6.9.2 Infrared, Optical and Ultraviolet observations

The IR, optical and UV wavelengths cover the frequencies from ($9\times10^{12} - 2\times10^{15}$ Hz - green and turquoise data points in Figure 6.41). All IR observations presented here were taken with the Spitzer IR observatory in 2008 and the data was retrieved from the Spitzer Heritage Archive[2]. The optical R-band data was

[2]http://irsa.ipac.caltech.edu/data/SPITZER/docs/spitzerdataarchives/sha/

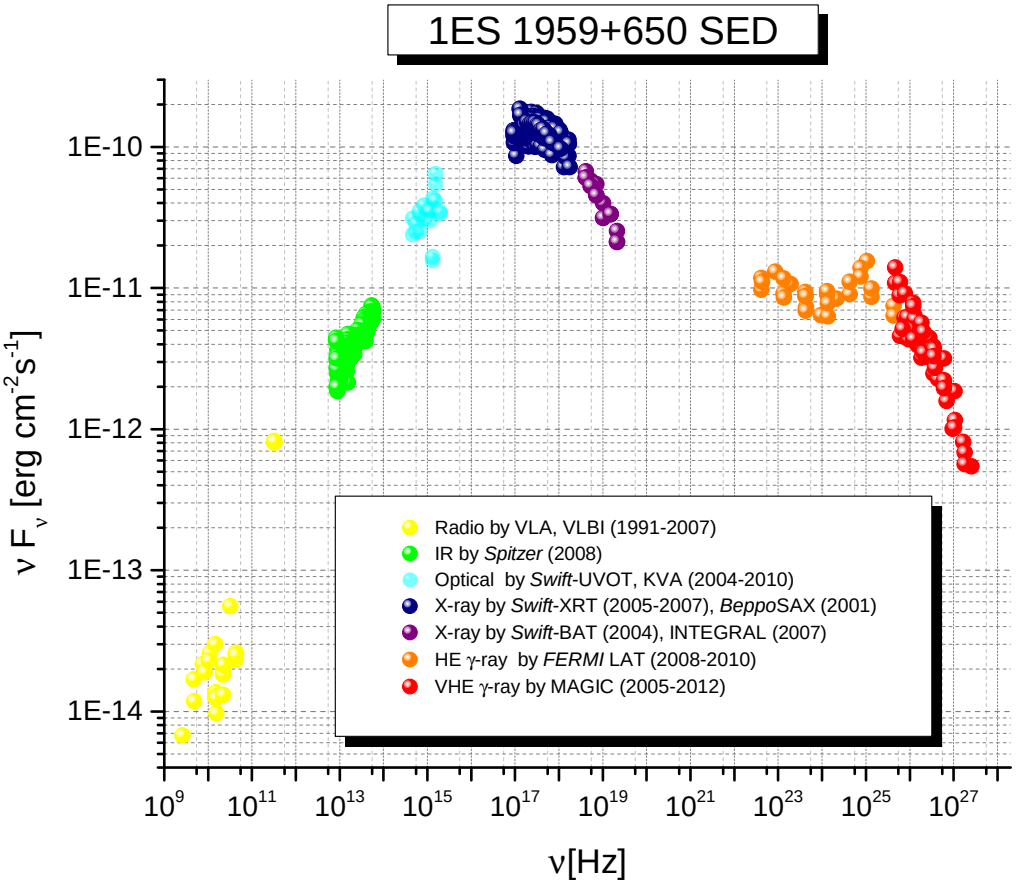

Figure 6.41: One of the best covered SED of any HBL of 1ES 1959+650 including the here analyzed MAGIC 2009 to 2012 data.

recorded with the KVA observatory as well as G-band observations with Palomar 60 from 2004 till 2010 were used. In addition, the UV data has been taken from the *Swift*-UVOT observations.

6.9.3 X-Ray observations

The first X-ray observations of 1ES 1959+650 were observed with *Beppo*SAX in 2001. Since then nearly annual observations were performed by satellites like *Swift*-RXT, *Swift*-BAT and INTEGRAL. These data were used for the covering of the synchrotron curvature. The X-ray data span a range from $(5\times10^{16} - 3\times10^{19}$ Hz - blue and purple data points in Figure 6.41). An important characteristic feature in case of blazars is the strong and significant flux variation in the X-ray band. In case of 1ES 1959+650 a X-ray flux variability of about a factor

of four is visible (soft-X-rays - blue points in Figure 6.41). In the hard X-ray (purple points) instead, a trend to less variability and quiescent states as for the HE and VHE γ-ray regime is observed.

6.9.4 γ-Ray observations

For the coverage of the IC curvature, as already discussed in Section 6.8, measurements from the *Fermi* LAT, and data from previous MAGIC observations as well as data from the here presented results (from 2009 to 2012) was used. In particular, as already noted in Subsection 6.9.3, all the here presented γ-ray measurements in the range from ($5\times10^{22} - 5\times10^{27}$ Hz - orange and red data points in Figure 6.41) were taken during a quiescent state of 1ES 1959+650. The orange *Fermi* LAT data points depicted in Figure 6.41 represent the observations from 6, 11, 24 and 27 months of the *Fermi* LAT survey provided by [Pan13], whereas the red points cover the full MAGIC quiescent state observations performed from 2005 till 2012.

6.10 Modeling of the SED data points of 1ES 1959+650

The SED of blazars exhibits, as shown in Section 6.9, a generic two-curvature structure: one peak with a maximum in optical to X-ray band and a second peak located in the γ-ray bands. The radiation is produced in a highly beamed plasma jet and the double peaked SED is normally attributed to a population of relativistic electrons. As briefly mentioned above, it is known that the first peak is produced by synchrotron emission in the magnetic field of the jet and the second peak is caused by IC scattering of low-energy photons ([Ree67]). The low-energy photons can be external to the jet (EC scattering, [DS93]) or are produced within the jet via synchrotron radiation (SSC, [MGC92]). In order to investigate and make constraints on the physical parameters behind observed emissions a number of different models have been developed to explain the SED of blazars. Looking at the most simplest approach, the dominant physical processes are restricted to only one emission region. From this region the synchrotron and the IC emission is radiated. Such one zone emission model using SSC processes is applied to the 1ES 1959+650 SED data and described in the next section below.

One zone synchrotron self-Compton model

Today it is known that the radio emission from blazars is caused by synchrotron emission which is produced in processes when charged particles e.g electrons move through a magnetic field. In the most simple model, the one zone SSC

model, and as the name is already suggesting it, it is assumed that the γ-radiation is produced in a single zone jet. The acceleration region is thought to be a spherical "blob" with radius R and bulk Lorentz factor $\Gamma = E_e / m_e c^2$ containing charged particles that is traveling along the jet under a small angle θ to the line of sight [Wag08]. Along the way, the charged particles of the density ρ interact with magnetic fields, which leads to the synchrotron radiation. Another assumption is that a diffuse shock acceleration mechanism is responsible for the initial electron acceleration. The spectrum of the electron injection can be approximated by a broken power law with indices $n_1 < 3$ and $n_2 > 3$ below and above a break energy $\gamma_b m_e c^2$. The energy distribution of the electrons has the form $N(\gamma)$=kγ^{-n_1} if $\gamma < \gamma_{\text{break}}$ and $N(\gamma)$=k$\gamma_{\text{break}}^{n_2-n_1}$ if $\gamma > \gamma_b$ [BS12]. Besides, one also has to take the synchrotron cooling effects into account; in this case the spectrum is showing a break point where radiative cooling becomes dominant. Thus the energy spectrum can be described by three parameters E_{min}, E_{max} and E_{break}. Consequently, as shown in [KTK02] it becomes evident that in the presence of randomly oriented magnetic fields B, which is assumed to be approximately constant, an isotropic electron population with such spectrum, as shown above, is able to develop a synchrotron photon population as already observed in a different number of blazars. Furthermore, the one zone SSC model also assumes that the seed photons needed for the IC scattering and the photons produced on the synchrotron process are identical [Wag08]. As shown in Figure 6.41 the typical two peaks structure is visible. The second peak is the result, assuming to the one zone SSC model, of the photon upscattering to VHE regime by the same electron population that created the synchrotron radiation and the first peak in the SED. In addition, [TMG98] have demonstrated how the IC and synchrotron branches are correlated assuming in particular SSC processes and Doppler boosting. The Doppler boosting factor also used for the one zone SSC modeling is defined by $\delta = [\Gamma(1 - \beta\cos\theta)]^{-1}$ with the bulk velocity of the plasma βc. This parameter describes the effects of time dilatation, boosting and jet focusing. All in all, the simple one zone SSC model is described by nine free parameters, namely those which describe the emission region: strength of the magnetic field B, the size of the blob represented by R and δ, those which characterize the electron injection γ_{min}, γ_{max}, γ_{break} and n_1,n_2 as well as the electron density K plus the time variability timescale t_{acc} vs. t_{esc}. For the modeling of the 1ES 1959+650 SED a modified one zone SSC model (see Figure 6.42) developed by [WS10], known as the self consistent SSC model, using n_1, n_2 as well as γ_{min}, γ_{max}, γ_{break} as free parameters is applied. The corresponding values for the parameters are listed in Table 6.11. In Figure 6.42 one can see that this approach overestimates the flux in the hard X-ray range (see purple points). Moreover, it is clearly evident that this model fails to describe the SED in the *Fermi* LAT

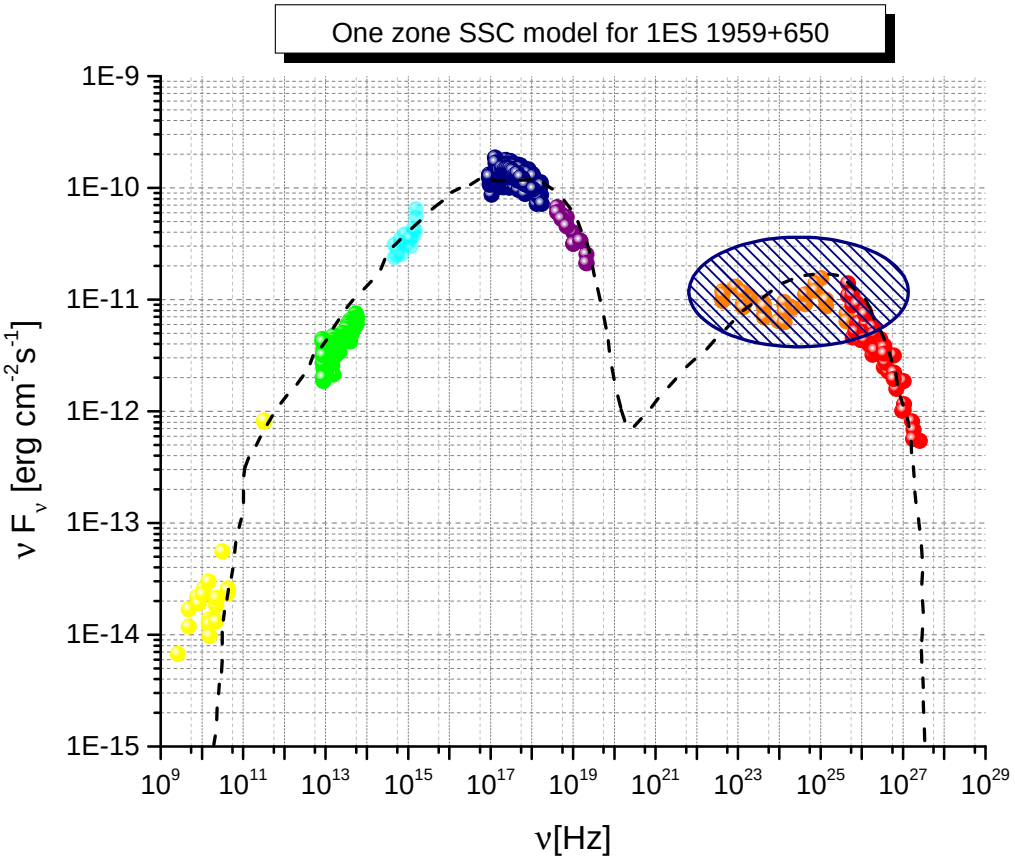

Figure 6.42: One zone Synchrotron Self-Compton model.

range (orange points) as marked by the blue dashed ellipse. Such finding is very unusual, since the single zone SSC model still belongs to the first choice of modeling templates, and opens again questions concerning the emission mechanism of HE and VHE photons in 1ES 1959+650.

Two zone synchrotron self-Compton model

As shown in the previous section and Figure 6.42 it is not always possible to represent the emission of different blazars by a simple SSC model. In fact, the more data we gather on blazars, thanks to improved sensitivity of various γ-experiments e.g. *Fermi* LAT, H.E.S.S., MAGIC, VERITAS, the more distinct and complex their SED appear to be. Thus, further approaches are necessary in order to describe different SEDs of blazars. Another well known model is the so called two zone SSC model. This model drops the SSC constraints that the up-scattering charged particles and the up-scatter photons have to originate

in the same region, giving more free parameters and thus more possibilities to model the SED of a blazar. More precisely, taking into account two independent radiation zones, it practically doubles the number of free parameters compared to the one zone SSC models revealing a strong explanatory power. Such model was also applied to the observed SED of 1ES 1959+650 as shown in Figure 6.43. The model parameters are listed in Table 6.11 the first row shows the parameters for the low energetic emission region and the second one for the high emission region respectively. Moreover, the numbers are determined by a self-consistent model by [WS10] depending on the acceleration and emission time including further no free parameters like: t_{acc}/t_{esc}=0.95 s as well as the acceleration Region $R_{acc_{LE}} = 1 \times 10^{14}$ cm, $R_{acc_{HE}} = 6 \times 10^{13}$ cm. In comparison with the one zone SSC model the two zone SSC model provided by M. Weidinger [WS10] and adapted from [Bac11] fits the SED of 1ES 1959+650 reasonably well, but still with an overestimation of the *Fermi* LAT curvature as already pointed out in Section 6.8. Nevertheless, it is currently the most favored model for 1ES 1959+650 and this study. As described in [Bac11] there were already several efforts done by trying to apply a hadronical model on the 1ES 1959+650 SED data. Unfortunately, due to high energy emission which is comprised by synchrotron emission of protons and emission by protons induced cascades the modeling occur to be very difficult. In particular the featureless cascade emission has to be very fine-tuned to be able to explain the spectral shape of the 1ES 1959+650 HE and VHE region and strongly relying on the EBL model (for more information about the EBL see Section 1.4). Besides, the flaring activities should also be taken into account including an additional emission region and increasing the number of parameters even further. Consequently, at the current stage it is still not possible to claim with a sufficient accurateness if or if not hadronic mechanism are responsible for the HE and VHE emissions in 1ES 1959+650.

Table 6.11: Model parameters used for fitting the SED of 1ES 1959+650 in Figure 6.42 and Figure 6.43.

Model	γ_{min}	γ_{break}	γ_{max}	n_1	n_2	$B\,[G]$	$K\,[cm^{-3}]$	$R\,[cm]$	δ
One zone SSC	3	11×10^3	650×10^3	1.95	2.95	0.29	800×10^3	70×10^{14}	31
Two zone SSC (LE)	800	8×10^3	65×10^3	2.60	3.60	0.81	190×10^3	20×10^{14}	20
Two zone SSC (HE)	1600	25×10^3	600×10^3	2.13	3.13	0.44	3.75×10^3	20×10^{14}	46

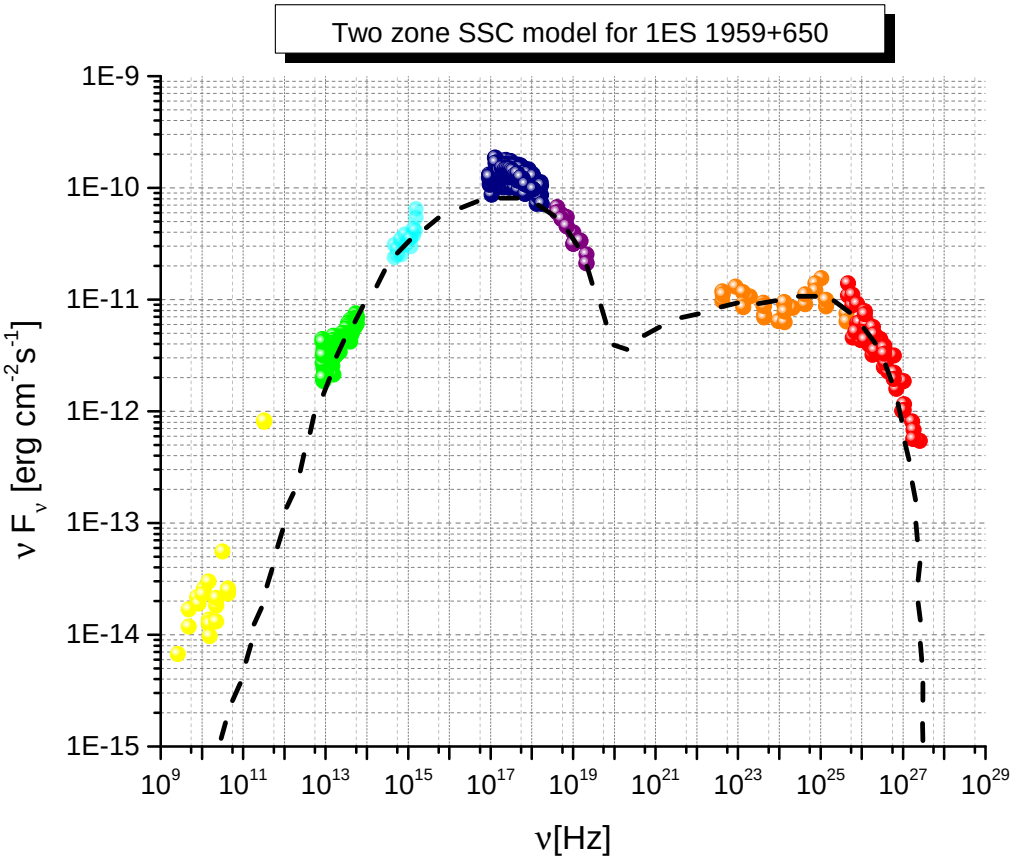

Figure 6.43: Two zone Synchrotron Self-Compton model.

6.11 Summary and Conclusions

In this chapter the analysis of two last monitoring years of VHE γ-ray observations from 2009 to 2010 as well as the observations during the historical strongest optical flare in May 2012 were presented. The essential findings of this work are summarized in the following enumeration:

- The overall flux above 300 GeV from 2005 to 2012 shows only a modest variability on yearly timescale, within a variability of factor 3, corresponding to a variability of 5% to 12% of the Crab Nebula flux. Such quiescent state behavior over a long period of time has already been observed in other blazars, such as PG 1553+113 [AAA+12d].

- No clear intra-night variability on smaller time-scales (15 min binning) is evident from the analyzed data sample in 2012 for 1ES 1959+650.

- Despite the hints of variability on the level flux, the differential flux from each year is in a very good agreement with previous results. For this reason an average mean differential flux and photon index of

$$F(E) = (2.10 \pm 0.10) \times 10^{-12} \times \left(\frac{E}{1\,\mathrm{TeV}}\right)^{-2.56\pm0.05} \ \mathrm{ph\ TeV^{-1}cm^{-2}s^{-1}} \quad (6.11)$$

  were derived.

- A single night flare was detected on May 30$^{\mathrm{th}}$ with a γ-ray rate four times higher than in measured low states . The integral flux of this flare was determined to be: F$>$300 GeV=$(8.2 \pm 1.6) \times 10^{-11}\mathrm{cm^{-2}s^{-1}}$ corresponding to ~70% C.U. whereas the differential flux and the spectral index are:

$$(1.82 \pm 0.25) \times 10^{-9} \times \left(\frac{E}{250\,\mathrm{GeV}}\right)^{-2.29\pm0.29} \ \mathrm{ph\ GeV^{-1}cm^{-2}s^{-1}} \quad (6.12)$$

- In addition, a correlation study during the distinct flare for different wavelength bands was performed. From the X-ray and VHE-γ-ray light curve it seems again that both wavelength bands are not connected with each other giving again a hint of a measured *orphan flare* from this source.

- Furthermore, a strong correlation between the VHE γ-ray results and the 15 GHz radio bands during the distinct flare was found. This result strongly indicates that the nearly coincident flux enhancement in both wavelengths have a common emission region which is undoubtedly produced in the jet region and not in the BLR [KAA$^+$09]. Such finding was already found by different authors i.e. [NTV$^+$11] and supports very well the assumption that both wavelengths have for this particular flare a co-spacial origin with a radio core and emerging superluminal blobs which were found in the MOJAVE skymaps. From further multi-epoch VLBA radio study of 1959+650 which are planed to be carried out in the future further important parameter like the jet speed or component ejection can be determined and thus revealing further important parameters for the modeling of this blazar.

- In contrast, for the optical (R-band) and VHE γ-ray wavelengths only a hint of correlation of c_{coeff} = 0.5 and an delay of 55 days (γ-ray leads optical) is obtained by this study. Such delays are expected, as shown in [ESR12], in case of moving shocks along the jet and different opacities of the medium. Also further time lag studies can provide a powerful tool to resolve the structure of relativistic jets and their radiative environment.

Finally, out of the correlation study between the optical and the VHE-γ-ray range during the strongest optical outburst in 2012 again no correlation could be found between both wavelengths as well as between the optical and radio wavelengths. This indicates strongly, that the dissimilarity between the optical and radio variations have a different structure of the emitting plasma and thus synchrotron radiation. For this reason, the optical synchrotron radiation might be emitted in the BLR whereas the radio emission, as already discussed above, is emmerging from the blob regions in the jet.

- From the 2008-2010 MAGIC monitoring observations and the *Fermi* LAT (2008-2010) results the first quiescent state IC peak value for the blazar 1ES 1959+650 with (34.98 ± 1.40)GeV was estimated.

- In addition, when comparing the peak position from a quiescent state spectrum with a flare one (54.48 ± 6.20)GeV, a shift to higher energies also seems to occur. Such correlation between flux level and peak position was already reported for different blazars e.g. Mrk 421 as reported in [Ste12].

- Another interesting finding is the concave spectral shape of the *Fermi* LAT spectrum of 1ES 1959+650. This shape was compared with other prominent blazars like Mrk 421 and Mrk 501 where a huge difference in the shape was found. Today, only the HBL, 1ES 0502+675 shows a similar HE γ-ray spectral shape. This feature can be interpreted as indication of either two emitting components e.g. SSC and EC, in the HE γ-ray SED or it could be a turnover from the synchrotron to the HE component [AAA$^+$10d].

- For the study of the SED, the mean differential spectrum measured by MAGIC was combined with simultaneous and historical data at other wavelengths. The SED was modeled with two different leptonic SSC models. On the one hand with a simple one zone SSC model where the model fail to describe the data accordingly and on the other hand with a two zone SSC model, where the fitting agrees well, but still in few cases under or overestimating the measured data. It should be noted, since a SED modeling should be performed for each VHE γ-ray flare independently in order to estimate the exact emission region of the radiation the here presented modeling is only addressed for the quiescent VHE γ-ray state for this blazar.

Finally, at the current stage it is still not possible to claim with a sufficient accuracy whether or not hadronic mechanism are responsible for the HE and

VHE γ-ray emissions in 1ES 1959+650.

The next chapter presents the analysis results of the blazar 1ES 0033+595 which was discovered in the VHE γ-ray range during this thesis.

CHAPTER 7

DISCOVERY OF THE LONG HUNTED BLAZAR 1ES 0033+595

The BL Lac object 1ES 0033+595 has been detected for the first time in 2011 in the VHE γ-ray with a statistical significance of 5.5 σ [Mar11], thanks to the excellent sensitivity of the MAGIC stereoscopic system in the energy range below few hundreds of GeV. In this chapter the discovery of this blazar is presented with new spectral properties in the VHE γ-ray range: MAGIC observed this source between August and October 2009 for nearly 24 h, in the commissioning phase of the MAGIC stereoscopic system. The integral flux above 150 GeV is estimated to be (2.2±0.4)% of the Crab Nebula flux and the VHE spectrum has a photon index of (3.8±0.7). In addition, the source did not show any variability during the MAGIC observations. Since the redshift of this source is unknown, an empirical approach by [PBM+11] was used in order to determine a new redshift of ($z = 0.34 \pm 0.05$). Finally, for the first time, based on the new redshift, the SED of 1ES 0033+595 has been reconstructed and modeled using a single zone SSC model.

7.1 The Blazar 1ES 0033+595 and its properties

1ES 0033+595 is a blazar near the galactic plane. It is located in the Cassiopeia region near the bright star Gam Cas at RA:00:35:52.63 and DEC.:59:50:04.56. This blazar is classified as extreme HBL object with synchrotron emission peaking near 10^{19} Hz ($\log\nu_{\rm peak}$ = 18.93 as shown in Figure 7.1, [NTV06]). So far, optical observations of 1ES 0033+595 were not able to resolve the host galaxy to determine a photometric redshift and thus the redshift of the blazar remains uncertain. There are two different values available in the literature: [Per00] tentatively measured z = 0.086, while others have argued that it is

more distant ([STF05], $z > 0.24$). For this reason, it is still difficult to judge which value of both is the correct one and thus this issue is investigated in this work in detail.
From the historical point of view, 1ES 0033+595 was detected for the first time as a hard X-ray source by the Einstein Slew Survey in 1992 [EPS+92]. In 1996 it has been observed by the Hubble Space Telescope as part of the snapshot survey of BL Lac objects, and was resolved into two point-like sources with a separation of 1.58 arcsec [SUF+99] (see Figure 7.2). These two objects with nearly similar brightness were explained in [SUF+99] as multiple images of a gravitationally lensed system. However, the **V**ery **L**arge **A**rray (VLA) astrometric observations performed in 1997 did not detect a second radio source, ruling out that possibility [RGS03].

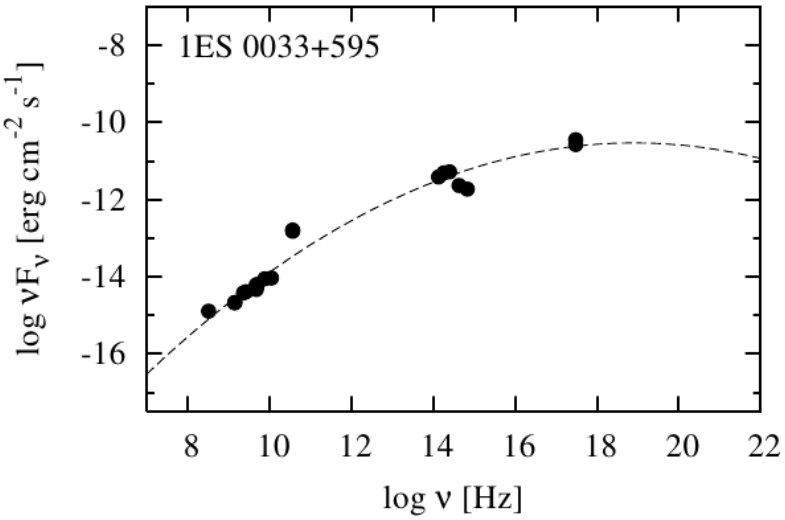

Figure 7.1: The synchrotron peak of 1ES 0033+595 taken from [NTV06].

In the following years this source was observed by the X-ray satellite *Beppo*SAX in December 1999. Due to high galactic absorption it could only be detected in the LECS instrument above 0.4 keV and in the PDS instrument up to ~ 60 keV [CGG+01]. Furthermore, this source was also detected with the INTEGRAL satellite in 2003 in the energy band (20 – 50 keV) with a statistical significance of 5.2 σ [dHK+06]. In addition, during the observations of [KHid05] in 2005 the source was a factor of 2.4 brighter. The fact that all three X-ray observations show different flux levels emphasize very well the variable X-ray nature of this BL Lac object. With its large field of view and nearly continuous sky coverage the **B**urst **A**lert **T**elescope (BAT) instrument on-board the *Swift* satellite could also detect 1ES 0033+595 during the first 22 months of observation [TBM10].

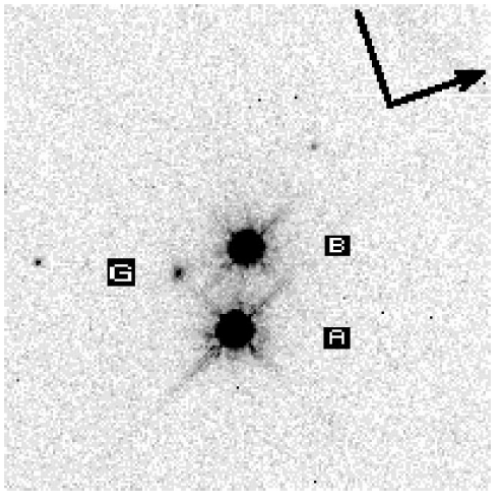

Figure 7.2: 1ES 0033+595 observed by the Hubble Space telescope. It is assumed that **B** is the true BL Lac object and **A** is a star. **G** is a faint galaxy also in the FoV. The image is taken from [SUF+99].

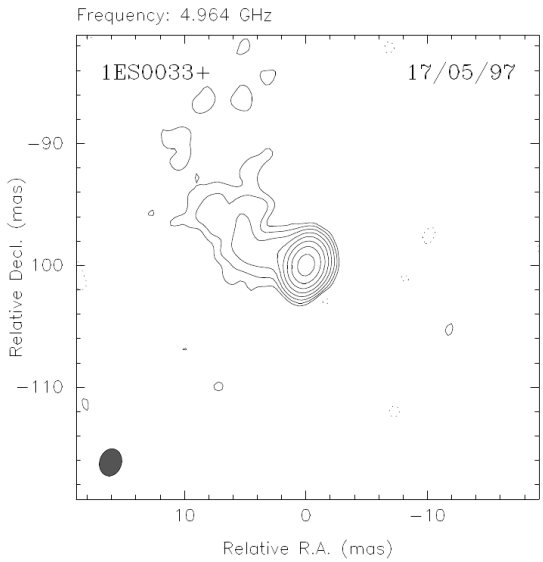

Figure 7.3: 1ES 0033+595 observed with the radio VLBA telescopes in the frequency of 4.96 GHz. The image is taken from [RGS03].

In the HE γ-ray range the source was first detected with the *Fermi* LAT during its 5.5 month survey [AAA+09b]. Since then it belongs to the part of the Fermi bright AGN catalog, with a spectrum consistent with a power law with $\Gamma = 2.00 \pm 0.13$ and a Flux of $F(> 200\,\mathrm{MeV}) = (20.30 \pm 5.11) \times 10^{-9} \mathrm{cm}^{-2}\mathrm{s}^{-1}$ [AAA+09b]. Looking at the VHE γ-ray band this source was first observed for 12 h in December 1995 with the Whipple 10 m telescope. These observations yielded only upper limits, $F(> 430\,\mathrm{GeV}) < 1.85 \times 10^{-11} \mathrm{cm}^{-2}\mathrm{s}^{-1}$, 17% of the Crab Nebula flux [HBB04].

7.2 MAGIC observations of 1ES 0033+595

MAGIC observations of this source in the VHE γ-ray range were motivated by the *Beppo*SAX observations and results explained in [CG02].
Therein 1ES 0033+595 was one of the most promising candidates for TeV emission. MAGIC first observation of this object started in 2006 and later in 2008 for about 5 h. Since no strong activity could be found in the data, only a flux upper limit at 95% confidence level has been obtained, MAGIC: $F(> 170\,\mathrm{GeV}) < 2.4 \times 10^{-11} \mathrm{cm}^{-2}\mathrm{s}^{-1}$, 9.7% of the Crab Nebula flux [AAA+11c].
New observations in 2009 during the commissioning phase of the MAGIC stereoscopic system, as described in detail in this work, led to the discovery of the source in the VHE γ-ray range and were announced in an ATEL on October 27$^{\mathrm{th}}$, 2011 [Mar11], and reported in [ULM+12].
The MAGIC telescopes observed 1ES 0033+595 from August 17$^{\mathrm{th}}$ until October 14$^{\mathrm{th}}$, 2009, for a total observation time of 23.5 h. These observations were performed during the commissioning phase of the MAGIC stereoscopic system, as already mentioned in Section 6.4, where 1ES 1959+650 was observed in the same period. Since this particular data was taken in the so-called "soft stereo trigger mode", a non-standard stereo data trigger condition, a dedicated MC γ-ray simulation sample has been generated on the high-performance cluster in Dortmund and adopted in the zenith range from 05° – 35° during this work for this source. As for 1ES 1959+650, the survey of 1ES 0033+595 was carried out in the so-called wobble observation mode [FSLo94], in which the pointing direction alternates every 20 min between two positions, offset by ±0.4° in RA from the source. The data was taken at zenith angles ranging between 31° and 35°, which resulted in an analysis energy threshold of 125 GeV (for more informations about the energy threshold see Subsection 5.3.2). After the application of standard quality checks based on the rate of the stereo events and the distributions of basic image parameters, 19.7 h of data were selected to derive the results. Since in the commissioning phase difficult trigger conditions were given, the cut threshold of the L3 rate was relaxed to $L3 > 25$ Hz.

In addition, further rejected data were affected mainly by non-optimal atmospheric conditions during the data taking, as already mention in the previous Chapter 6, were the analysis results of the 1ES 1959+650 were presented. The whole data sample before the quality selection is listed in the Appendix C, Table C.1 whereas the data sample after quality cuts is reported in Table 7.1.

Table 7.1: 1ES 0033+595 discovery data set. From left to right: dates in dd / mm / yy, effective time of observation in hours, zenith angle distribution, rate of the event after the image cleaning in Hz and the significance of each observation night.

Date	Eff. time[h]	Zenith [°]	Mean L3 Rate [Hz]	Significance [σ]
17 / 08 / 2009	0.28	33-34	30	0.47
18 / 08 / 2009	1.30	31-34	30	-0.23
19 / 08 / 2009	1.88	31-34	35	1.85
20 / 08 / 2009	0.70	31-34	40	2.08
21 / 08 / 2009	0.68	31-34	45	1.29
22 / 08 / 2009	1.75	31-34	45	2.52
23 / 08 / 2009	1.90	33-34	30	1.49
24 / 08 / 2009	1.94	31-34	45	1.75
25 / 08 / 2009	1.64	31-34	45	1.81
26 / 08 / 2009	1.19	31-34	40	0.83
27 / 08 / 2009	1.05	31-34	45	2.09
28 / 08 / 2009	1.88	31-34	35	2.20
29 / 08 / 2009	1.16	31-34	45	0.68
11 / 10 / 2009	0.52	31-34	35	-0.44
12 / 10 / 2009	0.89	31-33	40	1.44
13 / 10 / 2009	0.97	31-34	35	0.47

The data analysis was performed using the standard software package MARS, as already described in previous Chapter 4, including the latest standard routines for stereoscopic analysis [AAA+11d, Lom11]. The whole procedure was similar to that one described in Section 6.4 and Section 6.5 for 1ES 1959+650, with one exception in the energy range.
For the signal search in the 1ES 0033+595 data sample low energy range cuts in the program `"Odie"` have been used. There the cuts in `Size`, `Hadronness` and the θ^2 differ significantly.

Thus, following cuts

```
Odie.cuts: MHadronness.fHadronness < 0.28
           && MHillas_1.fSize > 55
           && MHillas_2.fSize > 55
           && MStereoParDisp.fEnergy >50
Odie.signalCut: 0.026
Odie.psf40: 0.10
Odie.nWobbleOff: 1
```

have been applied to the 1ES 0033+595 data. Also these cuts were optimized by means of contemporaneous Crab Nebula data and MC simulations. In computing the significance of the signal coming from the 1ES 0033+595 sky region, single cuts in `Hadronness` and θ^2 optimized for energies close to the energy threshold were applied. Conversely, while deriving the spectrum and the light curve of the source, multiple cuts optimized in logarithmic energy bins were considered, as already described in Subsection 6.3.4.

7.2.1 Signal search and the final discovery of 1ES 0033+595

As mentioned above, the signal from 1ES 0033+595 could only be estimated applying the low energy signal cuts. In the full range above 250 GeV the source seems to be less significant. Only in the range from (50-250) GeV a detection signal above $5\,\sigma$ is given. Figure. 7.4 shows the θ^2-plot where excess of 372.0 events in the fiducial signal region with $\theta^2 < 0.026$ degrees, corresponding to a significance of $5.5\,\sigma$ is found.
The corresponding significance skymap in low energy range of the sky region around 1ES 0033+595 is shown in Figure 7.5. A hot spot at $\sim 6\,\sigma$ significance level is consistent to the 1ES 0033+595 sky position. Comparing the extension of the excess to the PSF of MAGIC, the source has a point-like appearance.

This is the first time, that a signal in the VHE γ-ray range could be detected for 1ES 0033+595.

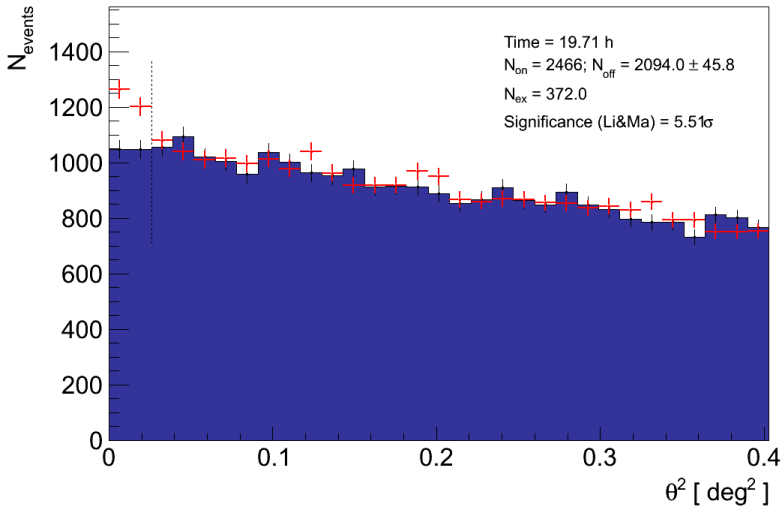

Figure 7.4: θ^2 distributions of the 1ES 0033+595 signal and background estimation from 19.7 h of MAGIC stereo observations taken between August 17th and October 14th, 2009. The region between zero and the vertical dashed line (at 0.026 degrees) represents the signal region.

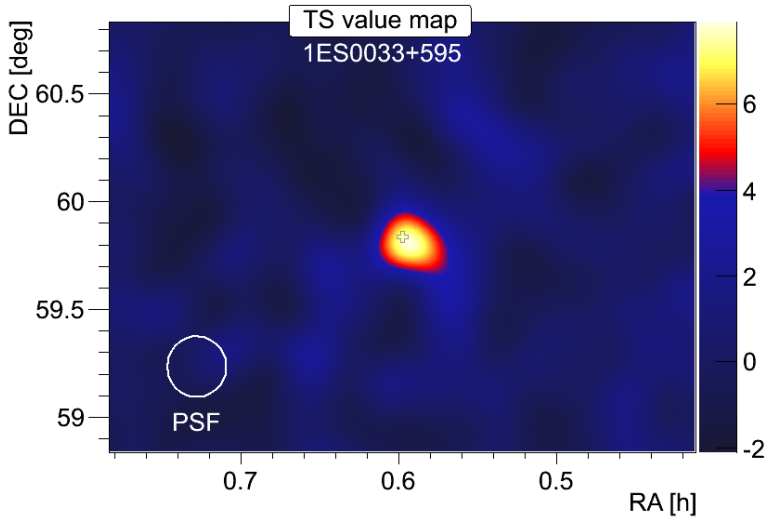

Figure 7.5: Significance skymap of the sky region around 1ES 0033+595 from 19.7 h of MAGIC stereo observations taken between August 17th and October 14th, 2009. The 1ES 0033+595 position is marked with an empty cross. The PSF of 0.1 degree is also displayed.

7.2.2 Temporal behavior of 1ES 0033+595

Since 1ES 0033+595 did not show any strong variability in the previous observation years in 2006 and 2008 that would lead to a detection, in 2009 it was also rather faint. The mean flux above 150 GeV is $F(>150\,\mathrm{GeV}) = (7.1 \pm 1.3) \times 10^{-12}\,\mathrm{cm}^{-2}\,\mathrm{s}^{-1}$, corresponding to (2.2±0.4)% of the Crab Nebula flux. This discovery is a very good example of the improved sensitivity of the MAGIC stereoscopic system. In the energy range between (50 – 200) GeV the MAGIC telescopes sensitivity is a factor of 3 better than the one of a single telescope. The August to October 2009 light curve of 1ES 0033+595 computed for an energy threshold of 150 GeV and with a weekly binning is shown in Figure 7.6. No evidence of strong variability can be derived from these measurements. In fact, fitting the light curve with a constant flux hypothesis yields a χ^2/NDF=3.7/3, corresponding to a probability $P(\chi^2) = 0.3$.

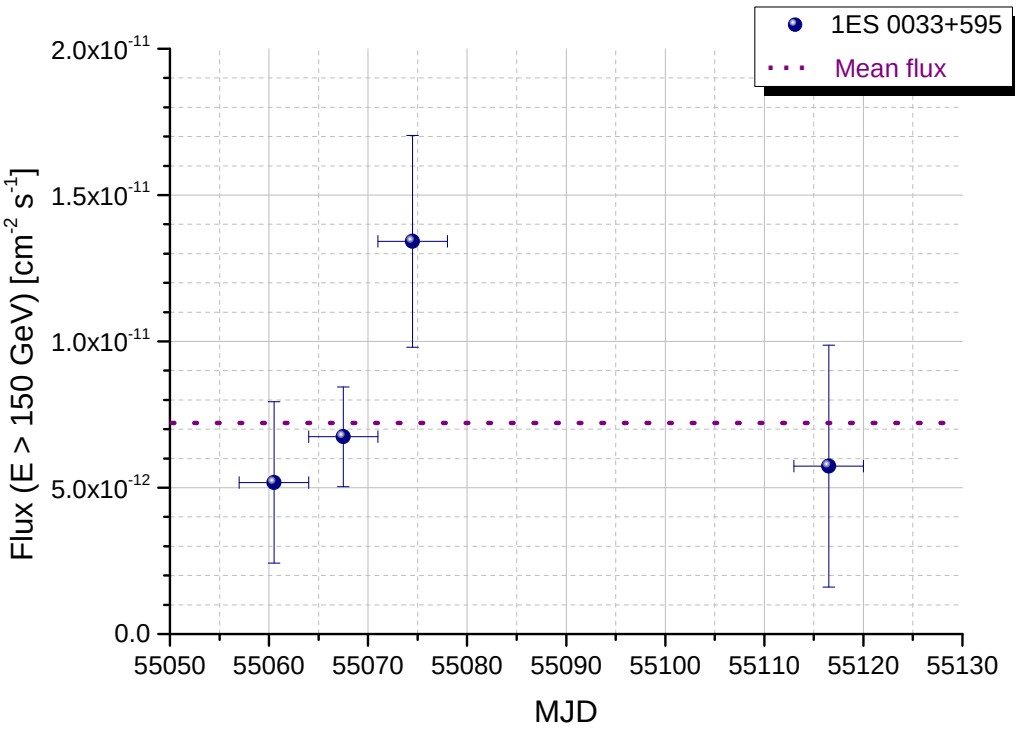

Figure 7.6: 1ES 0033+595 light curve between August and October 2009 above an energy threshold of 150 GeV, and with a week time-scale binning. No hints of significant variability are seen in the data. The dashed horizontal line represents the constant function resulting from the fit to the data.

7.2.3 The different energy spectrum of 1ES 0033+595

In Figure 7.7, the unfolded differential energy spectrum, using the *Bertero* method, of the source derived from the MAGIC observations is shown. The 1ES 0033+595 spectrum between 125 GeV and 500 GeV can also be described by a simple power law (χ^2/NDF=2.86/4):

$$\frac{\mathrm{d}N}{\mathrm{d}E} = N_0 \left(\frac{E}{250\ \mathrm{GeV}} \right)^{\Gamma}, \tag{7.1}$$

with a photon index of $\Gamma = -3.80 \pm 0.70$, and a normalization constant at 250 GeV of $N_0 = (2.01 \pm 0.45) \times 10^{-11} \mathrm{cm}^{-2}\mathrm{s}^{-1}\mathrm{TeV}^{-1}$.

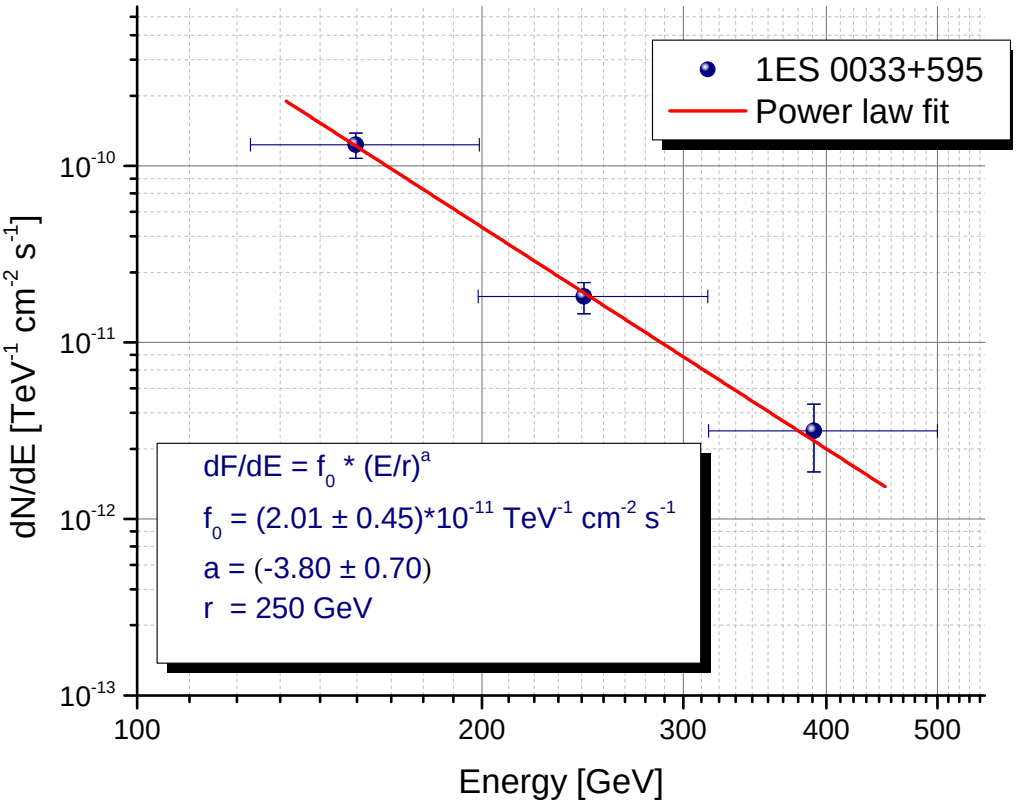

Figure 7.7: 1ES 0033+595 differential energy spectrum measured with MAGIC between 125 GeV and 500 GeV. The power law fit to the data is also shown (red line).

This is the first time that the differential energy spectrum of 1ES 0033+595 at VHE γ-ray range has been estimated. The energy threshold of the MAGIC stereo system allows furthermore to almost connect the spectrum to the *Fermi* LAT points [AAA+09b] as it will be shown in the following section.

7.3 1ES 0033+595 visible in other wavelengths

In this section the observations from the radio, optical, X-ray and the HE γ-ray range are presented. The data from the optical and HE γ-ray surveys was taken simultaneous with the MAGIC observations, whereas the radio, and X-ray data were used from the NED archive [1].

7.3.1 Radio observations

The archival radio data provided by NED are taken from the 91 m telescope in Green Bank from an observations carried out in 1987 as well as from the Texas Interferometer during a 1974 – 1983 survey in the range from 4.85 Hz and 365 Hz, respectively. The data is used, since no simultaneous observations were performed with MAGIC, only for completeness in the SED and not for the modeling itself.

7.3.2 Optical observations

The simultaneous optical observation for 1ES 0033+595 are conducted, like in case of 1ES 1959+650, with the Tuorla Observatory, using the 60 cm KVA telescope on La Palma and the 1 m telescope at Tuorla. For 1ES 0033+595 the regular optical observations in R-band started already in 2003.
As outlined in Figure 7.8, during a ten year KVA survey, the source shows only a marginal flux variability and also during the MAGIC observation window (bottom panel in Figure 7.8) no significant variability was found. In addition, comparing the optical R-band flux from 1ES 0033+595 with the one from 1ES 1959+650 (Figure 6.2), RGB 0136+3906 (Figure 8.2) and PKS 1717+177 (Figure 9.5) then again 1ES 0033+595 seems to be very faint ($F < 1$ mJy) also in this wavelength. During the MAGIC observation days the average optical flux was 0.21 mJy which corresponds to $R = 17.93$ mag. To derive the νF_ν in the optical band the contribution from near-by star 0.22 mJy is subtracted from the measured flux ([NPT+07]) in addition the brightness was corrected for galactic absorption by $R = 2.35$ mag ([SFD98]). The average νF_ν during the MAGIC observations corresponds to $8.47 \pm 0.5 \times 10^{-11}\,\mathrm{cm}^{-2}\mathrm{s}^{-1}$.

[1] http://ned.ipac.caltech.edu/

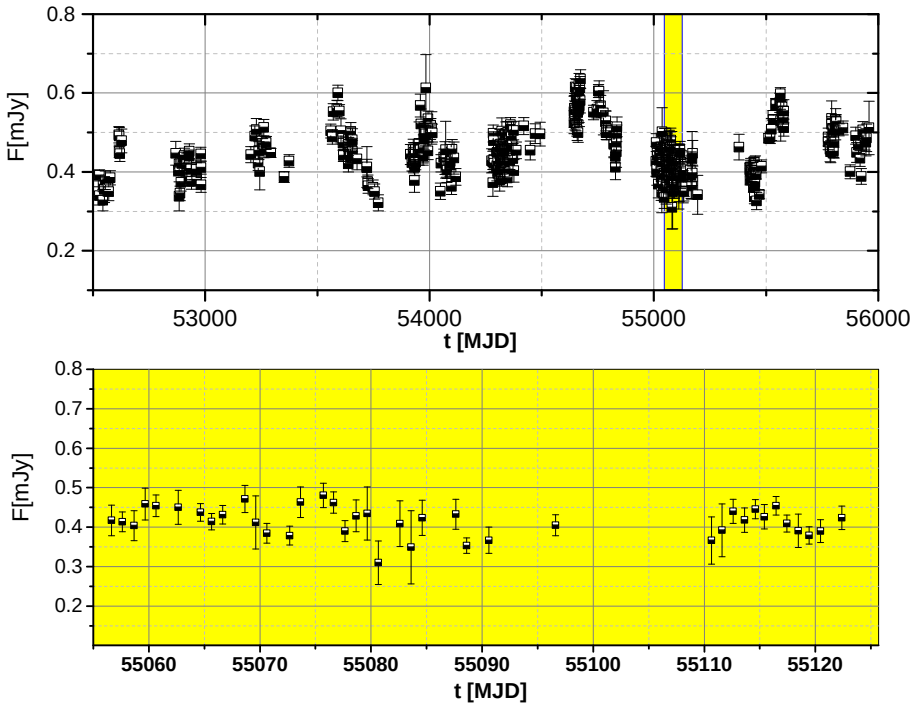

Figure 7.8: 1ES 0033+595 optical light curve between 2003 and 2013, from Tuorla/KVA telescopes. The contribution of the host galaxy (0.22 mJy) has not been subtracted. The MAGIC observation window in 2009 is indicated by the vertical lines in the top panel whereas the bottom panel present the enlarge version. The data was provided by [Lin12].

7.3.3 X-ray observations

As already mentioned above, unfortunately during the MAGIC observation window in 2009, there were no simultaneous X-ray data by *Swift* or INTEGRAL available. Thus, archival data provided by NED from the observation periods from 2004 to 2008 from both experiments is used as listed in Table 7.2.

Swift

The *Swift* satellite, launched in November 2004 ([GCG+04]), is equipped with three telescopes, **B**urst **A**lert **T**elescope (BAT) ([BBC+05]) which detects γ-rays in a range from 15 to 150 keV with a field of view of about 2 sr.
The further instruments are, the **X**-**R**ay **T**elescope (XRT) (300 eV – 10 keV) as well as the **U**ltra**V**iolet/**O**ptical **T**elescope (UVOT) (170 nm – 650 nm) with an arc-second positional accuracy ([BHN+05], [RKM+05]).

INTEGRAL

In comparison to *Swift* the INTEGRAL observatory ([WCD+03]) was launched by a Russian rocket-launcher PROTON on 17th October 2002 ([EDJ+03]). This observatory is equipped with four telescopes. In the present work data from the detector ISGRI of the telescope IBIS ([ULD+03]) in the energy range from 20 – 100 keV is used. This instrument provides the best combination of field of view, sensitivity and angular resolution for this study.

Table 7.2: Results of X-ray observations performed with *Swift* and INTEGRAL from 2004 to 2008.

Experiment	Flux [10^{-11}erg cm^{-2}s^{1}]	Frequency [10^{19}Hz]
Swift	1.96±0.34	2.53
Swift	2.50±0.40	1.99
INTEGRAL	0.30	1.69
INTEGRAL	1.03±0.15	1.45
INTEGRAL	1.89	1.45

7.3.4 HE γ-ray observations

For the contemporaneous IC curvature resolution a dedicated *Fermi* LAT analysis was performed by Sara Buson and Valentina Tronconi from the *Fermi* LAT collaboration. Normally *Fermi* LAT operates in all-sky survey mode, scanning the entire sky every 3 h, therefore it can provide observation of 1ES 0033+595 simultaneous with MAGIC. *Fermi* data was collected from August 17th, 2009 to October 14th, 2009. In addition, to make a comparison with the behavior of the source over a wider time interval, a dedicated analysis from the beginning of the *Fermi* LAT mission, that spans from August 4th, 2008 (beginning of scientific operation of LAT) to October 28th, 2011, was performed. The data analysis of 1ES 0033+595 is challenging because this source is located near the galactic plane, therefore the analysis was restricted to the 300 MeV – 300 GeV energy range. Following results were obtained for 1ES 0033+595 from a dedicated simultaneous *Fermi* LAT analysis: The flux is $(8.0 \pm 3.6) \times 10^{-9}$ cm^{-2} s^{-1} and the spectral index is -1.7 ± 0.2. In comparison, for the 38 month time interval, the flux is $(6.6 \pm 1.0) \times 10^{-9}$ cm^{-2} s^{-1} and the spectral index is -1.9 ± 0.1. For spectral analysis, in the first case the full energy range was divided in 4 energy bins: 2 bins for the 300 MeV – 10 GeV range and 2 bins for the 10 GeV – 300 GeV range. In the latter case the full energy range was divided in 6 equal energy bins. The achieved results from the *Fermi* LAT analysis are outlined

together with simultaneous MAGIC data in Figure 7.9.
Since this source is also in the HE γ-ray range very week, only a good overlapping between the MAGIC and *Fermi* LAT measurements can be achieved with a long-term survey (for the 38 month time interval) due to more available statistics, as presented with the black triangle in Figure 7.9.

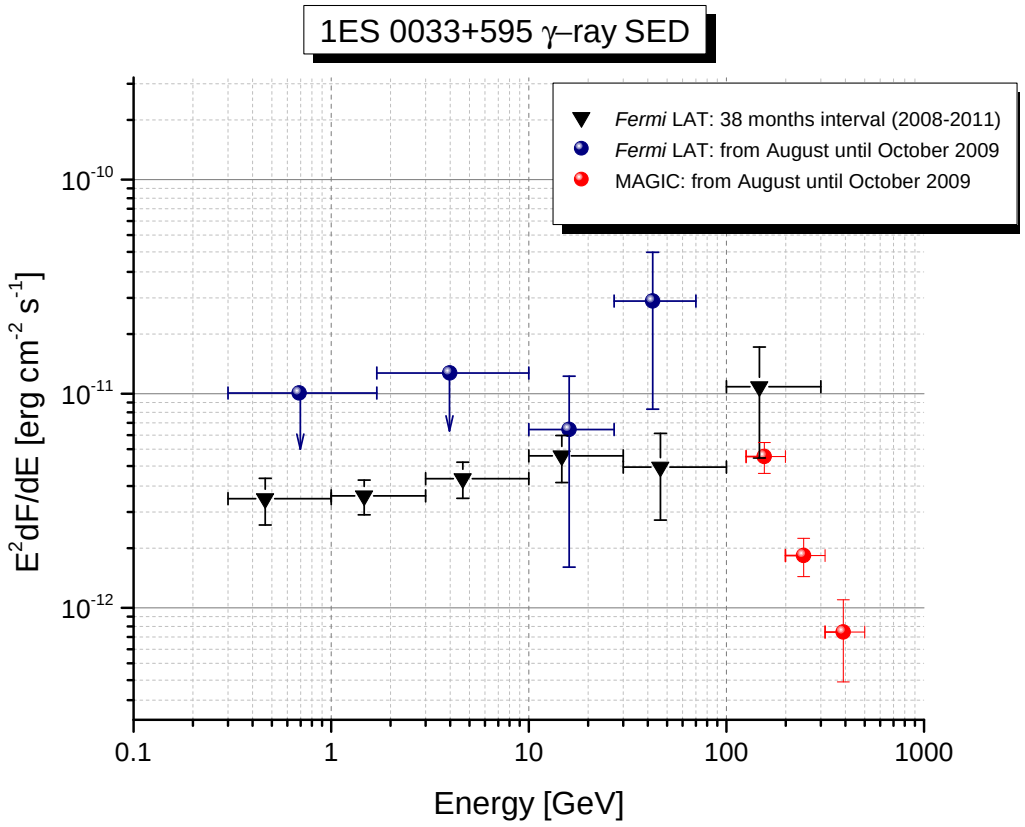

Figure 7.9: The first IC curvature from 1ES 0033+595 described with *Fermi* LAT and MAGIC data.

7.4 The inverse Compton peak of 1ES 0033+595

Like in the case of 1ES 1959+650 also here the determination of the IC peak value is obtained. For the logarithmic parabola fit only overlapping data points, as shown in Figure 7.10, from *Fermi* LAT and MAGIC are used. Since both measurements suffer from a lack of statistics the here presented results should be treated as a preliminary estimation. The logarithmic parabola was fitted to

the *Fermi* LAT and MAGIC data in the following vertex notation:

$$\nu F_\nu = \nu^{\mathrm{IC}}_{\mathrm{peak}} F_{\nu^{\mathrm{IC}}_{\mathrm{peak}}} \times 10^{b[\log(\nu/\nu^{\mathrm{IC}}_{\mathrm{peak}})]} \tag{7.2}$$

where $\nu^{\mathrm{IC}}_{\mathrm{peak}} F_{\nu^{\mathrm{IC}}_{\mathrm{peak}}}$ is the peak flux at the peak frequency $\nu^{\mathrm{IC}}_{\mathrm{peak}}$ and b the curvature parameter. From the logarithmic parabola fit following values could be estimated: b=-0.41±0.05, $\nu^{IC}_{\mathrm{peak}} F_{\nu^{IC}_{\mathrm{peak}}}$ =(7.98±0.34)×10^{-12} erg cm^{-2} s^{-1} and ν^{IC}_{peak}=(1.39±0.55)×10^{25} Hz. The ν^{IC}_{peak} corresponds to (57.48±22.74) GeV which is similar to the previous findings for the IC peak from 1ES 1959+650 (see Section 6.8).

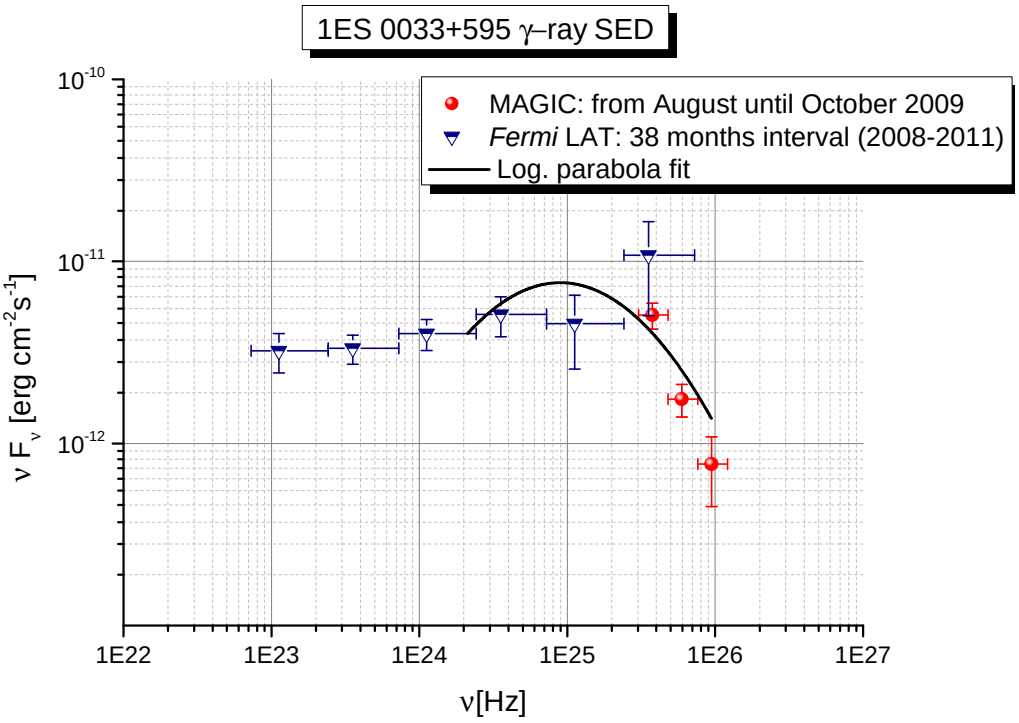

Figure 7.10: The IC peak estimation of 1ES 0033+595 described with a logarithmic parabola using *Fermi* LAT (blue triangle) and MAGIC data (red circles).

7.5 The redshift of 1ES 0033+595

As anticipated in Section 7.1, due to its featureless optical spectrum, as shown in Figure 7.11, high galactic absorption, and a foreground star with a separation of 1.58 arcsec, the estimation of a proper redshift of 1ES 0033+595 is

highly difficult. From the findings in Subsection 7.2.3 the VHE spectrum appears to be extremely soft (photon index $\Gamma \sim 4$), as it is expected by the absorption of VHE photons throughout interaction with the EBL (see Section 1.4) if the source is located at relatively large redshift [SdS92]. Such absorption process is characterized by a function of the energy of the photon and of the distance it has traveled. Thus, from empirical findings, spectra with indices $\Gamma \sim 4$ have been observed in blazars located at redshifts above 0.2, [AAA+12e].

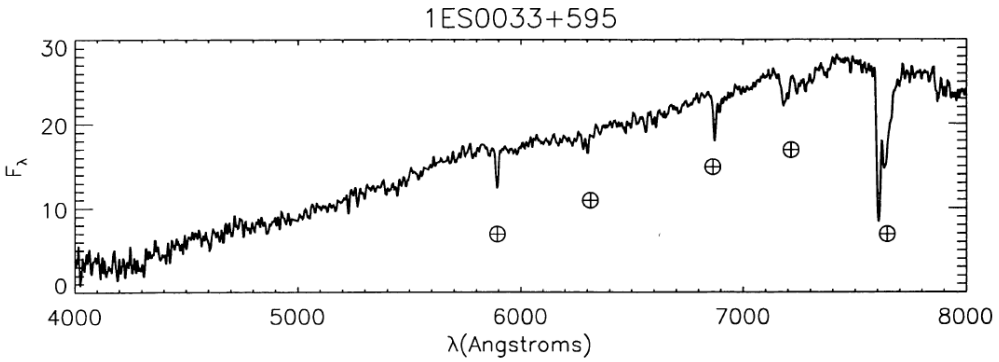

Figure 7.11: Spectroscopy measurements of 1ES 0033+595 showing a featureless spectrum with no emission lines [PSS+96].

One of the recent developed redshift determination methods is the empirical approach of [PBM+11]. The method assumes that the intrinsic spectrum at TeV energies (e.g., observed with MAGIC) cannot be harder than that in the GeV band (observed with *Fermi* LAT). The underlying assumption is, that the VHE spectrum corrected for the absorption of TeV photons by the EBL via photon-photon interaction should still be softer than the γ-ray spectrum observed by *Fermi* LAT, [PBM+11]. The spectrum shown in Figure 7.13 was corrected using the Franceschini EBL model [FRV08] (see Appendix C, Figure C.1) in the fine steps of redshift until the slope of the deabsorbed spectrum equals the one in the GeV-band. In this case a value of $z^* = 0.58 \pm 0.12$ is obtained which corresponds to an upper limit on the redshift. In addition, an estimate of the true distance can be achieved using the linear relation between z and the true redshift. This relation was the result of a systematic study carried out on blazars with known distances. The extracted redshift of 1ES 0033+595 using the inverse formula (for more details see [PBM+11]) results in $z_{\rm rec} = 0.34 \pm 0.05$. This finding confirms very well firstly the already predicted higher redshift above 0.2 throughout the photon index of $\Gamma \sim 4$ and secondly the estimation of a lower limit ($z > 0.24$) by [STF05]. Therefore in the following discussions the new redshift estimation of $z_{\rm rec} = 0.34 \pm 0.05$ is used.

7.6 Spectral Energy Distribution of 1ES 0033+595

As already pointed out in the previous sections, this is the first time that the reconstructed SED from radio to TeV energies of 1ES 0033+595 is presented, as displayed in Figure 7.12. The yellow data points present the archival radio data (NED), the green points are the optical data from the KVA observations and archival data (NED), the blue and the purple points represent the archival X-ray data by *Swift* and INTEGRAL (NED) and the orange and the red data points are the *Fermi* LAT and MAGIC points obtained during this work. From the reconstructed SED as for 1ES 1959+650 again the typical two peaks structure becomes evident. In order to model this particular SED a SSC model is used as described in the next subsection.

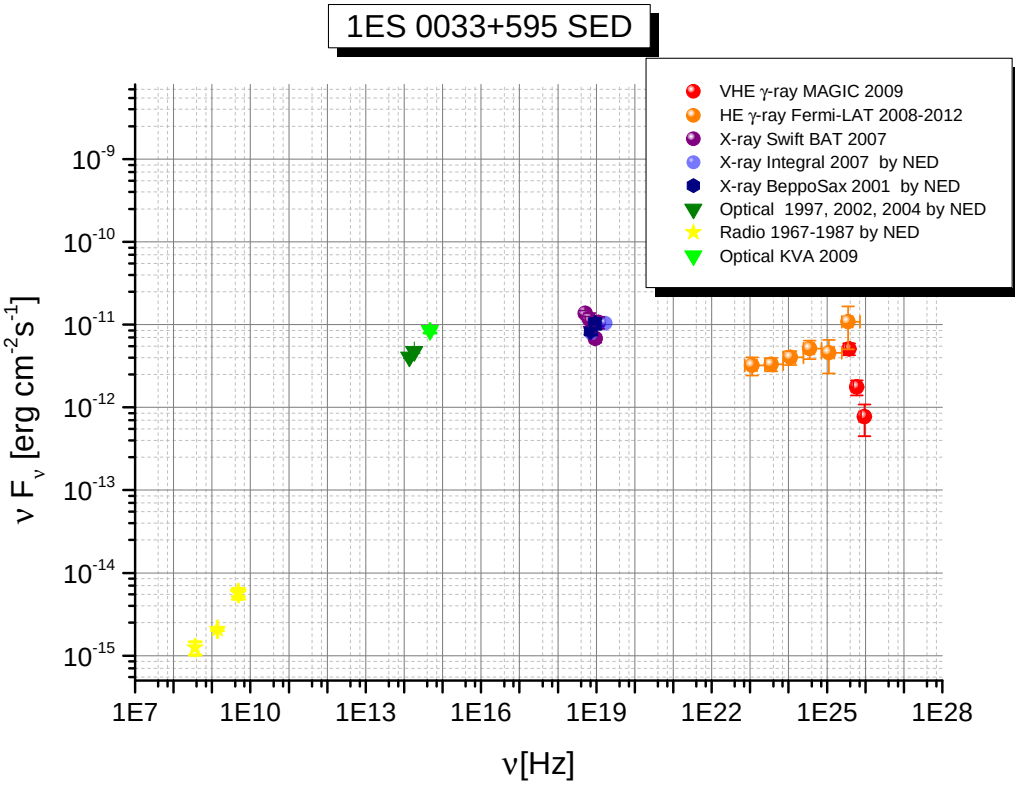

Figure 7.12: Reconstructed SED for 1ES 0033+595 from radio to TeV range.The yellow data points present the archival radio data (NED), the green points are the optical data from the KVA observations and archival data (NED), the blue and the purple points represent the archival X-ray data by *Swift* and INTEGRAL (NED) and the orange and the red data points are the *Fermi* LAT and MAGIC points obtained during this work.

7.7 Modeling of the SED of 1ES 0033+595

As anticipated above, the emission characteristics of BL Lac objects are generally well reproduced by the one-zone leptonic model, in which a population of relativistic electrons inside a region moving down the jet emit through synchrotron and synchrotron self-Compton mechanisms, [TMG98]. The spectral energy distribution of 1ES 0033+595 was modeled with such one-zone leptonic model using the χ^2-minimization method by N. Mankuzhiyil fully described in [MAP+12]. The emission region was assumed to be spherical, with radius R, filled with a tangled magnetic field of intensity B and relativistic electrons, emitting synchrotron and synchrotron self-Compton radiation. The energy distribution of the electrons follows a smoothed broken power law with normalization K between the Lorentz factors $\gamma_{\rm min}$ and $\gamma_{\rm max}$, with slopes n_1 and n_2 below and above the break at $\gamma_{\rm break}$. The relativistic boosting is represented by the Doppler factor δ. In Figure 7.13, where MAGIC data was corrected for the extragalactic absorption using the model of Franceschini [FRV08] (see Appendix C, Figure C.1), the modeled SED with an assumed redshift of $z = 0.34$ for 1ES 0033+595 is presented. The obtained values of the model parameters are summarized in Table 7.3. A comparison with other HBL type objects (i.e. [TGG+10], [AAA+12b], [AAA+12e]) shows that the model parameters used here for the SED fitting are compatible with those obtained for other HBL class objects.

Table 7.3: Model parameters used for fitting the SED in Figure 7.13.

z	$\gamma_{\rm min}$	$\gamma_{\rm break}$	$\gamma_{\rm max}$	n_1	n_2	B [G]	K [cm^{-3}]	R [cm]	δ
0.34	1000	3.7×10^4	2.9×10^6	2.0	3.2	0.2	3.7×10^2	65×10^{15}	36

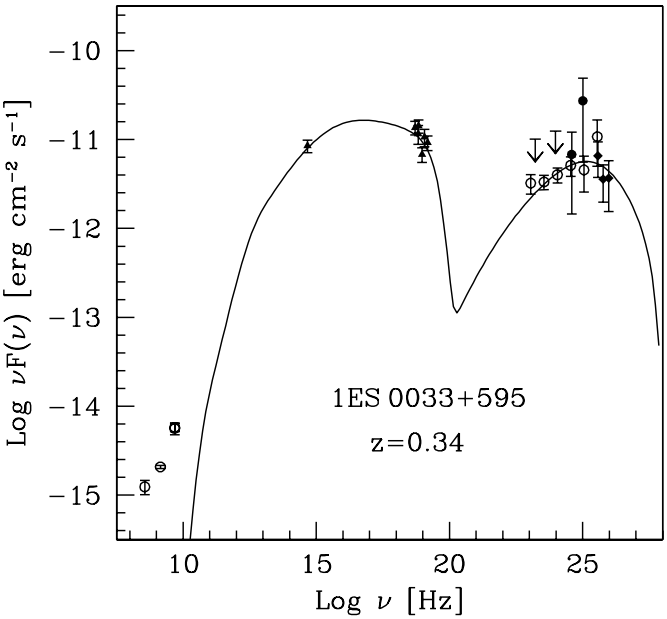

Figure 7.13: The SED from low to high energies with assumed redshift $z = 0.34$ simultaneous KVA data where the contribution of nearby star has been subtracted and the flux has been corrected for galactic extinction (filled triangle), INTEGRAL, *Swift* BAT archival data from 2004-2008 (filled triangle), simultaneous *Fermi* LAT data (filled circle) and MAGIC data corrected for the extragalactic absorption using the model of [FRV08] (filled diamond). The 3 year *Fermi* LAT data (open circle) and archival radio data from the Green Bank and Texas observatory (open circle) is also shown.

7.8 Summary and Conclusions

In this work the first detection of VHE γ-ray emission from 1ES 0033+595 has been reported.

- From the 2009 MAGIC data the source is clearly detected at 5.5 σ significance level.
- Its discovery was announced on October 27$^{\text{th}}$ in an ATEL [Mar11].
- The spectrum can be well described with a power law fit with a photon index of (3.80±0.70).
- The integral flux above 150 GeV is estimated to be (2.20±0.40)% of the Crab Nebula flux. No significant variability was found in the recorded MAGIC data.

- In connection with the *Fermi* LAT results and MAGIC data the first preliminary estimation of the IC peak could be obtained, yielding: $\nu^{\mathrm{IC}}_{\mathrm{1ES\,0033+595peak}}$=(57.48±22.74) GeV
- The comparison of the herein presented multiwavelength data confirms the typical HBL blazar subclass behavior of this source: it shows marginal variability in the optical R-band, is variable in X-rays, followed by a hard spectrum in the *Fermi* LAT regime and its discovery in the VHE γ-ray range.
- Moreover, the MAGIC detection of 1ES 0033+595 in the VHE γ-ray range confirms the prediction as promising VHE γ-ray emitter by the [CG02] list predicted already more than a decade ago.
- Since the redshift of this source is unknown, but crucial for a accurate SED modeling, a new estimation ($z = 0.34 \pm 0.05$) with the empirical approach by [PBM+11] was performed.
- This result is in a good agreement with the lower limit of $z > 0.24$ reported in [STF05] as well as with the empirical findings where higher redshift sources above 0.2 are characterized throughout the photon index of $\Gamma \sim 4$.
- Finally, a comparison with other HBL type objects as presented in e.g. [TGG+10], [AAA+12b], [AAA+12d] shows that the model parameters used here for the SED fitting are compatible with those obtained for other HBL class objects and thus confirming again the classification of this source being a HBL type object.

The following chapter presents another analysis and the corresponding results of a blazar known as B3 0133+388 which was also discovered during this work.

CHAPTER 8

DISCOVERY OF THE BLAZAR B3 0133+388 (RGB 0136+3905)

The BL Lac object B3 0133+388 is an unknown distance blazar which was observed by the MAGIC telescopes for the first time in November 2009. The analysis of this data lead to the first discovery at 5.6 σ significance level in the VHE γ-range of this source. In this chapter, the discovery of the VHE γ-ray emission is presented, showing new properties of this blazar in the VHE γ-ray range. The MAGIC telescopes observed B3 0133+388 between November 7$^{\text{th}}$ until November 26$^{\text{th}}$ for nearly 20 h in stereo mode. The integral flux above 150 GeV is estimated to be (3.6±0.9)% of the Crab Nebula flux and the VHE spectrum has a photon index of (3.82±0.70). In addition, the source did not show any variability during the MAGIC observations. Since the redshift of this source is unknown, an empirical approach by [PBM+11] was used in order to determine a new redshift of ($z = 0.46 \pm 0.05$). Finally, for the first time, based on the new redshift, the SED of B3 0133+388 has been reconstructed and modeled using a single zone SSC model.

8.1 The Blazar B3 0133+388 and its properties

The unknown distance blazar B3 0133+388 also known as RGB J0136+3905, located at RA: 01:36:32.59 and DEC.: 39:05:59.18 was discovered for the first time in 1977 during a radio observation and listed in the third Bologna sky survey of 408 MHz radio objects ([FGT85]). It was later detected also in various other energy bands i.e. in the X-rays with ROSAT ([BSF+97]), and identified spectroscopically as a BL Lac object, with an IBL sub-classification by [LKC+98] and [LKF+99], respectively. In contrast [NTV06] classified this source as HBL object with a synchrotron emission peaking at $10^{16.59}$ Hz, as shown in Figure 8.1. Thus, today the sub-classification of this source is still under debate.

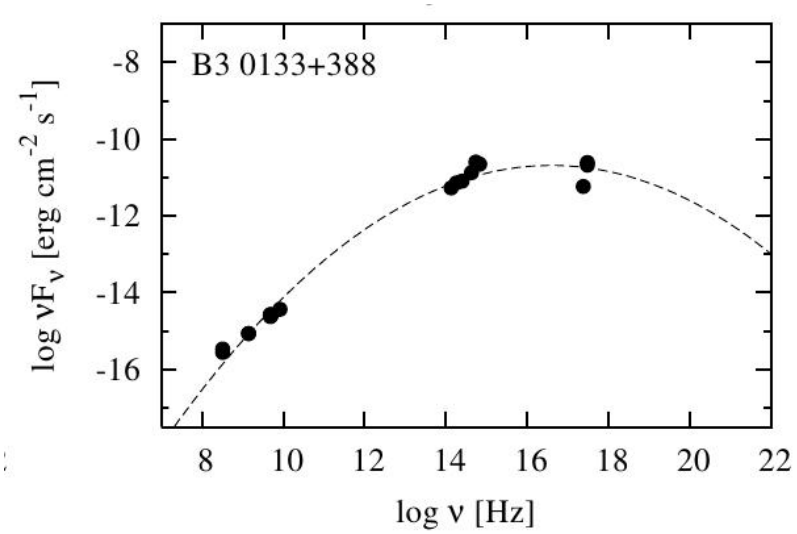

Figure 8.1: The synchrotron peak of B3 0133+388. The figures is taken from [NTV06].

From optical observation performed at the beginning of the 21st century with the NOT only a point source could be revealed (see Figure 8.2.) In 2009 this source was detected by the *Fermi* LAT observatory during its first three months of survey and listed since then in the Bright Active Galactic Nuclei Source List [AAA$^+$09a]. Moreover, based on the radio, optical, and X-ray spectral properties, this blazar was proposed by [CG02] to be a promising VHE γ-ray emitter under the assumption that the redshift was less than 0.2.

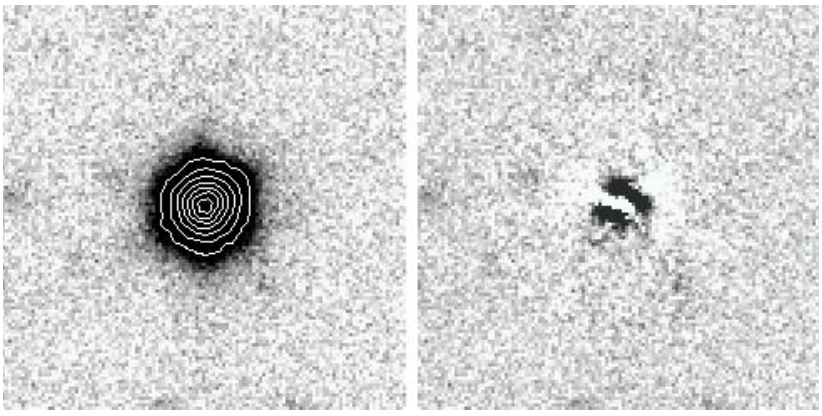

Figure 8.2: Optical image of B3 0133+388 observed with the NOT. The host galaxy has been removed. The figure is adapted from [Nil13].

8.2 First MAGIC observations of B3 0133+388

As discussed above, B3 0133+388 has been detected in several other wavelengths, except in the VHE γ-ray range until July 2012 where its discovery was announced on the 5th International Symposium on High-Energy Gamma-Ray Astronomy (*GAMMA 2012*) [MM12]. Up to date, the potential scientific impact of increasing the number of VHE γ-ray blazars is still crucial. With a good sampled fraction of well-measured VHE γ-ray blazars, population study, as shown in Chapter 10, becomes more and more possible. From such study constrains on the EBL (see Section 1.4 and Subsection 10.3.4) and its evolution, as well as the nature of the cosmic rays can be derived. Motivated by these aspects and because B3 0133+388 was one of the most promising VHE γ-ray blazars where its extrapolation of the *Fermi* LAT flux agrees within the sensitivity of the MAGIC stereoscopic system, as displayed in Figure 8.3, this source was observed for the first time by MAGIC in November 2009.

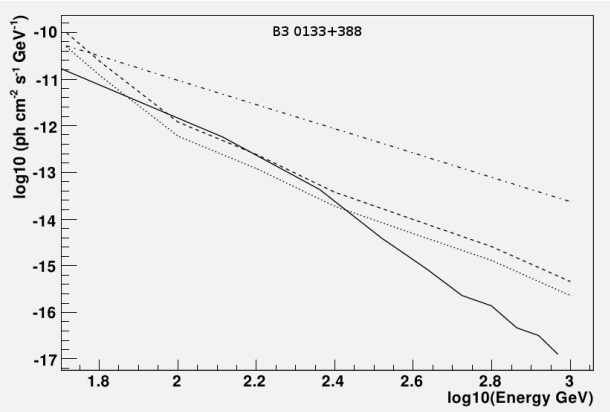

Figure 8.3: Flux extrapolation for B3 0133+388 (black solid line). The top dotted dashed line represents the Crab Nebula spectrum. The dashed line is the M I sensitivity by considering it as two times less the sensitivity of the MAGIC stereo system. The dotted line represents the MAGIC stereo sensitivity. The figure is adapted from [Man09].

The stereoscopic observations with MAGIC and the improved performance of the telescopes has been resulted in the discovery of this source in the VHE γ-ray range. The B3 0133+388 survey was carried out from November 6$^{\text{th}}$ until November 26$^{\text{th}}$ for a total of 20 h of observations. Out of this sample, as presented in detail in Appendix D, Table E.1, only 6.5 h of good quality data after quality selections (see previous Subsection 6.3.1) remain, as outlined in Table 8.1.

Table 8.1: B3 0133+388 discovery data set. From left to right: dates in dd / mm / yy, effective time of observation in hours, zenith angle distribution, rate of the event after the image cleaning in Hz and the significance of each observation night.

Date	Eff. time[h]	Zenith [°]	Mean Rate [Hz]	Significance [σ]
10 / 11 / 2009	1.31	13-29	80	2.56
11 / 11 / 2009	0.58	22-31	82	1.24
15 / 11 / 2009	1.40	13-31	82	3.46
16 / 11 / 2009	0.13	12-14	76	1.88
19 / 11 / 2009	0.39	17-31	83	1.56
20 / 11 / 2009	0.30	15-27	89	1.82
21 / 11 / 2009	0.83	14-34	77	0.57
24 / 11 / 2009	1.57	10-34	70	2.21

The zenith angle distribution that was conducted for this observations has a range from 10° to 35°. Furthermore, all data was taken in wobble mode, as for the previously presented observations of 1ES 1959+650 in Chapter 6 and 1ES 0033+595 in Chapter 7. Also in this case the data analysis of B3 0133+388 is performed using the standard software package MARS [AAA+08b, AAA+09c], as described in Chapter 4, including the latest standard routines for stereoscopic analysis [AAA+11d, Lom11]. The whole stereo data analysis procedure was similar to that one described in Section 6.4, Section 6.5 for 1ES 1959+650 and for 1ES 0033+595 in Section 7.2, respectively.

8.2.1 Signal search and the discovery of B3 0133+388

Due to improved sensitivity of the MAGIC stereoscopic system mostly in the low energy range also this improvement led to a discovery of a new VHE γ-ray blazar. Similar to 1ES 0133+595 the strongest signal of B3 0133+388 was only found in the low energy range between (50 – 250) GeV by applying the low energy standard cuts:

```
Odie.cuts: MHadronness.fHadronness < 0.28
           && MHillas_1.fSize > 55
           && MHillas_2.fSize > 55
           && MStereoParDisp.fEnergy >50
Odie.signalCut: 0.026
Odie.psf40: 0.10
Odie.nWobbleOff: 1
```

In the full range above 250 GeV the source seems to be almost non-significant. Only in the range from (50 – 250) GeV a detection signal above $5\,\sigma$ is given. Figure 8.4 shows the θ^2-plot where an excess of 279.0 events, corresponding to a significance of $5.6\,\sigma$ is found. The significance was calculated according to the Equation 17 by Li and Ma [LM83] (for a detailed θ^2-plot description see also Subsection 4.1.6).

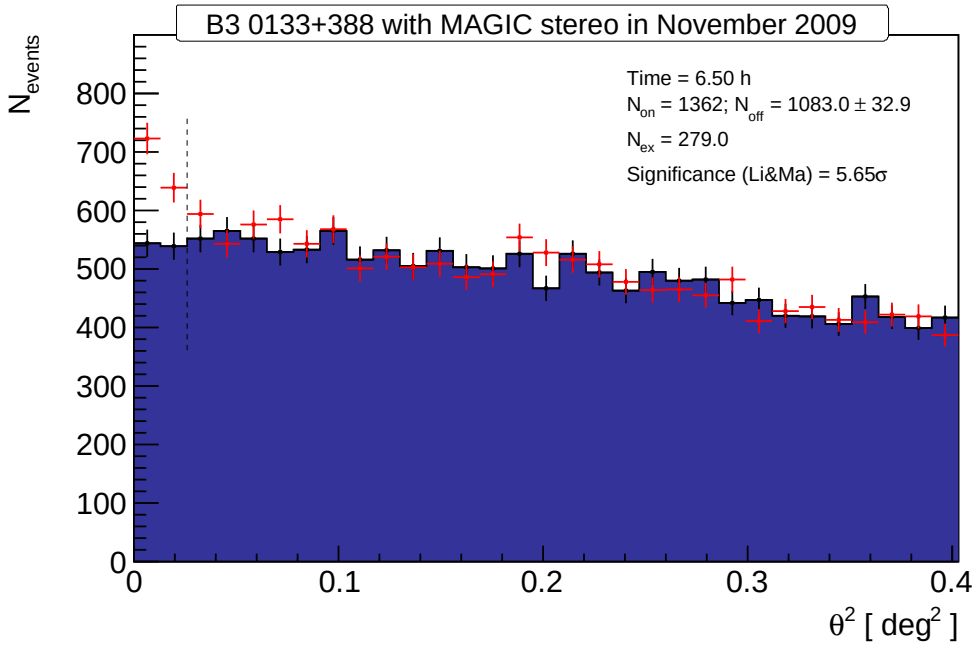

Figure 8.4: θ^2 distribution of the B3 0133+388 signal and background estimation from 6.5 h of MAGIC stereo observations taken in November 2009.
The signal of B3 0133+388 is restricted only to the low energy range.

The corresponding significance skymap in the low energy range (50 – 250) GeV of the signal from B3 0133+388 is displayed in Figure 8.5. A hot spot at $\sim 8\,\sigma$ significance level is consistent to the B3 0133+388 sky position. Like the other here presented blazars this source has also a point-like appearance in the low energy range. For more details about the sky-mapping procedure adopted in the MAGIC stereo analysis chain see i.e. [Lom11].

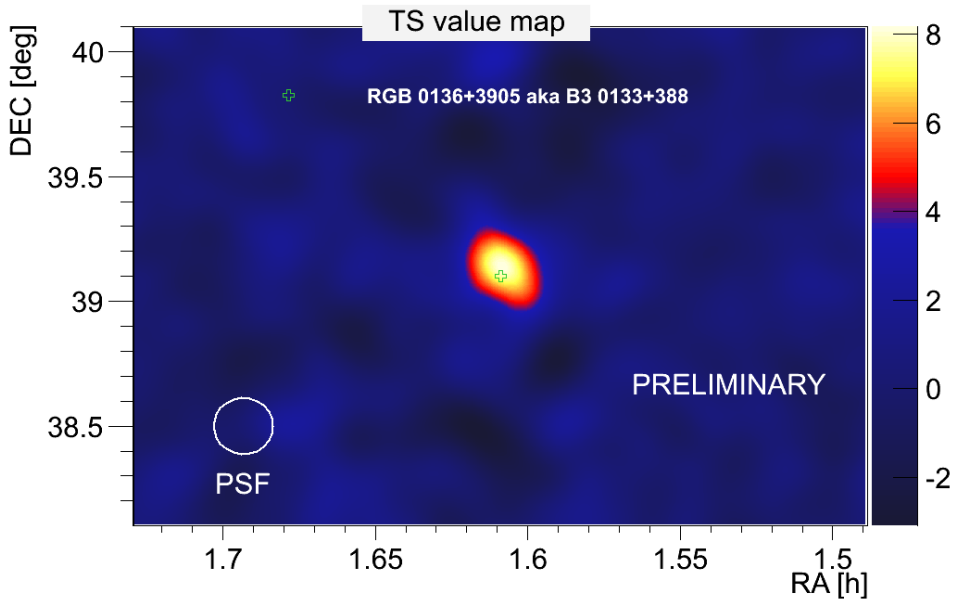

Figure 8.5: Significance skymap of the sky region around B3 0133+388 from MAGIC stereo observations taken in November 2009. The nominal position of this source is marked with the empty cross.

8.2.2 Temporal behavior of B3 0133+388

In this subsection the temporal evolution during the MAGIC observation from November 10$^{\text{th}}$ until November 24$^{\text{th}}$, 2009 of B3 0133+388 is studied. Thus, the integral flux emission during the two observation weeks is determined. The temporal bins are selected according to the significance of the signal, where a 3-days binning is set. The here obtained light curves, as outlined in Figure 8.6 above 100 GeV and above 150 GeV (for further comparisons) are compatible with a steady emission of flux:
$F_{>100\,\text{GeV}} = (3.09 \pm 0.63) \times 10^{-11}\text{cm}^{-2}\,\text{s}^{-1}$ with χ^2/NDF=0.17/2 corresponding to a probability P(χ^2)=0.9 and
$F_{>150\,\text{GeV}} = (1.18 \pm 0.30) \times 10^{-11}\text{cm}^{-2}\,\text{s}^{-1}$ with χ^2/NDF=2.47/2 corresponding to a probability P(χ^2)=0.3, respectively. To sum up, the integral flux above 100 GeV is estimated to be (5.7±1.1)% of the Crab Nebula flux whereas the integral flux above 150 GeV is measured to be (3.65±0.95)% of the Crab Nebula flux for B3 0133+388 in the VHE γ-ray range. In addition, no evidence of variability can be derived from these measurements.

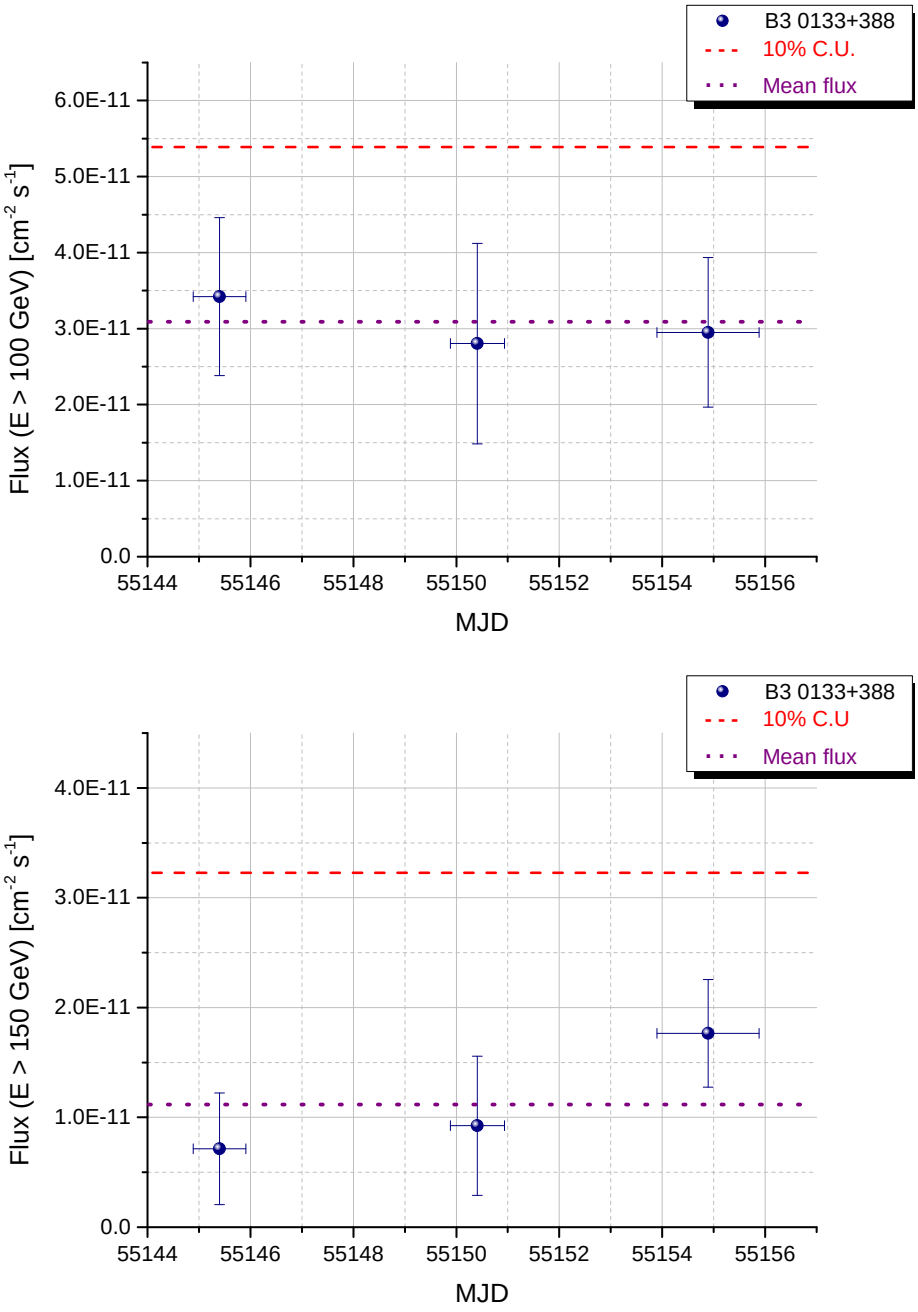

Figure 8.6: B3 0133+3885 light curves between November 10th to November 24th above an energy threshold of 100 GeV and 150 GeV, respectively, and with a 3-day time-scale binning. No hints of variability are seen in the data. The dashed purple horizontal line represents the constant function resulting from the fit to the data.

8.2.3 Differential energy spectrum of B3 0133+388

In this subsection, the first VHE γ-ray differential energy spectrum of the blazar B3 0133+388 is presented. For the differential energy spectrum calculation, as shown in Figure 8.7, 30 bins between 10 GeV to 50 TeV are set. The cuts for the calculation of the spectrum are selected according to the corresponding efficiency on the MC simulation data, as described in previous sections e.g. Subsection 6.4.3. For the θ^2 cut and for the `Hadronness` cut values of 75% are chosen, respectively. For the spectrum of B3 0133+388 a significant signal between $(2-3)\sigma$ significance is found in only three energy bins in the energy range between 80 GeV to 325 GeV. In addition, the first bin in Figure 8.7, with the bin center at 50 GeV is not taken into account due to the energy threshold of 100 GeV for this analysis.

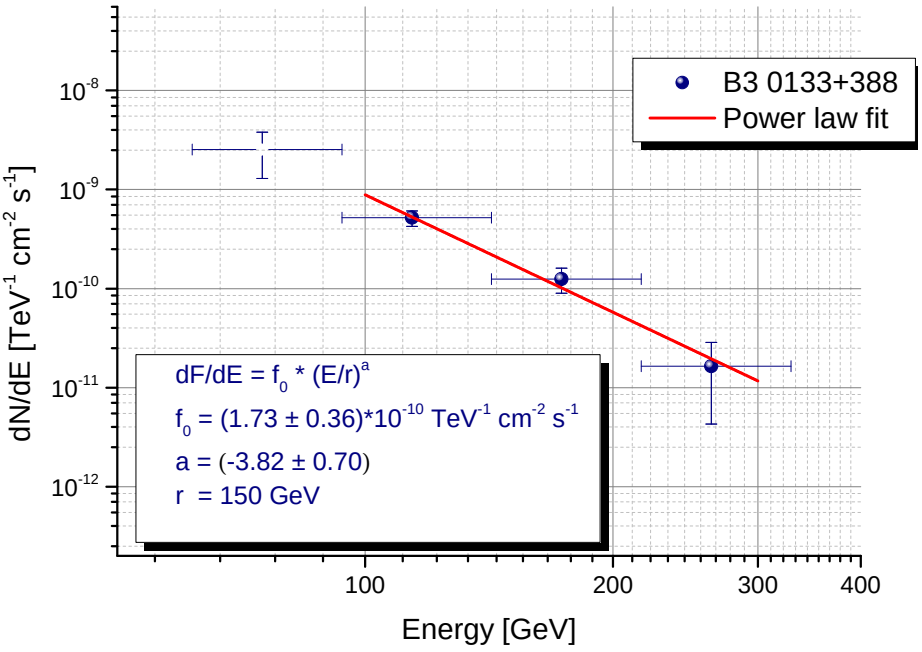

Figure 8.7: The differential energy spectrum of B3 0133+388 fitted by a power law between (100 – 300) GeV. The power law fit to the data is also shown (red line).

As for 1ES 0033+595 the spectrum of B3 0133+388 has been fitted by a simple power law between 100 GeV and 300 GeV of the form:

$$\frac{\mathrm{d}N}{\mathrm{d}E} = N_0 \left(\frac{E}{150\,\mathrm{GeV}} \right)^{\Gamma}, \tag{8.1}$$

in units of cm^{-2} s^{-1} TeV^{-1}, with a photon index of $\Gamma = -3.82 \pm 0.70$, and a normalization constant at 150 GeV of $N_0 = (1.73 \pm 0.36) \times 10^{-10} cm^{-2} s^{-1} TeV^{-1}$ and with χ^2/NDF=0.52/2, corresponding to a probability of $P(\chi^2) = 0.77$. This result also confirms, as already noticed during the signal search analysis, that the VHE γ-ray emission is concentrated mostly at low energies below 300 GeV.

8.2.4 Other γ-ray experiment observations: VERITAS

During the last five years the VERITAS collaboration observed B3 0133+388 together with five other promising VHE γ-ray blazars between September 2009 and June 2010 (MJD 55122 – 55383) [AAA+12f]. The motivation by the VERITAS collaboration to observe this source in the VHE γ-ray regime was nearly similar to MAGIC's derived from nearly the same assumption for this object which are: A bright and hard spectrum in the *Fermi* LAT results and a power-law fit extrapolation suggesting integral flux levels between (1 – 12)% of the Crab Nebula flux above 150 GeV after accounting for the absorption by the EBL [AAA+12f]. Out of this observations of B3 0133+388 performed from October 18th, 2009 till October 25th, 2009 during a 9.9 h exposure, the VERITAS collaboration could only derived flux upper limits (1.7% C.U. above 165 GeV) for this source. Moreover, they suggested, that the non-detection of this blazar can be explained due to a spectral steeping of the high-energy spectrum that can be explained firstly by intrinsic curvature, secondly by redshift-dependent EBL absorption and finally by uncorrelated variability. In Figure 8.8 the SSC modeling of the SED of B3 0133+388 during simultaneous observations in different wavelengths and three different redshift values assumptions ($z = 0.2, 0.3$ and 0.4) is shown. In fact, the hard LAT spectrum and low VERITAS upper limit determined for this blazar suggest a steeping of the γ-ray spectrum at $E \geq 100$ GeV which can be explained by the EBL absorption effect if a redshift of $z \geq 0.4$ is assumed. In addition, out of the low state observations with VERITAS a redshift-independent explanation of the evident spectral softening could by made by [AAA+12f] suggesting that only the SED model at $z = 0.4$ is compatible with the VERITAS upper limit which coincidently is in a good agreement with balanced radiation and particle energy. All in all, the here presented findings by the VERITAS observations confirm very good the here found results for the spectral properties, the integral flux estimations and the redshift constrains (see Section 8.5) for this very distant blazar, during this work.

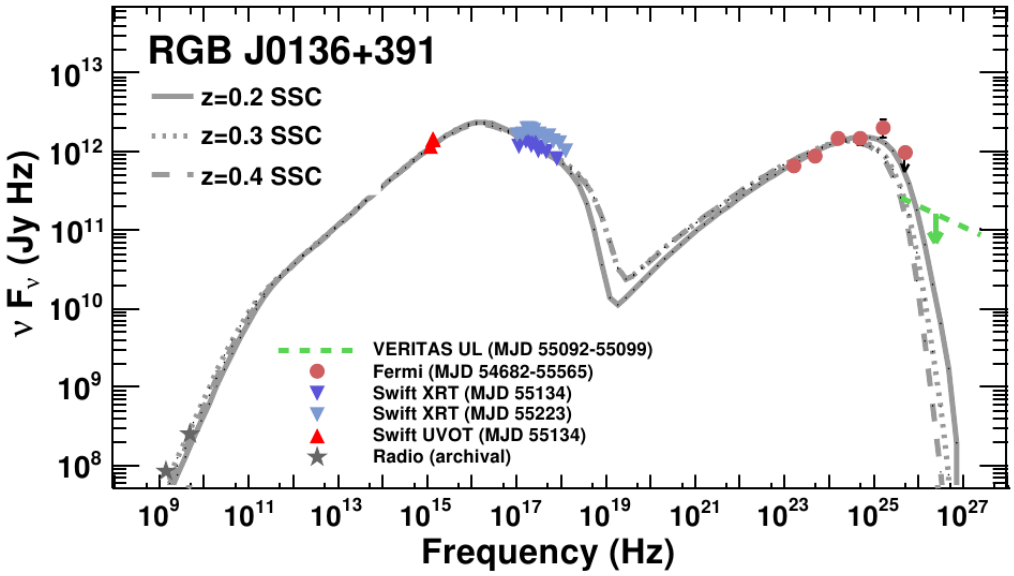

Figure 8.8: SED from VERITAS observations in 2009 yielding only flux upper limits from B3 0133+388. The figure is adapted from [AAA+12f].

8.3 B3 0133+388 visible in other wavelengths

In this section the observations from the radio, optical, X-ray, and the HE γ-ray range are presented. Part of the data from the UV, optical, X-ray and HE γ-ray surveys were taken simultaneously or semi-simultaneously with the MAGIC observations, whereas the radio, and some of the X-ray data is used from the NED archive [1].

8.3.1 Radio observations

The archival radio data provided by NED are taken from VLA (1.4 GHz) observations recorded in 2001 and the **V**ery **L**ong **B**aseline **I**nterferometry (VLBI) (2.3 GHz and 8.4 Hz) carried out in 2007. These data are used, since they are not simultaneous with the MAGIC observation, only for the completeness in the SED and not for the modeling itself (see Figure 8.14.). The corresponding values of the archival radio is listed in Table 8.2.

[1] http://ned.ipac.caltech.edu/

Table 8.2: B3 0133+388 results of radio observations performed by VLA and VLBI from 2001 to 2007.

Experiment	Flux [10^{-15}erg cm^{-2}s^{1}]	Frequency [10^{9}Hz]
VLBI-8.4 Hz (2007)	2.27	8.40
VLBI-2.3 Hz (2007)	1.15	2.30
VLA-1.4 Hz (2001)	8.23	1.40

8.3.2 Optical observations

The simultaneous optical observation for B3 0133+388 are conducted, like in case of 1ES 1959+650 and 1ES 0033+595, by the Tuorla Observatory, using the 60 cm KVA telescope on La Palma and the 1 m telescope at Tuorla. For this source the regular optical observations in R-band started already in 2003. As outlined in Figure 8.9, during a ten year KVA survey, the source shows only significant variability in the middle of 2005. In the following years the optical R-band flux shows marginal variability and also during the MAGIC observations in 2009. Furthermore, for completeness archival data from 2MASS observations recorded at the end of 1999 in various bands (J, H K_s) are listed in Table 8.3, as well as semi-simultaneous *Swift*-UVOT observations performed in October 30th, 2009.

Table 8.3: B3 0133+388 results of UV and optical observations performed by *Swift*-UVOT, KVA, and 2MASS observations, 1999-2009.

Experiment	Flux [10^{-11}erg cm^{-2}s^{1}]	Frequency [10^{15}Hz]
Swift-UVOT (2009)	1.160±0.150	1.14
Swift-UVOT (2009)	1.440±0.300	1.34
KVA (2009)	0.154±0.050	0.468
2MASS (1999)	0.750±0.021	0.240
2MASS (1999)	0.700±0.020	0.182
2MASS (1999)	0.560±0.010	0.138

8.3.3 X-ray observations

As already mentioned above, unfortunately during the MAGIC observation window in 2009, there were no simultaneous X-ray data by *Swift*-XRT available. Thus semi-simultaneous data from the observation period in October 30th, 2009 and January 27th, 2010 are used. Moreover, some archival X-ray

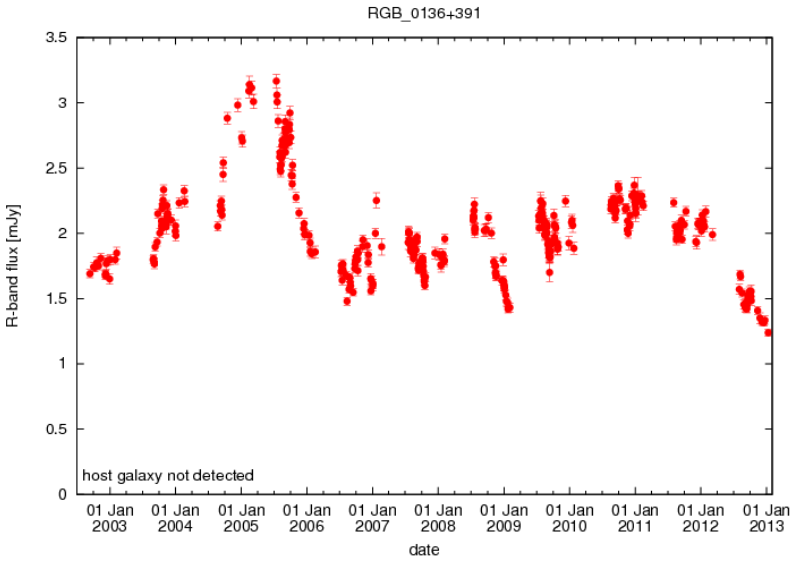

Figure 8.9: B3 0133+388 optical light curve between 2003 and 2013, from Tuorla/KVA telescopes. The figure is taken from [Nil12].

data conducted by *Beppo*SAX and ROSAT from the observation periods from 2001 to 2004 could be found in the NED archive, as listed in Table 8.4.

Table 8.4: B3 0133+388 results of X-ray observations performed by *Beppo*SAX, ROSAT and *Swift*-XRT from 2001 to 2010.

Experiment	Flux [10^{-11} erg cm^{-2} s^{1}]	Frequency [10^{17} Hz]
*Beppo*SAX (2001)	1.4	0.145
ROSAT (2003)	2.33	3.020
ROSAT (2004)	9.59	3.020
Swift-XRT (2009)	1.21±1.00	0.145
Swift-XRT (2010)	2.14±1.00	0.145

8.3.4 HE γ-ray observations

In order to achieve a contemporaneous IC curvature resolution a dedicated *Fermi* LAT analysis was performed by Carlo Romoli from the *Fermi* LAT collaboration (for a detailed description of the *Fermi* LAT satellite see [AAA^{+}10f]). Normally *Fermi* LAT operates in all-sky survey mode, scanning the entire sky every 3 h, therefore it can provide observation for different sources simulta-

neous with MAGIC. Due to a very low and constant flux of this source in the HE γ-ray regime (see Figure 8.10) the *Fermi* LAT analysis has to be enlarged before and after the simultaneous MAGIC observations in order to achieve sufficient statistics to derive a HE γ-ray spectrum. In addition, to find a better overlapping with MAGIC, the analysis has been done in a subinterval of 45 days centered in the period of the MAGIC observations.

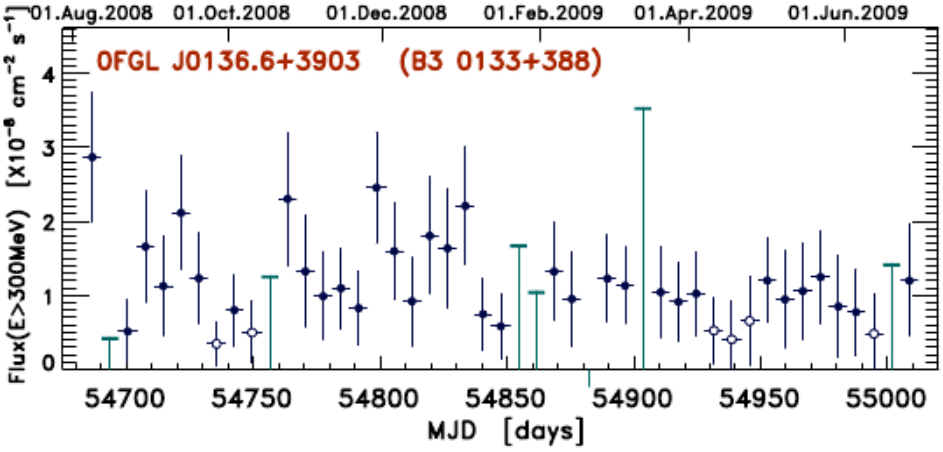

Figure 8.10: HE γ-ray light curve of B3 0133+388 with constant emission in the first eleven months of *Fermi* LAT observations. The figure is taken from [AAA+10b].

The *Fermi* LAT data was collected from October 26th, 2009 to December 12th, 2009. Furthermore, to make a comparison with the behavior of the source over a wider time interval, a dedicated analysis from the beginning of the *Fermi* mission, that is August 4th, 2008, to October 28th, 2010, was taken from the 2FGL catalog. Following results were obtained for B3 0133+388 from a dedicated *Fermi* LAT analysis: for the semi-simultaneous analysis, the flux is $(6.4 \pm 1.7) \times 10^{-13}$ ph cm^{-2} s^{-1} MeV^{-1} and the spectral index is -1.61 ± 0.17. For the 24 month time interval (2FGL catalog), the flux is $(7.25 \pm 0.41) \times 10^{-13}$ ph cm^{-2} s^{-1} MeV^{-1} and the spectral index is -1.69 ± 0.04. The obtained results from the *Fermi* LAT analysis are outlined together with simultaneous MAGIC data in Figure 8.11. Since this source shows also a low signal in the HE γ-ray range, only a good agreement between the MAGIC and *Fermi* LAT measurements can be achieved with the data from the 2FGL catalog (more available statistics), as presented with the blue triangle in Figure 8.11.

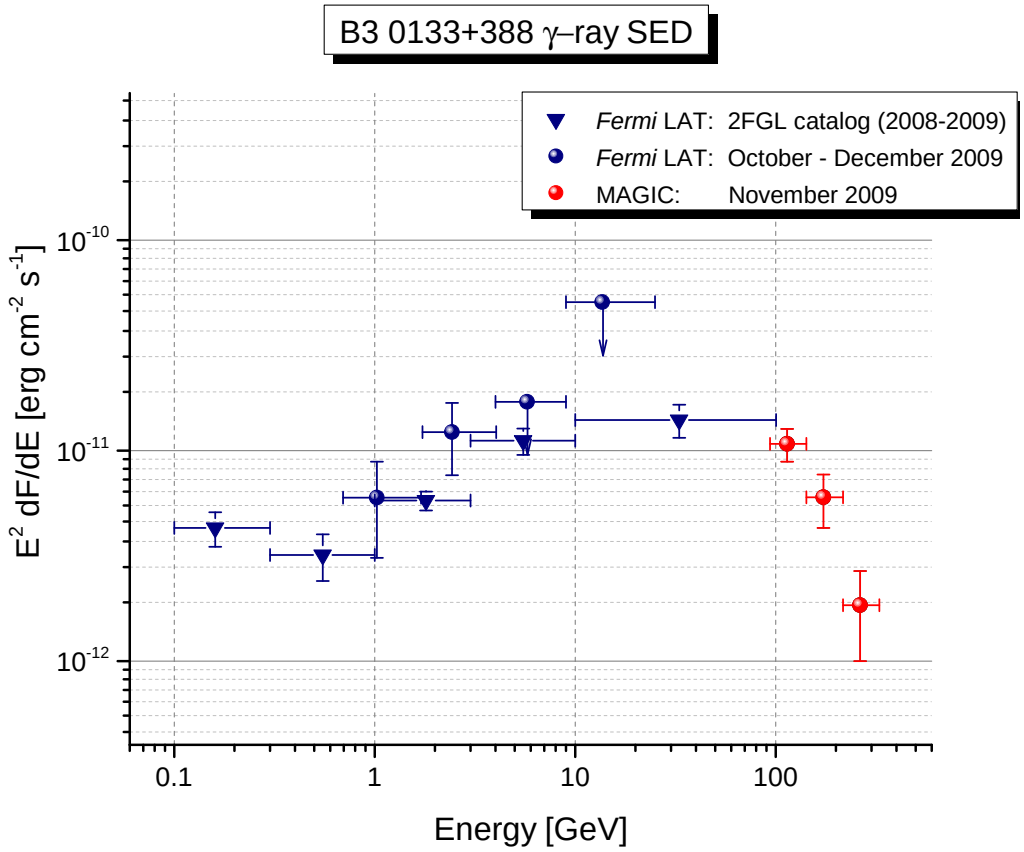

Figure 8.11: The first inverse Compton curvature from B3 0133+388 described with *Fermi* LAT and MAGIC data.

8.4 The inverse Compton peak of B3 0133+388

Also for this new detected source the IC peak has been studied. For the logarithmic parabola fit only overlapping data points, as shown in Figure 8.12, from *Fermi* LAT (2FGL catalog) and MAGIC are used. Since both measurements suffer like in case of 1ES 0033+595, from a lack of statistics the here presented results should be treated as a preliminary estimation. The logarithmic parabola was fitted to the *Fermi* LAT and MAGIC data in following vertex notation:

$$\nu F_\nu = \nu^{\mathrm{IC}}_{\mathrm{peak}} F_{\nu^{\mathrm{IC}}_{\mathrm{peak}}} \times 10^{b[\log(\nu/\nu^{\mathrm{IC}}_{\mathrm{peak}})]} \tag{8.2}$$

where $\nu^{\mathrm{IC}}_{\mathrm{peak}} F_{\nu^{\mathrm{IC}}_{\mathrm{peak}}}$ is the peak flux at the peak frequency $\nu^{\mathrm{IC}}_{\mathrm{peak}}$ and b the curvature parameter. From the logarithmic parabola fit following values could be estimated: b=-0.21±0.06, $\nu^{\mathrm{IC}}_{\mathrm{peak}} F_{\nu^{\mathrm{IC}}_{\mathrm{peak}}}$=(1.80±0.24)×10^{-11} erg cm^{-2} s^{-1} and

ν^{IC}_{peak}=(4.9 ± 0.35) × 10^{24} Hz. The ν^{IC}_{peak} corresponds to (20.26±1.44) GeV which is compatible with the previous obtained IC peaks values of 1ES 1959+650 (see Section 6.8) or 1ES 0033+595 (see Section 7.4).

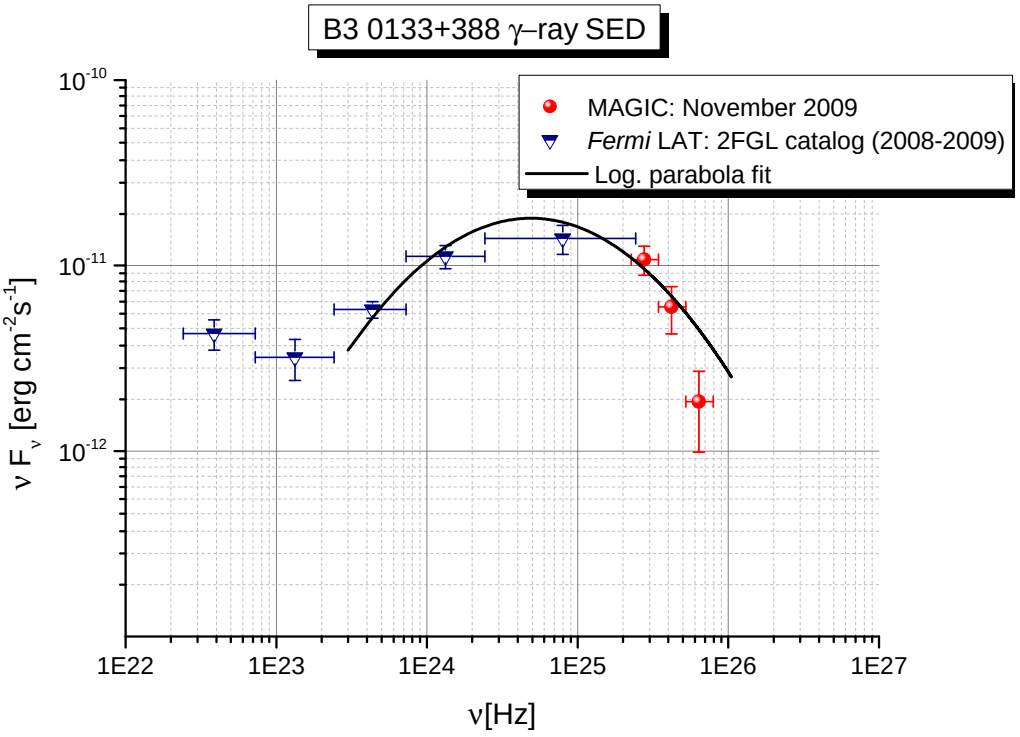

Figure 8.12: The IC peak of B3 0133+388 described with a logarithmic parabola using *Fermi* LAT (blue triangle) and MAGIC data (red circles).

8.5 The redshift of B3 0133+388

As pointed out at the beginning of this chapter, B3 0133+388 has like the previous presented blazar, 1ES 0033+595 (see Chapter 7), an unknown redshift. In the past 10 years several attempts were done in order to derive the redshift of this source. Already the authors [LKC+98] who identified B3 0133+388 first as a BL Lac object saw a featureless optical spectrum, followed by [WXDH00], [BCTB00], [CMA+02] and [PPG+07] which failed to detect any spectral features. In addition, also recent spectroscopic redshift measurements using the Keck Low Resolution Imaging Spectrometer on September 17th (MJD 55091), 2009 [AAA+12f] reveal again a featureless power law spectrum, as shown in Figure 8.13 [AAA+12f]. On December 7th, 2008 B3 0133+388 was observed also

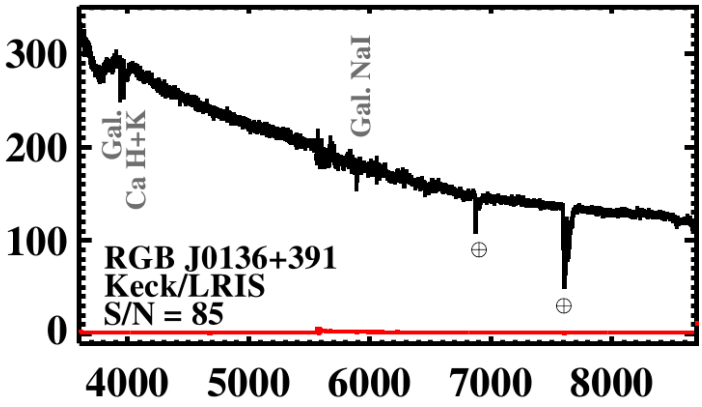

Figure 8.13: Spectroscopy measurements of B3 0133+388 showing a featureless spectrum with no emission lines [AAA+12f].

by the NOT throughout an I-band filter with almost uniform transmission between 725 nm and 825 nm during an epoch when the optical nucleus was in an low state [NPV+12]. This deep survey found the surface brightness profiles of this source to be consistent with a point source and determined a lower limit for the host galaxy brightness by applying simulations of $z > 0.40$, for this object [NPV+12]. As shown in Subsection 8.2.3, the VHE γ-ray spectrum of B3 0133+388 as in the case of 1ES 0033+595 appears again to be extremely soft (photon index $\Gamma \sim 4$). Such feature is expected, as already anticipated in Section 7.5, by the absorption of VHE photons throughout interaction with the EBL if the source is located at relatively large redshift $z > 0.2$, [SdS92]. This result gives again a hint that this source must be located much further than $z > 0.2$ as already predicted by the VERITAS collaboration [AAA+12f]. In order to drive constrains from the HE and VHE γ-ray results toward a new redshift estimation again the empirical method of [PBM+11] is used (for a detailed explanation of this method see Section 7.5 and [PBM+11]). The spectrum shown in Figure 8.15 was corrected using the Franceschini EBL model [FRV08] (see Appendix D, Figure D.1 and Figure D.2) in the fine steps of redshift until the slope of the deabsorbed spectrum equals the one in the GeV-band. In this case a value of $z^* = 0.78 \pm 0.20$ is obtained which corresponds to an upper limit on the redshift for this source. The extracted redshift of B3 0133+388 using the inverse formula (for more details see [PBM+11]) results in $z_{\rm rec} = 0.46 \pm 0.05$. This finding confirms perfectly well the already predicted higher redshift above 0.2 throughout the photon index of $\Gamma \sim 4$ and the VERITAS collaboration as well as the estimation of a lower limit ($z > 0.40$) by [NPV+12]. Therefore in the following discussions the new redshift estimation of $z_{\rm rec} = 0.46 \pm 0.05$ is used for this object.

8.6 Spectral Energy Distribution of B3 0133+388

As already mentioned at the beginning of this chapter, this is the first time that the reconstructed SED from radio to TeV energies of B3 0133+388 is presented. Figure 8.14 displays the reconstructed SED for this source containing archival, semi-simultaneous and contemporaneous B3 0133+388 measurements.

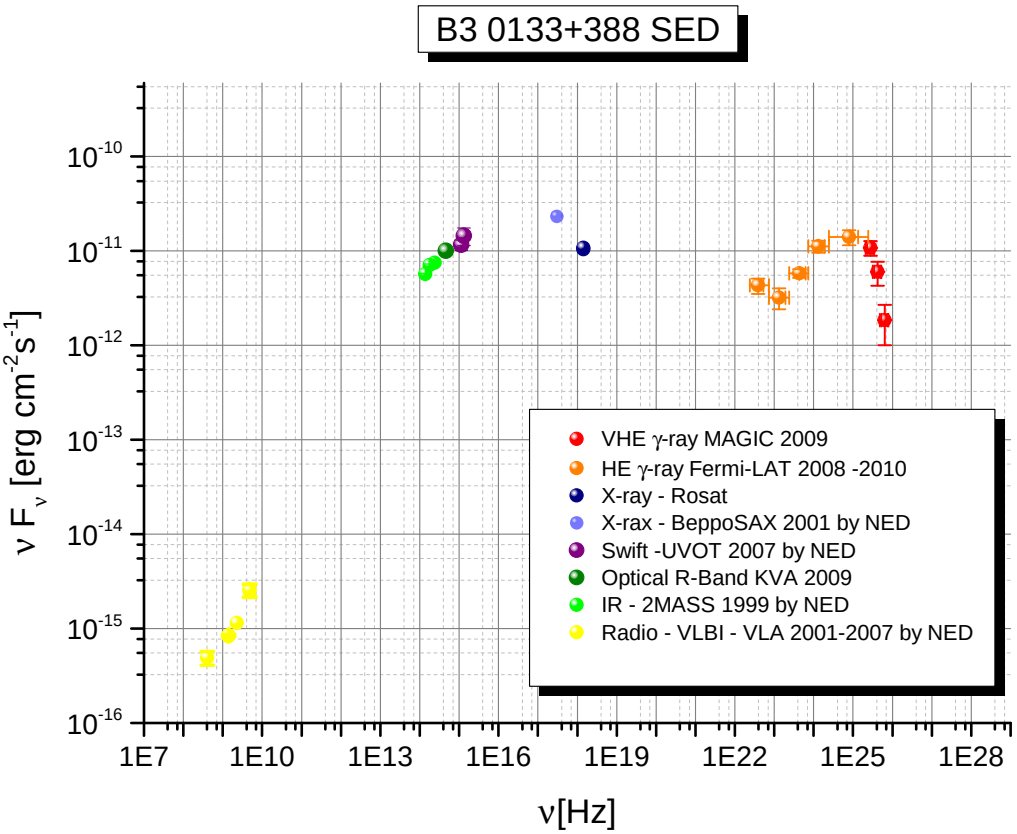

Figure 8.14: Reconstructed SED for B3 0133+388 from radio to TeV range.The yellow data points present the archival radio data (NED), the green points are the optical data from the KVA observations and archival data (NED), the blue and the purple points represent the archival X-ray data by *Swift*-XRT and the archival *Beppo*SAX, ROSAT (NED) and the orange and the red data points are the *Fermi* LAT and MAGIC points obtained during this work.

The yellow data points present the archival radio data, as described in Subsection 8.3.1; the green points are the optical data from the KVA observations and the *Swift*-UVOT surveys as well as archival data from 2MASS (Subsection 8.3.2); blue and purple points represent the semi-simulations X-ray data

by *Swift*-XRT and the archival *Beppo*SAX, ROSAT measurements, that are described in Subsection 8.3.3 and the orange and the red data points are the *Fermi* LAT and MAGIC points obtained during this work. Also in this case, the reconstructed SED of B3 0133+388 shows a typical two peaks structure. In order to model this particular SED a siple SSC model, as described in the next subsection, is used.

8.7 Modeling of the SED of B3 0133+388

The SED of B3 0133+388 was again modeled with the a one-zone leptonic SSC model by N. Mankuzhiyil using the χ^2-minimization method fully described in [MAP+12]. This modeling is applied to the most contemporaneous measurements as shown in Figure 8.14. The emission region was assumed to be spherical, with radius R, filled with a tangled magnetic field of intensity B and relativistic electrons, emitting synchrotron and synchrotron self-Compton radiation. The energy distribution of the electrons follows a smoothed broken power law with normalization K between the Lorentz factors $\gamma_{\rm min}$ and $\gamma_{\rm max}$, with slopes n_1 and n_2 below and above the break at $\gamma_{\rm break}$. The relativistic boosting is represented by the Doppler factor δ. In figure 8.15, where MAGIC data was corrected for the extragalactic absorption using the model of [FRV08], the modeled SED for B3 0133+388 is presented. The obtained values of the model parameters for the redshift $z = 0.46$, are summarized in Table 8.5. Again a comparison with other HBL type objects i.e. [TGG+10, AAA+12b, AAA+12e] shows that the model parameters used here for the SED fitting are compatible with those obtained for other HBL class sources, thus supporting the classification of B3 0133+388 as a HBL object.

Table 8.5: Model parameters used for fitting the SED in Figure 8.15.

z	$\gamma_{\rm min}$	$\gamma_{\rm break}$	$\gamma_{\rm max}$	n_1	n_2	B [G]	K [cm^{-3}]	R [cm]	δ
0.46	1000	5.5×10^4	4.1×10^6	2.0	4.2	0.11	5.2×10^2	36×10^{15}	29

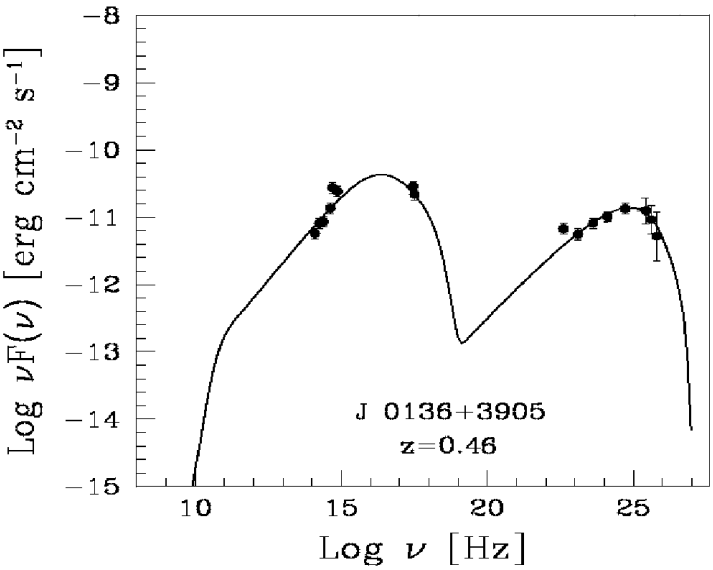

Figure 8.15: The SED of B3 0133+388 using for the first time HE and VHE γ-ray data for the SSC modeling.

8.8 Summary and Conclusions

In this work the second discovery of a new detected blazar B3 0133+388 was reported. Following summarized findings regarding B3 0133+388 could be obtained during this work:

- From the first MAGIC observations performed in 2009 for this source a clearly signal at 5.6 σ significance level was found.
- Its discovery was announced on the 5 th International Symposium on High-Energy Gamma-Ray Astronomy (*GAMMA 2012*) [MM12].
- The spectrum can be well described with a power law fit with a photon index of (3.82±0.70) and the differential flux rapidly decreases with energy (no excess above 300 GeV).
- The integral flux above 100 GeV is estimated to be (5.7±1.1)% of the Crab Nebula flux.
- For the energy range above 150 GeV the results yields (3.65±0.95)% of the Crab Nebula where in both cases no variability was found in the recorded MAGIC data.

- The comparison with previous VERITAS observations of B3 0133+388, where a flux upper limit was derived for this object:
  VERITAS: $F_{E>165\,\mathrm{GeV}} = 4.9\times10^{-12}$ ph cm^{-2} s^{-1}, 1.7% C.U. [AAA$^+$12f]),
  shows a compatible result between both experiments:
  VERITAS: $F_{E>165\,\mathrm{GeV}} = 8.3\pm0.3\times10^{-12}$ ph cm^{-2} s^{-1}, 2.8±1.1% C.U.).
  It has to be stressed, that since blazars are strongly variable sources only simultaneous observations can provide the best matching results.

- In connection with the *Fermi* LAT and MAGIC results the first preliminary estimation of the IC peak could be obtained,
  yielding: $\nu^{\mathrm{IC}}_{\mathrm{B3\,0133+388peak}}$=(20.26±1.44) GeV, which is in good agreement with previous findings for other BL Lac objects of the HBL subclass.

- Moreover, the MAGIC detection of B3 0133+388 in the VHE γ-ray range shows that the extrapolation method of *Fermi* LAT flux states is a hugely useful tool in order to find other VHE extragalactic γ-ray emitters.

- In addition, also the prediction of B3 0133+388 as promising VHE γ-ray emitter by the [CG02] list, more than a decade ago, could be confirmed in this study.

- Since the redshift of this source is unknown, but crucial for a accurate SED modeling, a new estimation ($z = 0.46\pm0.05$) with the empirical approach by [PBM$^+$11] was performed.

- This result is in a very good agreement with the lower limit of $z > 0.4$ presented in [NPV$^+$12], with the prediction of the VERITAS collaboration ($z > 0.4$) and with the empirical findings where higher redshift sources above 0.2 are characterized throughout the photon index of $\Gamma \sim 4$.

- In summary, a comparison with other HBL type objects i.e. [TGG$^+$10, AAA$^+$12b, AAA$^+$12e] shows that the model parameters used here for the SED fitting are compatible with those obtained for other HBL class objects, thus supporting the classification of B3 0133+388 as a HBL source.

The last analysis chapter presents the detection of a LBL object that is known as PKS 1717+177 (OT +129), which was detected in this work in the archival data of MAGIC stand-alone observations performed in 2009.

CHAPTER 9

THE CASE OF PKS 1717+177

PKS 1717+177 (OT +129) is a low-frequency-peaked BL Lac that is still undetected in the VHE γ-ray range. In this last analysis chapter the first analysis results of PKS 1717+177 observation obtained with the MI telescope in 2009 are reported, giving a strong hint of signal for a potential new discovery. MAGIC observed this source for the first time between April 19th to August 28th in 2009 for about 35 hours, where part of the data was taken in the soft stereo trigger mode. Out of the stand-alone MI analysis a signal at 6 σ level is reported. The integral flux above 200 GeV is estimated to be ~4% of the Crab Nebula flux and the VHE spectrum has a photon index of (2.65±0.39). It is important to emphasize, that this source did not show any variability during the MAGIC observations although this source was simultaneously detected to be in its historical strongest optical state. In consequence of these findings, also in this case no VHE γ-ray correlation with the optical band could be found giving again the indication that different emission regions are responsible for the VHE γ-ray and optical radiation. Finally, also in this context a simple SSC model was used for the PKS 1717+177 SED modeling, confirming previous assumption that a one zone SSC model is not a satisfactory model for this particular source.

9.1 The Blazar PKS 1717+177 and its properties

PKS 1717+177 also known as OT +129 is a blazar located at RA:17:19:13.05 DEC.:17:45:06.43 with a known redshift of $z = 0.137$. This source belongs to the subclass of BL Lacs objects called LBL [VV93] with synchrotron emission peaking near 10^{13} Hz ($\log\nu_{peak} = 13.08$, [NTV06]), as displayed in Figure 9.1. Today, this kind of objects with an extremely low value of the peak frequency of the synchrotron component (the maximum of the first SED peak is found in the IR-optical range) are poorly known and only few of them (i.e. BL Lacertae

or S5 0716+714) has been detected in the VHE γ-ray range.

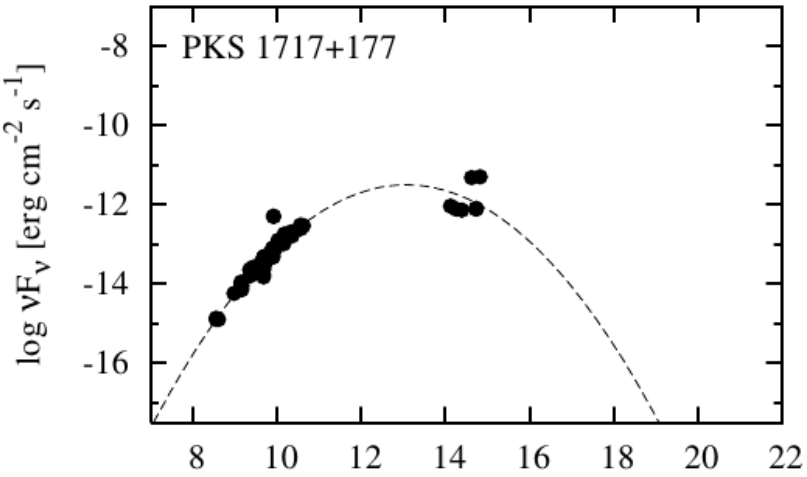

Figure 9.1: PKS 1717+177 synchrotron emission peak near 10^{13} Hz. The figure is taken from [NTV06].

From the chronological point of view this source was already detected in the radio ([FDK69]) and optical ([HMA+74]) wavelength in the 20th century. In the optical band it has been identified by [HMA+74] as a star-like or slightly diffuse object with 18.5 mag. Also the NOT shows, as depicted in Figure 9.2, only a star-like appearance of PKS 1717+177.

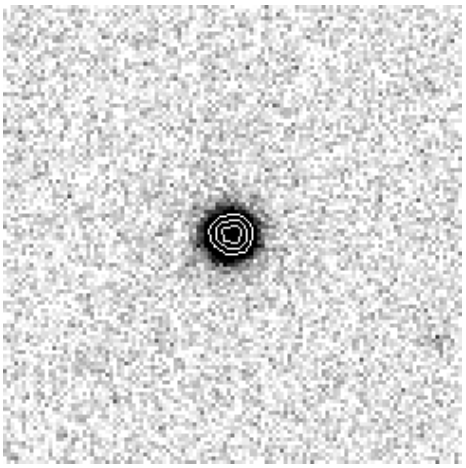

Figure 9.2: Optical image of PKS 1717+177 observed with the NOT where a star-like object is visible. The figure is taken from [Nil13].

Like most BL Lac type objects this source also shows strong optical polarization and has a spectrum which shows no emission lines between 5000 Å and 9000 Å [SRM+05], as displayed in Figure 9.3. Furthermore, due to absence of apparent spectral lines in the spectroscopic measurements of PKS 1717+177 only one value is quoted for this source in the literature with $z = 0.137$ reported by [SRM+05].

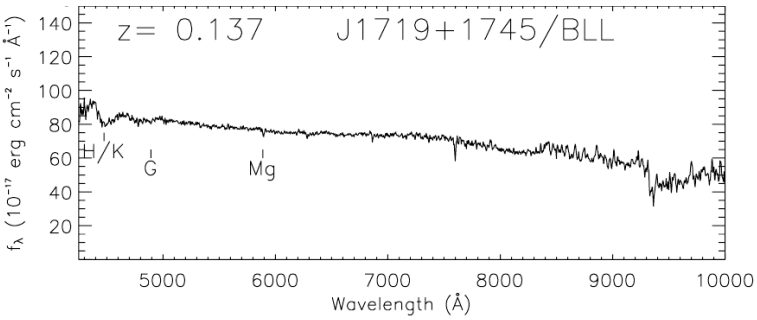

Figure 9.3: Spectroscopy measurements of PKS 1717+177 showing a featureless spectrum with no emission lines [SRM+05].

Further multiwavelength features of this particular LBL object are its marginal variability in the radio core and a flat spectrum in the radio band [PMW+85]. In the X-rays this source was already discovered in 1989 by the Einstein Observatory, [WW90], wheres in the HE γ-ray range it was detected for the first time by the *Fermi* LAT during the first three months of its observations [AAA+09a]. Only at the end of September 2008, PKS 1717+177 shows one short and bright flare, as shown in Figure 9.4, that was interestingly never measured again in the following observation years, [AAA+10b].

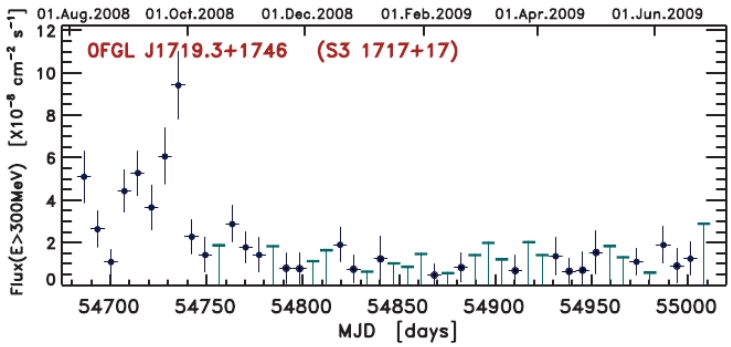

Figure 9.4: *Fermi* LAT light curve of PKS 1717+177 during its major activity in September 2008. The figure is taken from [AAA+10b].

The HE γ-ray spectrum of PKS 1717+177 is consistent with a flat power law with $\Gamma = 1.84 \pm 0.07$ and a Flux of $F(> 100\,\mathrm{MeV}) = (6.9 \pm 0.9) \times 10^{-8}\mathrm{cm}^{-2}\mathrm{s}^{-1}$ [AAA+09a]. These properties being a bright and hard *Fermi* LAT blazar made PKS 1717+177 one of the most promising candidate among low frequency peak objects being a TeV emitter.

9.2 MAGIC observations of PKS 1717+177

As already pointed out above, due to its spectral properties in the HE γ-ray range and showing great promise to be detected in the VHE γ-ray regime out of *Fermi* LAT flux extrapolation results, as explained in [TGG+10], this source was also selected to be observed with MAGIC. The first survey of this blazar with MAGIC started with a total observation time of 35 h from April 19$^{\mathrm{th}}$ to August 24$^{\mathrm{th}}$ in 2009. Like in the case of 1ES 1959+650 (see Chapter 6) this source was also observed in two different observation conditions firstly with only one telescope M I from April 19$^{\mathrm{th}}$ to August 10$^{\mathrm{th}}$ 2009 and secondly in the soft stereo trigger mode with both telescopes from August 11$^{\mathrm{th}}$ to August 24$^{\mathrm{th}}$ in 2009. In order to avoid any splitting in the data sample and because the observations in stereoscopic mode took only few hours (~2 h of good quality data in the commissioning phase) the whole analysis is obtained in stand-alone mode of M I. An interesting event of this source that accompanied the whole observation period with MAGIC was the historical strongest optical outburst observed from June to August 2009, as outlined in Figure 9.5 and where the source was also observed with MAGIC in this period as ToO object.

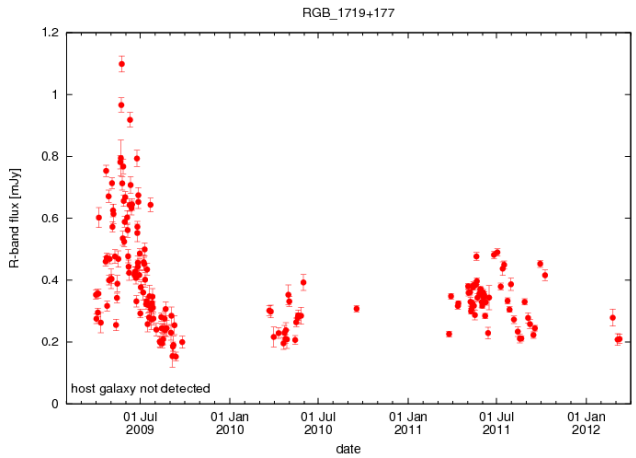

Figure 9.5: Optical R-band light curve, from Tuorla/KVA telescopes, of PKS 1717+177. The figure is taken from [Nil12].

Similar to previous analysis procedures, as described in Chapter 6, also in this case a data quality selection was performed on the whole data sample; after quality cuts (bad weather, unstable event rates and hardware problems, e.g. strong camera inhomogeneities) only 12.66 hours were retained. The whole observation sample of PKS 1717+177 is listed in Appendix E. Moreover, the whole survey was taken under moderate zenith angle conditions from 11° to 31° and in wobble mode (see Chapter 4). The observation nights that pass the quality selection criteria and that are used for the final analysis results are summarized in Table 9.1.

Table 9.1: PKS 1717+177 data set. From left to right: dates in dd / mm / yy, effective time of observation in hours, zenith angle distribution, rate of the event after the image cleaning in Hz and the significance of each observation night.

Date	Eff. time[h]	Zenith [°]	Mean Rate [Hz]	Significance [σ]
19 / 04 / 2009	1.31	23-30	250	1.32
21 / 04 / 2009	0.61	12-30	200	0.62
23 / 04 / 2009	1.01	13-31	130	0.95
24 / 04 / 2009	1.36	12-14	160	2.04
26 / 04 / 2009	0.93	11-31	250	1.97
21 / 05 / 2009	1.23	11-27	240	1.67
23 / 05 / 2009	1.66	11-27	240	0.52
15 / 06 / 2009	0.47	15-23	135	0.07
26 / 06 / 2009	0.32	12-19	165	2.56
27 / 06 / 2009	0.46	12-19	165	1.03
28 / 06 / 2009	1.03	11-20	170	0.39
01 / 07 / 2009	0.64	17-25	160	1.14
23 / 07 / 2009	0.27	14-22	145	0.70
25 / 07 / 2009	0.32	12-21	240	1.71
10 / 08 / 2009	0.44	11-19	260	0.91
13 / 08 / 2009	0.33	15-24	270	1.44
15 / 08 / 2009	0.59	15-28	285	2.42
16 / 08 / 2009	0.65	18-27	300	1.21
17 / 08 / 2009	0.32	17-27	270	0.44
19 / 08 / 2009	0.45	17-27	270	0.80
23 / 08 / 2009	0.37	17-21	180	0.24
24 / 08 / 2009	0.53	20-27	200	0.52

9.3 Data analysis and signal search

The stand-alone MI analysis follows the scheme outlined in Subsection 6.3. When defining the signal region as $\alpha < 8°$, an excess of 226.7 events over 946.3 background events yields a total significance of the 6.09 σ signal. The resulting *Alpha*-plot for `Size` = 300 and `Hadronness` = 0.08 is shown in Figure 9.6. In addition, a corresponding θ^2 distributions was also derived showing similar result of 6 σ with slightly relaxed `Hadronness` cut of 0.10 as displayed in Appendix E in Figure E.1.

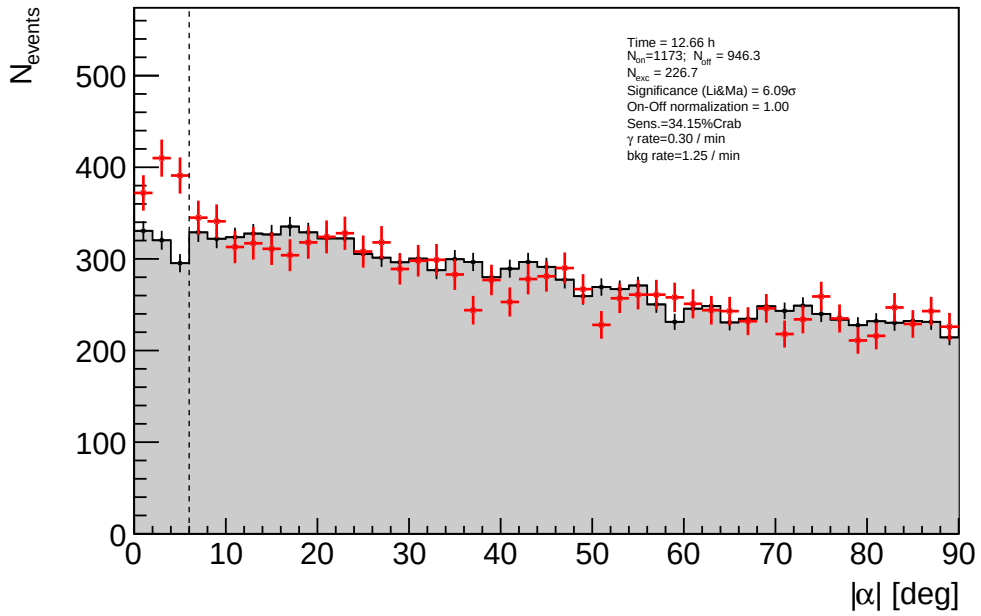

Figure 9.6: *Alpha*-plot for PKS 1717+177 from 12.66 hr of MAGIC observations taken between April 19th and August 24th, 2009. For $\alpha < 8°$ an excess at the 6 σ significance level is obtained.

A skymap (see Figure 9.7) for the signal region also shows an excess at the nominal position of PKS 1717+177 with a hot spot at ~6 σ significance level, confirming the detection of this blazar.

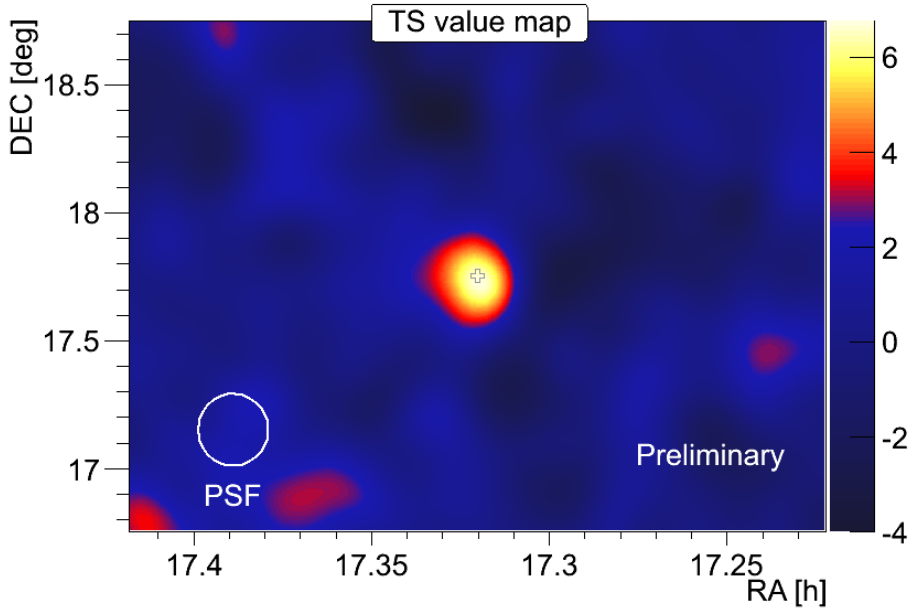

Figure 9.7: Significance skymap for the region around PKS 1717+177 from 12.4 h of MAGIC observations taken between April 19th and August 24th, 2009. The PKS 1717+17 position is marked with an empty cross. The PSF of about 0.1 degree is also displayed.

9.3.1 Temporal behavior of PKS 1717+177

The first VHE γ-ray light curve for PKS 1717+177 was determined for energies above 200 GeV. In this case the *Alpha*-analysis was used. The cuts in `Hadronness` and α are selected according to the cut efficiency in the MC sample, as discussed already in Subsection 6.3.4. For this analysis a `Hadronness` and an α cut of 0.7, respectively, are chosen. Moreover, the adapted `Size` cut was chosen similar to the detection cut of 300 phe. Due to a very low signal from this source a weekly time-scale binning was chosen. The light curve of PKS 1717+177 is shown in Figure 9.8. The integral Flux at E > 200 GeV is found to be $F > 200\,\mathrm{GeV} = (8.2 \pm 1.8) \times 10^{-12}\ \mathrm{cm}^{-2}\ \mathrm{s}^{-1}$ with a fit goodness of $\chi^2 = 4.01/7$ and $P(\chi^2) = 0.78$. This finding corresponds to a very low flux of only $\sim 4\%$ C.U. Unfortunately, the large error bars involved, due to the small signal detected, prevent any strong conclusions about a possible variability of the source emission processes so far.

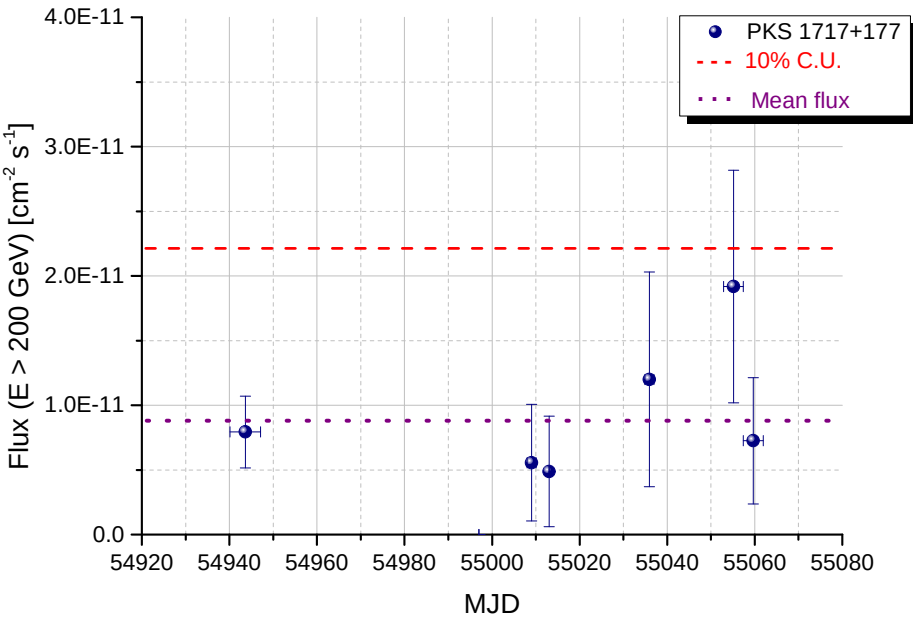

Figure 9.8: PKS 1717+177 light curve between April and August 2009 above an energy threshold of 200 GeV. A hint of variability is seen in the data, mostly around of August 16th.

9.3.2 Differential energy spectrum of PKS 1717+177

In order to determine the energy spectrum for PKS 1717+177 also here the *Alpha*-analysis is used for the given data set. For the different energy spectrum the same `Size`, `Hadronness` and α cuts were used as in case of the light curve. The unfolded differential energy spectrum is shown in Figure 9.9 using the *Bertero* unfolding method with the smallest χ^2 value. The other unfolding methods were also tested giving similar results within the error bars. Like in case of the other spectra obtained during this work, the spectrum of PKS 1717+177 can also be described well with a pure power law with a photon index of $\Gamma = -2.65 \pm 0.39$, and a normalization constant at 250 GeV of $N_0 = (3.84 \pm 0.38) \times 10^{-11} \mathrm{cm}^{-2}\mathrm{s}^{-1}\mathrm{TeV}^{-1}$. The fit goodness yields following results: $\chi^2/\mathrm{NDF} = 1.0/3$ with $\mathrm{P}\chi^2 = 80\%$. The significance of the signal found in each energy bin with corresponding mean flux are listed in Table 9.2. A significant signal between $1.8\,\sigma$ to $2.7\,\sigma$ significance is found in four energy bins, between 120 GeV to 1.2 TeV. The first energy in this spectrum is not taken into account due to the energy threshold of 180 GeV. Of particular concern in this context is the highest energy bin in the spectrum that exceeds the 1 TeV

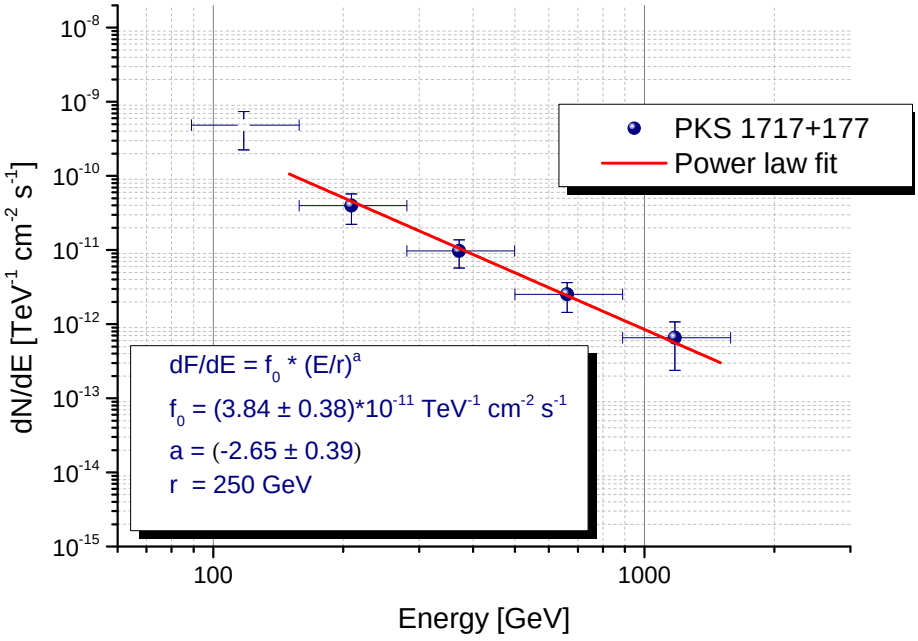

Figure 9.9: PKS 1717+177 differential energy spectrum measured by MAGIC between 125 GeV and 1.5 TeV. The power law fit to the data is also shown (red line).

range due to its relatively base redshift of $z = 0.137$ and the corresponding γ-ray opacity at that distance. Further assumptions about the EBL including particular remarks on PKS 1717+177 and the other blazars presented in this work are the topic of the upcoming Chapter 10.

Table 9.2: Spectral analysis of the PKS 1717+177 2009 sample - In the first column the mean energy of the bin is given; the corresponding bin significance is listed in the second column and the mean flux of each bin is found in the last column.

Mean Energy	Significance [σ]	Flux [$\mathrm{cm}^{-2}\ \mathrm{s}^{-1}\ \mathrm{TeV}^{-1}$]
117	2.16	$(4.83 \pm 2.57) \times 10^{-10}$
219	2.35	$(3.98 \pm 1.75) \times 10^{-11}$
370	1.90	$(9.75 \pm 4.01) \times 10^{-12}$
890	2.69	$(2.52 \pm 1.09) \times 10^{-12}$
1175	1.79	$(6.56 \pm 4.18) \times 10^{-13}$

9.4 The inverse Compton peak of PKS 1717+177

A first estimation of the IC peak of PKS 1717+177 is derived from the *Fermi* LAT observations from the 2FGL catalog (based on the first 24 months of survey data) and the here reported MAGIC results. In similar way as for the other blazars described in this work a logarithmic parabola fit was applied to the HE and VHE γ-ray measurements. The logarithmic parabola was fitted in following vertex notation of the form:

$$\nu F_\nu = \nu^{\mathrm{IC}}_{\mathrm{peak}} F_{\nu^{\mathrm{IC}}_{\mathrm{peak}}} \times 10^{b[\log(\nu/\nu^{\mathrm{IC}}_{\mathrm{peak}})]} \tag{9.1}$$

where $\nu^{\mathrm{IC}}_{\mathrm{peak}} F_{\nu^{\mathrm{IC}}_{\mathrm{peak}}}$ is the peak flux at the peak frequency $\nu^{\mathrm{IC}}_{\mathrm{peak}}$ and b the curvature parameter. From the logarithmic parabola fit following values could be estimated: b = -0.08±0.01, $\nu^{\mathrm{IC}}_{\mathrm{peak}} F_{\nu^{\mathrm{IC}}_{\mathrm{peak}}} = (4.40\pm0.33)\times10^{-12}\,\mathrm{erg\,cm^{-2}\,s^{-1}}$ and $\nu^{\mathrm{IC}}_{\mathrm{peak}} = (4.74 \pm 0.72) \times 10^{24}$ Hz. The IC peak ($\nu^{\mathrm{IC}}_{\mathrm{peak}}$) of PKS 1717+177 is found to be at (19.64±2.99) GeV. Figure 9.10 shows the corresponding IC peak for PKS 1717+177.

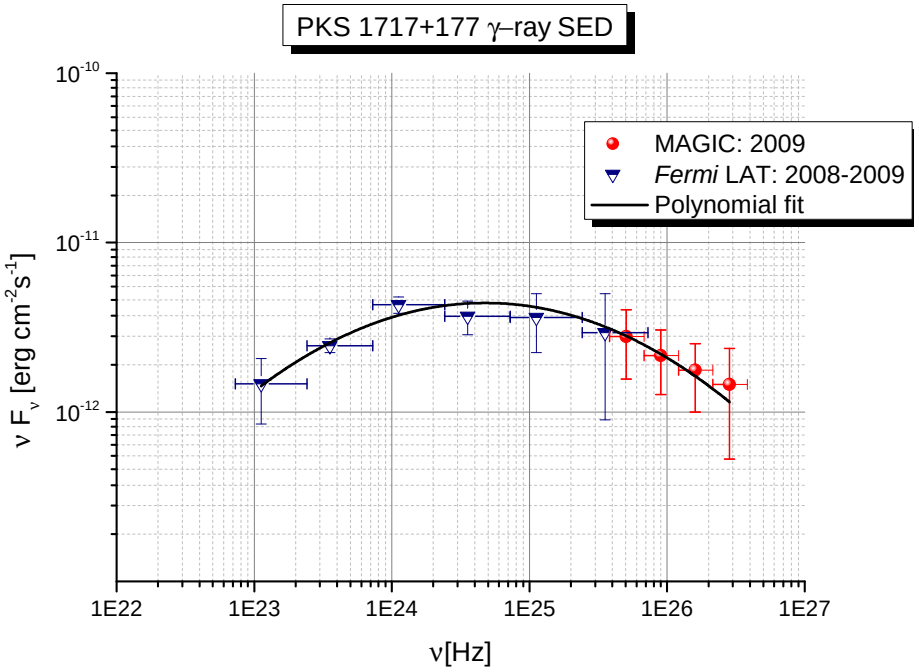

Figure 9.10: Spectral Energy Distribution of PKS 1717+177 in 2009. The figure is taken from [AAA+10c].

The obtained value shows very well, that the peak location for the LBL object is nearly similar to that one of the HBL objects as presented for 1ES 1959+650 in Section 6.8, for 1ES 0033+595 in Section 7.4 and finally for B3 0133+388 in Section 8.4. In conclusion, this result shows also that the peak location in the IC curvature doesn't reveal further information about new subclassifications criteria for the blazars.

9.5 Spectral Energy Distribution of PKS 1717+177

For the first reconstructed SED from the LBL object PKS 1717+177 archival and semi-simultaneous multiwavelength measurements were used. As in previous cases, the archival data for the radio, optical and X-ray observation was carried out from the NED archival. Figure 9.11 shows the reconstructed SED where most of the plotted data can be found in the radio band implying that PKS 1717+177 is a well established radio source.

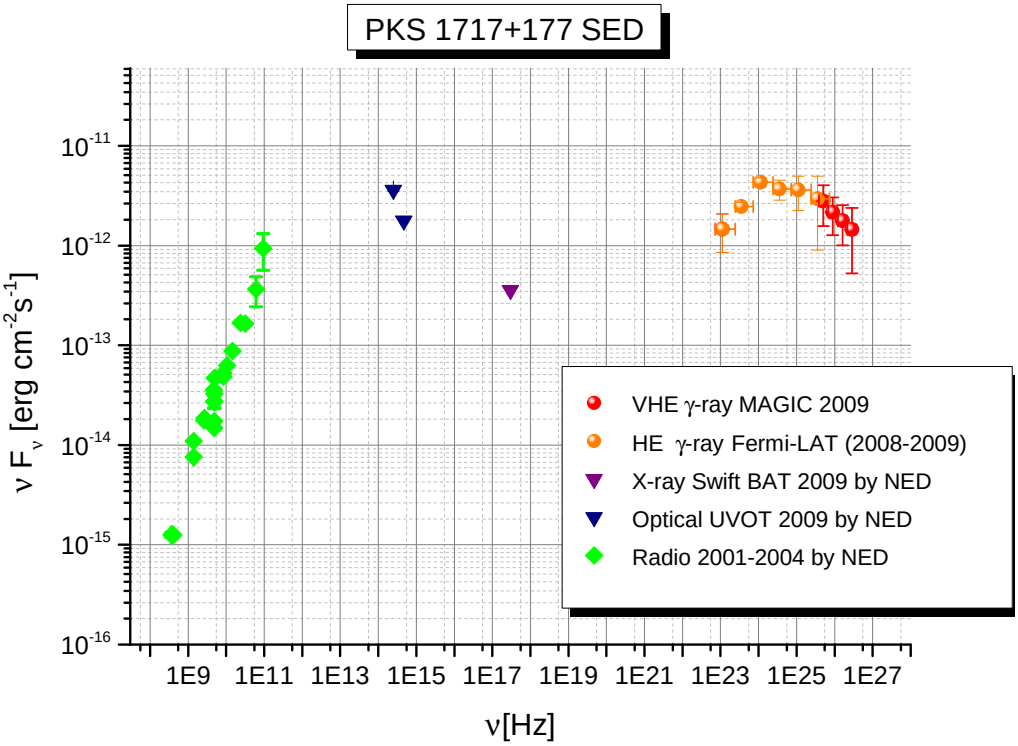

Figure 9.11: The SED of PKS 1717+177 in 2009 with the new analyzed MAGIC data points.

Most of the radio observations (green points in the SED) were performed by Effelsberg, Texas as well as VLBI and VLA observatories in the period from 1990 to 2009. The whole list of the used radio measurements for the reconstructed SED can be found in the Appendix E, Table E.6. In addition semi-simultaneous data from the *Fermi* LAT and MAGIC results from 2008 to 2009 (orange and red points) are drawn in the plot. Out of the reconstructed SED a very good LBL shape structure, where the synchrotron peak is located in the IR-optical range, becomes evident.

9.6 Modeling of the SED of PKS 1717+177

In order to use mostly simultaneous multiwavelength measurements for a SED modeling data from observations performed between 2008 to 2009 have been used to model the SED of PKS 1717+177 by F. Tavecchio, as presented in [TGG+10]. Before the MAGIC analysis was completed giving reasonable results, Tavecchio tried already to model the SED, as shown in Figure 9.12, without the MAGIC results in [TGG+10]. There a one zone synchrotron SSC model was applied to the measurements.
One of the major problems in order to model a LBL object is the fact that they have a large separation between the synchrotron and IC peaks in the SED which consequently requires large Doppler factors. The large separation between both curvatures is also strongly visible in case of PKS 1717+177, due to the *Fermi* LAT spectrum that continue to be hard up to the highest energies. As shown in Figure 9.12, the model established by Tavecchio [TGG+10] resulted by using two assumptions for the Doppler factor. In first case (solid line) a moderate value of the Doppler factor $\delta = 21$ is chosen. It can bee seen, that the fit with this factor underestimates the values measured by Fermi *LAT*. In the second case the author used also a somewhat extreme value of $\delta = 50$ (dashed line) were a better agreement between the data and the fit is visible. In consequence, it becomes evident that the simplest SSC model would be in case of fitting the IC peak in conflict with physical assumptions where δ cannot exceed 50 [Tav10]. An alternative approach suggested by [Tav10], is that the emission zone is not a single homogeneous region like in the modeling case of 1ES 1959+650 where a two zone assumption was applied (see Subsection 6.10). In particular, the approach assumes that the jet is structured into fractions, with a fast core or spline ($\Gamma = 15 - 20$) that is surrounded by a slower layer ($\Gamma = 3 - 5$). As already anticipated above, after a private communication, Tavecchio tried also to model the SED with the here presented spectral results for PKS 1717+177. Figure 9.13 shows the one zone synchrotron SSC model applying the *Fermi* LAT spectrum from 24 months of observa-

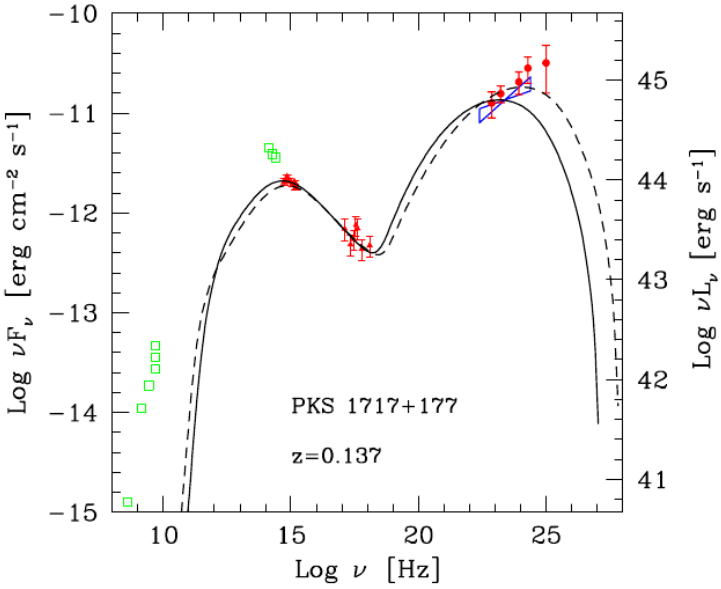

Figure 9.12: The SED of PKS 1717+177 without MAGIC data results. The optical and X-ray data are recorded on January 2009 with the satellite *Swift*. The first measurements of 3 months of *Fermi* LAT survey are summarized with the "butterfly". The solid line represents the one zone synchrotron SSC model with a Doppler factor $\delta = 21$. In contrast the dashed line is the result of the calculated fit using a somewhat extreme value of $\delta = 50$. The figure is taken from [Tav10].

tions (red circle) and also the measured MAGIC data points (green circle) and the EBL corrected spectral points (pink circle), since the EBL cannot be neglected at $z = 0.137$. The model parameters for this SED are listed in Table 9.3. Unfortunately, due to high systematic uncertainties of the stand-alone observations the MAGIC measurements lie between both Doppler factors, thus no strong conclusion on this parameter for this source can be derived. Moreover, it is also known that the one zone synchrotron SSC model gives only satisfactory result for most types of blazar when almost simultaneously data is used in the modeling procedure. For the PKS 1717+177 modeling, it is unfortunately not the case, since also semi-simultaneous data is used. In conclusion, for a real Doppler factor parameter test and any further assumptions it is crucial to obtain really simultaneous data for a SED modeling.

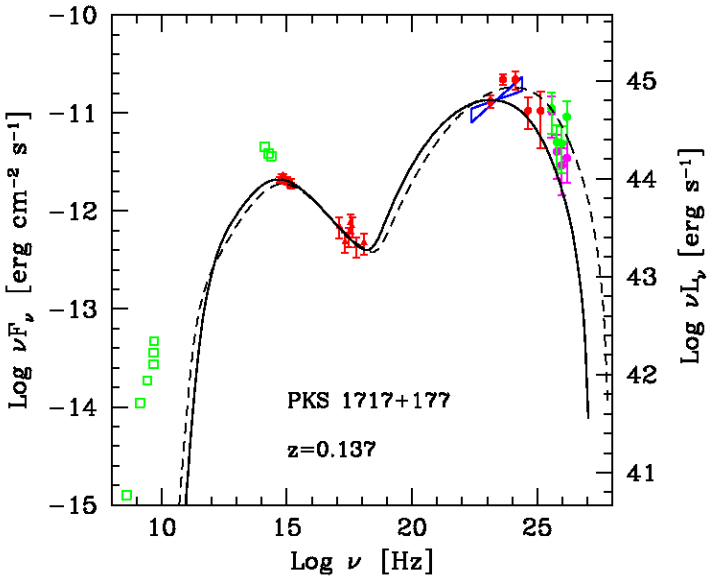

Figure 9.13: SED of PKS 1717+177 with MAGIC data results. The optical and X-ray data are recorded on January 2009 with the satellite *Swift*. The 24 months of *Fermi* LAT survey are summarized with the "butterfly". The solid line represents the one zone synchrotron SSC model with a Doppler factor $\delta = 20$, in contrast the dashed line is the result of the calculated fit using a somewhat extreme value of $\delta = 50$.

Table 9.3: Model parameters used for fitting the SED in Figure 9.13.

marker	$\gamma_{\min}$	γ_{break}	$\gamma_{\max}$	n_1	n_2	B [G]	K [cm^{-3}]	R [cm]	δ
solid line	500	8×10^3	6×10^5	2.0	3.6	0.05	6.3×10^5	3×10^{15}	21
dashed line	500	8×10^3	6×10^5	2.0	3.6	0.05	6.3×10^5	3×10^{15}	50

9.7 Summary and Conclusions

In this chapter a first analysis of PKS 1717+177 VHE γ-ray data taken with the stand-alone MAGIC telescope in 2009 is presented. Since the cross-check analysis for the discovery of this source is ongoing any announcements of this VHE γ-ray detection is not possible at this stage. Nevertheless, establishing PKS 1717+177 as VHE γ-ray source is expected as its interpolation result of the HE γ-ray flux gives very promising predictions. In this chapter the first VHE γ-ray results for this particular LBL object are presented with following summarized findings as listed below:

- Out of the signal search analysis in the 2009 M I stand alone data the source is clearly detected at $6\,\sigma$ significance level.
- The spectrum can be well described with a power law fit with an intermediate photon index between a hard and a soft slope of (2.65 ± 0.39).
- The integral flux above 200 GeV is estimated to be ~4% of the Crab Nebula flux where no variability can be seen. Of particular concern is also the result that no correlation between the optical, where simultaneously the strongest optical flare out of the source was measured, and the VHE γ-ray emission for this source is found. This result can be associated with different emission regions that are independently responsible for the VHE γ-ray and optical radiation.
- In connection with the *Fermi* LAT results and the here presented MAGIC data the first preliminary estimation of the IC peak could be obtained, yielding: $\nu^{\mathrm{IC}}_{\mathrm{PKS\,1717+177peak}} = (19.64\pm2.99)$ GeV. The presented values are in a good agreement with previous results of the other blazars. In fact, it seems that nearly all blazars independently of their subclassifications have their IC peaks in low states between 20 – 50 GeV.
- The reconstructed SED using archival radio and semi-simultaneous optical and X-ray data reveals again the synchrotron emission peak located in the IR-optical range.
- The modeled SED with a simple SSC model by Tavecchio including the here obtained MAGIC measurements gives not a conclusive value for the applied Doppler factors. It seems that *Fermi* LAT and MAGIC results lie between two Doppler factors, namely $\delta = 21$ and $\delta = 50$.
- In this context, also the one zone SSC model seems not to be a satisfactory model for this particular source.

- Finally, in order to make any further assumption regarding a real model parameter test it is crucial also in this case to obtain really simultaneous multiwavelength measurements.

The upcoming chapter presents a population study with all four sources analyzed in this work with a special focus on the cosmic evolution.

CHAPTER 10

BLAZAR POPULATION STUDY

In the first section of this chapter an overview about the current detected TeV blazars and their spectral features is given. The second section is dedicated to a study of different VHE γ-ray parameters and a comparison of the here discovered blazars brought into this context. Additionally, in the third section a synoptic overview of the newly detected blazars in connection with the EBL is performed. Finally, in the last section the new collected results are summarized and discussed in detail towards the cosmic evolution.

10.1 Blazars that have been discovered to date

Today, the extragalactic γ-ray sky is highly dominated by blazars, as already mentioned in previous chapters. In 2012 several new or recent discoveries of VHE γ-ray blazars were announced and presented, for instance B3 0133+388 (see Chapter 8) and 1ES 0033+595 (see Chapter 7) on the 5th International Symposium on High-Energy Gamma-Ray Astronomy (*GAMMA 2012*).
The most notable aspect in context of a population study is the fact that nearly all of the new announced VHE blazars are HBLs. Consequently, this type of blazars dominate the population of VHE blazars with their high synchrotron and IC peak frequencies. The modeling of this type of blazars, in the case that sufficient multiwavelength data was available, is in nearly all cases done with a one zone SSC model. This model has been proved to be very attractive due to its success by fitting a large number of objects and its relatively small number of fitting (free) parameters. However, as shown in Chapter 6 for 1ES 1959+650 and also for three more sources (PKS 1424+240, RGB J0648.7+1516 and RBS 0413) presented at the *GAMMA 2012* conference, the simple SSC model does not produce a satisfactory fit. For these exceptional HBLs, models like the two zone model or even a hadronic model provide far superior fits to the SEDs.

In order to investigate the acceleration processes in AGNs and also the EBL absorption effects, as described in Section 1.3 and Subsection 10.3.4, a large sample of blazars emitting in the VHE γ-ray range is desirable.

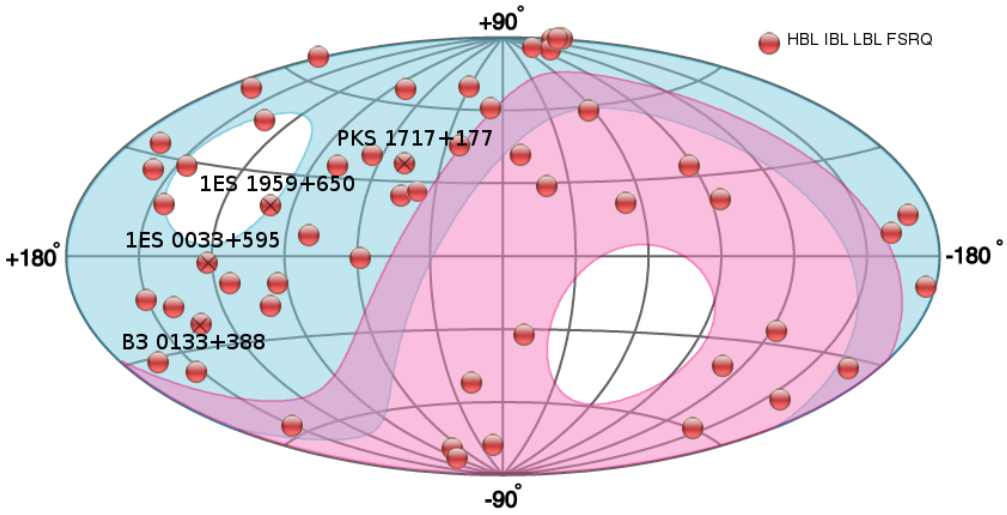

Figure 10.1: TeV skymap in galactic coordinates, as of March 2013, generated using [WH13]. Blue and pink shaded areas present MAGIC/VERITAS and H.E.S.S. visibility, respectively. A total of 53 sources consisting of 41 HBLs, 4 IBL, 4 LBL, 1 unknown type (IC310) and 3 FSRQs are shown.

As shown in Figure 10.1 and listed in Table 10.1, to date, the VHE γ-ray blazar sample comprises 41 HBLs, 4 IBL, 4 LBL, 3 FSRQ and 1 unknown type object (IC310) plus PKS 1717+177. The latter not yet fully considered as an established VHE γ-ray source (see Chapter 9). Table 10.1 is based on the TeV catalog by Wakely and Horan, [WH13]. The fourth column gives the type of the listed blazar where again a dominance of HBL objects is clearly visible. Furthermore, the redshift of the new detected blazars has also been enlarged during the past ten years of IAC telescopes observations. Recent announcement on the *GAMMA 2012* conference presented a new HBL with the name KUV 00311-1938 and a tentative redshift of $z \geq 0.51$. In addition, [FWD+13] reported recently a new redshift estimation of PKS 1424+240 with a lower limit of $z \geq 0.60$. This makes PKS 1424+240 today the most distant detected TeV blazar.

Table 10.1: Todays known VHE γ-ray emitting blazars.

Object Name	RA	Dec	Type	Redshift
Markarian 421	11 04 19.0	+38 11 41	HBL	z = 0.031
Markarian 501	16 53 52.2	+39 45 37	HBL	z = 0.034
1ES 2344+514	23 47 04.9	+51 42 17	HBL	z = 0.044
Markarian 180	11 36 26.4	+70 09 27	HBL	z = 0.045
1ES 1959+650	19 59 59.8	+65 08 55	HBL	z = 0.048
1ES 1727+502	17 28 18.6	+50 13 10	HBL	z = 0.055
PKS 0548-322	05 50 38.4	-32 16 12	HBL	z = 0.069
PKS 2005-489	20 09 27.0	-48 49 52	HBL	z = 0.071
RGB J0152+017	01 52 33.5	+01 46 40	HBL	z = 0.080
1ES 1741+196	17 43 57.8	+19 35 09	HBL	z = 0.083
SHBL J001355.9-185406	00 13 56.0	-18 54 07	HBL	z = 0.095
1ES 1312-423	13 15 03.4	-42 36 50	HBL	z = 0.105
PKS 2155-304	21 58 52.7	-30 13 18	HBL	z = 0.116
B3 2247+381	22 50 06.6	+38 25 58	HBL	z = 0.119
RGB J0710+591	07 10 26.4	59 09 00	HBL	z = 0.125
H 1426+428	14 28 32.6	+42 40 21	HBL	z = 0.129
1ES 1215+303	12 17 52.1	+30 07 01	HBL	z = 0.130
1ES 0806+524	08 09 59.0	+52 19 00	HBL	z = 0.138
1ES 0229+200	02 32 53.2	+20 16 21	HBL	z = 0.140
1RXS J101015.9-311909	10 10 15.0	-31 18 18	HBL	z = 0.143
H 2356-309	23 59 09.4	-30 37 23	HBL	z = 0.165
RX J0648.7+1516	06 48 45.6	+15 16 12	HBL	z = 0.179
1ES 1218+304	12 21 26.3	+30 11 29	HBL	z = 0.182
1ES 1101-232	11 03 36.5	-23 29 45	HBL	z = 0.186
1ES 0347-121	03 49 23.0	-11 58 38	HBL	z = 0.188
RBS 0413	03 19 47.0	+18 45 42	HBL	z = 0.190
1ES 1011+496	10 15 04.1	+49 26 01	HBL	z = 0.212
MS 1221.8+2452	12 24 24.2	+24 36 24	HBL	z = 0.218
1ES 0414+009	04 16 52.9	+01 05 20	HBL	z = 0.287
1ES 0033+595	00 35 53.0	+59 50 04	HBL	z = 0.340
1ES 0502+675	05 07 56.2	+67 37 24	HBL	z = 0.341
1ES 0647+250	06 50 46.5	+25 03 00	HBL	z = 0.450
PG 1553+113	15 55 44.7	+11 11 41	HBL	z = 0.450
B3 0133+388	01 36 32.0	+39 06 00	HBL	z = 0.460
KUV 00311-1938	00 33 34.2	-19 21 33	HBL	z $\geq$ 0.510
PKS 0447-439	04 49 28.2	-43 50 12	HBL	?
HESS J1943+213	19 43 55.0	+21 18 08	HBL	?

Object Name	RA	Dec	Type	Redshift
PKS 0301-243	03 03 26.5	-24 07 11	HBL	?
1ES 1440+122	14 42 48.3	+12 00 40	HBL	?
H1722+119	17 25 04.3	+11 52 15	HBL	?
3C66A	02 22 41.6	+43 02 35	IBL	z = 0.410
W Comae	12 21 31.7	+28 13 59	IBL	z = 0.102
PKS 1424+240	14 27 00.0	+23 47 40	IBL	z ≥ 0.630
VER J0521+211	05 21 55.0	+21 11 24	IBL	?
MAGIC J2001+435	20 01 13.5	+43 53 03	IBL	?
S5 0716+714	07 21 53.4	+71 20 36	LBL	z = 0.310
BL Lacertae	22 02 43.3	+42 16 40	LBL	z = 0.069
PKS 1717+177	17 19 13.0	+17 45 06	LBL	z = 0.137
PKS 1510-089	15 12 50.5	-09 06 00	FSRQ	z = 0.360
PKS 1222+21	12 24 54.4	+21 22 46	FSRQ	z = 0.432
3C279	12 56 11.1	-05 47 22	FSRQ	z = 0.536
IC 310	03 16 43.0	+41 19 29	?	z = 0.019

One important aspect in this context of blazars and the redshift is, that about one fourth of the population (see Table 10.1) does not have a secure redshift. For example the here presented two new discoveries of blazars 1ES 0033+595 and B3 0133+388 to name only a few. This lack of redshift information is due to the fact that optical emission lines are in most cases very weak or even absent in BL Lac objects, preventing direct redshift measurements. Another interesting aspect, as illustrated in Figure 10.2 is, that the majority of known-redshift TeV blazars is located at $z < 0.2$. The todays common explanations for this property lie on the one hand on the sensitivity of current IACT experiments (less luminous blazars are too weak to be detected) and on the other hand on the assumed absorption from the EBL which will be discussed in detail in Subsection 10.3.4. In the next section the most important common spectral features of the currently well established VHE γ-ray blazars listed in Table 10.2 are studied.

However, it has to be kept in mind that it can be expected that the number of detected TeV blazars will increase steadily, and the list and study shown here will be outdated by the time this thesis is published.

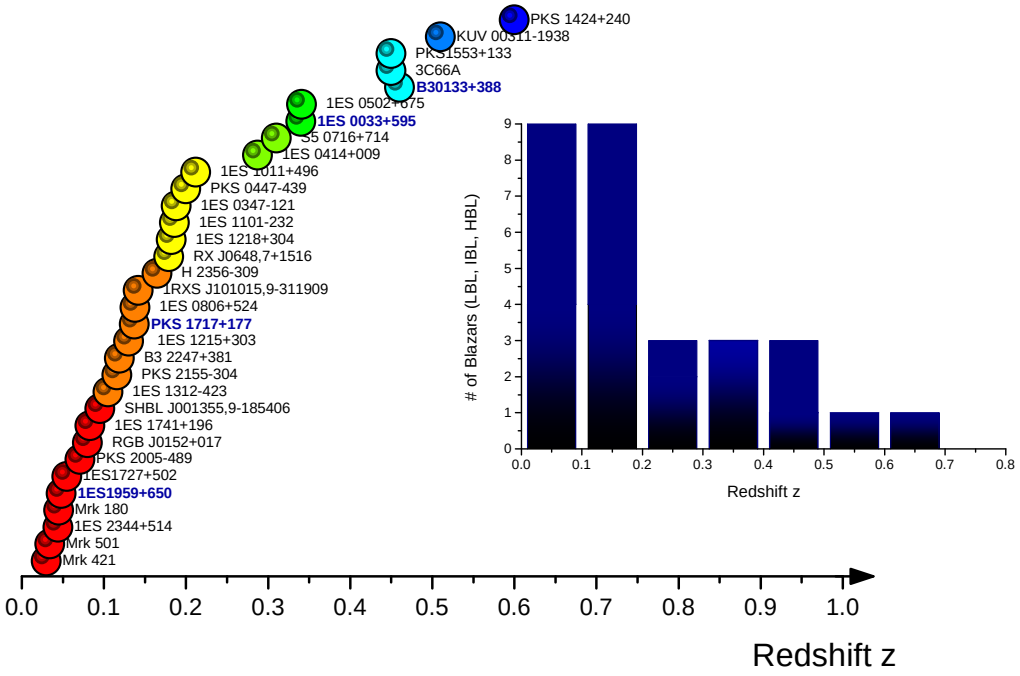

Figure 10.2: Redshift (z) distribution of TeV blazars as of 2013 March. Most of the blazars with known redshift are located at $z < 0.2$.

10.2 Population data sample

Since the launch of the *Fermi*-LAT satellite in 2008 and the improved sensitivity of the IACT experiments good quality spectra are available both from the *Fermi*-LAT in the HE γ-ray band ($0.1\,\text{GeV} < E < 100\,\text{GeV}$) and the VHE γ-ray regime ($E > 100\,\text{GeV}$) for more than three dozen sources. One should keep in mind that most of the blazars were detected in flare states, thus the here presented study, in order to achieve similar study conditions, is performed on a reduced sample in quiescent state (see Table 10.2). In addition, the TeV FSRQs (PKS 1510-089, PKS 1222+21 and 3C279) which are the most distant blazars with redshift ranging from 0.36 to 0.54 are also not taken into account due to a lack of measured data in quiescent state. The here presented study is similar to a part of earlier investigations carried out on a limited sample of TeV blazars by [Wag08]. Moreover, the chosen sample contains all blazars with a published VHE spectrum during a low state of activity before March 2013, including also the results for 1ES 1959+650, 1ES 0033+595, B3 0133+388 and PKS 1717+177 obtained during this work.

Table 10.2: VHE γ-ray emitting blazars in quiescent state used for the study.

Object Name	Redshift	Type	$F_{200\,\mathrm{GeV}}$ [erg cm^{-2}s^{-1}]	Γ_{TeV}	Reference
Mrk 421	0.030	HBL	9.0×10^{-11}	2.20±0.08	[ŞEBM13, AAA+07a]
Mrk 501	0.034	HBL	2.0×10^{-11}	2.53±0.10	[ŞEBM13, Dor13]
1ES 2344+514	0.044	HBL	1.5×10^{-11}	2.95±0.12	[ŞEBM13]
Mrk 180	0.045	HBL	1.0×10^{-11}	3.30±0.70	[ŞEBM13]
1ES 1959+650	0.048	HBL	1.0×10^{-11}	2.52±0.18	this work
1ES 1727+502	0.055	HBL	2.0×10^{-12}	2.70±0.50	[MAA+13]
1ES 1312-423	0.101	HBL	1.0×10^{-12}	2.85±0.47	[HAA+13a]
B3 2247+381	0.119	HBL	4.5×10^{-12}	3.20±0.50	[AAA+12a]
1ES 1215+303	0.130	HBL	5.9×10^{-12}	2.96±0.14	[AAA+12c]
PKS 1717+177	0.137	LBL	3.6×10^{-12}	2.65±0.12	this work
1ES 0806+524	0.138	HBL	6.2×10^{-12}	2.84±0.12	[ŞEBM13]
H 2356-309	0.165	HBL	2.5×10^{-12}	3.06±0.15	[ŞEBM13]
1ES 1218+304	0.182	HBL	1.0×10^{-11}	3.08±0.34	[ŞEBM13]
1ES 1101-232	0.186	HBL	3.0×10^{-12}	2.94±0.20	[ŞEBM13]
1ES 0347-121	0.188	HBL	4.0×10^{-12}	3.10±0.23	[ŞEBM13]
1ES 1011+496	0.212	HBL	6.5×10^{-12}	2.80±0.37	[ŞEBM13]
PKS 0301-243	0.266	HBL	5.6×10^{-12}	3.71±0.24	[ŞEBM13]
1ES 0033+595	0.340	HBL	2.0×10^{-12}	3.80±0.70	this work
1ES 0502+675	0.341	HBL	4.5×10^{-12}	3.41±0.42	[ŞEBM13]
PKS 1553+133	0.450	HBL	4.0×10^{-11}	3.40±0.10	[AAA+12e]
B3 0133+388	0.460	IBL/HBL	3.8×10^{-12}	3.85±0.70	this work
PKS 1424+240	0.603	IBL	1.5×10^{-11}	3.80±0.50	[ŞEBM13]

10.3 VHE γ-ray emission parameters

According to previous observations from different IACTs one can determine observables that characterize the jet emission in a blazar. In Table 10.2 measured fluxes above 200 GeV of all known VHE γ-ray emitting blazars in quiescent state are listed as well as the corresponding photon index in column three and column four, respectively. Moreover, the chosen spectra determined in quiescent state are assumed in all cases for simplicity to be pure power laws. Out of the VHE γ-ray observations two important observables can be extracted. On the one hand the photon index Γ which is determined, as already shortly mentioned above, by fitting the spectra with pure power laws over a selected spectral interval. As outlined in Table 10.2 the photon indices Γ in quiescent state vary from blazar to blazar between $\Gamma = 2.2 - 4.0$. In case of flaring states

such indices can change substantially for instance reaching values $\Gamma \leq 1.8$. On the other hand, the source luminosity L which is described in detail in the following subsection.

Luminosity and luminosity distance

The luminosity characterizes the emitted energy per time and steradian and thus is independent of the observer's distance [Wag08]. For the selected sample the luminosity is extracted at 200 GeV. This is an energy at which the γ-ray flux has been measured for all sources under this study avoiding extrapolation methods for a given spectrum. The apparent luminosity for a blazar can be calculated according to the following formula:

$$L = \frac{F \times 4\pi D_L^2}{(1+z)^{2-\Gamma}} \tag{10.1}$$

where F is the energy flux for energies E = 200 GeV, Γ the corresponding spectral index. Additionally z is the redshift and D_L is the luminosity distance with cosmological constants $\Omega_\lambda = 0.73$, $\Omega_k = 0$ and $\Omega_m = 0.26$ as well as the Hubble parameter $H_0 = 71.1\,\mathrm{km\,s^{-1}\,Mpc^{-1}}$ for each blazar.
In order to calculate the cosmological distances for instance for 1ES 1959+650, the redshift for this estimation is essential. The luminosity distance D_L for 1ES 1959+65 and its emitted photons in case of a flat Universe is described as

$$D_L = (1+z)\, D_H \int_0^z \frac{dz'}{E(z')} \tag{10.2}$$

with D_H=c/H_0 the Hubble distance and $E(z) = \sqrt{\Omega_m(1+z)^3 + \Omega_\Lambda}$ using the same constants as described above. The obtained luminosity distance for 1ES 1959+650 is then: $D_L = 200\,\mathrm{Mpc}$. For the correlation study presented in the next subsection, the main emphasis is put on the comparison of the newly detected TeV blazars and their new estimated redshifts with the blazars which have well known redshifts and spectral measurements.

10.3.1 Correlation between the photon index and the redshift

The first correlation study is done on the photon index Γ and the redshift z as shown in Figure 10.3. The here used correlation method is known as Pearson's r. The coefficient r is a measure of the linear correlation between two variables X and Y. The correlation coefficient ranges from -1 to 1. A value of 1 implies that a linear equation describes the relationship between X and Y perfectly. For this correlation study the corresponding linear coefficient was

found to be $r = 0.71$ and it shows a strong correlation dependency between both parameters. In Figure 10.3 one can also see that mostly sources with soft spectra ($\Gamma > 3.5$) are visible at large distances with $z > 0.2$.

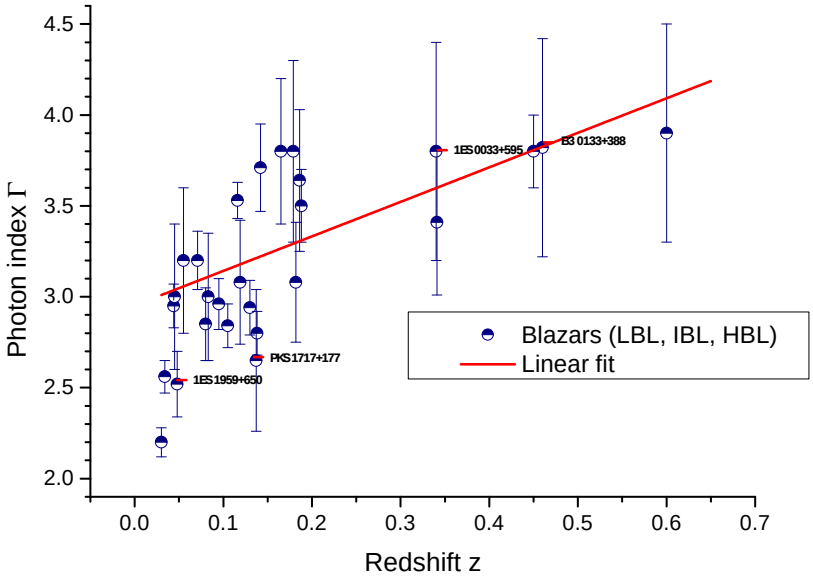

Figure 10.3: Photon index versus redshift. Interestingly, a strong correlation between both parameters with $r = 0.71$ is found.

At current stage there are two most reasonable explanations for this result: On the one hand a redshift-dependent evolution in the VHE γ-ray seems to occur when looking at further distances. This would be supported by the fact that a constant function does not provide a good description for the data and thus this result could be interpreted as a first model independent indication for the evidence for absorption of γ-ray photons on the EBL. On the other hand, since TeV blazars are chosen to be observed when passing different selection criteria, this finding could be also an artifact due to a TeV selection bias. Nevertheless, similar observations were reported by [AAA$^+$09b] and [ŞEBM13], in a study carried out on a sample of TeV-selected AGNs detected with *Fermi* LAT confirming this finding. However, also in this case it cannot be claimed with 100% certainty that the observed deficit of sources for large redshift is a real effect. Finally, the new estimated redshifts for 1ES 0033+595 and B3 0133+388 are in good agreement among other blazars with similar spectral indices.

10.3.2 Correlation between the photon index and the VHE γ-ray luminosity

In the second correlation study the photon index Γ and the luminosity L dependency is investigated, as illustrated in Figure 10.4. The corresponding linear correlation coefficient from the Pearson's r correlation was found to be $r = 0.57$ where a marginal correlation is found. For fluxes up to $4 \cdot 10^{45} \mathrm{erg\,s^{-1}}$ the spectral index seems to be fairly homogeneous. In addition, at higher luminosities mostly soft spectrum sources like 1ES 0033+595 or B3 0133+388 are detected.

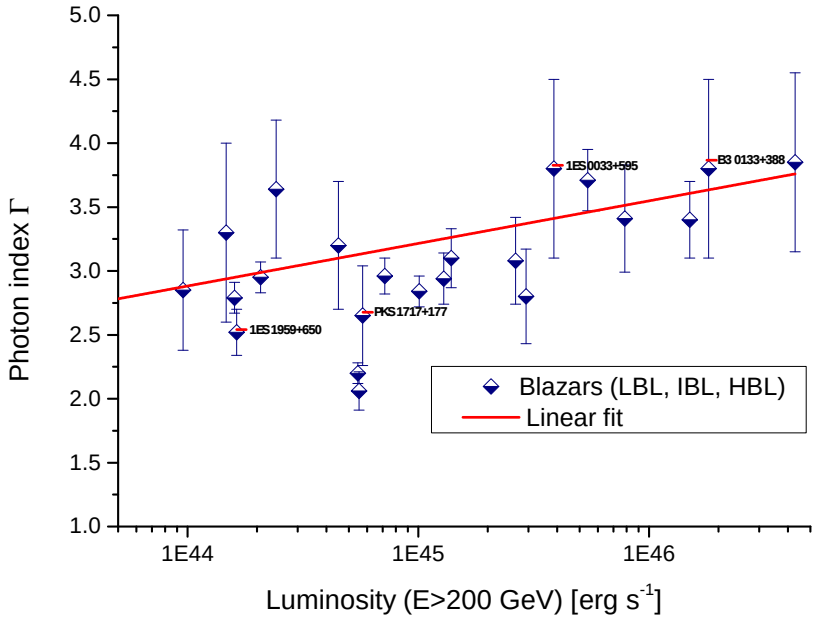

Figure 10.4: Photon index Γ versus luminosity distribution. For fluxes up to $4 \cdot 10^{45} \mathrm{erg\,s^{-1}}$, the spectral index distribution is nearly homogeneous.

10.3.3 Correlation between the luminosity and the redshift

In Figure 10.5 the correlation of the luminosity L versus redshift z for the selected blazar sample is shown. As already presented in [ŞEBM13], in this sample it becomes also evident that at higher redshifts $z > 0.2$ the sources tend to be scarce and much more luminous than sources of lower redshift $z < 0.1$. In this context a strong correlation of $r = 0.96$ is found. This result can be interpreted as the lack of sufficient sensitivity of todays build IACT experiments. More precisely, it means that todays instruments see only luminous sources

at high redshifts and that the less luminous ones are too weak to be detected. The common interpretation why we do not detect them in low redshifts is that we integrate over a much smaller volume and thus are less likely to see high-luminosity sources [ŞEBM13]. Moreover, one should keep in mind that if the luminosity is calculated for higher energies than 200 GeV and is corrected for EBL absorption, which is stronger at TeV energies and also higher redshift, the correlation in Figure 10.5 will be steeper.

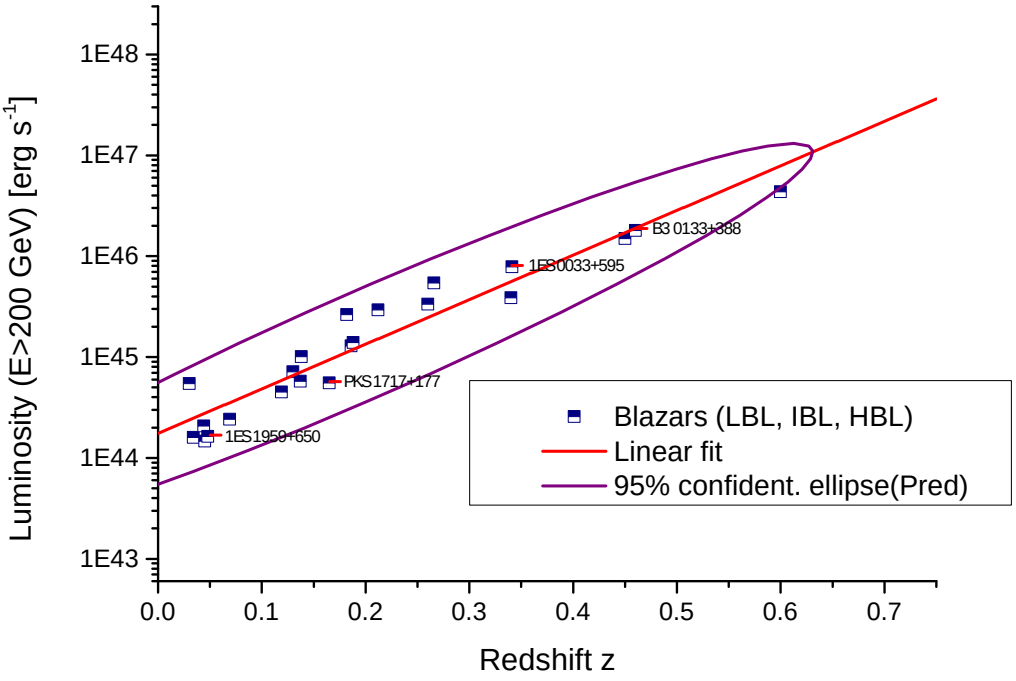

Figure 10.5: Luminosity versus redshift of 22 selected TeV blazars. As expected, at higher redshift less luminous objects are to week to be detected.

10.3.4 The γ-ray horizon

Apart from the γ-ray emission parameter study of blazars, a synoptic overview of the detected blazars in connection with the EBL can be performed. As described in Section 1.4 the EBL is the accumulated and reprocessed radiation of all the starlight produced over the age of the Universe. The measurements of the intensity and evolution of the EBL offer a critical test of cosmology and structure formation. Additionally, a detailed knowledge of this light density plays an important role in the determination of the **I**nter **G**alactic **M**agnetic **F**ield (IGMF) strength. The EBL measurements with a direct technique suf-

fer from the existence of foreground sources within our own solar system and Galaxy. Such difficulty can be overcome by use of VHE γ-ray emitting sources and their interaction mechanism with the EBL through pair production:

$$\gamma_{\mathrm{VHE}} + \gamma_{\mathrm{EBL}} \rightarrow e^{+} + e^{-}$$

There the observed VHE γ-ray spectrum alters in a distance-dependent manner. For this reason the measured spectrum (f_{obs}) in the VHE γ-ray regime from blazars might not be the true one (intrinsic source spectrum). As described in [AAB+06] the absorbed spectrum of the TeV photons has the form:

$$f_{\mathrm{obs}} = f_{\mathrm{source}} \times e^{-\tau(E)} \tag{10.3}$$

with $\tau(E)$ representing the optical depth at a given energy E. Today, the properties and parameter of the EBL (its spectrum) are not well known.
It is assumed that γ-rays of energy above 1 TeV typically interact with IR photons of wavelength larger than 1μm, such as those radiation emitted by the prototype galaxies. In contrast to γ-rays of energy below 1 TeV their interaction should occur in the presence of near-infrared, optical and UV photons, mostly from stars. In addition, from previous measurements a trend is visible that $\tau(1\,\mathrm{TeV}) > \tau(0.1\,\mathrm{TeV})$ leading to the effect that the EBL interaction will absorb more VHE photons and consequently deform the spectrum to a much steeper one. Such imprint, as already possibly found and discussed in Subsection 10.3.1, will be more visible in sources with larger redshifts ($z > 0.2$). In this case the optical depth is much larger, looking at the larger distance where their light will have statistically more opportunities to interact with the EBL on the way to the observer. Consequently, if the intrinsic VHE γ-ray spectrum can be measured properly, a precise measurement of the EBL SED as suggested in [AAB+06] and shown in Section 1.4, might be achieved. Today, there are unfortunately not more than 3 well studied blazars, namely Mrk 421, Mrk 501 and 1ES 1959+650, where the intrinsic spectral shape might be observed close by. But also for this blazars the problematic lies in their basic feature - the variability. In particular both Markarians are highly variable in the TeV range. The photon index of these sources lies within the rang of $\Gamma_{\mathrm{VHE}} \simeq 1.5 - 2.8$ [BS12]. As a result the strength of the EBL is in most cases overestimated and the correction for high redshift blazars lead to intrinsic spectra much harder than $\Gamma = 1.5$, which seems by far unrealistic, when one assumes that the hardest index obtained for the accelerated leptons is 1.5 [BS12].
The today's measured spectral shapes of various observed blazars (see Table 10.2) can give us only a few insights about the intrinsic spectrum in particular in case of large distant sources. In order to investigate this issue a function, which is known as the γ-**R**ay **h**orizon (GRH), $z_{\mathrm{GRH}}(E)$ (first shown

by Fazio & Stecker 1970[1]) with the energy-dependent distance z_{GRH} at which the optical depth reached τ=1 for a given energy $\tau(E,z) = 1$ was developed. This relation proves to be very useful to study the **M**etagalactic **R**adiation **F**ield (MRF) where all photons produced in the Universe, which are not absorbed, are accumulated in the MRF. In this way the theoretically predicted GRH can be compared (depending on the MRF model and cosmological parameters) with a measured one, by determining cut-off energies for large samples of γ-rays sources, especially blazars, at various redshifts [KBM$^+$04], as shown in Figure 10.6. The main difficulty in this study as nearly in every cosmic ray experiment lies in the lack of statistics and huge uncertainty about the truth shape of the γ-ray spectra before cosmological absorption has occurred. In nearly all cases of the here used and published spectra it is difficult to infer the cut-off due to poor statistics. Inspecting also the range of the likely intrinsic spectrum, low flux seems to be the consequence of heavy absorption owing to the comparatively high redshift sources $z > 0.2$. At redshifts $z > 0.2$ the GRH for the models by [KD10] and [DPR$^+$10] converge, since the optical depth becomes independent of the density of IR photons. The models differ mostly in the star formation rate, the dust properties as well as the IR density in the early Universe. Furthermore, the GRH shows also over the years that with decreasing IACT energy threshold, the Universe becomes "transparent", providing at the same time access to a larger source population, as shown here in this study. Due to the huge redshift, which increase the column depth for pair production, the expected cut-off energies are generally at lower energies as confirmed by the spectrum of B3 0133+388 and 1ES 0033+595 where the threshold conditions implies interactions with harder photons [KBM$^+$04]. Figure 10.6 shows the γ-ray horizon for two different EBL models ([KD10], [DPR$^+$10]) applying the cut-off energies from different Blazars (LBL, IBL, HBL) in comparison to the new discovered one, namely 1ES 0033+595, B3 0133+177 and hopefully soon PKS 1717+177.
Interestingly, it was found that in most cases the IACT observations are indeed detecting a decreasing flux with larger redshifts given by the GRH feature. The visible discrepancy between the here presented measurements and the two models can be traced firstly to the huge uncertainty factor in the measured spectrum, as already shortly anticipated above, as well as to the different formalism of the MRF which are used (for a detailed discussion see [KBM$^+$04]). In particular the estimations from the EBL models by [KD10] and [DPR$^+$10] shows that only 5 sources out of 20 have data points that correspond to an optical depth $\tau \geq 1$. The huge mismatch of the lowest redshift

[1] At the end of the 70s Greisen has already suggested that pair-production at high redshift between optical and gamma photons would produce a cut-off around 10 GeV.

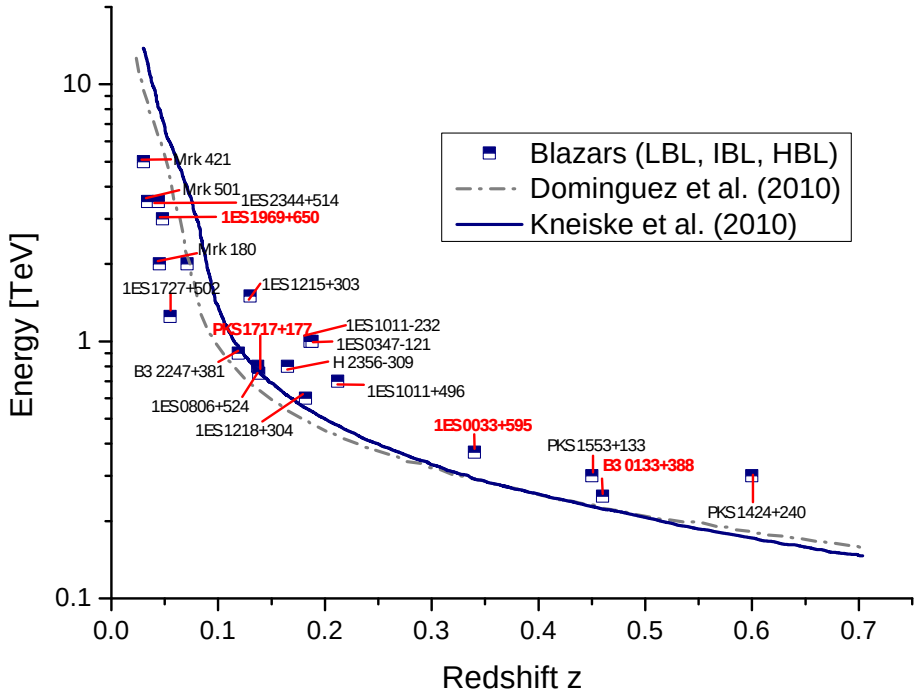

Figure 10.6: Energy as a function of the γ-ray horizon for two different EBL-models.

blazars are high because the optical depth for these cases becomes unity at energies larger than the energies observed by the IAC telescopes. In addition, at larger distances there are also few sources which can be treated as outlier, e.g. PKS 1424+240, with a recent established redshift of $z \geq 0.6$. From this result it can be seen that the energies at which the optical depth are 0.5, 1.0 (the standard definition of GRH) are in some case under estimated and that at the current stage the EBL absorption, which stands in connection with the cosmology is still not fully understood (indications for less absorption than the guaranteed EBL seems to occur). Such finding was already discussed by [FWD$^+$13] where an upturn of the absorption-corrected spectra at the $\tau \geq 2$ transition energy was found. In conclusion, these results show that a deeper study and understanding of the intrinsic spectra of blazars is needed if one wants to use the observed VHE γ-ray spectra for a complete and unambiguous empirical picture of the EBL. Furthermore, these final results open also the question how transparent the Universe for VHE γ-ray photons really is and which consequences new results will have for the estimation of the cosmological parameters that can also be derived from the GRH, as already shown in [DP13].

10.3.5 Summary and Conclusions

The here presented study of known VHE γ-ray emitting blazars in quiescent state yield following results which confirm very well the already presented findings in [ŞEBM13],[DP13] and [Wag08].

- There is a strong correlation found between the photon index and the redshift. Reasonable explanations could be on the one hand the evidence of VHE γ-ray absorption on the EBL and on the other an artifact due to TeV blazar selection bias.
- There is a second strong correlation found of the VHE γ-ray luminosity and the redshift. Thus, it seems that blazars at large distances tend to be scarce and much more luminous than those with lower redshift. The explanation for this results lies in the sensitivity of current IACT experiments which are still not sensitive enough to detect the less luminous blazars.
- Furthermore, at higher luminosities a trend becomes visible that mostly soft spectrum sources are detected. For luminosities up to $4{\cdot}10^{45}$ erg s^{-1} the photon index distribution is nearly homogeneous.
- In addition, a group of objects at very similar distances is found. Such clusters offer themselves for a comparison between the respective individual sources and further study.
- The lack of detection of high redshift sources in the VHE γ-ray regime with energies below 100 GeV allow no conclusions about the UV part of the MRF.
- The here obtained GRH shows that in most cases the IACT observations are indeed detecting a decreasing flux with larger redshifts given by the GRH feature. The estimations from different EBL models show that only 5 sources out of 20 have data points that correspond to an optical depth $\tau \geq 1$. For this reason, further investigations of the EBL, in order to understand the opacity of VHE γ-ray photons when traveling throughout the Universe evolution, are needed. Finally, the here presented results may indicate something new about the transparency of the Universe for γ-ray photons, the propagation of γ-ray photons over long distances or even new emission mechanisms of TeV blazars.

CHAPTER 11

CONCLUDING REMARKS AND DISCUSSION

The questions "How the cosmos developed since the Big Bang?" and in particular "How much light has been emitted by all galaxies since the Big Bang began" are one of the main motivating questions of this work. At present time, almost every photon from UV to far IR wavelengths ever emitted by all galaxies including also the prototype one is still moving through the Universe today. Somewhere along the way we would measure the number and energy (wavelength) of all those photons not only at the present time, but also throughout every developing epoch of the Universe, we might learn a lot about the fascinating mystery about the nature and evolution of the Universe. Out of these results it is assumed that the characteristic properties of differences or similarities of ancient galaxies with the galaxies we see today would be possible to derive. As of now, the accumulation of ancient and young photons found in the shelter of the deep Universe is known as the EBL. This background light and its accurate measurement is as fundamental to cosmology as measuring the heat radiation remaining from the Big Bang that is known as the CMB at radio wavelengths.

One of the extreme and well studied category of AGNs, known as blazar, has been shown during this work to be the best target for extragalactic VHE detections and one of the best candidates in order to study the EBL. The main interaction which allow to study the EBL and thus the opacity of the Universe to VHE γ-ray blazar emitting photons is the photon-photon pair production with the EBL.

In this context four different blazars are studied in detail during this work and connected together in a population study in order to derive cosmological constraints. The fascinating but still very complicating and thus challenging mul-

tiwavelength emission shown in a SED of each blazar is just the beginning to be understood. This work shows also the important impact of VHE γ-ray astrophysics and its extragalactic sources like the blazars for our understanding of the emission processes in this systems.

The first study of one of the closest ($z = 0.048$) known VHE γ-ray emitting blazars, 1ES 1959+650, demonstrates that a detail long-term study of a single object with a large survey over seven years of observations can provide very valuable scientific information about the emission regions and scenarios in this sources. The total amount of observation time, when starting its regular observations in 2005, has led in each observation year to a detection of VHE γ-ray emission of this object. In this work, the data collected from 2009 to 2012 is combined with previous observations (from 2005 to 2008). At this point it should be noted that the 1ES 1959+650 observations with MAGIC were carried out in two different observation conditions. The first observation period of this source was performed until July 2009 with the stand-alone M I telescope whereas in the second period (since August 2009) MAGIC was operated as a system of two telescopes in stereo mode. In addition, due to M I camera failure in 2012 the whole observations were performed again in stand-alone mode only with M II. For this reason different analysis approaches and MC simulations were used and adapted in this work. However, this very extended survey makes 1ES 1959+650 one of the longest and unique studied blazar at energies above 300 GeV. One of the first conclusions of this long-term study is that the overall flux above 300 GeV from 2005 to 2012 shows only a modest variability on yearly time-scale, within a factor 3, corresponding to a variation between 4% to 12% of the Crab Nebula flux. Only one distinct "flare" (strong flux enhancement) on May 30$^{\text{th}}$ 2009 was detected during the long-term study. The integral flux of this flare corresponds to ~70% of the Crab Nebula flux. In addition, the spectra show a hardening with increasing flux level, ranging from a mean low state spectrum described by a photon index of $\Gamma = -2.56 \pm 0.05$ to flare spectral index of $\Gamma = -2.29 \pm 0.29$. Interestingly evidence for a correlation with a delay of 1 – 2 days (where γ-radiation appear to lead radio) between the flux levels in simultaneously taken radio and VHE γ-ray data during the flare has been found. This result strongly indicates that the nearly coincident flux enhancement in both wavelengths have a common emission region which is undoubtedly produced in the jet region and not in the BLR [KAA$^+$09]. Such result was already observed by different authors i.e. [NTV$^+$11] and supports very well the assumption that both wavelengths have for this particular flare a co-spacial origin with a radio core and emerging superluminal blobs which were found in the MOJAVE skymaps. Further multi-epoch VLBI radio study of 1ES 1959+650 which are planned to be carried out

in the future can provide new important parameter like the jet speed or component ejection which can be used at the same time for the modeling of this blazar. In contrast, for the optical (R-band) and the VHE γ-ray wavelengths only a hint of correlation with a delay of 55 days (γ-rays lead optical) is found. Nevertheless, such delays are expected in case of a moving shock and different opacities of the medium as reported in [ESR12] or also as an effect of reprocessing. Also further time lag studies can provide a powerful tool to resolve the structure of relativistic jets and their radiative environment. Another interesting issue is found in the concave spectral shape of the *Fermi* LAT spectrum of 1ES 1959+650. Today, only the HBL 1ES 0502+675 with $z = 0.34$ shows similar inverse Compton shape. This feature can be interpreted as an indication of either two emitting components (e.g. SSC and EC, in the HE γ-ray SED), or it could be a turnover from the synchrotron to the HE component. Furthermore, the low state spectra measured at VHE γ-ray range are combined with simultaneous and archival data available for other wavelengths. In this case a clear two bump structure arises, in agreement with current models of blazar emission. Finally, for the case of 1ES 1959+650, the average SED for the low state in the γ-ray range is modeled with a two–zone SSC model, which currently presents the best fit for the unusual concave shape of the IC peak of this blazar.

On October 27$^{\text{th}}$ 2011, the MAGIC stereoscopic system discovered finally the long hunted blazar 1ES 0033+595 which was observed for the first time already in 2006. The final observations which led to the discovery of this object where performed in stereoscopic system during the commissioning phase of the second telescope M II in August 2009. 1ES 0033+595 is classified as extreme HBL object with synchrotron emission peaking near 10^{19} Hz ($\log\nu_{\text{peak}} = 18.93$) with uncertain redshift. Furthermore, this object was detected at clear significance level of $5.5\,\sigma$. The differential energy spectrum during a state of low γ-ray activity can be described by a power law between (125 – 500) GeV with a photon index of 3.80±0.70. From the spectral analysis the VHE γ-ray spectrum appears to be extremely soft (photon index $\Gamma \sim 4$), as it is expected by the absorption of VHE photons throughout interaction with the EBL if the source is located at relatively large redshift ($z = 0.2$). With the redshift estimation method following the empirical approach by [PMT11] a new value of $z = 0.34 \pm 0.5$ has been determined. This result is in a good agreement with the lower limit of $z > 0.24$ presented in [STF05] and with empirical findings, as described shortly, where higher redshift sources above 0.2 are characterized by a photon index of ~ 4. Moreover, the SED is modeled by fitting a single-zone SSC emission to the data and the model parameters used here for the SED fitting are compatible with those obtained for other HBL class objects.

Within the framework of this thesis, a second blazar B3 0133+388 with an unknown redshift has been discovered on July 10th 2012 [MM12]. However, due to its synchrotron emission peaking at $10^{16.59}$ Hz the sub-classification of this object being an IBL or HBL is still under debate. In the VHE γ-ray range this source was discovered by MAGIC at significance level of 5.6 σ. During the observations, which where performed in November 2009 in stereoscopic mode no significant variability could be detected and the temporal study yields a flux level of (3.6±0.9)% of the Crab Nebula flux above 150 GeV. Further analysis reveals a VHE γ-ray spectrum, which can be fitted by a power law, not extending the energies of 300 GeV and with spectral index of $\Gamma = 3.82 \pm 0.70$. In similarity with 1ES 0033+595 also this source has an extreme soft spectrum which indicates again a large distance of this object. The empirical approach of new redshift estimations was also applied to these spectral findings. In this case a new redshift of $z = 0.46 \pm 0.5$ has been derived. This makes B3 0133+388 the third most distant VHE emitting source detected with the MAGIC telescopes after PKS 1424+240 ($z = 0.61$) and 3C279 ($z = 0.54$). Furthermore, also in this case a SED modeling was performed on the simultaneous and archival multiwavelength data using a single-zone SSC emission model, which is in good agreement when fitting the multiwavelength data of B3 0133+388. Finally, the model parameters used here for the SED fitting are compatible with those obtained for other HBL class objects, thus supporting the classification of B3 0133+388 as a HBL source.

In the same analysis context a fourth and last blazar, namely the LBL object PKS 1717+177 is analyzed during this work. This source was detected at a significance level of 6 σ in the observation period between April to August 2009 in stand-alone mode with M I. This object is one of only four LBL objects seen currently in the VHE γ-ray range with a well measured redshift of $z = 0.137$. A preliminary temporal study (light curve) indicates a flux level of ~4% of the Crab Nebula flux above 200 GeV. Moreover, the preliminary spectrum (fitted with a power law) has an spectral index of 2.65±0.39 which is harder due to its lower redshift in comparison with the other here discovered sources. Similar to the previous mentioned sources a single-zone SSC emission model was applied to the SED where no conclusive value for the Doppler factor due to high systematic uncertainties of the stand-alone observations of M I could be derived.

As anticipated above, all four sources have been used for a population study in order to check their properties among other blazars that are detected in

the VHE regime and the cosmic evolution. Among the 22 blazars under study, which were selected because of their low state conditions, it becomes evident that most of these blazars with known redshift are located at $z < 0.2$. Interestingly, when plotting the photon index against the redshift a correlation has been found between both parameters. The VHE γ-ray spectra become softer with increasing redshift. At current stage two most reasonable explanations for this result are: On the one hand a redshift-dependent evolution in the VHE γ-ray seems to occur when looking at further distances. This would be supported by the fact that a constant function does not provide a good description for the data and thus this finding could be interpreted as a first model independent indication for the evidence for absorption of γ-ray photons on the EBL. On the other hand since TeV blazar are chosen to be observed when passing different selection criteria this result could be also an artifact due to a TeV selection bias. Nevertheless, similar observations were reported by [AAA$^+$09b] and [ŞEBM13], in a study carried out on a sample of TeV-selected AGNs detected with *Fermi* LAT confirming this finding but also there it cannot be claimed with 100% certainty that the observed deficit of sources for large redshift is a real effect. Another interesting result is found when looking at the photon index versus luminosity correlation. At higher luminosities a trend becomes visible that mostly soft spectrum sources are detected. In addition for luminosities up to $4{\cdot}10^{45}$ erg s^{-1} the photon index distribution is nearly homogeneous. Finally, when plotting the luminosity versus redshift again a strong correlation for this sample is visible. In this case, blazars at large distances tend to be scarce and much more luminous. The explanation for this result lies in the sensitivity of current IACT experiments which are yet not sensitive enough to detect the less luminous blazars.
Another interesting feature in the observed VHE γ-ray spectra of blazars as a consequence of EBL absorption is given by the cosmic γ-ray horizon (GRH). The GRH is by definition the energy at which the optical depth of the VHE photon and the EBL photon production becomes unity as a function of redshift. Thus, figuratively it gives an estimate of how far VHE γ-ray photons can travel through different epochs of the Universe evolution. Moreover, the γ-ray opacity due to EBL interactions has direct consequence for the determination of the intrinsic (origin) γ-ray spectra of a blazar, with the flux being suppressed by $e^{\tau(E,z)}$. For this reason, this energy- and redshift dependent flux suppression requires blazars to be exponentially brighter at large redshifts in order to be discovered in the VHE range. In the final study also such GRH was obtained for a selected blazar sample, as described above. Interestingly, it was found that in most cases the IACT observations are indeed detecting a decreasing flux with larger redshifts given by the GRH feature. The estimations from the EBL models by [KD10] and [DPR$^+$10] shows that only 5 sources

out of 20 have data points that correspond to an optical depth $\tau \geq 1$. The huge mismatch of the lowest redshift blazars is high because the optical depth for these cases becomes unity at energies larger than the energies observed by the IAC telescopes. In addition, at larger distances there are also few sources which can be treaded as outlier, e.g. PKS 1424+240, with a recent established redshift of $z \geq 0.6$. From this result it can be seen that the energies at which the optical depth are 0.5, 1.0 (the standard definition of GRH) are in some case under estimated and that at the current stage the EBL absorption which stand in connection with the cosmology is still not fully understood. This opens the question how transparent the Universe for VHE γ-ray photons really is and which consequences new results will have for the cosmology and also for the estimation of the cosmological parameters that can also be derived from the GRH, as already shown in [DP13].

The improved sensitivity due to the stereoscopic upgrade of the MAGIC telescopes was crucial in order to discover new blazars in the low energy VHE γ-ray range (70 – 250 GeV). Future observations with sensitivity improved IACT instruments have the potential to probe τ(E,z) in a more quantitative manner. In particular, new experiments are expected to provide VHE spectra with a better energy resolution, observed up to higher TeV energies (>10 TeV), and increase substantially the number of sources, which in consequence will improve the GRH and further interesting findings that can be derived from it. Today, the long-term future in order to study the cosmic evolution throughout extragalactic sources and especially blazars lies in the planned CTA. This project will consist of about 150 IAC telescopes which will cover an energy range between several tens of GeV to about 100 TeV and a sensitivity that will be ten times better than the one of current IACT instruments.
It is expected that within this project many still open questions, as already highlighted throughout this thesis, will be answered soon and thus shed more light on the Big Bang and the evolution epochs of the Universe.

APPENDIX: A

CRAB NEBULA

A.1 Referenced Crab Nebula analysis for 1ES 1959+650 in the second observation period in 2009

Date	$T_{\text{eff}}[h]$
18 / 08 / 09	0.22
20 / 08 / 09	0.08
23 / 08 / 09	0.49
24 / 08 / 09	0.69
28 / 08 / 09	0.51

Table A.1: Crab Nebula reference sample for 1ES 1959+650 in the second observation period in 2009. The data was taken under high zenith conditions (35°-46°).

A.1.1 The signal of the Crab Nebula in the second observation period in 2009

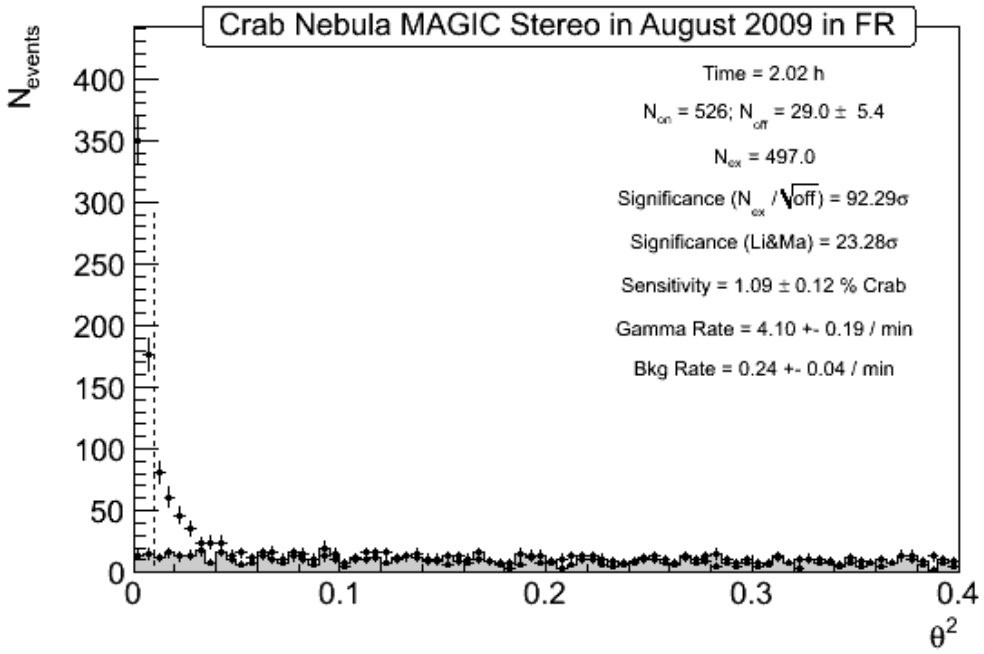

Figure A.1: Θ^2-Plot of the Crab Nebula signal and background estimation from 2.0 h of MAGIC stereo observations taken in August 2009. The data was taken under high zenith conditions (35°-46°).

A.1.2 Flux stability of the Crab Nebula in the second observation period in 2009

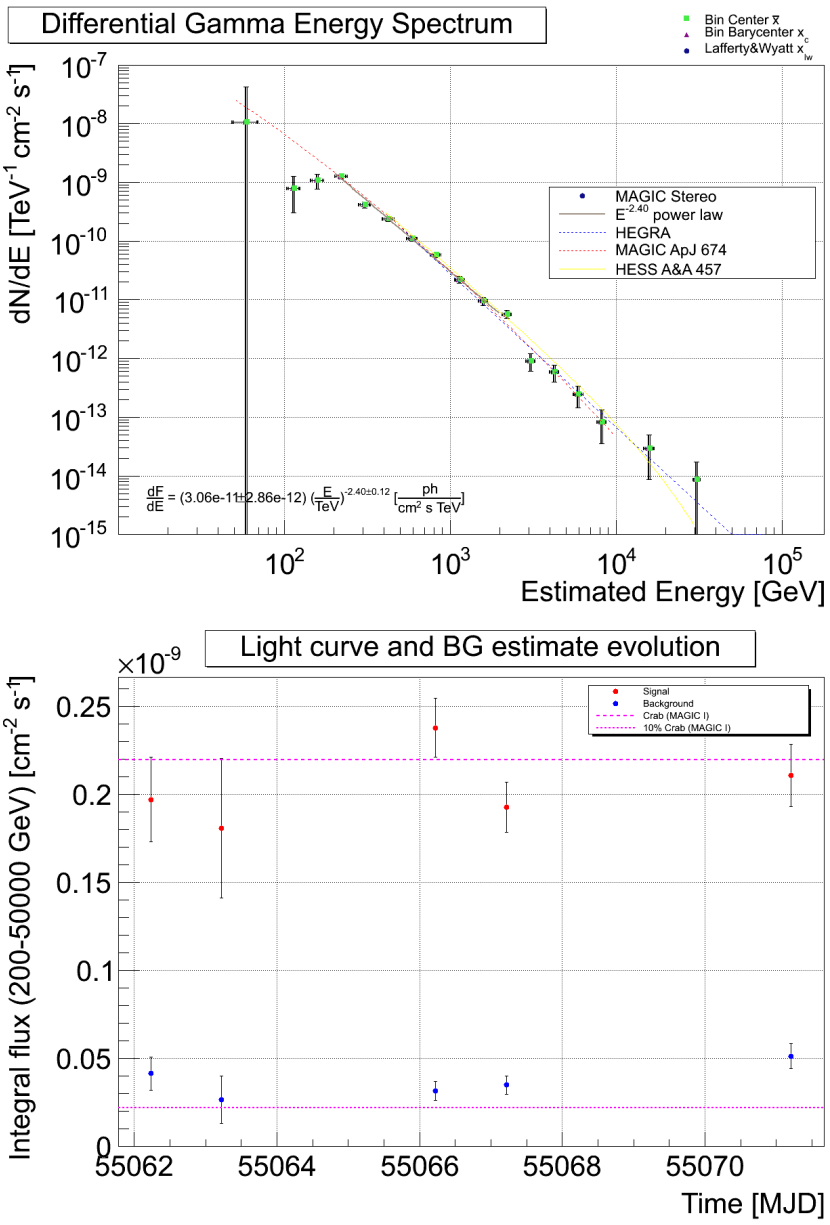

Figure A.2: Spectrum and Light curve of the Crab Nebula in the second observation period in 2009.

A.2 Referenced Crab Nebula analysis for 1ES 1959+650 in the observation period in 2010

Date	$T_{\text{eff}}[h]$
05 / 09 / 10	0.60
07 / 09 / 10	0.59
08 / 09 / 10	0.59

Table A.2: Crab Nebula referenced sample for 1ES 1959+650 in the observation period in 2010

A.2.1 The signal of the Crab Nebula in 2010

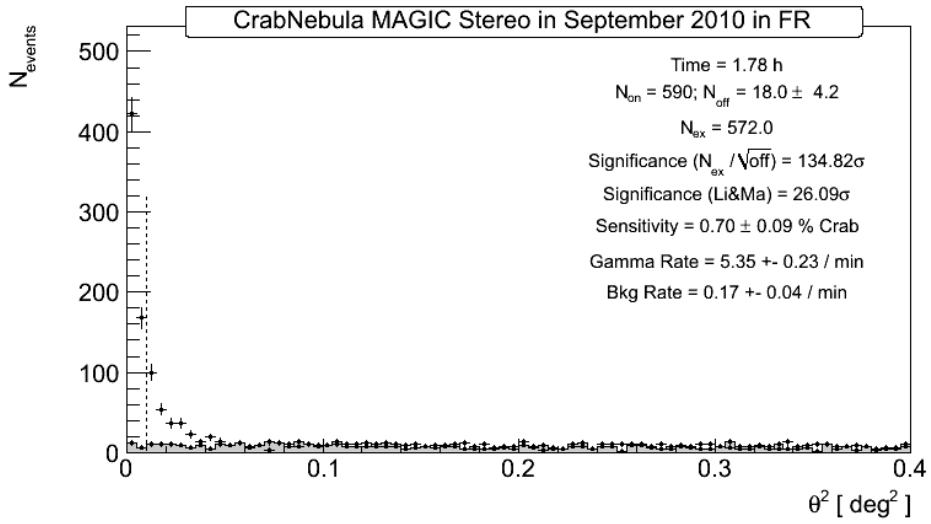

Figure A.3: Θ^2-Plot of the Crab Nebula signal and background estimation from 1.78 h of MAGIC stereo observations taken in September 2010. The data was taken under high zenith conditions (35°-46°).

A.2.2 Flux stability of the Crab Nebula in the observation period in 2010

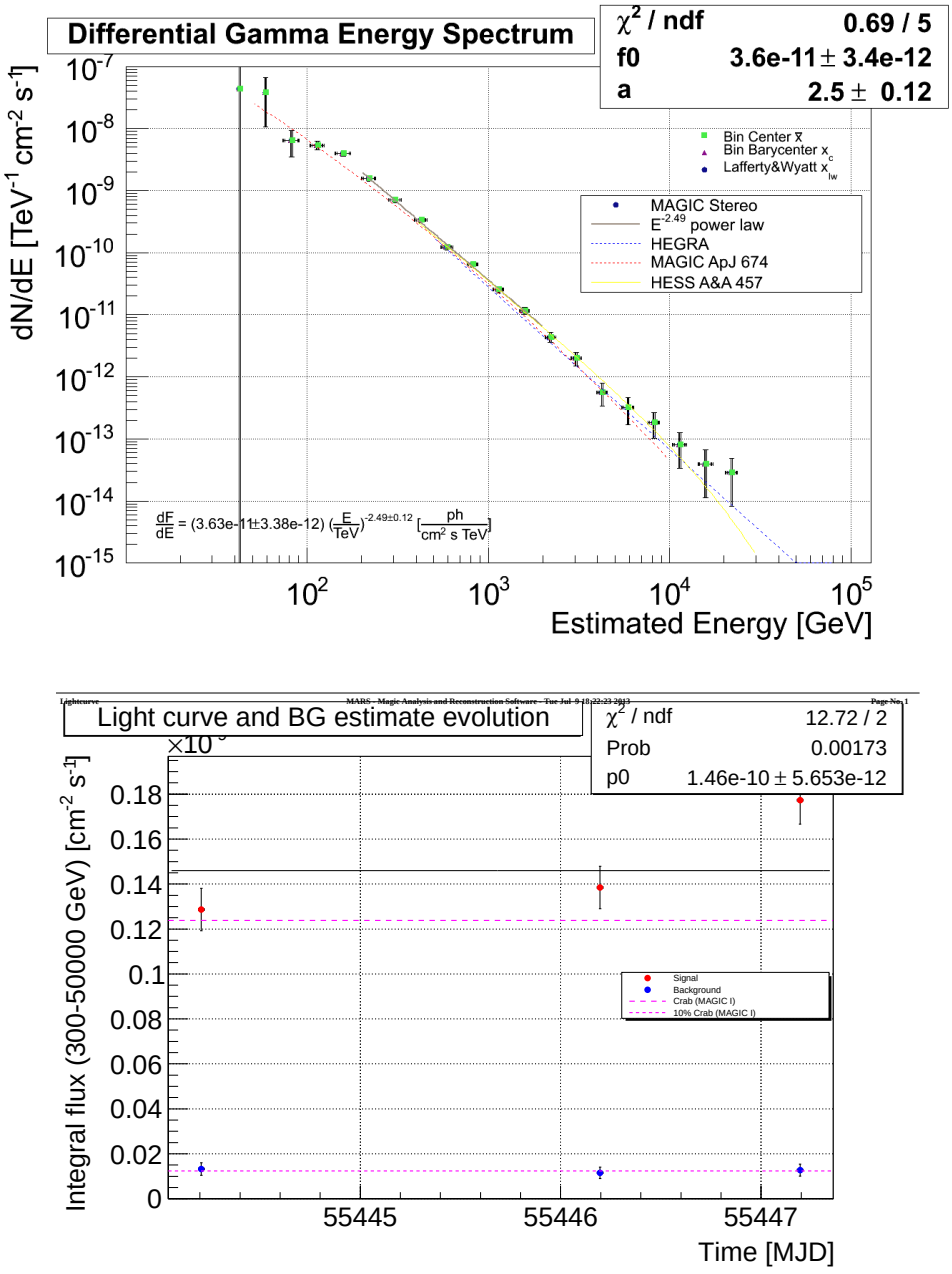

Figure A.4: Spectrum and Light curve of the Crab Nebula in 2010.

A.3 Referenced Crab Nebula sample for the B3 0133+388 analysis in 2009

Date	$T_{\text{eff}}[h]$
15 / 11 / 2009	0.47
16 / 11 / 2009	1.26
17 / 11 / 2009	0.36
19 / 11 / 2009	0.41

Table A.3: Crab Nebula referenced sample for the B3 0133+388 analysis in November 2009. The data was taken low high zenith conditions (10°-35°).

A.3.1 The signal of the Crab Nebula in the November 2009

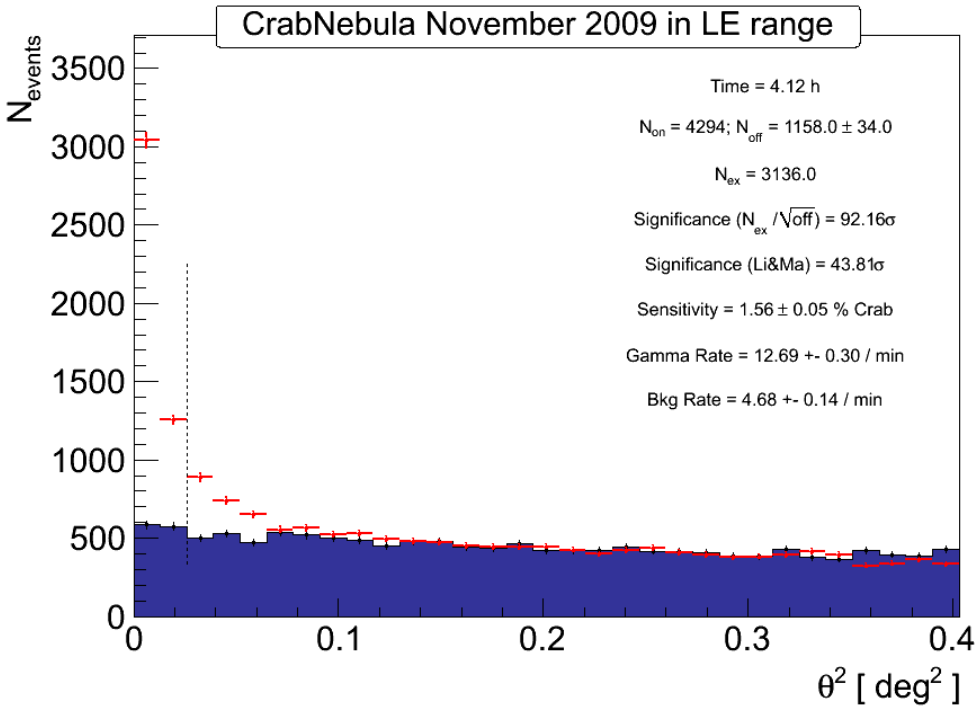

Figure A.5: Θ^2-Plot of the Crab Nebula signal and background estimation from 4.12 h of MAGIC stereo observations taken in November 2009. The data was taken low high zenith conditions (10°-35°).

A.3.2 Flux stability of the Crab Nebula in November 2009

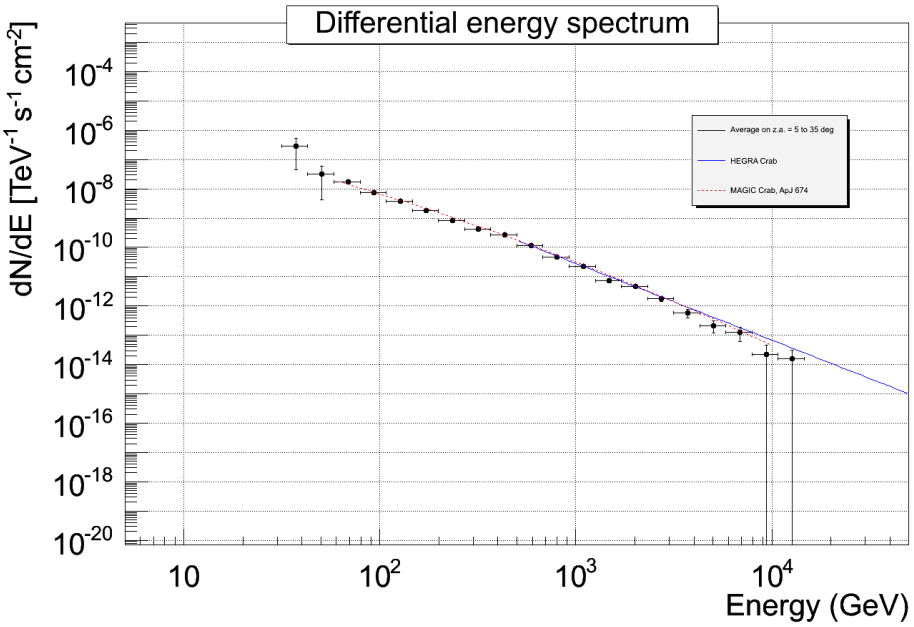

Figure A.6: Spectrum of the Crab Nebula in November 2009.

A.4 Referenced Crab Nebula sample for the PKS 1717+177 analysis in spring 2009

Date	$T_{\text{eff}}[h]$
23 / 01 / 2009	2.56
24 / 01 / 2009	1.49
14 / 03 / 2009	0.58
20 / 03 / 2009	0.74
22 / 03 / 2009	0.53

Table A.4: Crab Nebula referenced sample for the PKS 1717+177 analysis in spring 2009. The data was taken low high zenith conditions (10°-35°).

A.4.1 The signal of the Crab Nebula in spring 2009

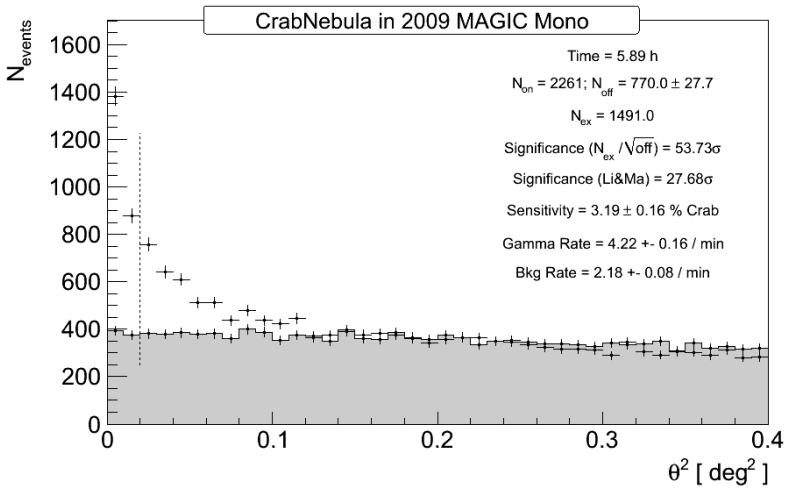

Figure A.7: Θ^2-Plot of the Crab Nebula signal and background estimation from 4.12 h of MAGIC stand-alone observations taken in spring 2009. The data was taken under low high zenith conditions (10°-35°).

A.4.2 Flux stability of the Crab Nebula in spring 2009

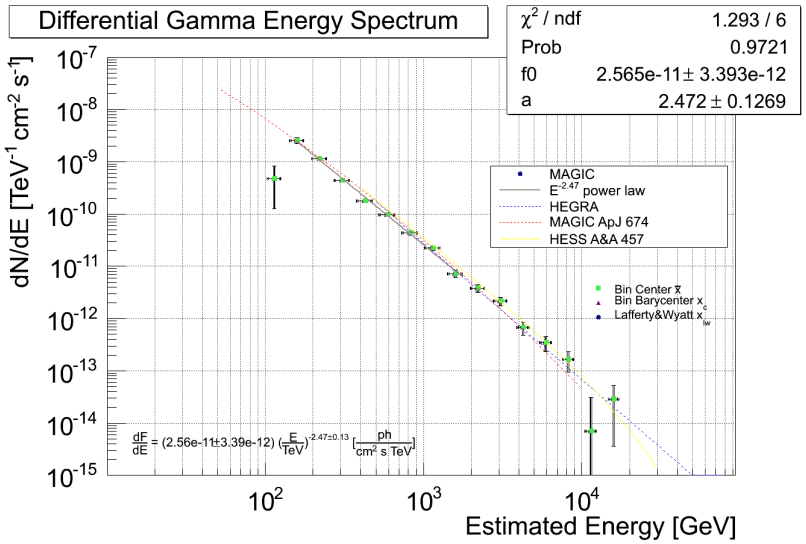

Figure A.8: Spectrum of the Crab Nebula in spring 2009.

APPENDIX: B

1ES 1959+650 DATA

B.1 Total data set used for the analysis

Table B.1: MAGIC I data taken in stand-alone mode in 2009. From left to right: dates in dd / mm / yy, effective time of observation in hours, Zenith angle distribution.

Date	Eff. time [h]	Zenith [°]
20 / 05 / 2009	0.71	42-47
21 / 05 / 2009	1.16	42-47
23 / 05 / 2009	0.20	36-38
24 / 05 / 2009	0.23	36-38
25 / 05 / 2009	0.25	36-38
26 / 05 / 2009	0.23	36-38
27 / 05 / 2009	0.20	36-38
28 / 05 / 2009	0.17	36-38
29 / 05 / 2009	0.21	36-38
30 / 05 / 2009	0.18	42-49
31 / 05 / 2009	0.24	42-49
01 / 06 / 2009	0.22	36-39
02 / 06 / 2009	0.19	36-39
03 / 06 / 2009	0.24	36-39
04 / 06 / 2009	0.21	36-39
05 / 06 / 2009	0.48	36-39
15 / 06 / 2009	1.38	40-48
19 / 06 / 2009	1.98	35-42
20 / 06 / 2009	1.31	40-46

Date	Eff. time [h]	Zenith [°]
22 / 06 / 2009	0.39	41-46
23 / 06 / 2009	0.03	41-46
24 / 06 / 2009	0.27	41-46
25 / 06 / 2009	0.33	41-46
26 / 06 / 2009	0.32	41-46
27 / 06 / 2009	0.32	41-46
28 / 06 / 2009	0.32	41-46
28 / 06 / 2009	0.33	41-46
01 / 07 / 2009	0.46	41-46
02 / 07 / 2009	0.33	41-46
03 / 07 / 2009	0.59	41-46
05 / 07 / 2009	0.51	41-46
29 / 07 / 2009	1.75	41-46
30 / 07 / 2009	1.23	41-46
31 / 07 / 2009	0.28	41-46

Table B.2: MAGIC I data taken in stereo mode in 2009. From left to right: dates in dd / mm / yy, effective time of observation in hours, zenith angle distribution.

Date	Eff. time [h]	Zenith [°]
13 / 08 / 2009	0.67	42-47
15 / 08 / 2009	0.73	42-47
26 / 08 / 2009	0.26	36-38
27 / 08 / 2009	0.14	36-38
28 / 08 / 2009	0.58	36-38
29 / 08 / 2009	1.21	36-38
30 / 08 / 2009	0.38	42-49
24 / 09 / 2009	0.58	36-39
26 / 09 / 2009	1.13	40-48
27 / 09 / 2009	1.33	35-42
28 / 09 / 2009	0.12	40-46
08 / 10 / 2009	0.08	41-46
11 / 10 / 2009	0.13	41-46
12 / 10 / 2009	0.10	41-46
21 / 10 / 2009	0.09	41-46
24 / 10 / 2009	0.14	41-46

Date	Eff. time [h]	Zenith [°]
25 / 10 / 2009	1.59	41-46
26 / 10 / 2009	1.89	41-46
27 / 10 / 2009	0.64	41-46

Table B.3: MAGIC I data taken in stereo mode in 2010. From left to right: dates in dd / mm / yy, effective time of observation in hours, zenith angle distribution.

Date	Eff. time [h]	Zenith [°]
23 / 05 / 2010	0.46	42-47
02 / 06 / 2010	2.24	36-42
03 / 06 / 2010	0.29	37-40
08 / 06 / 2010	1.30	36-38
06 / 08 / 2010	0.34	42-49
16 / 08 / 2010	0.83	36-39
20 / 08 / 2010	1.13	40-48
31 / 08 / 2010	1.33	35-42
02 / 09 / 2010	0.78	40-46
29 / 09 / 2010	0.49	41-46

Table B.4: SED: VHE data from 1ES 1959+650 by MAGIC from 2005 to 2012.

ν [Hz]	νF_ν [erg cm^{-2}s^{-1}]	σ_ν^- [Hz]	σ_ν^+ [Hz]	$\sigma_{\nu F_\nu}^-$ [erg cm^{-2}s^{-1}]	$\sigma_{\nu F_\nu}^+$ [erg cm^{-2}s^{-1}]
4.65E+25	1.09E-11	1.04E+25	1.33E+25	5.92E-12	5.92E-12
7.71E+25	4.70E-12	1.72E+25	2.21E+25	2.15E-12	2.15E-12
1.28E+26	2.59E-12	2.85E+25	3.66E+25	1.27E-12	1.27E-12
2.11E+26	3.26E-12	4.71E+25	6.06E+25	9.61E-13	9.61E-13
3.50E+26	2.48E-12	7.80E+25	1.00E+26	7.02E-13	7.02E-13
5.80E+26	9.92E-13	1.29E+26	1.66E+26	7.56E-13	7.56E-13
–	–	–	–	–	–
4.67E+25	1.40E-11	1.04E+25	1.33E+25	5.48E-12	5.48E-12
7.73E+25	6.13E-12	1.72E+25	2.22E+25	2.06E-12	2.06E-12

ν [Hz]	νF_ν [erg cm^{-2}s^{-1}]	σ_ν^- [Hz]	σ_ν^+ [Hz]	$\sigma_{\nu F_\nu}^-$ [erg cm^{-2}s^{-1}]	$\sigma_{\nu F_\nu}^+$ [erg cm^{-2}s^{-1}]
1.28E+26	6.43E-12	2.85E+25	3.68E+25	1.26E-12	1.26E-12
2.12E+26	4.78E-12	4.72E+25	6.07E+25	1.20E-12	1.20E-12
3.51E+26	3.86E-12	7.81E+25	1.01E+26	1.03E-12	1.03E-12
5.81E+26	2.19E-12	1.29E+26	1.67E+26	1.02E-12	1.02E-12
–	–	–	–	–	–
5.95E+25	8.89E-12	1.14E+25	2.27E+25	8.89E-12	2.23E-12
8.79E+25	6.23E-12	1.62E+25	3.36E+25	6.23E-12	1.41E-12
1.29E+26	6.03E-12	2.47E+25	4.96E+25	6.03E-12	1.36E-12
1.90E+26	3.97E-12	3.63E+25	7.25E+25	3.97E-12	1.38E-12
2.80E+26	4.44E-12	5.38E+25	1.08E+26	4.44E-12	1.46E-12
4.12E+26	3.01E-12	7.91E+25	1.58E+26	3.01E-12	1.57E-12
6.07E+26	3.16E-12	1.16E+26	2.33E+26	3.16E-12	1.67E-12
–	–	–	–	–	–
6.00E+25	1.10E-11	1.62E+25	3.24E+25	1.10E-11	3.93E-12
1.05E+26	5.12E-12	2.90E+25	5.80E+25	5.12E-12	2.13E-12
1.85E+26	3.20E-12	5.08E+25	1.02E+26	3.20E-12	2.10E-12
3.24E+26	3.73E-12	8.90E+25	1.78E+26	3.73E-12	2.06E-12
5.69E+26	5.05E-12	1.56E+26	3.12E+26	5.05E-12	2.67E-12
–	–	–	–	–	–
7.74E+25	9.16E-12	1.48E+25	1.96E+25	1.74E-12	1.74E-12
1.20E+26	7.85E-12	2.30E+25	3.05E+25	1.82E-12	1.82E-12
1.86E+26	5.69E-12	3.56E+25	4.72E+25	1.14E-12	1.14E-12
2.89E+26	3.63E-12	5.53E+25	7.32E+25	8.64E-13	8.64E-13
4.48E+26	2.27E-12	8.57E+25	1.14E+26	6.34E-13	6.34E-13
6.94E+26	1.58E-12	1.33E+26	1.76E+26	5.59E-13	5.59E-13
1.08E+27	1.16E-12	2.06E+26	2.73E+26	6.53E-13	6.53E-13
1.67E+27	8.10E-13	3.19E+26	4.23E+26	7.50E-13	7.50E-13
2.59E+27	5.44E-13	4.95E+26	6.56E+26	8.14E-13	8.14E-13
–	–	–	–	–	–
6.03E+25	4.57E-12	1.22E+25	1.59E+25	1.01E-12	1.01E-12
9.56E+25	4.33E-12	1.94E+25	2.53E+25	8.63E-13	8.63E-13
1.52E+26	3.92E-12	3.07E+25	4.00E+25	7.56E-13	7.56E-13
2.40E+26	3.25E-12	4.86E+25	6.34E+25	6.73E-13	6.73E-13
3.81E+26	2.71E-12	7.71E+25	1.01E+26	6.24E-13	6.24E-13
6.03E+26	2.04E-12	1.22E+26	1.59E+26	6.42E-13	6.42E-13
9.56E+26	1.01E-12	1.94E+26	2.53E+26	6.13E-13	6.13E-13
–	–	–	–	–	–
6.99E+25	5.15E-12	1.63E+25	2.23E+25	1.58E-12	1.58E-12

ν [Hz]	νF_ν [erg cm^{-2}s^{-1}]	σ_ν^- [Hz]	σ_ν^+ [Hz]	$\sigma_{\nu F_\nu}^-$ [erg cm^{-2}s^{-1}]	$\sigma_{\nu F_\nu}^+$ [erg cm^{-2}s^{-1}]
1.20E+26	4.34E-12	2.80E+25	3.83E+25	9.62E-13	9.62E-13
2.07E+26	3.49E-12	4.81E+25	6.59E+25	7.81E-13	7.81E-13
3.55E+26	3.69E-12	8.27E+25	1.13E+26	1.23E-12	1.23E-12
6.11E+26	2.22E-12	1.42E+26	1.95E+26	8.68E-13	8.68E-13
1.05E+27	1.86E-12	2.44E+26	3.35E+26	1.18E-12	1.18E-12
1.80E+27	6.81E-13	4.20E+26	5.75E+26	2.38E-12	2.38E-12
–	–	–	–	–	–
6.96E+25	1.68E-11	1.59E+25	2.26E+25	4.28E-12	4.28E-12
1.20E+26	7.41E-12	2.74E+25	3.89E+25	1.51E-12	1.51E-12
2.06E+26	4.90E-12	4.71E+25	6.69E+25	1.45E-12	1.45E-12
3.53E+26	3.28E-12	8.09E+25	1.15E+26	9.45E-13	9.45E-13
6.08E+26	1.95E-12	1.39E+26	1.98E+26	6.59E-13	6.59E-13
1.04E+27	1.03E-12	2.39E+26	3.40E+26	5.52E-13	5.52E-13
1.80E+27	5.64E-13	4.11E+26	5.84E+26	5.41E-13	5.41E-13

Table B.5: SED: HE data from 1ES 1959+650 by *Fermi* LAT from 2008 to 2010. The data was taken from [Pan13].

ν [Hz]	νF_ν [erg cm^{-2}s^{-1}]	σ_ν^- [Hz]	σ_ν^+ [Hz]	$\sigma_{\nu F_\nu}^-$ [erg cm^{-2}s^{-1}]	$\sigma_{\nu F_\nu}^+$ [erg cm^{-2}s^{-1}]
8.69E+22	1.30E-11	3.30E+22	3.30E+22	2.06E-12	2.06E-12
1.94E+23	1.07E-11	7.36E+22	7.36E+22	1.61E-12	1.61E-12
4.31E+23	7.29E-12	1.64E+23	1.64E+23	1.50E-12	1.50E-12
9.60E+23	6.40E-12	3.65E+23	3.65E+23	1.78E-12	1.78E-12
2.14E+24	8.42E-12	8.13E+23	8.13E+23	2.86E-12	2.86E-12
4.76E+24	1.73E-11	1.81E+24	1.81E+24	5.76E-12	5.76E-12
1.06E+25	1.55E-11	4.03E+24	4.03E+24	7.81E-12	7.81E-12
–	–	–	–	–	–
4.19E+22	1.18E-11	1.77E+22	3.07E+22	1.92E-12	1.92E-12
1.32E+23	1.17E-11	5.99E+22	1.09E+23	1.37E-12	1.37E-12
4.19E+23	9.37E-12	1.77E+23	3.07E+23	9.61E-13	9.61E-13
1.32E+24	8.99E-12	5.99E+23	1.09E+24	1.51E-12	1.51E-12
7.65E+24	1.39E-11	5.23E+24	1.65E+25	2.67E-12	2.67E-12
–	–	–	–	–	–
4.19E+22	9.74E-12	1.77E+22	3.07E+22	1.04E-12	1.04E-12
1.32E+23	9.16E-12	5.99E+22	1.09E+23	6.47E-13	6.47E-13
4.19E+23	8.78E-12	1.77E+23	3.07E+23	6.82E-13	6.82E-13

ν [Hz]	νF_ν [erg cm^{-2}s^{-1}]	σ_ν^- [Hz]	σ_ν^+ [Hz]	$\sigma_{\nu F_\nu}^-$ [erg cm^{-2}s^{-1}]	$\sigma_{\nu F_\nu}^+$ [erg cm^{-2}s^{-1}]
1.32E+24	9.48E-12	5.99E+23	1.09E+24	9.67E-13	9.67E-13
7.65E+24	1.20E-11	5.23E+24	1.65E+25	1.62E-12	1.62E-12
–	–	–	–	–	–
4.30E+22	1.11E-11	1.88E+22	3.34E+22	9.62E-13	9.62E-13
1.36E+23	8.56E-12	5.95E+22	1.06E+23	5.57E-13	5.57E-13
4.30E+23	6.89E-12	1.88E+23	3.34E+23	5.57E-13	5.57E-13
1.36E+24	6.28E-12	5.95E+23	1.06E+24	7.59E-13	7.59E-13
4.30E+24	9.06E-12	1.88E+24	3.34E+24	1.47E-12	1.47E-12
1.36E+25	8.66E-12	5.95E+24	1.06E+25	2.53E-12	2.53E-12
4.30E+25	7.49E-12	1.88E+25	3.34E+25	4.66E-12	4.66E-12
–	–	–	–	–	–
4.30E+23	8.75E-12	1.88E+23	3.35E+23	8.27E-13	8.27E-13
1.36E+24	7.78E-12	5.95E+23	1.06E+24	1.05E-12	1.05E-12
4.30E+24	1.11E-11	1.88E+24	3.35E+24	1.92E-12	1.92E-12
1.36E+25	9.90E-12	5.95E+24	1.06E+25	2.98E-12	2.98E-12
4.30E+25	6.38E-12	1.88E+25	3.35E+25	4.51E-12	4.51E-12

Table B.6: SED: X-ray data from 1ES 1959+650 *Swift*-RXT, *Swift*-BAT and INTEGRAL. The data was taken from the NED archival and [Bac11].

ν [Hz]	νF_ν [erg cm^{-2}s^{-1}]	σ_ν^- [Hz]	σ_ν^+ [Hz]	$\sigma_{\nu F_\nu}^-$ [erg cm^{-2}s^{-1}]	$\sigma_{\nu F_\nu}^+$ [erg cm^{-2}s^{-1}]
6.721E-11	7.254E17	7.254E17	7.647E-12	7.647E-12	4.111E18
5.747E-11	4.836E17	4.836E17	8.213E-12	8.213E-12	5.32E18
5.447E-11	1.33E18	1.33E18	6.687E-12	6.687E-12	7.133E18
3.994E-11	1.813E18	1.813E18	7.6E-12	7.6E-12	1.028E19
3.344E-11	3.022E18	3.022E18	9.327E-12	9.327E-12	1.511E19
2.539E-11	3.022E18	3.022E18	1.526E-11	1.526E-11	2.116E19
–	–	–	–	–	–
6.049E-11	7.254E17	7.254E17	3.504E-12	3.504E-12	3.504E-12
5.272E-11	4.836E17	4.836E17	4.103E-12	4.103E-12	4.103E-12
4.526E-11	1.33E18	1.33E18	4.003E-12	4.003E-12	4.003E-12
3.147E-11	1.813E18	1.813E18	4.219E-12	4.219E-12	4.219E-12
3.347E-11	3.022E18	3.022E18	5.287E-12	5.287E-12	5.287E-12
2.114E-11	3.022E18	3.022E18	8.964E-12	8.964E-12	8.964E-12

ν [Hz]	νF_ν [erg cm^{-2}s^{-1}]	σ_ν^- [Hz]	σ_ν^+ [Hz]	$\sigma_{\nu F_\nu}^-$ [erg cm^{-2}s^{-1}]	$\sigma_{\nu F_\nu}^+$ [erg cm^{-2}s^{-1}]

Table B.7: SED: X-ray data from 1ES 1959+650 by *Beppo*-SAX. The data was taken from the NED archival and [Bac11].

ν [Hz]	νF_ν [erg cm^{-2}s^{-1}]	σ_ν^- [Hz]	σ_ν^+ [Hz]	$\sigma_{\nu F_\nu}^-$ [erg cm^{-2}s^{-1}]	$\sigma_{\nu F_\nu}^+$ [erg cm^{-2}s^{-1}]
9.55E+16	1.09E-10	2.30E+16	2.30E+16	2.10E-12	2.10E-12
1.38E+17	1.30E-10	1.93E+16	1.93E+16	2.55E-12	2.55E-12
1.72E+17	1.27E-10	1.45E+16	1.45E+16	2.52E-12	2.52E-12
2.00E+17	1.23E-10	1.33E+16	1.33E+16	2.45E-12	2.45E-12
2.27E+17	1.21E-10	1.45E+16	1.45E+16	2.31E-12	2.31E-12
2.55E+17	1.22E-10	1.33E+16	1.33E+16	2.43E-12	2.43E-12
2.83E+17	1.22E-10	1.45E+16	1.45E+16	2.38E-12	2.38E-12
3.13E+17	1.18E-10	1.57E+16	1.57E+16	2.35E-12	2.35E-12
3.47E+17	1.18E-10	1.81E+16	1.81E+16	2.31E-12	2.31E-12
3.88E+17	1.12E-10	2.30E+16	2.30E+16	2.24E-12	2.24E-12
4.47E+17	1.07E-10	3.63E+16	3.63E+16	2.14E-12	2.14E-12
5.49E+17	1.06E-10	6.53E+16	6.53E+16	2.11E-12	2.11E-12
7.51E+17	8.91E-11	1.37E+17	1.37E+17	1.77E-12	1.77E-12
1.57E+18	7.59E-11	6.87E+17	6.87E+17	1.64E-12	1.64E-12
1.06E+17	8.64E-11	2.90E+16	2.90E+16	2.86E-12	2.86E-12
1.60E+17	1.02E-10	2.42E+16	2.42E+16	3.33E-12	3.33E-12
2.04E+17	1.00E-10	2.06E+16	2.06E+16	3.30E-12	3.30E-12
2.44E+17	1.09E-10	1.93E+16	1.93E+16	3.53E-12	3.53E-12
2.85E+17	9.99E-11	2.18E+16	2.18E+16	3.29E-12	3.29E-12
3.31E+17	1.03E-10	2.42E+16	2.42E+16	3.39E-12	3.39E-12
3.87E+17	1.01E-10	3.14E+16	3.14E+16	3.35E-12	3.35E-12
4.79E+17	9.54E-11	6.05E+16	6.05E+16	3.16E-12	3.16E-12
6.93E+17	8.77E-11	1.54E+17	1.54E+17	2.90E-12	2.90E-12
1.31E+18	7.19E-11	4.68E+17	4.68E+17	2.89E-12	2.89E-12
9.55E+16	1.06E-10	2.06E+16	2.06E+16	3.43E-12	3.43E-12
1.33E+17	1.38E-10	1.69E+16	1.69E+16	4.50E-12	4.50E-12
1.64E+17	1.16E-10	1.45E+16	1.45E+16	3.76E-12	3.76E-12
1.91E+17	1.27E-10	1.21E+16	1.21E+16	4.09E-12	4.09E-12
2.15E+17	1.24E-10	1.21E+16	1.21E+16	4.02E-12	4.02E-12

ν [Hz]	νF_ν [erg cm^{-2}s^{-1}]	σ_ν^- [Hz]	σ_ν^+ [Hz]	$\sigma_{\nu F_\nu}^-$ [erg cm^{-2}s^{-1}]	$\sigma_{\nu F_\nu}^+$ [erg cm^{-2}s^{-1}]
2.38E+17	1.29E-10	1.09E+16	1.09E+16	4.24E-12	4.24E-12
2.61E+17	1.27E-10	1.21E+16	1.21E+16	4.07E-12	4.07E-12
2.85E+17	1.29E-10	1.21E+16	1.21E+16	4.18E-12	4.18E-12
3.11E+17	1.25E-10	1.33E+16	1.33E+16	4.05E-12	4.05E-12
3.39E+17	1.25E-10	1.45E+16	1.45E+16	4.09E-12	4.09E-12
3.70E+17	1.22E-10	1.69E+16	1.69E+16	4.00E-12	4.00E-12
4.07E+17	1.23E-10	2.06E+16	2.06E+16	4.07E-12	4.07E-12
4.62E+17	1.15E-10	3.39E+16	3.39E+16	3.78E-12	3.78E-12
5.45E+17	1.20E-10	4.96E+16	4.96E+16	3.97E-12	3.97E-12
6.80E+17	1.08E-10	8.46E+16	8.46E+16	3.59E-12	3.59E-12
8.97E+17	1.10E-10	1.33E+17	1.33E+17	3.65E-12	3.65E-12
1.68E+18	8.63E-11	6.50E+17	6.50E+17	3.29E-12	3.29E-12
9.31E+16	1.31E-10	2.06E+16	2.06E+16	2.61E-12	2.61E-12
1.29E+17	1.86E-10	1.57E+16	1.57E+16	3.67E-12	3.67E-12
1.58E+17	1.61E-10	1.33E+16	1.33E+16	3.17E-12	3.17E-12
1.84E+17	1.61E-10	1.21E+16	1.21E+16	3.08E-12	3.08E-12
2.07E+17	1.58E-10	1.09E+16	1.09E+16	3.15E-12	3.15E-12
2.29E+17	1.64E-10	1.09E+16	1.09E+16	3.21E-12	3.21E-12
2.50E+17	1.58E-10	1.09E+16	1.09E+16	3.15E-12	3.15E-12
2.72E+17	1.66E-10	1.09E+16	1.09E+16	3.27E-12	3.27E-12
2.95E+17	1.63E-10	1.21E+16	1.21E+16	3.17E-12	3.17E-12
3.19E+17	1.67E-10	1.21E+16	1.21E+16	3.31E-12	3.31E-12
3.46E+17	1.61E-10	1.45E+16	1.45E+16	3.11E-12	3.11E-12
3.77E+17	1.58E-10	1.69E+16	1.69E+16	3.10E-12	3.10E-12
4.15E+17	1.59E-10	2.06E+16	2.06E+16	3.14E-12	3.14E-12
4.66E+17	1.60E-10	3.02E+16	3.02E+16	3.18E-12	3.18E-12
5.42E+17	1.59E-10	4.59E+16	4.59E+16	3.14E-12	3.14E-12
6.59E+17	1.49E-10	7.13E+16	7.13E+16	2.96E-12	2.96E-12
8.38E+17	1.46E-10	1.08E+17	1.08E+17	2.90E-12	2.90E-12
1.17E+18	1.44E-10	2.25E+17	2.25E+17	2.86E-12	2.86E-12
1.81E+18	1.20E-10	4.18E+17	4.18E+17	4.58E-12	4.58E-12
1.04E+17	1.22E-10	3.14E+16	3.14E+16	2.43E-12	2.43E-12
1.58E+17	1.57E-10	2.30E+16	2.30E+16	3.13E-12	3.13E-12
2.00E+17	1.75E-10	1.81E+16	1.81E+16	3.43E-12	3.43E-12
2.36E+17	1.77E-10	1.81E+16	1.81E+16	3.44E-12	3.44E-12
2.72E+17	1.80E-10	1.81E+16	1.81E+16	3.54E-12	3.54E-12
3.11E+17	1.74E-10	2.06E+16	2.06E+16	3.41E-12	3.41E-12
3.54E+17	1.79E-10	2.30E+16	2.30E+16	3.55E-12	3.55E-12

ν [Hz]	νF_ν [erg cm^{-2}s^{-1}]	σ_ν^- [Hz]	σ_ν^+ [Hz]	$\sigma_{\nu F_\nu}^-$ [erg cm^{-2}s^{-1}]	$\sigma_{\nu F_\nu}^+$ [erg cm^{-2}s^{-1}]
4.07E+17	1.83E-10	3.02E+16	3.02E+16	3.63E-12	3.63E-12
4.90E+17	1.82E-10	5.20E+16	5.20E+16	3.63E-12	3.63E-12
6.44E+17	1.79E-10	1.03E+17	1.03E+17	3.57E-12	3.57E-12
9.77E+17	1.61E-10	2.30E+17	2.30E+17	3.22E-12	3.22E-12
1.76E+18	1.35E-10	5.49E+17	5.49E+17	4.69E-12	4.69E-12
9.43E+16	1.20E-10	2.18E+16	2.18E+16	2.30E-12	2.30E-12
1.31E+17	1.86E-10	1.45E+16	1.45E+16	3.70E-12	3.70E-12
1.58E+17	1.53E-10	1.33E+16	1.33E+16	3.00E-12	3.00E-12
1.83E+17	1.60E-10	1.09E+16	1.09E+16	3.16E-12	3.16E-12
2.04E+17	1.54E-10	1.09E+16	1.09E+16	3.03E-12	3.03E-12
2.26E+17	1.52E-10	1.09E+16	1.09E+16	3.01E-12	3.01E-12
2.48E+17	1.61E-10	1.09E+16	1.09E+16	3.08E-12	3.08E-12
2.70E+17	1.65E-10	1.09E+16	1.09E+16	3.18E-12	3.18E-12
2.93E+17	1.56E-10	1.21E+16	1.21E+16	3.00E-12	3.00E-12
3.17E+17	1.61E-10	1.21E+16	1.21E+16	3.16E-12	3.16E-12
3.42E+17	1.58E-10	1.33E+16	1.33E+16	3.11E-12	3.11E-12
3.71E+17	1.57E-10	1.57E+16	1.57E+16	3.07E-12	3.07E-12
4.05E+17	1.60E-10	1.81E+16	1.81E+16	3.16E-12	3.16E-12
4.51E+17	1.54E-10	2.78E+16	2.78E+16	3.01E-12	3.01E-12
5.19E+17	1.48E-10	3.99E+16	3.99E+16	2.94E-12	2.94E-12
6.23E+17	1.46E-10	6.41E+16	6.41E+16	2.91E-12	2.91E-12
7.80E+17	1.39E-10	9.31E+16	9.31E+16	2.77E-12	2.77E-12
1.05E+18	1.32E-10	1.74E+17	1.74E+17	2.64E-12	2.64E-12
1.66E+18	1.12E-10	4.41E+17	4.41E+17	3.20E-12	3.20E-12
9.31E+16	1.28E-10	2.06E+16	2.06E+16	2.49E-12	2.49E-12
1.28E+17	1.26E-10	1.45E+16	1.45E+16	2.50E-12	2.50E-12
1.56E+17	1.52E-10	1.33E+16	1.33E+16	3.02E-12	3.02E-12
1.80E+17	1.66E-10	1.09E+16	1.09E+16	3.25E-12	3.25E-12
2.02E+17	1.57E-10	1.09E+16	1.09E+16	3.05E-12	3.05E-12
2.24E+17	1.61E-10	1.09E+16	1.09E+16	3.09E-12	3.09E-12
2.45E+17	1.58E-10	1.09E+16	1.09E+16	3.05E-12	3.05E-12
2.67E+17	1.57E-10	1.09E+16	1.09E+16	3.09E-12	3.09E-12
2.90E+17	1.53E-10	1.21E+16	1.21E+16	2.97E-12	2.97E-12
3.14E+17	1.56E-10	1.21E+16	1.21E+16	3.09E-12	3.09E-12
3.40E+17	1.56E-10	1.33E+16	1.33E+16	3.07E-12	3.07E-12
3.69E+17	1.56E-10	1.57E+16	1.57E+16	3.03E-12	3.03E-12
4.04E+17	1.47E-10	1.93E+16	1.93E+16	2.92E-12	2.92E-12
4.51E+17	1.48E-10	2.78E+16	2.78E+16	2.95E-12	2.95E-12

ν [Hz]	νF_ν [erg cm^{-2}s^{-1}]	σ_ν^- [Hz]	σ_ν^+ [Hz]	$\sigma_{\nu F_\nu}^-$ [erg cm^{-2}s^{-1}]	$\sigma_{\nu F_\nu}^+$ [erg cm^{-2}s^{-1}]
5.19E+17	1.50E-10	3.99E+16	3.99E+16	2.96E-12	2.96E-12
6.28E+17	1.37E-10	6.89E+16	6.89E+16	2.74E-12	2.74E-12
7.97E+17	1.34E-10	1.00E+17	1.00E+17	2.67E-12	2.67E-12
1.11E+18	1.26E-10	2.08E+17	2.08E+17	2.52E-12	2.52E-12
1.70E+18	1.05E-10	3.88E+17	3.88E+17	3.61E-12	3.61E-12
9.43E+16	1.22E-10	2.18E+16	2.18E+16	2.37E-12	2.37E-12
1.33E+17	1.65E-10	1.69E+16	1.69E+16	3.23E-12	3.23E-12
1.63E+17	1.46E-10	1.33E+16	1.33E+16	2.91E-12	2.91E-12
1.89E+17	1.50E-10	1.21E+16	1.21E+16	2.94E-12	2.94E-12
2.13E+17	1.49E-10	1.21E+16	1.21E+16	2.91E-12	2.91E-12
2.37E+17	1.44E-10	1.21E+16	1.21E+16	2.80E-12	2.80E-12
2.61E+17	1.50E-10	1.21E+16	1.21E+16	2.91E-12	2.91E-12
2.87E+17	1.45E-10	1.33E+16	1.33E+16	2.79E-12	2.79E-12
3.13E+17	1.46E-10	1.33E+16	1.33E+16	2.89E-12	2.89E-12
3.42E+17	1.40E-10	1.57E+16	1.57E+16	2.74E-12	2.74E-12
3.77E+17	1.35E-10	1.93E+16	1.93E+16	2.66E-12	2.66E-12
4.23E+17	1.28E-10	2.66E+16	2.66E+16	2.54E-12	2.54E-12
4.91E+17	1.28E-10	4.11E+16	4.11E+16	2.54E-12	2.54E-12
6.08E+17	1.21E-10	7.62E+16	7.62E+16	2.42E-12	2.42E-12
8.25E+17	1.05E-10	1.40E+17	1.40E+17	2.10E-12	2.10E-12
1.48E+18	8.36E-11	5.10E+17	5.10E+17	1.94E-12	1.94E-12
9.43E+16	1.26E-10	2.18E+16	2.18E+16	2.46E-12	2.46E-12
1.33E+17	1.68E-10	1.69E+16	1.69E+16	3.35E-12	3.35E-12
1.64E+17	1.42E-10	1.45E+16	1.45E+16	2.80E-12	2.80E-12
1.91E+17	1.50E-10	1.21E+16	1.21E+16	2.99E-12	2.99E-12
2.16E+17	1.46E-10	1.33E+16	1.33E+16	2.80E-12	2.80E-12
2.42E+17	1.47E-10	1.21E+16	1.21E+16	2.91E-12	2.91E-12
2.67E+17	1.47E-10	1.33E+16	1.33E+16	2.81E-12	2.81E-12
2.94E+17	1.48E-10	1.33E+16	1.33E+16	2.91E-12	2.91E-12
3.22E+17	1.43E-10	1.45E+16	1.45E+16	2.85E-12	2.85E-12
3.53E+17	1.42E-10	1.69E+16	1.69E+16	2.77E-12	2.77E-12
3.92E+17	1.32E-10	2.18E+16	2.18E+16	2.62E-12	2.62E-12
4.45E+17	1.34E-10	3.14E+16	3.14E+16	2.67E-12	2.67E-12
5.32E+17	1.24E-10	5.56E+16	5.56E+16	2.48E-12	2.48E-12
7.00E+17	1.07E-10	1.12E+17	1.12E+17	2.13E-12	2.13E-12
1.10E+18	9.68E-11	2.89E+17	2.89E+17	1.93E-12	1.93E-12
1.76E+18	7.18E-11	3.71E+17	3.71E+17	3.54E-12	3.54E-12

Table B.8: SED: Infrared data from 1ES 1959+650 by *Spitzer*. The data is taken from [Bac11].

ν [Hz]	νF_ν [erg cm^{-2}s^{-1}]	σ_ν^- [Hz]	σ_ν^+ [Hz]	$\sigma_{\nu F_\nu}^-$ [erg cm^{-2}s^{-1}]	$\sigma_{\nu F_\nu}^+$ [erg cm^{-2}s^{-1}]
5.78E+13	6.07E-12	–	–	6.72E-16	6.72E-16
5.75E+13	6.75E-12	–	–	4.53E-16	4.53E-16
5.71E+13	6.77E-12	–	–	4.99E-16	4.99E-16
5.68E+13	6.94E-12	–	–	5.92E-16	5.92E-16
5.65E+13	7.20E-12	–	–	3.92E-16	3.92E-16
5.62E+13	6.83E-12	–	–	3.86E-16	3.86E-16
5.58E+13	7.03E-12	–	–	4.08E-16	4.08E-16
5.55E+13	7.32E-12	–	–	3.95E-16	3.95E-16
5.52E+13	7.22E-12	–	–	4.07E-16	4.07E-16
5.49E+13	6.70E-12	–	–	3.81E-16	3.81E-16
5.46E+13	6.14E-12	–	–	4.10E-16	4.10E-16
5.43E+13	6.66E-12	–	–	3.58E-16	3.58E-16
5.40E+13	7.51E-12	–	–	3.67E-16	3.67E-16
5.37E+13	7.35E-12	–	–	3.94E-16	3.94E-16
5.34E+13	6.57E-12	–	–	4.00E-16	4.00E-16
5.32E+13	6.47E-12	–	–	3.86E-16	3.86E-16
5.29E+13	6.35E-12	–	–	3.86E-16	3.86E-16
5.26E+13	6.47E-12	–	–	4.02E-16	4.02E-16
5.23E+13	5.72E-12	–	–	3.92E-16	3.92E-16
5.20E+13	5.94E-12	–	–	3.83E-16	3.83E-16
5.18E+13	5.74E-12	–	–	3.74E-16	3.74E-16
5.15E+13	6.83E-12	–	–	3.78E-16	3.78E-16
5.12E+13	6.76E-12	–	–	3.68E-16	3.68E-16
5.10E+13	6.08E-12	–	–	4.33E-16	4.33E-16
5.07E+13	6.56E-12	–	–	3.75E-16	3.75E-16
5.04E+13	6.68E-12	–	–	4.01E-16	4.01E-16
5.02E+13	6.15E-12	–	–	3.64E-16	3.64E-16
4.99E+13	5.80E-12	–	–	3.54E-16	3.54E-16
4.97E+13	5.90E-12	–	–	3.40E-16	3.40E-16
4.94E+13	6.29E-12	–	–	3.80E-16	3.80E-16
4.92E+13	6.44E-12	–	–	3.51E-16	3.51E-16
4.90E+13	6.52E-12	–	–	3.34E-16	3.34E-16
4.87E+13	6.45E-12	–	–	3.21E-16	3.21E-16
4.85E+13	6.41E-12	–	–	3.04E-16	3.04E-16
4.82E+13	6.08E-12	–	–	3.54E-16	3.54E-16

ν [Hz]	νF_ν [erg cm^{-2}s^{-1}]	σ_ν^- [Hz]	σ_ν^+ [Hz]	$\sigma_{\nu F_\nu}^-$ [erg cm^{-2}s^{-1}]	$\sigma_{\nu F_\nu}^+$ [erg cm^{-2}s^{-1}]
4.80E+13	5.54E-12	–	–	4.01E-16	4.01E-16
4.78E+13	5.54E-12	–	–	3.72E-16	3.72E-16
4.75E+13	6.23E-12	–	–	3.35E-16	3.35E-16
4.73E+13	6.44E-12	–	–	3.32E-16	3.32E-16
4.71E+13	6.40E-12	–	–	3.26E-16	3.26E-16
4.69E+13	5.91E-12	–	–	3.27E-16	3.27E-16
4.67E+13	6.65E-12	–	–	3.21E-16	3.21E-16
4.64E+13	6.52E-12	–	–	3.16E-16	3.16E-16
4.62E+13	6.42E-12	–	–	3.14E-16	3.14E-16
4.60E+13	6.71E-12	–	–	3.33E-16	3.33E-16
4.58E+13	6.56E-12	–	–	3.54E-16	3.54E-16
4.56E+13	6.28E-12	–	–	3.97E-16	3.97E-16
4.54E+13	5.98E-12	–	–	3.91E-16	3.91E-16
4.52E+13	5.94E-12	–	–	3.97E-16	3.97E-16
4.50E+13	6.09E-12	–	–	3.83E-16	3.83E-16
4.48E+13	6.19E-12	–	–	3.84E-16	3.84E-16
4.46E+13	5.50E-12	–	–	4.62E-16	4.62E-16
4.44E+13	5.23E-12	–	–	4.45E-16	4.45E-16
4.42E+13	5.60E-12	–	–	4.54E-16	4.54E-16
4.40E+13	6.44E-12	–	–	4.96E-16	4.96E-16
4.38E+13	5.24E-12	–	–	9.34E-16	9.34E-16
4.36E+13	5.82E-12	–	–	4.88E-16	4.88E-16
4.34E+13	5.26E-12	–	–	5.30E-16	5.30E-16
4.32E+13	4.93E-12	–	–	5.55E-16	5.55E-16
4.30E+13	5.62E-12	–	–	6.57E-16	6.57E-16
4.28E+13	5.94E-12	–	–	7.02E-16	7.02E-16
4.26E+13	5.46E-12	–	–	6.30E-16	6.30E-16
4.25E+13	5.07E-12	–	–	6.36E-16	6.36E-16
4.23E+13	5.64E-12	–	–	5.75E-16	5.75E-16
4.21E+13	5.53E-12	–	–	5.21E-16	5.21E-16
4.19E+13	6.09E-12	–	–	5.07E-16	5.07E-16
4.17E+13	6.02E-12	–	–	5.00E-16	5.00E-16
4.16E+13	6.04E-12	–	–	5.15E-16	5.15E-16
4.14E+13	6.01E-12	–	–	5.30E-16	5.30E-16
4.12E+13	5.78E-12	–	–	7.46E-16	7.46E-16
4.11E+13	6.14E-12	–	–	5.34E-16	5.34E-16
4.09E+13	5.70E-12	–	–	5.20E-16	5.20E-16
4.07E+13	4.79E-12	–	–	5.33E-16	5.33E-16

ν [Hz]	νF_ν [erg cm^{-2}s^{-1}]	σ_ν^- [Hz]	σ_ν^+ [Hz]	$\sigma_{\nu F_\nu}^-$ [erg cm^{-2}s^{-1}]	$\sigma_{\nu F_\nu}^+$ [erg cm^{-2}s^{-1}]
4.05E+13	5.13E-12	–	–	4.96E-16	4.96E-16
4.04E+13	5.80E-12	–	–	4.88E-16	4.88E-16
4.02E+13	5.45E-12	–	–	5.10E-16	5.10E-16
4.01E+13	4.92E-12	–	–	5.15E-16	5.15E-16
3.99E+13	6.05E-12	–	–	5.86E-16	5.86E-16
3.97E+13	6.54E-12	–	–	6.31E-16	6.31E-16
3.96E+13	4.20E-12	–	–	4.10E-16	4.10E-16
4.09E+13	2.96E-12	–	–	3.14E-16	3.14E-16
4.05E+13	6.06E-12	–	–	3.27E-16	3.27E-16
4.02E+13	6.14E-12	–	–	3.17E-16	3.17E-16
3.99E+13	5.61E-12	–	–	2.93E-16	2.93E-16
3.96E+13	5.01E-12	–	–	2.79E-16	2.79E-16
3.93E+13	5.30E-12	–	–	2.93E-16	2.93E-16
3.90E+13	5.22E-12	–	–	2.83E-16	2.83E-16
3.87E+13	5.56E-12	–	–	2.57E-16	2.57E-16
3.84E+13	4.99E-12	–	–	2.43E-16	2.43E-16
3.81E+13	6.20E-12	–	–	2.42E-16	2.42E-16
3.78E+13	5.51E-12	–	–	2.35E-16	2.35E-16
3.75E+13	5.32E-12	–	–	2.18E-16	2.18E-16
3.72E+13	5.84E-12	–	–	2.14E-16	2.14E-16
3.69E+13	5.89E-12	–	–	1.99E-16	1.99E-16
3.67E+13	5.57E-12	–	–	2.07E-16	2.07E-16
3.87E+13	5.56E-12	–	–	2.57E-16	2.57E-16
3.84E+13	4.99E-12	–	–	2.43E-16	2.43E-16
3.81E+13	6.20E-12	–	–	2.42E-16	2.42E-16
3.78E+13	5.51E-12	–	–	2.35E-16	2.35E-16
3.75E+13	5.32E-12	–	–	2.18E-16	2.18E-16
3.72E+13	5.84E-12	–	–	2.14E-16	2.14E-16
3.69E+13	5.89E-12	–	–	1.99E-16	1.99E-16
3.67E+13	5.57E-12	–	–	2.07E-16	2.07E-16
3.64E+13	5.69E-12	–	–	2.03E-16	2.03E-16
3.61E+13	5.78E-12	–	–	2.05E-16	2.05E-16
3.59E+13	5.42E-12	–	–	1.95E-16	1.95E-16
3.56E+13	5.59E-12	–	–	1.92E-16	1.92E-16
3.53E+13	6.14E-12	–	–	2.28E-16	2.28E-16
3.51E+13	5.82E-12	–	–	3.78E-16	3.78E-16
3.99E+13	5.42E-12	–	–	3.39E-16	3.39E-16
3.96E+13	5.33E-12	–	–	3.58E-16	3.58E-16

ν [Hz]	νF_ν [erg cm^{-2}s^{-1}]	σ_ν^- [Hz]	σ_ν^+ [Hz]	$\sigma_{\nu F_\nu}^-$ [erg cm^{-2}s^{-1}]	$\sigma_{\nu F_\nu}^+$ [erg cm^{-2}s^{-1}]
3.93E+13	5.94E-12	–	–	3.20E-16	3.20E-16
3.90E+13	5.74E-12	–	–	2.76E-16	2.76E-16
3.87E+13	5.79E-12	–	–	2.53E-16	2.53E-16
3.84E+13	5.29E-12	–	–	2.58E-16	2.58E-16
3.81E+13	5.70E-12	–	–	2.39E-16	2.39E-16
3.78E+13	5.96E-12	–	–	2.26E-16	2.26E-16
3.75E+13	5.63E-12	–	–	2.15E-16	2.15E-16
3.72E+13	5.49E-12	–	–	2.00E-16	2.00E-16
3.69E+13	5.93E-12	–	–	1.85E-16	1.85E-16
3.67E+13	5.65E-12	–	–	1.79E-16	1.79E-16
3.64E+13	5.53E-12	–	–	1.73E-16	1.73E-16
3.61E+13	5.73E-12	–	–	1.78E-16	1.78E-16
3.59E+13	5.45E-12	–	–	1.73E-16	1.73E-16
3.56E+13	5.48E-12	–	–	1.64E-16	1.64E-16
3.53E+13	5.44E-12	–	–	1.60E-16	1.60E-16
3.51E+13	5.22E-12	–	–	1.61E-16	1.61E-16
3.48E+13	5.12E-12	–	–	1.64E-16	1.64E-16
3.46E+13	4.85E-12	–	–	1.61E-16	1.61E-16
3.44E+13	5.24E-12	–	–	1.49E-16	1.49E-16
3.41E+13	5.23E-12	–	–	1.57E-16	1.57E-16
3.39E+13	5.16E-12	–	–	1.46E-16	1.46E-16
3.37E+13	5.03E-12	–	–	1.52E-16	1.52E-16
3.34E+13	4.97E-12	–	–	1.57E-16	1.57E-16
3.32E+13	5.03E-12	–	–	1.65E-16	1.65E-16
3.30E+13	5.14E-12	–	–	1.62E-16	1.62E-16
3.28E+13	5.06E-12	–	–	1.72E-16	1.72E-16
3.26E+13	5.00E-12	–	–	1.68E-16	1.68E-16
3.23E+13	4.94E-12	–	–	1.69E-16	1.69E-16
3.21E+13	4.90E-12	–	–	1.72E-16	1.72E-16
3.19E+13	5.11E-12	–	–	3.02E-16	3.02E-16
3.17E+13	4.89E-12	–	–	3.79E-16	3.79E-16
3.15E+13	5.48E-12	–	–	3.67E-16	3.67E-16
3.13E+13	4.69E-12	–	–	3.38E-16	3.38E-16
3.11E+13	4.72E-12	–	–	3.14E-16	3.14E-16
3.09E+13	4.65E-12	–	–	1.80E-16	1.80E-16
3.04E+13	4.59E-12	–	–	1.73E-16	1.73E-16
3.02E+13	4.55E-12	–	–	1.51E-16	1.51E-16
3.00E+13	4.99E-12	–	–	2.43E-16	2.43E-16

ν [Hz]	νF_ν [erg cm^{-2}s^{-1}]	σ_ν^- [Hz]	σ_ν^+ [Hz]	$\sigma_{\nu F_\nu}^-$ [erg cm^{-2}s^{-1}]	$\sigma_{\nu F_\nu}^+$ [erg cm^{-2}s^{-1}]
2.98E+13	4.68E-12	–	–	1.43E-16	1.43E-16
2.96E+13	4.60E-12	–	–	1.38E-16	1.38E-16
2.95E+13	4.60E-12	–	–	1.26E-16	1.26E-16
2.93E+13	4.68E-12	–	–	1.50E-16	1.50E-16
2.91E+13	4.55E-12	–	–	1.26E-16	1.26E-16
2.89E+13	4.56E-12	–	–	1.22E-16	1.22E-16
2.88E+13	4.53E-12	–	–	1.29E-16	1.29E-16
2.86E+13	4.39E-12	–	–	1.27E-16	1.27E-16
2.84E+13	4.57E-12	–	–	1.22E-16	1.22E-16
2.83E+13	4.70E-12	–	–	1.20E-16	1.20E-16
2.81E+13	4.83E-12	–	–	1.27E-16	1.27E-16
2.80E+13	4.45E-12	–	–	1.30E-16	1.30E-16
2.78E+13	4.59E-12	–	–	1.31E-16	1.31E-16
2.77E+13	4.46E-12	–	–	1.28E-16	1.28E-16
2.75E+13	4.36E-12	–	–	1.31E-16	1.31E-16
2.74E+13	4.69E-12	–	–	1.47E-16	1.47E-16
2.72E+13	4.72E-12	–	–	1.37E-16	1.37E-16
2.71E+13	4.56E-12	–	–	1.42E-16	1.42E-16
2.69E+13	4.39E-12	–	–	1.31E-16	1.31E-16
2.68E+13	4.53E-12	–	–	1.34E-16	1.34E-16
2.66E+13	4.48E-12	–	–	1.41E-16	1.41E-16
2.65E+13	4.13E-12	–	–	1.41E-16	1.41E-16
2.63E+13	4.40E-12	–	–	1.38E-16	1.38E-16
2.62E+13	4.46E-12	–	–	1.46E-16	1.46E-16
2.61E+13	4.39E-12	–	–	1.52E-16	1.52E-16
2.59E+13	4.35E-12	–	–	1.68E-16	1.68E-16
2.58E+13	4.40E-12	–	–	1.96E-16	1.96E-16
2.57E+13	4.74E-12	–	–	1.91E-16	1.91E-16
2.55E+13	5.00E-12	–	–	1.84E-16	1.84E-16
2.54E+13	4.67E-12	–	–	1.73E-16	1.73E-16
2.53E+13	4.65E-12	–	–	1.84E-16	1.84E-16
2.51E+13	4.60E-12	–	–	1.89E-16	1.89E-16
2.50E+13	4.59E-12	–	–	1.74E-16	1.74E-16
2.49E+13	4.55E-12	–	–	1.81E-16	1.81E-16
2.48E+13	4.51E-12	–	–	1.94E-16	1.94E-16
2.46E+13	4.59E-12	–	–	1.80E-16	1.80E-16
2.45E+13	4.24E-12	–	–	1.65E-16	1.65E-16
2.44E+13	4.09E-12	–	–	2.48E-16	2.48E-16

ν [Hz]	νF_ν [erg cm^{-2}s^{-1}]	σ_ν^- [Hz]	σ_ν^+ [Hz]	$\sigma_{\nu F_\nu}^-$ [erg cm^{-2}s^{-1}]	$\sigma_{\nu F_\nu}^+$ [erg cm^{-2}s^{-1}]
2.43E+13	4.29E-12	–	–	1.71E-16	1.71E-16
2.42E+13	4.18E-12	–	–	2.76E-16	2.76E-16
2.40E+13	4.22E-12	–	–	1.65E-16	1.65E-16
2.39E+13	4.37E-12	–	–	1.54E-16	1.54E-16
2.38E+13	4.34E-12	–	–	1.47E-16	1.47E-16
2.37E+13	4.23E-12	–	–	1.40E-16	1.40E-16
2.36E+13	4.30E-12	–	–	1.44E-16	1.44E-16
2.35E+13	4.32E-12	–	–	1.48E-16	1.48E-16
2.34E+13	4.36E-12	–	–	1.83E-16	1.83E-16
2.32E+13	4.23E-12	–	–	1.92E-16	1.92E-16
2.31E+13	4.34E-12	–	–	1.85E-16	1.85E-16
2.30E+13	4.32E-12	–	–	1.54E-16	1.54E-16
2.29E+13	4.23E-12	–	–	1.45E-16	1.45E-16
2.28E+13	4.32E-12	–	–	1.49E-16	1.49E-16
2.27E+13	4.29E-12	–	–	1.56E-16	1.56E-16
2.26E+13	4.33E-12	–	–	1.52E-16	1.52E-16
2.25E+13	4.25E-12	–	–	1.54E-16	1.54E-16
2.24E+13	3.92E-12	–	–	1.62E-16	1.62E-16
2.23E+13	4.14E-12	–	–	1.65E-16	1.65E-16
2.22E+13	3.92E-12	–	–	1.63E-16	1.63E-16
2.21E+13	4.07E-12	–	–	1.76E-16	1.76E-16
2.20E+13	3.97E-12	–	–	1.81E-16	1.81E-16
2.19E+13	3.97E-12	–	–	1.83E-16	1.83E-16
2.18E+13	3.39E-12	–	–	1.98E-16	1.98E-16
2.17E+13	3.72E-12	–	–	1.97E-16	1.97E-16
2.16E+13	4.02E-12	–	–	2.02E-16	2.02E-16
2.15E+13	4.11E-12	–	–	2.07E-16	2.07E-16
2.14E+13	4.06E-12	–	–	2.24E-16	2.24E-16
2.13E+13	3.97E-12	–	–	2.31E-16	2.31E-16
2.13E+13	3.98E-12	–	–	2.37E-16	2.37E-16
2.12E+13	4.38E-12	–	–	2.35E-16	2.35E-16
2.13E+13	4.25E-12	–	–	2.88E-16	2.88E-16
2.12E+13	3.79E-12	–	–	2.68E-16	2.68E-16
2.11E+13	4.24E-12	–	–	2.07E-16	2.07E-16
2.09E+13	4.14E-12	–	–	1.68E-16	1.68E-16
2.08E+13	3.87E-12	–	–	1.84E-16	1.84E-16
2.07E+13	4.15E-12	–	–	2.31E-16	2.31E-16
2.06E+13	4.34E-12	–	–	2.29E-16	2.29E-16

ν [Hz]	νF_ν [erg cm^{-2}s^{-1}]	σ_ν^- [Hz]	σ_ν^+ [Hz]	$\sigma_{\nu F_\nu}^-$ [erg cm^{-2}s^{-1}]	$\sigma_{\nu F_\nu}^+$ [erg cm^{-2}s^{-1}]
2.05E+13	4.23E-12	–	–	2.47E-16	2.47E-16
2.03E+13	4.10E-12	–	–	2.38E-16	2.38E-16
2.02E+13	3.89E-12	–	–	2.65E-16	2.65E-16
2.01E+13	4.01E-12	–	–	2.83E-16	2.83E-16
2.00E+13	4.21E-12	–	–	2.08E-16	2.08E-16
1.99E+13	4.16E-12	–	–	1.96E-16	1.96E-16
1.98E+13	4.67E-12	–	–	1.83E-16	1.83E-16
1.97E+13	4.11E-12	–	–	1.81E-16	1.81E-16
1.95E+13	4.04E-12	–	–	2.02E-16	2.02E-16
1.94E+13	4.08E-12	–	–	1.92E-16	1.92E-16
1.93E+13	3.92E-12	–	–	1.86E-16	1.86E-16
1.92E+13	3.97E-12	–	–	1.89E-16	1.89E-16
1.91E+13	3.87E-12	–	–	1.66E-16	1.66E-16
1.90E+13	3.99E-12	–	–	1.79E-16	1.79E-16
1.89E+13	3.89E-12	–	–	2.06E-16	2.06E-16
1.88E+13	4.58E-12	–	–	2.54E-16	2.54E-16
1.87E+13	3.81E-12	–	–	3.21E-16	3.21E-16
1.86E+13	4.17E-12	–	–	2.60E-16	2.60E-16
1.85E+13	3.56E-12	–	–	2.36E-16	2.36E-16
1.84E+13	3.56E-12	–	–	1.97E-16	1.97E-16
1.83E+13	3.75E-12	–	–	1.95E-16	1.95E-16
1.82E+13	3.75E-12	–	–	2.20E-16	2.20E-16
1.81E+13	3.72E-12	–	–	1.95E-16	1.95E-16
1.81E+13	3.65E-12	–	–	1.77E-16	1.77E-16
1.80E+13	3.58E-12	–	–	1.97E-16	1.97E-16
1.79E+13	3.48E-12	–	–	2.00E-16	2.00E-16
1.78E+13	3.17E-12	–	–	2.50E-16	2.50E-16
1.77E+13	3.33E-12	–	–	3.03E-16	3.03E-16
1.76E+13	3.75E-12	–	–	2.38E-16	2.38E-16
1.75E+13	4.21E-12	–	–	2.87E-16	2.87E-16
1.74E+13	3.61E-12	–	–	3.56E-16	3.56E-16
1.73E+13	3.68E-12	–	–	2.36E-16	2.36E-16
1.73E+13	3.78E-12	–	–	2.43E-16	2.43E-16
1.72E+13	3.98E-12	–	–	1.93E-16	1.93E-16
1.71E+13	3.69E-12	–	–	1.93E-16	1.93E-16
1.70E+13	3.80E-12	–	–	2.09E-16	2.09E-16
1.69E+13	3.50E-12	–	–	2.20E-16	2.20E-16
1.69E+13	3.10E-12	–	–	2.28E-16	2.28E-16

ν [Hz]	νF_ν [erg cm^{-2}s^{-1}]	σ_ν^- [Hz]	σ_ν^+ [Hz]	$\sigma_{\nu F_\nu}^-$ [erg cm^{-2}s^{-1}]	$\sigma_{\nu F_\nu}^+$ [erg cm^{-2}s^{-1}]
1.68E+13	3.21E-12	–	–	2.84E-16	2.84E-16
1.67E+13	3.82E-12	–	–	2.89E-16	2.89E-16
1.66E+13	3.48E-12	–	–	3.01E-16	3.01E-16
1.65E+13	3.41E-12	–	–	2.85E-16	2.85E-16
1.65E+13	3.68E-12	–	–	3.41E-16	3.41E-16
1.64E+13	3.57E-12	–	–	2.88E-16	2.88E-16
1.63E+13	3.71E-12	–	–	2.60E-16	2.60E-16
1.62E+13	3.31E-12	–	–	2.71E-16	2.71E-16
1.62E+13	3.94E-12	–	–	2.86E-16	2.86E-16
1.60E+13	3.38E-12	–	–	2.45E-16	2.45E-16
1.59E+13	3.30E-12	–	–	2.46E-16	2.46E-16
1.59E+13	3.35E-12	–	–	2.64E-16	2.64E-16
1.58E+13	3.63E-12	–	–	2.49E-16	2.49E-16
1.57E+13	3.66E-12	–	–	2.52E-16	2.52E-16
1.57E+13	4.05E-12	–	–	3.37E-16	3.37E-16
1.56E+13	3.05E-12	–	–	3.87E-16	3.87E-16
1.55E+13	4.10E-12	–	–	3.61E-16	3.61E-16
1.55E+13	4.73E-12	–	–	5.01E-16	5.01E-16
1.53E+13	4.02E-12	–	–	3.54E-16	3.54E-16
1.53E+13	3.79E-12	–	–	3.65E-16	3.65E-16
1.52E+13	3.45E-12	–	–	3.17E-16	3.17E-16
1.51E+13	3.59E-12	–	–	2.96E-16	2.96E-16
1.51E+13	3.79E-12	–	–	3.10E-16	3.10E-16
1.50E+13	4.33E-12	–	–	3.72E-16	3.72E-16
1.49E+13	3.68E-12	–	–	4.12E-16	4.12E-16
1.49E+13	2.96E-12	–	–	3.69E-16	3.69E-16
1.47E+13	2.55E-12	–	–	6.59E-16	6.59E-16
1.46E+13	3.73E-12	–	–	4.42E-16	4.42E-16
1.46E+13	3.93E-12	–	–	4.66E-16	4.66E-16
1.44E+13	4.08E-12	–	–	3.94E-16	3.94E-16
1.44E+13	3.80E-12	–	–	4.28E-16	4.28E-16
1.56E+13	2.13E-12	–	–	1.60E-16	1.60E-16
1.55E+13	3.35E-12	–	–	2.51E-16	2.51E-16
1.53E+13	3.62E-12	–	–	2.97E-16	2.97E-16
1.52E+13	3.41E-12	–	–	1.93E-16	1.93E-16
1.51E+13	3.54E-12	–	–	2.21E-16	2.21E-16
1.49E+13	3.91E-12	–	–	2.11E-16	2.11E-16
1.48E+13	3.09E-12	–	–	2.17E-16	2.17E-16

ν [Hz]	νF_ν [erg cm^{-2}s^{-1}]	σ_ν^- [Hz]	σ_ν^+ [Hz]	$\sigma_{\nu F_\nu}^-$ [erg cm^{-2}s^{-1}]	$\sigma_{\nu F_\nu}^+$ [erg cm^{-2}s^{-1}]
1.47E+13	3.41E-12	–	–	2.06E-16	2.06E-16
1.46E+13	3.81E-12	–	–	2.31E-16	2.31E-16
1.44E+13	3.50E-12	–	–	2.04E-16	2.04E-16
1.43E+13	3.21E-12	–	–	2.14E-16	2.14E-16
1.42E+13	3.05E-12	–	–	1.63E-16	1.63E-16
1.41E+13	2.88E-12	–	–	1.63E-16	1.63E-16
1.47E+13	3.11E-12	–	–	4.38E-16	4.38E-16
1.46E+13	3.48E-12	–	–	3.25E-16	3.25E-16
1.44E+13	2.76E-12	–	–	5.43E-16	5.43E-16
1.43E+13	3.07E-12	–	–	3.35E-16	3.35E-16
1.42E+13	2.81E-12	–	–	2.27E-16	2.27E-16
1.41E+13	3.26E-12	–	–	2.67E-16	2.67E-16
1.40E+13	3.44E-12	–	–	2.49E-16	2.49E-16
1.39E+13	2.67E-12	–	–	2.34E-16	2.34E-16
1.38E+13	3.03E-12	–	–	1.98E-16	1.98E-16
1.37E+13	3.62E-12	–	–	2.25E-16	2.25E-16
1.36E+13	3.36E-12	–	–	2.03E-16	2.03E-16
1.35E+13	3.31E-12	–	–	1.63E-16	1.63E-16
1.34E+13	2.87E-12	–	–	1.72E-16	1.72E-16
1.33E+13	3.29E-12	–	–	1.92E-16	1.92E-16
1.32E+13	3.13E-12	–	–	2.18E-16	2.18E-16
1.31E+13	2.74E-12	–	–	2.08E-16	2.08E-16
1.30E+13	2.96E-12	–	–	1.55E-16	1.55E-16
1.29E+13	3.18E-12	–	–	1.81E-16	1.81E-16
1.28E+13	3.03E-12	–	–	2.26E-16	2.26E-16
1.27E+13	3.13E-12	–	–	1.66E-16	1.66E-16
1.26E+13	3.13E-12	–	–	1.43E-16	1.43E-16
1.25E+13	3.16E-12	–	–	1.58E-16	1.58E-16
1.24E+13	3.15E-12	–	–	1.88E-16	1.88E-16
1.23E+13	2.90E-12	–	–	1.73E-16	1.73E-16
1.22E+13	2.92E-12	–	–	1.60E-16	1.60E-16
1.22E+13	2.92E-12	–	–	2.29E-16	2.29E-16
1.21E+13	3.17E-12	–	–	1.62E-16	1.62E-16
1.20E+13	2.75E-12	–	–	1.83E-16	1.83E-16
1.19E+13	3.01E-12	–	–	1.81E-16	1.81E-16
1.18E+13	3.21E-12	–	–	1.84E-16	1.84E-16
1.17E+13	3.05E-12	–	–	1.62E-16	1.62E-16
1.16E+13	3.14E-12	–	–	1.55E-16	1.55E-16

ν [Hz]	νF_ν [erg cm^{-2}s^{-1}]	σ_ν^- [Hz]	σ_ν^+ [Hz]	$\sigma_{\nu F_\nu}^-$ [erg cm^{-2}s^{-1}]	$\sigma_{\nu F_\nu}^+$ [erg cm^{-2}s^{-1}]
1.13E+13	2.75E-12	–	–	1.25E-16	1.25E-16
1.12E+13	2.90E-12	–	–	1.54E-16	1.54E-16
1.12E+13	3.07E-12	–	–	1.67E-16	1.67E-16
1.11E+13	2.87E-12	–	–	1.54E-16	1.54E-16
1.10E+13	3.09E-12	–	–	1.57E-16	1.57E-16
1.10E+13	2.93E-12	–	–	1.56E-16	1.56E-16
1.09E+13	3.41E-12	–	–	1.42E-16	1.42E-16
1.08E+13	3.84E-12	–	–	1.76E-16	1.76E-16
1.08E+13	2.56E-12	–	–	1.99E-16	1.99E-16
1.07E+13	2.40E-12	–	–	2.02E-16	2.02E-16
1.06E+13	2.94E-12	–	–	2.52E-16	2.52E-16
1.06E+13	2.67E-12	–	–	1.83E-16	1.83E-16
1.05E+13	2.65E-12	–	–	1.57E-16	1.57E-16
1.04E+13	2.67E-12	–	–	1.57E-16	1.57E-16
1.04E+13	2.79E-12	–	–	1.77E-16	1.77E-16
1.03E+13	2.17E-12	–	–	1.69E-16	1.69E-16
1.03E+13	2.60E-12	–	–	1.73E-16	1.73E-16
1.02E+13	3.06E-12	–	–	1.80E-16	1.80E-16
1.01E+13	2.77E-12	–	–	1.85E-16	1.85E-16
1.01E+13	2.87E-12	–	–	1.80E-16	1.80E-16
1.00E+13	2.79E-12	–	–	1.71E-16	1.71E-16
9.97E+12	2.75E-12	–	–	1.87E-16	1.87E-16
9.91E+12	2.99E-12	–	–	2.91E-16	2.91E-16
9.86E+12	3.25E-12	–	–	6.71E-16	6.71E-16
9.80E+12	2.69E-12	–	–	2.82E-16	2.82E-16
9.75E+12	2.63E-12	–	–	2.39E-16	2.39E-16
9.70E+12	2.63E-12	–	–	2.60E-16	2.60E-16
9.64E+12	2.49E-12	–	–	3.09E-16	3.09E-16
9.59E+12	2.98E-12	–	–	2.68E-16	2.68E-16
9.54E+12	2.62E-12	–	–	3.14E-16	3.14E-16
9.49E+12	3.17E-12	–	–	2.64E-16	2.64E-16
9.44E+12	2.26E-12	–	–	2.60E-16	2.60E-16
9.39E+12	2.54E-12	–	–	2.88E-16	2.88E-16
9.34E+12	3.24E-12	–	–	2.90E-16	2.90E-16
9.29E+12	2.63E-12	–	–	2.86E-16	2.86E-16
9.24E+12	2.53E-12	–	–	3.00E-16	3.00E-16
9.19E+12	2.91E-12	–	–	3.28E-16	3.28E-16
9.15E+12	2.44E-12	–	–	3.38E-16	3.38E-16

ν [Hz]	νF_ν [erg cm^{-2}s^{-1}]	σ_ν^- [Hz]	σ_ν^+ [Hz]	$\sigma_{\nu F_\nu}^-$ [erg cm^{-2}s^{-1}]	$\sigma_{\nu F_\nu}^+$ [erg cm^{-2}s^{-1}]
9.10E+12	2.18E-12	–	–	3.15E-16	3.15E-16
9.05E+12	2.55E-12	–	–	3.53E-16	3.53E-16
9.01E+12	2.80E-12	–	–	3.93E-16	3.93E-16
8.96E+12	2.47E-12	–	–	3.86E-16	3.86E-16
8.92E+12	1.85E-12	–	–	6.49E-16	6.49E-16
8.87E+12	3.63E-12	–	–	5.77E-16	5.77E-16
8.83E+12	1.90E-12	–	–	6.07E-16	6.07E-16
8.70E+12	3.31E-12	–	–	5.53E-16	5.53E-16
8.65E+12	2.68E-12	–	–	4.64E-16	4.64E-16
8.57E+12	2.00E-12	–	–	5.41E-16	5.41E-16
8.53E+12	3.17E-12	–	–	6.17E-16	6.17E-16
8.49E+12	4.44E-12	–	–	6.88E-16	6.88E-16
8.45E+12	4.18E-12	–	–	1.25E-15	1.25E-15
8.29E+12	5.68E-12	–	–	1.66E-15	1.66E-15

Table B.9: SED: Optical data from 1ES 1959+650 by KVA, 2MASS, *Swift*-UVOT. The data was taken from [Bac11].

ν [Hz]	νF_ν [erg cm^{-2}s^{-1}]	σ_ν^- [Hz]	σ_ν^+ [Hz]	$\sigma_{\nu F_\nu}^-$ [erg cm^{-2}s^{-1}]	$\sigma_{\nu F_\nu}^+$ [erg cm^{-2}s^{-1}]
4.61E+14	3.11E-11	–	–	–	–
4.61E+14	2.39E-11	–	–	5.11E-12	5.11E-12
–	–	–	–	–	–
5.48E+14	2.52E-11	3.86E+13	3.86E+13	2.52E-12	2.52E-12
6.83E+14	2.53E-11	7.58E+13	7.58E+13	2.53E-12	2.53E-12
8.65E+14	3.12E-11	9.80E+13	9.80E+13	3.12E-12	3.12E-12
1.15E+15	3.00E-11	1.54E+14	1.54E+14	3.00E-12	3.00E-12
1.34E+15	3.74E-11	1.48E+14	1.48E+14	3.74E-12	3.74E-12
1.56E+15	5.44E-11	2.65E+14	2.65E+14	5.44E-12	5.44E-12
–	–	–	–	–	–
5.48E+14	2.87E-11	3.86E+13	3.86E+13	1.34E-12	1.34E-12
6.83E+14	3.29E-11	7.58E+13	7.58E+13	1.39E-12	1.39E-12
8.65E+14	3.68E-11	9.80E+13	9.80E+13	1.83E-12	1.83E-12
1.15E+15	3.60E-11	1.54E+14	1.54E+14	1.70E-12	1.70E-12
1.34E+15	4.33E-11	1.48E+14	1.48E+14	2.28E-12	2.28E-12
1.56E+15	6.49E-11	2.65E+14	2.65E+14	3.08E-12	3.08E-12
–	–	–	–	–	–
6.60E+14	3.50E-11	–	–	2.07E-13	2.07E-13
8.37E+14	3.87E-11	–	–	2.14E-13	2.14E-13
1.12E+15	3.53E-11	–	–	3.54E-13	3.54E-13
1.50E+15	4.18E-11	–	–	2.54E-12	2.54E-12
–	–	–	–	–	–
1.96E+15	3.38E-11	2.36E+14	3.31E+14	9.05E-13	9.05E-13
1.32E+15	1.57E-11	2.91E+14	3.26E+14	6.41E-13	6.41E-13
–	–	–	–	–	–
1.96E+15	3.48E-11	2.36E+14	3.31E+14	9.69E-13	9.69E-13
1.32E+15	1.67E-11	2.91E+14	3.26E+14	4.74E-13	4.74E-13

Table B.10: SED: Radio data from 1ES 1959+650 by VLBI and VLA. The data was taken from [Bac11].

ν [Hz]	νF_ν [erg cm^{-2}s^{-1}]	σ_ν^- [Hz]	σ_ν^+ [Hz]	$\sigma_{\nu F_\nu}^-$ [erg cm^{-2}s^{-1}]	$\sigma_{\nu F_\nu}^+$ [erg cm^{-2}s^{-1}]
4.61E+14	3.11E-11	–	–	–	–
4.61E+14	2.39E-11	–	–	5.11E-12	5.11E-12
–	–	–	–	–	–
5.48E+14	2.52E-11	3.86E+13	3.86E+13	2.52E-12	2.52E-12
6.83E+14	2.53E-11	7.58E+13	7.58E+13	2.53E-12	2.53E-12
8.65E+14	3.12E-11	9.80E+13	9.80E+13	3.12E-12	3.12E-12
1.15E+15	3.00E-11	1.54E+14	1.54E+14	3.00E-12	3.00E-12
1.34E+15	3.74E-11	1.48E+14	1.48E+14	3.74E-12	3.74E-12
1.56E+15	5.44E-11	2.65E+14	2.65E+14	5.44E-12	5.44E-12
–	–	–	–	–	–
5.48E+14	2.87E-11	3.86E+13	3.86E+13	1.34E-12	1.34E-12
6.83E+14	3.29E-11	7.58E+13	7.58E+13	1.39E-12	1.39E-12
8.65E+14	3.68E-11	9.80E+13	9.80E+13	1.83E-12	1.83E-12
1.15E+15	3.60E-11	1.54E+14	1.54E+14	1.70E-12	1.70E-12
1.34E+15	4.33E-11	1.48E+14	1.48E+14	2.28E-12	2.28E-12
1.56E+15	6.49E-11	2.65E+14	2.65E+14	3.08E-12	3.08E-12
–	–	–	–	–	–
6.60E+14	3.50E-11	–	–	2.07E-13	2.07E-13
8.37E+14	3.87E-11	–	–	2.14E-13	2.14E-13
1.12E+15	3.53E-11	–	–	3.54E-13	3.54E-13
1.50E+15	4.18E-11	–	–	2.54E-12	2.54E-12
–	–	–	–	–	–
1.96E+15	3.38E-11	2.36E+14	3.31E+14	9.05E-13	9.05E-13
1.32E+15	1.57E-11	2.91E+14	3.26E+14	6.41E-13	6.41E-13
–	–	–	–	–	–
1.96E+15	3.48E-11	2.36E+14	3.31E+14	9.69E-13	9.69E-13
1.32E+15	1.67E-11	2.91E+14	3.26E+14	4.74E-13	4.74E-13

B.2 Flare Spectrum

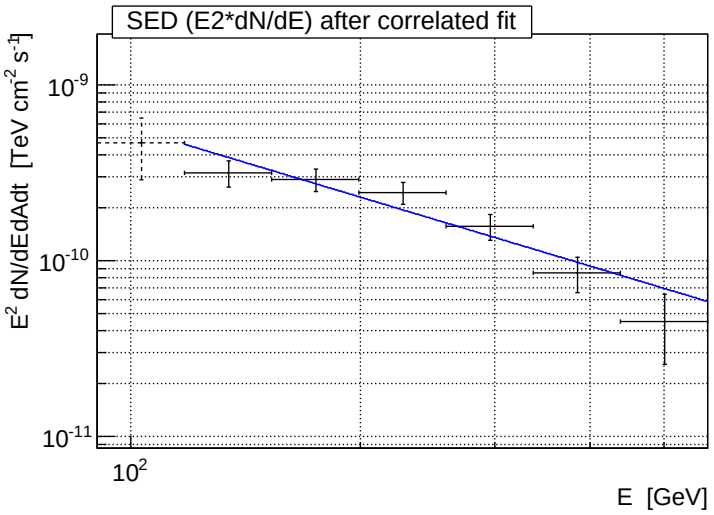

Figure B.1: 1ES 1959+650 flare SED fitted with a pure power law.

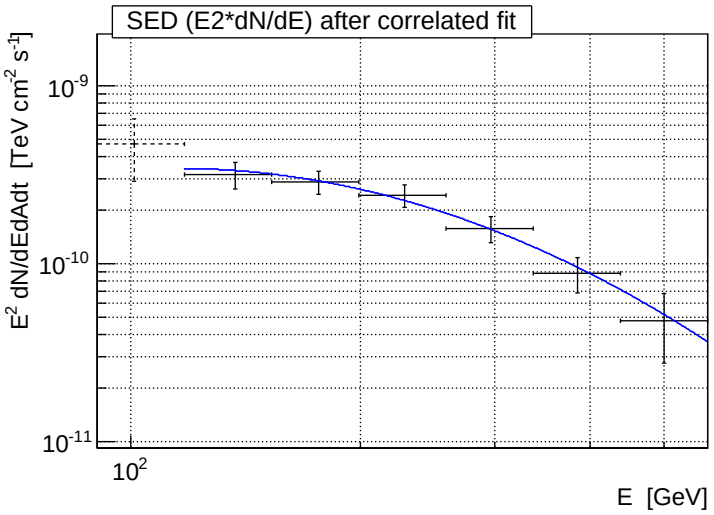

Figure B.2: 1ES 1959+650 flare SED fitted with a curve power law.

B.3 Corros Correlation

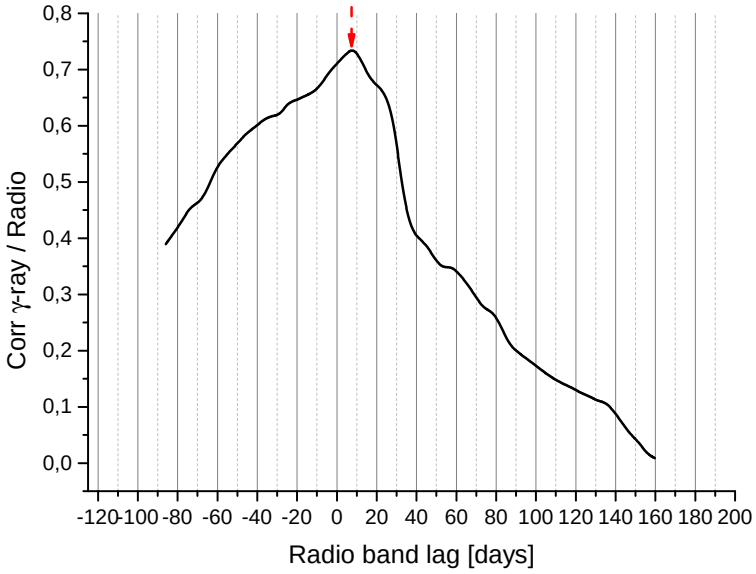

Figure B.3: 1ES 1959+650 radio-γ-ray lag.

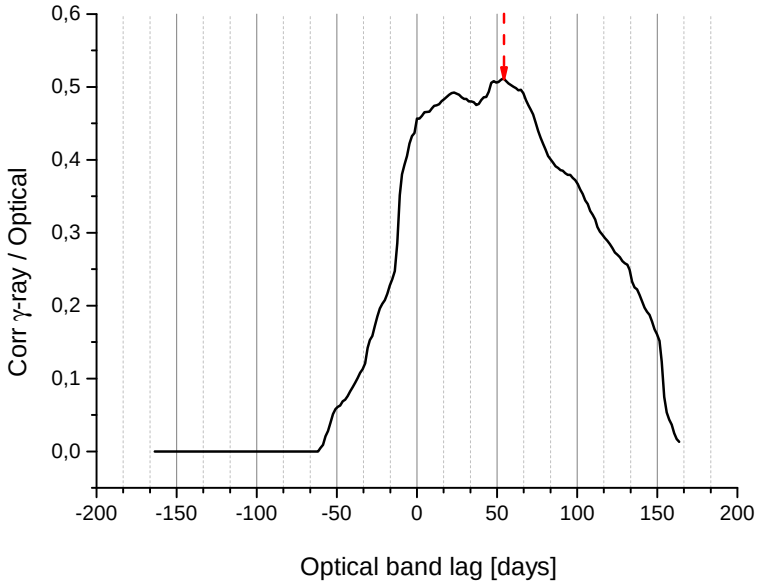

Figure B.4: 1ES 1959+650 optical-γ-ray lag.

APPENDIX: C

1ES 0033+505 DATA

C.1 Total data set used for the analysis

Table C.1: 1ES 0033+595 total data set. From left to right: dates in dd / mm / yy, observation time in hours, zenith angle distribution and rate of the event after the image cleaning in Hz.

Date	Observation time[h]	Zenith [°]	Mean L1 Rate [Hz]
17 / 08 / 2009	0.28	33-34	189
18 / 08 / 2009	1.30	31-34	200
19 / 08 / 2009	1.88	31-34	225
20 / 08 / 2009	0.70	31-34	200
21 / 08 / 2009	0.68	31-34	215
22 / 08 / 2009	1.75	31-34	250
23 / 08 / 2009	1.90	33-34	250
24 / 08 / 2009	1.94	31-34	225
25 / 08 / 2009	1.64	31-34	190
26 / 08 / 2009	1.19	31-34	250
27 / 08 / 2009	1.05	31-34	250
28 / 08 / 2009	1.88	31-34	200
29 / 08 / 2009	1.16	31-34	250
30 / 08 / 2009	1.16	31-34	250
15 / 09 / 2009	0.22	31-32	225
17 / 09 / 2009	0.05	31-31	300
11 / 10 / 2009	0.52	31-34	300
12 / 10 / 2009	1.15	31-33	200

Date	Observation time[h]	Zenith [°]	Mean L1 Rate [Hz]
13 / 10 / 2009	1.22	31-34	250
14 / 10 / 2009	0.85	31-33	250

Table C.2: SED: VHE data from 1ES 0033+595 by MAGIC

ν [Hz]	νF_ν [erg cm^{-2}s^{-1}]	σ^-_ν [Hz]	σ^+_ν [Hz]	$\sigma^-_{\nu F_\nu}$ [erg cm^{-2}s^{-1}]	$\sigma^+_{\nu F_\nu}$ [erg cm^{-2}s^{-1}]
3.75E+25	5.08E-12	7.18E+24	1.06E+25	8.29E-13	8.29E-13
5.94E+25	1.76E-12	1.14E+25	1.68E+25	3.57E-13	3.57E-13
9.43E+25	7.70E-13	1.80E+25	2.66E+25	3.20E-13	3.20E-13

Table C.3: SED: HE data from 1ES 0033+595 by *Fermi* LAT

ν [Hz]	νF_ν [erg cm^{-2}s^{-1}]	σ^-_ν [Hz]	σ^+_ν [Hz]	$\sigma^-_{\nu F_\nu}$ [erg cm^{-2}s^{-1}]	$\sigma^+_{\nu F_\nu}$ [erg cm^{-2}s^{-1}]
1.12E-23	3.23E-12	3.94E-22	1.29E-23	7.92E-13	7.92E-13
3.54E-23	3.33E-12	1.12E-23	3.70E-23	6.11E-13	6.11E-13
1.12E-24	4.02E-12	3.95E-23	1.29E-24	7.73E-13	7.73E-13
3.54E-24	5.12E-12	1.12E-24	3.71E-24	1.27E-12	1.27E-12
1.12E-25	4.55E-12	3.95E-24	1.29E-25	1.98E-12	1.98E-12
3.54E-25	1.08E-11	1.12E-25	3.70E-25	5.77E-12	5.77E-12

Table C.4: SED: X-ray data from 1ES 0033+595 by *Swift-BAT*. The data was taken from the NED archival.

ν [Hz]	νF_ν [erg cm^{-2}s^{-1}]	σ^ν [erg cm^{-2}s^{-1}]
5.13E+18	1.37E-11	1.14E-12
6.62E+18	1.16E-11	2.20E-12
9.37E+18	6.81E-12	7.39E-13
1.15E+19	1.07E-11	1.73E-12

Table C.5: SED: X-ray data from 1ES 0033+595 by INTEGRAL. The data was taken from the NED archival.

ν [Hz]	νF_ν [erg cm^{-2}s^{-1}]	σ^ν [erg cm^{-2}s^{-1}]
1.69E+19	1.04E-11	1.88E-12
1.69E+19	3.00E-12	–
1.45E+19	1.87E-11	–
9.31E+18	1.03E-11	1.50E-12
7.25E+18	8.00E-12	–
6.84E+18	1.42E-11	1.09E-12
1.53E+19	9.24E-12	1.03E-12

Table C.6: SED: X-ray data from 1ES 0033+595 by *Beppo*-SAX. The data was taken from the NED archival.

ν [Hz]	νF_ν [erg cm^{-2}s^{-1}]	σ^ν [erg cm^{-2}s^{-1}]
9.31E+18	1.03E-11	1.50E-12
7.25E+18	8.33E-12	7.57E-13
1.45E+18	8.20E-11	7.00E-12

Table C.7: SED: Optical data from 1ES 0033+595 by KVA, 2MASS, *Swift*-UVOT.The data was taken from the NED archival.

ν [Hz]	νF_ν [erg cm^{-2}s^{-1}]	σ^ν [erg cm^{-2}s^{-1}]
4.68E+14	1.02E-12	2.81E-14
4.37E+14	6.56E-13	4.83E-14
2.40E+14	4.85E-12	2.14E-13
1.82E+14	4.74E-12	2.36E-13
1.38E+14	4.08E-12	1.73E-13
4.68E+14	8.47E-12	5.00E-13

Table C.8: SED: Radio data from 1ES 0033+595 by VLBI and VLA. The data was taken from the NED archival.

ν [Hz]	νF_ν [erg cm^{-2}s^{-1}]	σ^ν [erg cm^{-2}s^{-1}]
4.85E+09	5.63E-15	8.44E-16
4.85E+09	5.77E-15	5.82E-16
1.40E+09	2.08E-15	8.12E-17
3.65E+08	1.24E-15	2.26E-16

C.2 Deabsorbed spectrum of 1ES 0033+595

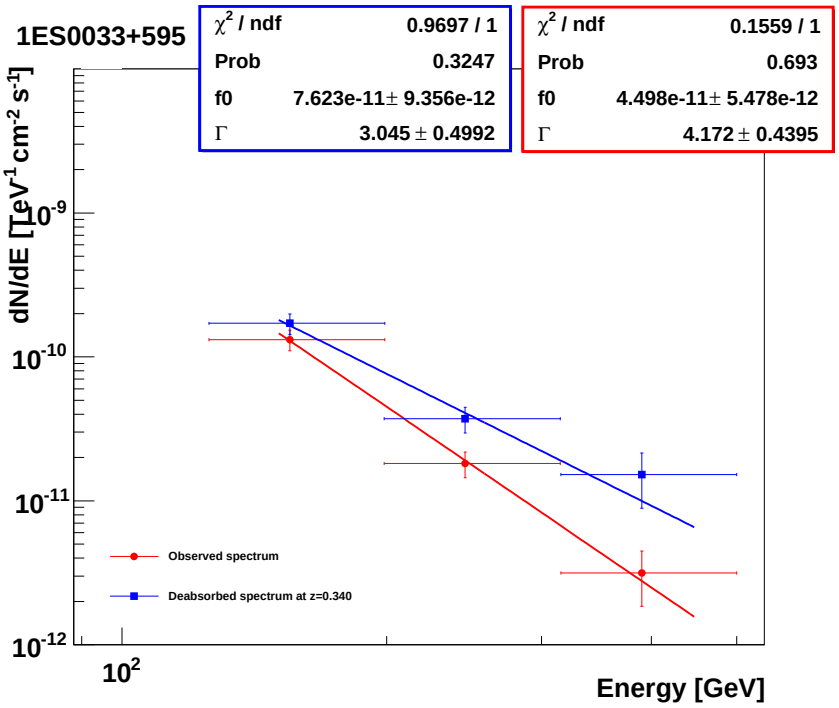

Figure C.1: Deabsorbed 1ES 0033+595 spectrum at $z = 0.34$

APPENDIX: D

B3 0133+388

D.1 Total data set used for the analysis

Table D.1: B3 0133+388 full data set. From left to right: dates in dd / mm / yy, observation time in hours, zenith angle distribution and rate of the event after the image cleaning in Hz.

Date	Obs. time[h]	Zenith [°]	Mean Rate [Hz]
06 / 11 / 2009	0.10	33-34	26
07 / 11 / 2009	0.55	17-30	45
09 / 11 / 2009	0.30	12-30	85
11 / 11 / 2009	0.58	22-31	82
15 / 11 / 2009	1.40	13-31	82
16 / 11 / 2009	0.13	12-14	76
19 / 11 / 2009	1.10	17-31	83
20 / 11 / 2009	0.50	15-27	89
21 / 11 / 2009	1.40	14-34	77
22 / 11 / 2009	2.00	15-35	63
23 / 11 / 2009	1.50	14-35	23
24 / 11 / 2009	4.00	10-34	45
25 / 11 / 2009	3.00	10-24	33
26 / 11 / 2009	4.00	10-35	22

Table D.2: SED: VHE data from B3 0133+388 by MAGIC

ν [Hz]	νF_ν [erg cm^{-2}s^{-1}]	σ^-_ν [Hz]	σ^+_ν [Hz]	$\sigma^-_{\nu F_\nu}$ [erg cm^{-2}s^{-1}]	$\sigma^+_{\nu F_\nu}$ [erg cm^{-2}s^{-1}]
2.76E+25	1.08E-11	4.91E+24	6.87E+24	1.91E-12	1.91E-12
4.19E+25	6.00E-12	7.47E+24	1.04E+25	1.71E-12	1.71E-12
6.37E+25	1.84E-12	1.13E+25	1.59E+25	8.35E-13	8.35E-13

Table D.3: SED: HE data from B3 0133+388 by *Fermi* LAT

ν [Hz]	νF_ν [erg cm^{-2}s^{-1}]	σ^-_ν [Hz]	σ^+_ν [Hz]	$\sigma^-_{\nu F_\nu}$ [erg cm^{-2}s^{-1}]	$\sigma^+_{\nu F_\nu}$ [erg cm^{-2}s^{-1}]
3.87E+22	4.30E-12	1.45E+22	3.39E+22	8.00E-13	8.00E-13
1.33E+23	3.20E-12	6.05E+22	1.09E+23	7.00E-13	7.00E-13
4.35E+23	5.80E-12	1.93E+23	2.90E+23	6.00E-13	6.00E-13
1.33E+24	1.12E-11	6.04E+23	1.09E+24	1.60E-12	1.60E-12
7.98E+24	1.40E-11	5.56E+24	1.64E+25	2.50E-12	2.50E-12

Table D.4: SED: X-ray data from B3 0133+388 by *Swift-BAT* and *Beppo*-SAX. The data was taken from the NED archival.

ν [Hz]	νF_ν [erg cm^{-2}s^{-1}]	σ^ν [erg cm^{-2}s^{-1}]
1.45E+18	1.04E-11	–
1.45E+18	1.08E-11	–
3.02E+17	2.33E-11	–
3.02E+17	9.60E-12	–

Table D.5: SED: Optical data from B3 0133+388 by KVA, 2MASS, *Swift*-UVOT.The data was taken from the NED archival.

ν [Hz]	νF_ν [erg cm^{-2}s^{-1}]	σ^ν [erg cm^{-2}s^{-1}]
2.40E+14	7.50E-12	2.07E-13
1.82E+14	7.04E-12	2.01E-13
1.38E+14	5.66E-12	1.30E-13
1.14E+15	1.16E-11	1.50E-12
1.34E+15	1.44E-11	3.00E-12

Table D.6: SED: Radio data from B3 0133+388 by VLBI and VLA. The data was taken from the NED archival.

ν [Hz]	νF_ν [erg cm^{-2}s^{-1}]	σ^ν [erg cm^{-2}s^{-1}]
4.85E+09	2.52E-15	3.88E-16
4.85E+09	2.57E-15	3.86E-16
2.30E+09	1.15E-15	–
1.40E+09	8.23E-16	–
1.40E+09	8.47E-16	2.66E-17
4.08E+08	4.90E-16	8.22E-17

D.2 Deabsorbed spectrum of B3 0133+38

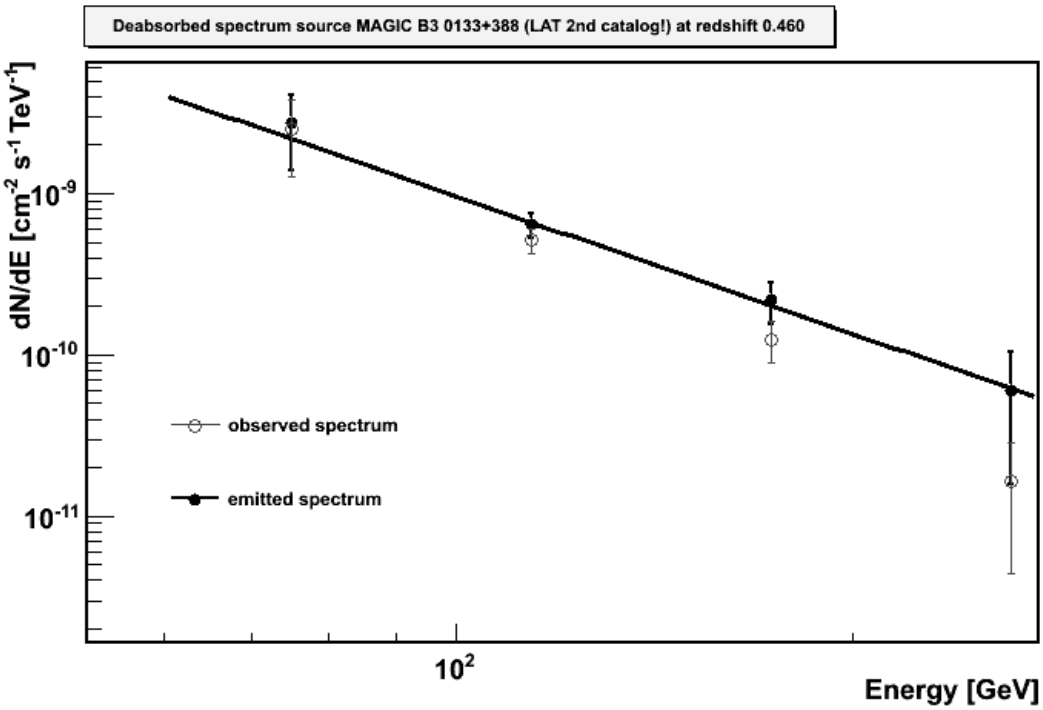

Figure D.1: Deabsorbed B3 0133+388 spectrum at $z = 0.46$.

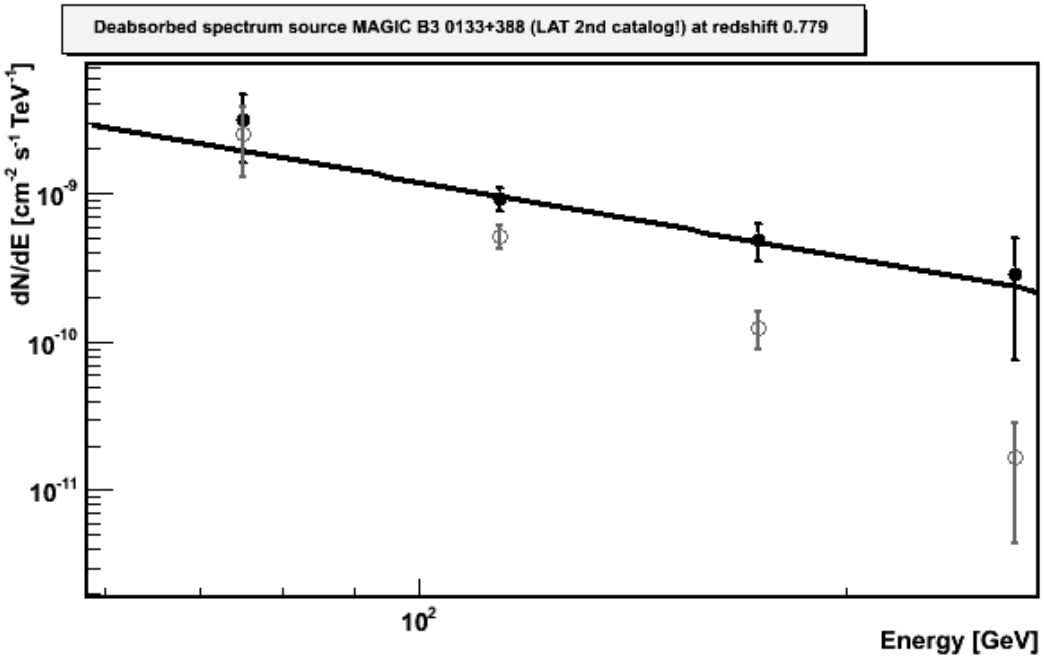

Figure D.2: Deabsorbed B3 0133+388 spectrum at $z = 0.78$.

APPENDIX: E

PKS 1717+177 DATA

E.1 Total data set used for the analysis

Table E.1: PKS 1717+177 full data set. From left to right: dates in dd / mm / yy, observation time in hours, zenith angle distribution and rate of the event after the image cleaning in Hz.

Date	Eff. time[h]	Zenith [°]	Mean Rate [Hz]
19 / 04 / 2009	0.48	23-30	250
21 / 04 / 2009	1.55	12-30	200
22 / 04 / 2009	0.30	12-30	270
23 / 04 / 2009	1.40	13-31	260
24 / 04 / 2009	1.88	12-14	240
25 / 04 / 2009	0.33	12-14	250
26 / 04 / 2009	1.90	11-31	250
20 / 05 / 2009	0.01	11-27	130
21 / 05 / 2009	0.30	15-18	240
23 / 05 / 2009	1.51	11-29	100
25 / 05 / 2009	0.60	12-19	250
15 / 06 / 2009	0.47	15-23	250
25 / 06 / 2009	1.58	15-23	260
26 / 06 / 2009	1.57	12-19	165
27 / 06 / 2009	2.22	12-19	165
28 / 06 / 2009	1.74	11-15	180
30 / 06 / 2009	0.41	11-20	170
01 / 07 / 2009	0.57	17-25	160

Date	Eff. time[h]	Zenith [°]	Mean Rate [Hz]
23 / 07 / 2009	0.86	14-22	145
25 / 07 / 2009	0.67	12-21	240
10 / 08 / 2009	0.45	11-19	260
11 / 08 / 2009	1.05	11-19	270
12 / 08 / 2009	1.47	11-19	290
13 / 08 / 2009	1.43	15-24	300
15 / 08 / 2009	0.92	15-28	280
16 / 08 / 2009	0.82	18-27	300
17 / 08 / 2009	0.83	18-27	300
19 / 08 / 2009	1.57	17-27	220
20 / 08 / 2009	0.39	18-27	300
21 / 08 / 2009	0.85	18-27	142
22 / 08 / 2009	0.86	18-27	300
23 / 08 / 2009	0.70	17-21	180
24 / 08 / 2009	0.53	20-27	200

Table E.2: SED: VHE data from PKS 1717+177 by MAGIC

ν [Hz]	νF_ν [erg cm^{-2}s^{-1}]	σ^-_ν [Hz]	σ^+_ν [Hz]	$\sigma^-_{\nu F_\nu}$ [erg cm^{-2}s^{-1}]	$\sigma^+_{\nu F_\nu}$ [erg cm^{-2}s^{-1}]
5.06E+25	2.79E-12	1.23E+25	1.74E+25	1.23E-12	1.23E-12
8.99E+25	2.16E-12	2.19E+25	3.10E+25	8.89E-13	8.89E-13
1.60E+26	1.77E-12	3.90E+25	5.51E+25	7.66E-13	7.66E-13
2.84E+26	1.45E-12	6.93E+25	9.81E+25	9.26E-13	9.26E-13

Table E.3: SED: HE data from PKS 1717+177 by *Fermi* LAT

ν [Hz]	νF_ν [erg cm^{-2}s^{-1}]	σ^-_ν [Hz]	σ^+_ν [Hz]	$\sigma^-_{\nu F_\nu}$ [erg cm^{-2}s^{-1}]	$\sigma^+_{\nu F_\nu}$ [erg cm^{-2}s^{-1}]
1.12E+23	1.46E-12	3.94E+22	1.30E+23	6.10E-13	6.10E-13
3.55E+23	2.47E-12	1.13E+23	3.71E+23	2.30E-13	2.30E-13
1.12E+24	4.31E-12	3.96E+23	1.30E+24	4.80E-13	4.80E-13
3.55E+24	3.68E-12	1.13E+24	3.71E+24	8.30E-13	8.30E-13
1.12E+25	3.61E-12	3.96E+24	1.30E+25	1.37E-12	1.37E-12
3.55E+25	2.94E-12	1.13E+25	3.71E+25	2.04E-12	2.04E-12

Table E.4: SED: X-ray data from PKS 1717+177 by *Swift-BAT*. The data was taken from the NED archival.

ν [Hz]	νF_ν [erg cm^{-2}s^{-1}]	σ^ν [erg cm^{-2}s^{-1}]
1.25E+18	1.60E-12	–
3.02E+17	3.57E-13	–

Table E.5: SED: Optical data from PKS 1717+177 by 2MASS, *Swift*-UVOT.The data was taken from the NED archival.

ν [Hz]	νF_ν [erg cm^{-2}s^{-1}]	σ^ν [erg cm^{-2}s^{-1}]
4.68E+14	1.77E-12	–
2.50E+14	3.60E-12	6.70E-14

Table E.6: SED: Radio data from PKS 1717+177 by VLBI and VLA. The data was taken from the NED archival.

ν [Hz]	νF_ν [erg cm^{-2}s^{-1}]	σ^ν [erg cm^{-2}s^{-1}]
9.40E+10	9.40E-13	3.76E-13
6.10E+10	3.66E-13	1.22E-13
3.20E+10	1.65E-13	–
2.40E+10	1.68E-13	–
1.46E+10	8.75E-14	–
1.05E+10	6.29E-14	–
8.40E+09	4.87E-14	–
8.40E+09	4.87E-14	–
8.35E+09	5.23E-14	–
5.00E+09	4.70E-14	–
4.85E+09	2.73E-14	4.10E-15
4.85E+09	3.27E-14	–
4.85E+09	2.75E-14	3.73E-15
4.83E+09	1.49E-14	–
4.83E+09	1.73E-14	–
4.78E+09	3.57E-14	–
2.70E+09	1.86E-14	–
2.64E+09	1.77E-14	–

ν [Hz]	νF_ν [erg cm^{-2}s^{-1}]	σ^ν [erg cm^{-2}s^{-1}]
1.40E+09	7.60E-15	2.28E-16
1.40E+09	1.10E-14	–
4.08E+08	1.26E-15	–
3.65E+08	1.26E-15	7.67E-17

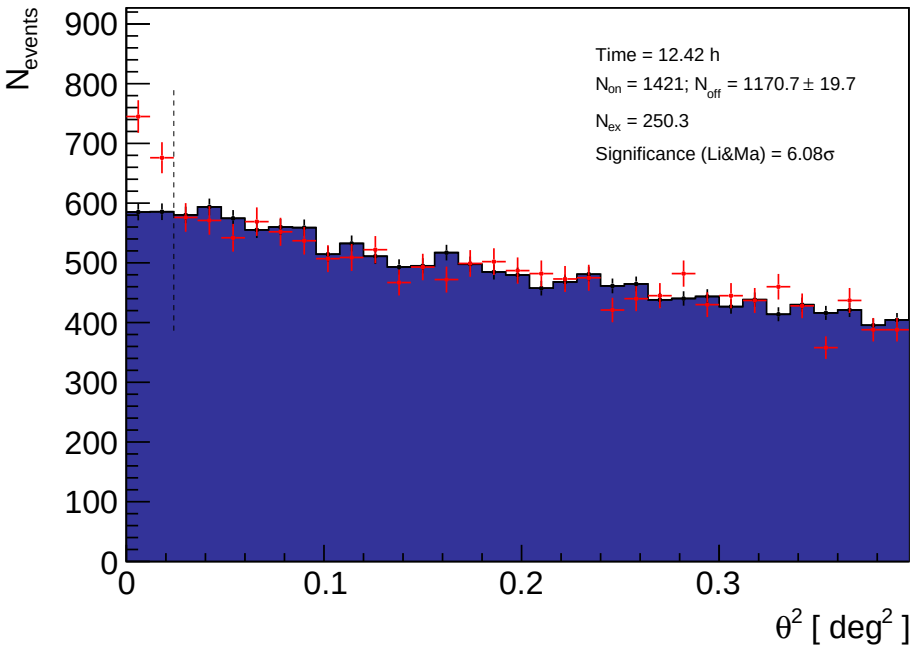

Figure E.1: θ^2 distributions of the PKS 1717+177 signal and background estimation from 12.4 hr of MAGIC observations taken between April 19 th and August 24 th, 2009, above an energy threshold of 150 GeV

List of Figures

List of Tables

REFERENCES

[A+08] J. Albert et al. FADC signal reconstruction for the MAGIC Telescope. *Nucl.Instrum.Meth.*, A594:407–419, 2008. 68, 123

[AAA+06a] J. Albert, E. Aliu, H. Anderhub, et al. Discovery of Very High Energy γ-Rays from Markarian 180 Triggered by an Optical Outburst. *ApJ*, 648:L105–L108, September 2006. 136

[AAA+06b] E. Aliu, H. Anderhub, L. A. Antonelli, P. Antoranz, et al. Observation of Very High Energy Gamma-Ray Emission from the Active Galactic Nucleus 1ES 1959+650 Using the MAGIC Telescope. *ApJ*, 639:761–765, March 2006. 105

[AAA+07a] J. Albert, E. Aliu, H. Anderhub, P. Antoranz, A. Armada, et al. Observations of Markarian 421 with the MAGIC Telescope. *ApJ*, 663:125–138, July 2007. 222

[AAA+07b] J. Albert, E. Aliu, H. Anderhub, P. Antoranz, et al. Discovery of Very High Energy γ-Rays from 1ES 1011+496 at z = 0.212. *ApJ*, 667:L21–L24, September 2007. 136

[AAA+07c] J. Albert, E. Aliu, H. Anderhub, P. Antoranz, et al. Variable Very High Energy γ-Ray Emission from Markarian 501. *ApJ*, 669:862–883, November 2007. 137

[AAA+07d] J. Albert, E. Aliu, H. Anderhub, et al. Unfolding of differential energy spectra in the MAGIC experiment. *Nuclear Instruments and Methods in Physics Research A*, 583:494–506, December 2007. 85

[AAA+08a] J. Albert, E. Aliu, H. Anderhub, P. Antoranz, A. Armada, et al. Implementation of the Random Forest Method for the Imaging Atmospheric Cherenkov Telescope MAGIC. *Nucl.Instrum.Meth.*, A588:424–432, 2008. 74, 75

[AAA+08b] J. Albert, E. Aliu, H. Anderhub, et al. VHE γ-Ray Observation of the Crab Nebula and its Pulsar with the MAGIC Telescope. *ApJ*, 674:1037–1055, February 2008. 70, 89, 95, 184, 285

[AAA+08c] E. Aliu, H. Anderhub, L. A. Antonelli, P. Antoranz, et al. Observation of Pulsed γ-Rays Above 25 GeV from the Crab Pulsar with MAGIC. *Science*, 322:1221–, November 2008. 88

[AAA+09a] A. A. Abdo, M. Ackermann, I. Agudo, M. Ajello, et al. Bright Active Galactic Nuclei Source List from the First Three Months of the Fermi Large Area Telescope All-Sky Survey. *ApJ*, 700:597–622, July 2009. 182, 203, 204

[AAA+09b] A. A. Abdo, M. Ackermann, I. Agudo, M. Ajello, et al. Fermi Observations of TeV-Selected Active Galactic Nuclei. *ApJ*, 707:1310–1333, December 2009. 164, 170, 224, 235

[AAA+09c] E. Aliu, H. Anderhub, L. A. Antonelli, et al. Improving the performance of the single-dish Cherenkov telescope MAGIC through the use of signal timing. *Astroparticle Physics*, 30:293–305, January 2009. 59, 184

[AAA+09d] H. Anderhub, L. A. Antonelli, P. Antoranz, M. Backes, et al. Discovery of very High Energy γ-Rays from the Blazar S5 0716+714. *ApJ*, 704:L129–L133, October 2009. 136

[AAA+10a] A. A. Abdo, M. Ackermann, I. Agudo, M. Ajello, et al. Fermi Large Area Telescope Observations of the Crab Pulsar And Nebula. *ApJ*, 708:1254–1267, January 2010. 88

[AAA+10b] A. A. Abdo, M. Ackermann, I. Agudo, M. Ajello, et al. Gamma-ray Light Curves and Variability of Bright Fermi-detected Blazars. *ApJ*, 722:520–542, October 2010. 193, 203, 292

[AAA+10c] A. A. Abdo, M. Ackermann, I. Agudo, M. Ajello, et al. The Spectral Energy Distribution of Fermi Bright Blazars. *ApJ*, 716:30–70, June 2010. 39, 41, 210, 283, 293

[AAA+10d] A. A. Abdo, M. Ackermann, M. Ajello, L. Baldini, et al. Spectral Properties of Bright Fermi-Detected Blazars in the Gamma-Ray Band. *ApJ*, 710:1271–1285, February 2010. 147, 159, 289

[AAA+10e] A. A. Abdo, M. Ackermann, M. Ajello, et al. Fermi Large Area Telescope Observations of the Crab Pulsar And Nebula. *ApJ*, 708:1254–1267, January 2010. 88

[AAA+10f] A. A. Abdo, M. Ackermann, M. Ajello, et al. The First Catalog of Active Galactic Nuclei Detected by the Fermi Large Area Telescope. *ApJ*, 715:429–457, May 2010. 192

[AAA+10g] J. Aleksić, H. Anderhub, L. A. Antonelli, P. Antoranz, et al. MAGIC TeV gamma-ray observations of Markarian 421 during multiwavelength campaigns in 2006. *A&A*, 519:A32, September 2010. 137

[AAA+10h] J. Aleksić, H. Anderhub, L. A. Antonelli, et al. MAGIC TeV gamma-ray observations of Markarian 421 during multiwavelength campaigns in 2006. *A&A*, 519:A32, September 2010. 148

[AAA+11a] A. A. Abdo, M. Ackermann, M. Ajello, L. Baldini, J. Ballet, G. Barbiellini, D. Bastieri, K. Bechtol, R. Bellazzini, B. Berenji, et al. Fermi Large Area Telescope Observations of Markarian 421: The Missing Piece of its Spectral Energy Distribution. *ApJ*, 736:131, August 2011. 147

[AAA+11b] A. A. Abdo, M. Ackermann, M. Ajello, L. Baldini, J. Ballet, G. Barbiellini, D. Bastieri, K. Bechtol, R. Bellazzini, B. Berenji, et al. Fermi Large Area Telescope Observations of Markarian 421: The Missing Piece of its Spectral Energy Distribution. *ApJ*, 736:131, August 2011. 151, 290

[AAA+11c] J. Aleksić, L. A. Antonelli, P. Antoranz, et al. Gamma-ray Excess from a Stacked Sample of High- and Intermediate-frequency Peaked Blazars Observed with the MAGIC Telescope. *ApJ*, 729:115, March 2011. 164

[AAA+11d] J. Aleksić, L. A. Antonelli, P. Antoranz, et al. Observations of the Blazar 3C 66A with the Magic Telescopes in Stereoscopic Mode. *ApJ*, 726:58, January 2011. 165, 184

[AAA+12a] J. Aleksić, E. A. Alvarez, L. A. Antonelli, P. Antoranz, et al. Discovery of VHE γ-ray emission from the BL Lacertae object B3 2247+381 with the MAGIC telescopes. *A&A*, 539:A118, March 2012. 222

[AAA+12b] J. Aleksić, E. A. Alvarez, L. A. Antonelli, P. Antoranz, et al. Discovery of VHE γ-rays from the blazar 1ES 1215+303 with the MAGIC telescopes and simultaneous multi-wavelength observations. *A&A*, 544:A142, August 2012. 136, 177, 179, 198, 200

[AAA+12c] J. Aleksić, E. A. Alvarez, L. A. Antonelli, P. Antoranz, et al. Discovery of VHE γ-rays from the blazar 1ES 1215+303 with the MAGIC telescopes and simultaneous multi-wavelength observations. *A&A*, 544:A142, August 2012. 222

[AAA+12d] J. Aleksić, E. A. Alvarez, L. A. Antonelli, et al. Performance of the MAGIC stereo system obtained with Crab Nebula data. *Astroparticle Physics*, 35:435–448, February 2012. 76, 85, 86, 105, 123, 128, 142, 157, 179

[AAA+12e] J. Aleksić, E. A. Alvarez, L. A. Antonelli, et al. PG 1553+113: Five Years of Observations with MAGIC. *ApJ*, 748:46, March 2012. 175, 177, 198, 200, 222

[AAA+12f] E. Aliu, S. Archambault, T. Arlen, et al. VERITAS Observations of Six Bright, Hard-spectrum Fermi-LAT Blazars. *ApJ*, 759:102, November 2012. 189, 190, 195, 196, 200, 292

[AAB+03] F. Aharonian, A. Akhperjanian, M. Beilicke, et al. Detection of TeV gamma-rays from the BL Lac 1ES 1959+650 in its low states and during a major outburst in 2002. *A&A*, 406:L9–L13, July 2003. 103

[AAB+06] F. Aharonian, A. G. Akhperjanian, A. R. Bazer-Bachi, et al. A low level of extragalactic background light as revealed by γ-rays from blazars. *A&A*, 440:1018–1021, April 2006. 227

[ABB+13] H. Anderhub, M. Backes, A. Biland, V. Boccone, and others. Design and Operation of FACT – The First G-APD Cherenkov Telescope. *ArXiv e-prints*, April 2013. 105

[AGK+01] A. Achterberg, Y. A. Gallant, J. G. Kirk, et al. Particle acceleration by ultrarelativistic shocks: theory and simulations. *MNRAS*, 328:393–408, December 2001. 88

[Bac11] Michael Backes. *Long-term observations of the TeV blazar 1ES 1959+650 - Temporal and spectral behavior in the multi-wavelength context*. PhD thesis, TU Dortmund University, December 2011. 101, 102, 146, 148, 151, 156, 250, 251, 255, 266, 267, 287, 296

[BB03] W. Bednarek and M. Bartosik. Gamma-rays from the pulsar wind nebulae. *A&A*, 405:689–702, July 2003. 89

[BBC+05] S. D. Barthelmy, L. M. Barbier, J. R. Cummings, et al. The Burst Alert Telescope (BAT) on the SWIFT Midex Mission. *Space Sci. Rev.*, 120:143–164, October 2005. 171

[BCTB00] F. E. Bauer, J. J. Condon, T. X. Thuan, and J. J. Broderick. RBSC-NVSS sample. I. (Bauer+, 2000). *VizieR Online Data Catalog*, 212:90547, November 2000. 195

[BDB+10] M. Béthermin, H. Dole, A. Beelen, et al. Spitzer deep and wide legacy mid- and far-infrared number counts and lower limits of cosmic infrared background. *A&A*, 512:A78, March 2010. 35, 283

[BDW+09] T. Bretz, D. Dorner, R. M. Wagner, et al. The drive system of the major atmospheric gamma-ray imaging Cherenkov telescope. *Astroparticle Physics*, 31:92–101, March 2009. 85

[Ber89] M. Bertero. Linear inverse and ill-posed problems. volume 75, pages 1–120. Academic Press, New York, 1989. 81

[Ber00] K. Bernlohr. Impact of atmospheric parameters on the atmospheric Cherenkov technique. *Astroparticle Physics*, 12:255–268, January 2000. 53, 284

[BGA+08] A. Biland, M. Garczarczyk, H. Anderhub, et al. The Active Mirror Control of the MAGIC Telescopes. In *International Cosmic Ray Conference*, volume 3 of *International Cosmic Ray Conference*, pages 1353–1356, 2008. 59

[BGF+09] D. Borla Tridon, F. Goebel, D. Fink, et al. Performance of the Camera of the MAGIC II Telescope. *ArXiv e-prints*, June 2009. 64

[BHH12] M. Boetcher, D.E Harris, and Krawczynski H. *Relativistic Jets from Active Galacic Nuclei*. Wiley-VCH, 2012. 39

[BHN+05] D. N. Burrows, J. E. Hill, J. A. Nousek, et al. The Swift X-Ray Telescope. *Space Sci. Rev.*, 120:165–195, October 2005. 171

[Boe10] M. Boettcher. Models for the Spectral Energy Distributions and Variability of Blazars. *ArXiv e-prints*, June 2010. 40, 42

[BS12] V. Beckman and C. Shrader. *Active Galactic Nuclei*. Wiley-VCH, 2012. p.186 - p.187. 31, 32, 33, 34, 35, 37, 38, 39, 120, 146, 154, 227, 283

[BSF+97] W. Brinkmann, J. Siebert, E. D. Feigelson, R. I. Kollgaard, S. A. Laurent-Muehleisen, W. Reich, E. Fuerst, P. Reich, W. Voges, J. Truemper, and R. McMahon. ROSAT detected quasars. II. (Brinkmann+ 1997). *VizieR Online Data Catalog*, 332:30739, February 1997. 181

[BWE91] R. H. Becker, R. L. White, and A. L. Edwards. A new catalog of 53,522 4.85 GHz sources. *ApJS*, 75:1–229, January 1991. 100

[CBB+97] M. Catanese, P. J. Boyle, A. M. Burdett, et al. First Results from a Search for TeV Emission from BL Lacs Out to Z = 0.2. In *International Cosmic Ray Conference*, volume 3 of *International Cosmic Ray Conference*, page 277, 1997. 103

[CG02] L. Costamante and G. Ghisellini. TeV candidate BL Lac objects. *A&A*, 384:56–71, March 2002. 164, 179, 182, 200

[CGG+01] L. Costamante, G. Ghisellini, P. Giommi, et al. Extreme synchrotron BL Lac objects. Stretching the blazar sequence. *A&A*, 371:512–526, May 2001. 162

[CGS+09] J. Cortina, F. Goebel, T. Schweizer, et al. Technical Performance of the MAGIC Telescopes. *ArXiv e-prints*, July 2009. 105, 106

[Cha09] C. Chandra. NASA's Great Observatories' View of the Crab Nebula. http://www.spitzer.caltech.edu/images/2857-sig09-009-NASA-s-Great-Observatories-View-of-the-Crab-Nebula, November 2009. 88, 285

[CMA+02] A. Caccianiga, M. J. Marcha, S. Anton, et al. The CLASS blazar survey. II. (Caccianiga+, 2002). *VizieR Online Data Catalog*, 732:90877, March 2002. 195

[Cor13] J. Cortina. MAGIC and VERITAS detect an unprecedented flaring activity from Mrk 421 in very high energy gamma-rays . *The Astronomer's Telegram*, 3976:1, April 2013. 112

[CSC+11] E. Carmona, J. Sitarek, P. Colin, et al. Performance of the MAGIC Stereo System. *ArXiv e-prints*, October 2011. 63

[DBB+08] M. Doro, D. Bastieri, A. Biland, F. Dazzi, L. Font, M. Garczarczyk, M. Ghigo, E. Giro, F. Goebel, R. Kosyra, E. Lorenz, M. Mariotti, R. Mirzoyan, L. Peruzzo, G. Pareschi, and J. Zapatero. The reflective surface of the MAGIC telescope. *Nuclear Instruments and Methods in Physics Research A*, 595:200–203, September 2008. 59

[dHK+06] P. R. den Hartog, W. Hermsen, L. Kuiper, et al. INTEGRAL survey of the Cassiopeia region in hard X rays. *A&A*, 451:587–602, May 2006. 162

[Dol13] D. Dole. Cosmic Background Light. http://www.andrewjaffe.net/blog/2011/09/passion-for-lig.html, February 2013. 32, 283

[Dor13] Marlene Dort. *The talkative AGN next door:Broad-band spectral variability of the TeV blazar Markarian 501*. PhD thesis, TU Dortmund University, März 2013. 81, 222

[DP13] A. Domínguez and F. Prada. Measurement of the expansion rate of the Universe from gamma-ray attenuation. *ArXiv e-prints*, May 2013. 229, 230, 236

[DPR+10] A. Domínguez, J. R. Primack, D. J. Rosario, et al. Extragalactic background light inferred from AEGIS galaxy-SED-type fractions. *MNRAS*, 410:2556–2578, February 2010. 37, 228, 235

[DS93] C. D. Dermer and R. Schlickeiser. Model for the High-Energy Emission from Blazars. *ApJ*, 416:458, October 1993. 153

[EDJ+03] N. A. Eismont, A. V. Ditrikh, G. Janin, et al. Orbit design for launching INTEGRAL on the Proton/Block-DM launcher. *A&A*, 411:L37–L41, November 2003. 172

[EPS+92] M. Elvis, D. Plummer, J. Schachter, G. Fabbiano, et al. The Einstein Slew Survey. *ApJS*, 80:257–303, May 1992. 100, 162

[ESR12] B. Eichmann, R. Schlickeiser, and W. Rhode. Differences of leptonic and hadronic radiation production in flaring blazars. *The Astrophysical Journal*, 749(2):155, 2012. 122, 158, 233

[FBB+08] G. Fossati, J. H. Buckley, I. H. Bond, et al. Multiwavelength Observations of Markarian 421 in 2001 March: An Unprecedented View on the X-Ray/TeV Correlated Variability. *ApJ*, 677:906–925, April 2008. 142

[FDK69] L. T. Fitch, R. S. Dixon, and J. D. Kraus. A high-sensitivity 1415-MHz survey between declinations of 0 and 20 north. *AJ*, 74:612–688, June 1969. 202

[FGT85] A. Ficarra, G. Grueff, and G. Tomassetti. A new Bologna sky survey at 408 MHz. *A&AS*, 59:255–347, February 1985. 181

[FMC+98] G. Fossati, L. Maraschi, A. Celotti, A. Comastri, et al. A unifying view of the spectral energy distributions of blazars. *MNRAS*, 299:433–448, September 1998. 40

[FRV08] A. Franceschini, G. Rodighiero, and M. Vaccari. Extragalactic optical-infrared background radiation, its time evolution and the cosmic photon-photon opacity. *A&A*, 487:837–852, September 2008. 175, 177, 178, 196, 198, 291

[FSLo94] V. P. Fomin, A. A. Stepanian, R. C. Lamb, and others. New methods of atmospheric Cherenkov imaging for gamma-ray astronomy. I. The false source method. *Astroparticle Physics*, 2:137–150, May 1994. 64, 164

[FWD+13] A. Furniss, D. A. Williams, C. Danforth, M. Fumagalli, et al. The Firm Redshift Lower Limit of the Most Distant TeV-detected Blazar PKS 1424+240. *ApJ*, 768:L31, May 2013. 218, 229

[GBB+08] F. Goebel, M. Backes, T. Bretz, et al. Long term monitoring of bright TeV Blazars with the MAGIC telescope. In *International Cosmic Ray Conference*, volume 3 of *International Cosmic Ray Conference*, pages 1025–1028, 2008. 105

[GC91] P. C. Gregory and J. J. Condon. The 87GB catalog of radio sources covering delta between O and + 75 deg at 4.85 GHz. *ApJS*, 75:1011–1291, April 1991. 100

[GCG+04] N. Gehrels, G. Chincarini, P. Giommi, et al. The Swift Gamma-Ray Burst Mission. *ApJ*, 611:1005–1020, August 2004. 171

[Gia13] G. Giavitto. *Observing the VHE Gamma-Ray Sky with the MAGIC Telescopes: the Blazar B3 2247+381 and the Crab Pulsar* . PhD thesis, IFAE, Barcelona, February 2013. 89, 286

[GM96] G. Ghisellini and P. Madau. On the origin of the gamma-ray emission in blazars. *MNRAS*, 280:67–76, May 1996. 41

[HAA+13a] H. E. S. S. Collaboration, A. Abramowski, F. Acero, F. Aharonian, et al. H.E.S.S and Fermi-LAT discovery of gamma rays from the blazar 1ES 1312-423. *ArXiv e-prints*, June 2013. 222

[HAA+13b] H.E.S.S. Collaboration, A. Abramowski, F. Acero, F. Aharonian, et al. Measurement of the extragalactic background light imprint on the spectra of the brightest blazars observed with H.E.S.S. *A&A*, 550:A4, February 2013. 36, 283

[Han13] W. F. Hanlon. Updated cosmic ray spectrum. Retrieved on 2013-05-07. http://www.physics.utah.edu/~whanlon/spectrum.html, March 2013. 26, 283

[Hay08] Masaaki Hayashida. *Observation of Very-High-Energy Gamma-Rays from Blazars with the MAGIC Telescope*. PhD thesis, University of Technology, Munich, March 2008. 105, 142

[HBB+03] J. Holder, I. H. Bond, P. J. Boyle, et al. Detection of TeV Gamma Rays from the BL Lacertae Object 1ES 1959+650 with the Whipple 10 Meter Telescope. *ApJ*, 583:L9–L12, January 2003. 103

[HBB04] D. Horan, H. M. Badran, and I. H. others Bond. Constraints on the Very High Energy Emission from BL Lacertae Objects. *ApJ*, 603:51–61, March 2004. 164

[HBK+08] M. Hayashida, C. Bigongiari, D. Kranich, et al. First simultaneous multiwavelength observation for the BL Lac object, 1ES1959+650 in a low state with MAGIC and Suzaku/Swift. In *International Cosmic Ray Conference*, volume 3 of *International Cosmic Ray Conference*, pages 1021–1024, 2008. 143, 144, 145

[Hil85] A. M. Hillas. Cerenkov light images of EAS produced by primary gamma. In F. C. Jones, editor, *International Cosmic Ray Conference*, volume 3 of *International Cosmic Ray Conference*, pages 445–448, August 1985. 69

[HMA+74] D. G. Hoskins, H. S. Murdoch, R. L. Adgie, J. H. Crowther, and H. Gent. Optical identifications for 45 radio sources based on accurate positions. *MNRAS*, 166:235–248, February 1974. 202

[HNS+99] J. Heidt, K. Nilsson, A. Sillanpää, L. O. Takalo, and T. Pursimo. High-resolution imaging of Einstein Slew Survey BL Lacertae objects. *A&A*, 341:683–692, January 1999. 100, 286

[Hor03] D. Horns. Multi-wavelength Observations of the TeV Blazars Mkn 421, 1ES1959+650, and H1426+428 with the HEGRA Cherenkov Telescopes and the RXTE X-ray Satellite. In L. O. Takalo and E. Valtaoja, editors, *High Energy Blazar Astronomy*, volume 299 of *Astronomical Society of the Pacific Conference Series*, page 13, July 2003. 103

[HST+09] C. C. Hsu, K. Satalecka, M. Thom, M. Backes, E. Bernardini, G. Bonnoli, N. Galante, F. Goebel, E. Lindfors, P. Majumdar, A. Stamerra, and R. M.

Wagner. Monitoring of bright blazars with MAGIC telescope. *ArXiv e-prints*, July 2009. 105, 126

[Jog09] Tobias Jogler. *Detailed study of the binary system LS I +61° 303 in VHE gamma-rays with the MAGIC telescope*. PhD thesis, Technische Universität München, December 2009. 64, 65, 68, 69, 74, 75, 285

[JSN+12] M. Janiak, M. Sikora, K. Nalewajko, R. Moderski, and G. M. Madejski. On the Origin of the γ-Ray/Optical Lags in Luminous Blazars. *ApJ*, 760:129, December 2012. 121, 122

[KAA+09] Y. Y. Kovalev, H. D. Aller, M. F. Aller, D. C. Homan, M. Kadler, K. I. Kellermann, Y. A. Kovalev, M. L. Lister, M. J. McCormick, A. B. Pushkarev, E. Ros, and J. A. Zensus. The Relation Between AGN Gamma-Ray Emission and Parsec-Scale Radio Jets. *ApJ*, 696:L17–L21, May 2009. 122, 158, 232

[KBM+04] T. M. Kneiske, T. Bretz, K. Mannheim, et al. Implications of cosmological gamma-ray absorption. II. Modification of gamma-ray spectra. *A&A*, 413:807–815, January 2004. 228

[KD10] T. M. Kneiske and H. Dole. A lower-limit flux for the extragalactic background light. *A&A*, 515:A19, June 2010. 37, 228, 235

[KGL+12] S. Klepser, G. Giavitto, M. Lopez, T. Y. Saito, T. Schweizer, I. Šnidarić, R. Zanin, and the Magic Collaboration. Phase-resolved Crab pulsar measurements from 25 to 400 GeV with the MAGIC telescopes. *Journal of Physics Conference Series*, 375(5):052022, July 2012. 88

[KHH+04] H. Krawczynski, S. B. Hughes, D. Horan, et al. Multiwavelength Observations of Strong Flares from the TeV Blazar 1ES 1959+650. *ApJ*, 601:151–164, January 2004. 103, 116, 117, 137, 287

[KHid05] L. Kuiper, W. Hermsen, J. in't Zand, and P. R. den Hartog. INTEGRAL detection of three AGN in the Cassiopeia region including a new source IGR J02097+5222. *The Astronomer's Telegram*, 662:1, November 2005. 162

[KTK02] M. Kino, F. Takahara, and M. Kusunose. Energetics of TeV Blazars and Physical Constraints on Their Emission Regions. *ApJ*, 564:97–107, January 2002. 154

[LBC+01] R. W. Lessard, J. H. Buckley, V. Connaughton, et al. A new analysis method for reconstructing the arrival direction of TeV gamma rays using a single imaging atmospheric Cherenkov telescope. *Astroparticle Physics*, 15:1–18, March 2001. 74

[Lin12] E. Lindfors. Privat communication, February 2012. 134, 171, 289, 290

[LKC+98] S. A. Laurent-Muehleisen, R. I. Kollgaard, R. Ciardullo, et al. Radio-loud Active Galaxies in the Northern ROSAT All-Sky Survey. III. New Spectroscopic Identifications from the RASS-Green Bank BL Lacertae Survey. *ApJS*, 118:127–175, September 1998. 181, 195

[LKF+99] S. A. Laurent-Muehleisen, R. I. Kollgaard, E. D. Feigelson, W. Brinkmann, and J. Siebert. The RGB Sample of Intermediate BL Lacertae Objects. *ApJ*, 525:127–143, November 1999. 181

[LM83] T.-P. Li and Y.-Q. Ma. Analysis methods for results in gamma-ray astronomy. *ApJ*, 272:317–324, September 1983. 77, 185

[Lom11] S. Lombardi. Advanced stereoscopic gamma-ray shower analysis with the MAGIC telescopes. In *International Cosmic Ray Conference*, volume 3 of *International Cosmic Ray Conference*, page 262, 2011. 67, 69, 165, 184, 185

[Lon92] Malcom Sim Longair. *High Energy Astrophysics*, volume 1. Cambridge University Press, 1992. 44, 284

[Lon11] M.S. Longair. *High Energy Astrophysics*. Cambridge University Press, 2011. 28

[Lyu03] Y. E. Lyubarsky. The termination shock in a striped pulsar wind. *MNRAS*, 345:153–160, October 2003. 89

[MAA+13] MAGIC Collaboration, J. Aleksić, L. A. Antonelli, P. Antoranz, et al. Discovery of very high energy gamma-ray emission from the blazar 1ES 1727+502 with the MAGIC Telescopes. *ArXiv e-prints*, February 2013. 222

[Man09] N. Mankuzhiyil. Observation of the unknown-redshift BL Lac B3 0133+388. Proposal: MAGIC application for observing time Cycle 5, February 2009. 183, 291

[MAP+12] N. Mankuzhiyil, S. Ansoldi, M. Persic, E. Rivers, R. Rothschild, and F. Tavecchio. Emitting Electrons and Source Activity in Markarian 501. *ApJ*, 753:154, July 2012. 177, 198

[Mar11] M. Mariotti. VHE detection of the blazar 1ES 0033+595 by MAGIC. *The Astronomer's Telegram*, 3719:1, October 2011. 161, 164, 178

[MBFH05] C. Masterson, W. Benbow, S. Funk, and H.E.S.S. Collaboration. Observations of the Crab nebula with H.E.S.S. In F. A. Aharonian, H. J. Völk, and D. Horns, editors, *High Energy Gamma-Ray Astronomy*, volume 745 of *American Institute of Physics Conference Series*, pages 617–621, February 2005. 87

[MBH+80] F. E. Marshall, E. A. Boldt, S. S. Holt, R. B. Miller, R. F. Mushotzky, L. A. Rose, R. E. Rothschild, and P. J. Serlemitsos. The diffuse X-ray background spectrum from 3 to 50 keV. *ApJ*, 235:4–10, January 1980. 33

[MDK+13] N. Milke, M. Doert, S. Klepser, D. Mazin, V. Blobel, and W. Rhode. Solving inverse problems with the unfolding program TRUEE: Examples in astroparticle physics. *Nuclear Instruments and Methods in Physics Research A*, 697:133–147, January 2013. 81

[MGC92] L. Maraschi, G. Ghisellini, and A. Celotti. A jet model for the gamma-ray emitting blazar 3C 279. *ApJ*, 397:L5–L9, September 1992. 153

[MGC+09] A. Moralejo, M. Gaug, E. Carmona, et al. MARS, the MAGIC Analysis and Reconstruction Software. *ArXiv e-prints*, July 2009. 67

[MHZ10] M. Meyer, D. Horns, and H.-S. Zechlin. The Crab Nebula as a standard candle in very high-energy astrophysics. *A&A*, 523:A2, November 2010. 90, 286

[MLP+97] R. Mirzoyan, E. Lorenz, D. Petry, et al. On the influence of afterpulsing in PMTs on the trigger threshold of multichannel light detectors in self-trigger mode. *Nuclear Instruments and Methods in Physics Research A*, 387:74–78, February 1997. 68

[MM12] D. Mazin and MAGIC Collaboration. Highlights from the MAGIC telescopes. In F. A. Aharonian, W. Hofmann, and F. M. Rieger, editors, *American Institute of Physics Conference Series*, volume 1505 of *American Institute of Physics Conference Series*, pages 186–193, December 2012. 183, 199, 234

[Moj13] C. Mojave. MOJAVE/2cm Survey Data Archive. http://www.physics.purdue.edu/astro/MOJAVE/sourcepages/1959+650.shtml, February 2013. 118, 119, 288

[NAB+93] P. L. Nolan, Z. Arzoumanian, D. L. Bertsch, J. Chiang, and at al. Observations of the Crab pulsar and nebula by the EGRET telescope on the Compton Gamma-Ray Observatory. *ApJ*, 409:697–704, June 1993. 87

[Nil12] K. Nilsson. Optical light curves of Blazars. http://users.utu.fi/kani/1m/, December 2012. 192, 204, 292

[Nil13] K. Nilsson. Images of RGB BL Lacertae objects. http://www.astro.utu.fi/research/agn100/images/0136.html, February 2013. 101, 182, 202, 287, 291, 292

[Nis99] T. Nishiyama. Detection of a new TeV gamma-ray source of BL Lac object 1ES 1959+650. In *International Cosmic Ray Conference*, volume 3 of *International Cosmic Ray Conference*, page 370, August 1999. 103

[NPT+07] K. Nilsson, M. Pasanen, L. O. Takalo, E. Lindfors, A. Berdyugin, S. Ciprini, and J. Pforr. Host galaxy subtraction of TeV candidate BL Lacertae objects. *A&A*, 475:199–207, November 2007. 170

[NPV+12] K. Nilsson, T. Pursimo, C. Villforth, E. Lindfors, et al. Redshift constraints for RGB 0136+391 and PKS 0735+178 from deep optical imaging. *A&A*, 547:A1, November 2012. 196, 200

[NTV06] E. Nieppola, M. Tornikoski, and E. Valtaoja. Spectral energy distributions of a large sample of BL Lacertae objects. *A&A*, 445:441–450, January 2006. 101, 102, 161, 162, 181, 182, 201, 202, 287, 290, 291, 292

[NTV+11] E. Nieppola, M. Tornikoski, E. Valtaoja, et al. Correlation between Fermi/LAT gamma-ray and 37 GHz radio properties of northern AGN averaged over 11 months. *A&A*, 535:A69, November 2011. 122, 158, 232

[OVR13] C. OVRO 40m Group. Radio light curves of Blazars. http://www.astro.caltech.edu/ovroblazars/data/data.php?page=data_return&source=J1959+6508, June 2013. 118

[PAC+92] M. Punch, C. W. Akerlof, M. F. Cawley, et al. Detection of TeV photons from the active galaxy Markarian 421. *Nature*, 358:477, August 1992. 103

[Pan13] D. Paneque. Privat communication, February 2013. 153, 249, 296

[PBM+11] E. Prandini, G. Bonnoli, L. Maraschi, M. Mariotti, and F. Tavecchio. TeV blazars and their distance. *ArXiv e-prints*, January 2011. 161, 175, 179, 181, 196, 200

[Per91] D. H. Perkins. *Hochenergiephysik*. Addison-Wesley-Verlag, Bonn, München, Reading„ 1991. 46

[Per00] E. S. Perlman. X-ray selected BL lacs and blazars. In B. L. Dingus, M. H. Salamon, and D. B. Kieda, editors, *American Institute of Physics Conference Series*, volume 515 of *American Institute of Physics Conference Series*, pages 53–65, June 2000. 161

[Pf09] A. Pichel and for the VERITAS Collaboration. Highlights from the Whipple 10-m Blazar Monitoring Program. *ArXiv e-prints*, July 2009. 105

[Pla13] C. Planck Group. Planck Cosmic Microwave Background. http://i.space.com/images/i/000/027/298/original/planck-cosmic-microwave-background-map.jpg, April 2013. 33, 283

[PMT11] E. Prandini, M. Mariotti, and F. Tavecchio. Constraining blazars distances with combined GeV and TeV data. *ArXiv e-prints*, November 2011. 233

[PMW+85] R. A. Preston, D. D. Morabito, J. G. Williams, et al. A VLBI survey at 2.29 GHz. *AJ*, 90:1599–1641, September 1985. 203

[PPG+07] S. Piranomonte, M. Perri, P. Giommi, H. Landt, and P. Padovani. High energy peaked BL Lacs optical spectros. (Piranomonte+, 2007). *VizieR Online Data Catalog*, 347:787, October 2007. 195

[PSS+96] E. S. Perlman, J. T. Stocke, J. F. Schachter, M. Elvis, E. Ellingson, C. M. Urry, M. Potter, C. D. Impey, and P. Kolchinsky. The Einstein Slew Survey Sample of BL Lacertae Objects. *ApJS*, 104:251, June 1996. 104, 175, 287, 291

[RBP05] A. Reimer, M. Böttcher, and S. Postnikov. Neutrino Emission in the Hadronic Synchrotron Mirror Model: The "Orphan" TeV Flare from 1ES 1959+650. *ApJ*, 630:186–190, September 2005. 103

[Ree67] M. J. Rees. Studies in radio source structure-I. A relativistically expanding model for variable quasi-stellar radio sources. *MNRAS*, 135:345, 1967. 153

[RGS03] T. A. Rector, D. C. Gabuzda, and J. T. Stocke. The Radio Structure of High-Energy-Peaked BL Lacertae Objects. *AJ*, 125:1060–1072, March 2003. 162, 163, 290

[RKM+05] P. W. A. Roming, T. E. Kennedy, K. O. Mason, et al. The Swift Ultra-Violet/Optical Telescope. *Space Sci. Rev.*, 120:95–142, October 2005. 171

[RL79] G.B. Rybicki and A.P. Lightman. *Radiative Processes in Astrophysics*. A Wiley-Interscience publication. Wiley, 1979. 28

[Sat10] Konstancja Satalecka. *Multimessenger studies of point-sources using the IceCube neutrino telescope and the MAGIC gamma-ray telescope*. PhD thesis, Humboldt-University Berlin, May 2010. 105, 142

[Sch94] M. Schmelling. The method of reduced cross-entropy A general approach to unfold probability distributions. *Nuclear Instruments and Methods in Physics Research A*, 340:400–412, February 1994. 81

[SdS92] F. W. Stecker, O. C. de Jager, and M. H. Salamon. TeV gamma rays from 3C 279 - A possible probe of origin and intergalactic infrared radiation fields. *ApJ*, 390:L49–L52, May 1992. 175, 196

[ŞEBM13] G. D. Şentürk, M. Errando, M. Böttcher, and R. Mukherjee. Gamma-ray Observational Properties of TeV-detected Blazars. *ApJ*, 764:119, February 2013. 222, 224, 225, 226, 230, 235

[SFD98] D. J. Schlegel, D. P. Finkbeiner, and M. Davis. Maps of Dust Infrared Emission for Use in Estimation of Reddening and Cosmic Microwave Background Radiation Foregrounds. *ApJ*, 500:525, June 1998. 170

[SHB+09] K. Satalecka, C.-C. Hsu, E. Bernardini, G. Bonnoli, N. Galante, F. Goebel, E. Lindfors, P. Majumdar, A. Stamerra, and R. Wagner. Monitoring of Bright Blazars with MAGIC in the 2007/2008 Season. In D. Bastieri and R. Rando, editors, *American Institute of Physics Conference Series*, volume 1112 of *American Institute of Physics Conference Series*, pages 223–232, April 2009. 105

[Sid08] N. Sidro. *Discovery and characterization of the binary system LSI +61.303 in very high energy gamma-rays with MAGIC*. PhD thesis, Institut de Fiysica d'Altes Energies Universitat Autonoma de Barcelona, 2008. 45, 284

[SR68] D. H. Staelin and E. C. Reifenstein, III. Pulsating Radio Sources near the Crab Nebula. *Science*, 162:1481–1483, December 1968. 87

[SRM+05] D. Sowards-Emmerd, R. W. Romani, P. F. Michelson, S. E. Healey, and P. L. Nolan. A Northern Survey of Gamma-Ray Blazar Candidates. *ApJ*, 626:95–103, June 2005. 203, 292

[SSP+93] J. F. Schachter, J. T. Stocke, E. Perlman, M. Elvis, R. Remillard, A. Granados, J. Luu, J. P. Huchra, R. Humphreys, C. M. Urry, and J. Wallin. Ten new BL Lacertae objects discovered by an efficient X-ray/radio/optical technique. *ApJ*, 412:541–549, August 1993. 100

[Ste12] Burkhard Steinke. *First study of fast variability in Markarian 421 with the MAGIC stereoscopic system*. PhD thesis, Technische Universität München, April 2012. 39, 46, 49, 51, 52, 54, 55, 62, 63, 69, 76, 115, 116, 149, 159, 284, 285

[STF05] B. Sbarufatti, A. Treves, and R. Falomo. Imaging Redshifts of BL Lacertae Objects. *ApJ*, 635:173–179, December 2005. 162, 175, 179, 233

[SUF+99] R. Scarpa, C. M. Urry, R. Falomo, J. E. Pesce, R. Webster, M. O'Dowd, and A. Treves. The Hubble Space Telescope Survey of BL Lacertae Objects: Gravitational Lens Candidates and Other Unusual Sources. *ApJ*, 521:134–144, August 1999. 162, 163, 290

[TA77] Andrey N. Tikhonov and Vasiliy Y. Arsenin. *Solutions of ill-posed problems*. V. H. Winston & Sons, Washington, D.C.: John Wiley & Sons, New York, 1977. Translated from the Russian, Preface by translation editor Fritz John, Scripta Series in Mathematics. 81

[TAB+09] D. Tescaro, J. Aleksic, M. Barcelo, et al. The readout system of the MAGIC-II Cherenkov Telescope. *ArXiv e-prints*, July 2009. 64

[Tav10] F. Tavecchio. Gamma-ray emission from AGNs. *ArXiv e-prints*, January 2010. 212, 213, 293

[TBM10] J. Tueller, W. H. Baumgartner, and C. B. others Markwardt. The 22 Month Swift-BAT All-Sky Hard X-ray Survey. *ApJS*, 186:378–405, February 2010. 162

[TGG+10] F. Tavecchio, G. Ghisellini, G. Ghirlanda, L. Foschini, and L. Maraschi. TeV BL Lac objects at the dawn of the Fermi era. *MNRAS*, 401:1570–1586, January 2010. 148, 149, 177, 179, 198, 200, 204, 212

[TMG98] F. Tavecchio, L. Maraschi, and G. Ghisellini. Constraints on the Physical Parameters of TeV Blazars. *ApJ*, 509:608–619, December 1998. 154, 177

[Ton06] Nadia Tonello. *Study of the VHE gamma-ray emission from the Active Galactic Nucleus 1ES1959+650*. PhD thesis, University of Technology, Munich, February 2006. 29, 30, 105

[TVT+94] M. Tornikoski, E. Valtaoja, H. Terasranta, et al. Correlated radio and optical variations in a sample of active galactic nuclei. *A&A*, 289:673–710, September 1994. 122

[ULD+03] P. Ubertini, F. Lebrun, G. Di Cocco, et al. IBIS: The Imager on-board INTEGRAL. *A&A*, 411:L131–L139, November 2003. 172

[ULM+12] M. Uellenbeck, S. Lombardi, N. Mankuzhiyil, M. Palatiello, et al. Discovery of the long hunted blazar 1ES 0033+595 by the MAGIC telescopes. In F. A. Aharonian, W. Hofmann, and F. M. Rieger, editors, *American Institute of Physics Conference Series*, volume 1505 of *American Institute of Physics Conference Series*, pages 494–497, December 2012. 164

[UM09] (Thom) Uellenbeck M. Anaylse der Quelle 1ES 1959+650 mit MAGIC und die Implementierung eines Webinterfaces für die automatische Monte-Carlo-Produktion. Master's thesis, TU Dortmund University, July 2009. 105, 142, 143, 144, 145

[UP95] C. M. Urry and P. Padovani. Unified Schemes for Radio-Loud Active Galactic Nuclei. *PASP*, 107:803, September 1995. 38, 39

[VAA+11] VERITAS Collaboration, E. Aliu, T. Arlen, T. Aune, et al. Detection of Pulsed Gamma Rays Above 100 GeV from the Crab Pulsar. *Science*, 334:69–, October 2011. 88

[VP12] T. M. Venters and V. Pavlidou. Probing the Intergalactic Magnetic Field with the Anisotropy of the Extragalactic Gamma-ray Background. *ArXiv e-prints*, January 2012. 34

[VV93] M.-P. Veron-Cetty and P. Veron. Spectroscopic observations of sixteen BL Lacertae candidates. *A&AS*, 100:521–529, September 1993. 201

[Wag08] Robert Wagner. *Very High Energy Blazar Astrophysics*. PhD thesis, TU Munich University, June 2008. 35, 37, 44, 46, 47, 50, 51, 52, 116, 148, 154, 221, 223, 230, 284, 289

[Wag09] R. Wagner. The MAGIC telescopes. https://wwwmagic.mpp.mpg.de/gallery/pictures/, May 2009. 58, 284

[Wag11] R. Wagner. Monitoring of bright, nearby Active Galactic Nuclei with the MAGIC telescopes. In *International Cosmic Ray Conference*, volume 8 of *International Cosmic Ray Conference*, page 143, 2011. 105

[WCD+03] C. Winkler, T. J.-L. Courvoisier, G. Di Cocco, et al. The INTEGRAL mission. *A&A*, 411:L1–L6, November 2003. 172

[WCF+89] T. C. Weekes, M. F. Cawley, D. J. Fegan, K. G. Gibbs, A. M. Hillas, P. W. Kowk, R. C. Lamb, D. A. Lewis, D. Macomb, N. A. Porter, P. T. Reynolds, and G. Vacanti. Observation of TeV gamma rays from the Crab nebula using the atmospheric Cerenkov imaging technique. *ApJ*, 342:379–395, July 1989. 90

[WH13] S. Wakely and D. Horan. TeVcat. http://tevcat.uchicago.edu, February 2013. 218, 293

[WS10] M. Weidinger and F. Spanier. Modelling the variability of 1ES1218+30.4. *A&A*, 515:A18, June 2010. 154, 156

[WW90] D. M. Worrall and B. J. Wilkes. X-ray spectra of compact extragalactic radio sources. *ApJ*, 360:396–407, September 1990. 203

[WXDH00] J. Y. Wei, D. W. Xu, X. Y. Dong, and J. Y. Hu. RASS AGN sample (Wei+, 1999). *VizieR Online Data Catalog*, 413:90575, February 2000. 195

[Zan06] Roberta Zanin. Observation and analysis of vhe gamma emission from the agn 1es1959+650 with the magic telescope. Master's thesis, Universita di Padova, September 2006. 105, 142

[Zan11a] R. Zanin. MAGIC measurement of the Crab Nebula spectrum over three decades in energy. In *International Cosmic Ray Conference*, volume 7 of *International Cosmic Ray Conference*, page 71, 2011. 91, 286

[Zan11b] Roberta Zanin. *Observation of the Crab pulsar wind nebula and microquasar candidates with MAGIC*. PhD thesis, Universitat Autonoma de Barcelona, September 2011. 72, 73, 74, 75, 78, 285

ACKNOWLEDGEMENTS

At this point, I would like to thank my supervisor Prof. Dr. Dr. Wolfgang Rhode for giving me the possibility of writing a Ph.D. thesis in this exciting field of research and for his support throughout the last four years.

Further, I would like to thank Prof. Dr. Westphal for his willingness and his efforts involved in being the second assessor of this thesis.

I thank the astroparticle physics working group at TU Dortmund, with whom I shared the wonderful and exciting adventure of making research in the field of VHE γ–ray astrophysics. In this context my special thanks are dedicated to Marlene Doert for sharing a birthday and many discussions and thoughts (not only about physics ;-), as well as to Michael Backes and Nikola Strah for critical questions and encouragement over the years.

My thanks also go to my proofreaders Sebastian Uellenbeck, Nikola Strah, Natalia Lewandowska, Nijil Mankuzhiyil and Tobias Fischer-Wasels. Their comments and suggestions helped a lot to improve this work.

Unter diesen Danksagungen möchte ich ganz besonders meiner Familie danken. Sie hat in den vergangenen fast vier Jahren nur zu gut verstehen gelernt, weshalb so oft in Danksagungen von Unterstützung, Verständnis sowie Geduld die Rede ist.

Nicht zuletzt möchte ich ganz besonders meinen Eltern, Iwona und Czesław dafür danken, dass sie immer an mich geglaubt haben und mich immer auf meinem gesamten Lebensweg unterstützt haben.
Dziękuję za wszystko. Jesteście wspaniali!

Abschließen möchte ich insbesondere meinem Ehemann Sebastian Uellenbeck dafür Danken, dass er immer zu mir gestanden hat und mich immer bei der Verwirklichung meiner Träume unterstützt hatte :-).